Photoproduction of pion pairs off nucleons

Inauguraldissertation

zur
Erlangung der Würde eines Doktors der Philosophie
vorgelegt der
Philosophisch-Naturwissenschaftlichen Fakultät
der Universität Basel

von

Markus Oberle

aus Full-Reuenthal, AG

Basel, 2014

Genehmigt von der Philosophisch-Naturwissenschaftlichen Fakultät auf Antrag von

Prof. Dr. B. Krusche
Prof. Dr. V. Metag

Basel, 20. Mai 2014

Prof. Dr. Jörg Schibler
Dekan

Abstract

In the absence of a solution for Quantum Chromodynamics (QCD) in the low energy regime, so called effective models are being used to describe the nucleon and its excited states. These models include the basic symmetries from QCD, but on the other hand, compared to quarks and gluons, use higher lying degrees of freedom.

Experimental contributions are mandatory to validate these models and fix free parameters. Today still most of the world-data in this field was obtained by meson-induced excitation of the nucleon. Even though numerous excited states of the nucleon could be identified, the number of model predicted states is much higher. This is known as the missing resonance problem. One explanation could be that some excited states just couple weakly to πN (KN) and hence the excitation via photons was proposed to further test the model predictions.

During the last 15 years, much experimental effort was made at various photoproduction facilities like MAMI, ELSA, JLab or ESRF and a large number of states could be confirmed, but the missing resonance problem could not be solved. Higher lying resonances ($M > 1.6$ GeV) decay preferably via sequential decays with many meson final states, and especially double pion decay channels are assumed to dominate in this region. The reactions investigated in this work, namely $\gamma p(n) \rightarrow \pi^0\pi^0 p(n)$, $\gamma n(p) \rightarrow \pi^0\pi^0 n(p)$, $\gamma p \rightarrow \pi^0\pi^0 p$, $\gamma p(n) \rightarrow \pi^0\pi^+ n(n)$, $\gamma n(p) \rightarrow \pi^0\pi^- p(p)$, $\gamma p \rightarrow \pi^0\pi^+ n$ thus form the primary source of information on photocouplings of higher lying resonances.

This work explores neutral and mixed-charge double pion production channels up to invariant masses of the final state center-of-mass system of about 1.9 GeV and presents unpolarized as well as single-polarized observables. All results have high precision, are compared to different model predictions, and will considerably constrain future model analyses in the field of double pion photoproduction and beyond.

The data of this work were taken at MAMI in four different experiments with liquid hydrogen and deuterium targets in 2007 and 2009 and include over 600 hours of beam time. A longitudinally polarized electron beam was used to produce circularly polarized bremsstrahlung photons with energies up 1.4 GeV. The reaction products, charged pions, photons and nucleons, were detected in the combined calorimeter consisting of Crystal Ball and TAPS.

Total and differential cross sections, invariant mass distributions of $N\pi$ and $\pi\pi$ and beam helicity asymmetries were computed in the fully reconstructed final state center-of-mass system. Effects from Fermi motion in the deuteron target could be reliably defolded leading to a good agreement between free and quasifree proton data, and thus the neutron results can be interpreted as a good approximation of free neutron data.

Beam-helicity asymmetries for $\gamma n(p) \rightarrow \pi^0\pi^0 n(p)$ and $\gamma n(p) \rightarrow \pi^0\pi^- p(p)$ have been measured for the first time and published together with the results from the proton data. Especially for the mixed-charge results, the available model calculations fail to reproduce the data, and for the neutral channel data, an unexpected similarity for proton and neutron results was observed.

Total and differential cross sections as well as invariant mass distributions of $N\pi$ and $\pi\pi$ for $\gamma n(p) \rightarrow \pi^0\pi^- p(p)$ have also been measured for the first time and previous results for $\gamma p(n) \rightarrow \pi^0\pi^+ n(n)$ could be reproduced and extended into the third resonance region.

Contents

List of Figures

List of Tables

Chapter 1

Introduction

In this first chapter the investigation of excited nucleon states and some difficulties will be briefly introduced. In section 1.1 a basic introduction is given followed by a more detailed contemplation of photoproduction of pseudoscalar mesons in section 1.2. Sections 1.3 and 1.4 will guide through theoretical background, effective models and the experimental history of the neutral and the mixed-charge double pion channels. In section 1.5 the most important points from the previous sections are summarized and the realization of this work is motivated.

1.1 Excited Nucleon States

Valence quarks, gluons and quark-antiquark pairs are the building blocks of the nucleon as we know it today. The force is the strong interaction and the basic theory of it is Quantum Chromodynamics (QCD). The resolvability via perturbative methods of this theory depends strongly on the energy scale and decreases rapidly towards lower energies due to the growing coupling constant. The nucleon, lying in the low energy regime, where the peturbative approach fails, forms thus an extremely complicated system in terms of QCD.

In the absence of a direct solution for QCD, lattice gauge theory calculations combined with methods from chiral perturbation theory, in order to extrapolate to physical quark masses, is one of the most successful theoretical approaches and yields some nucleon properties with good accuracy [2, 3]. Most recent progress came also from the application of the Dyson-Schwinger equation to the QCD Lagrangian [4, 5, 6]. With this approach lattice QCD results could reproduce the excitation spectrum known from calculations based on nonrelativistic constituent quark models.

Still one should not forget that these calculations are not yet fully matured and will improve strongly in the future and, therefore, most theoretical predictions nowadays are still coming from effective, by Quantum Chromodynamics inspired

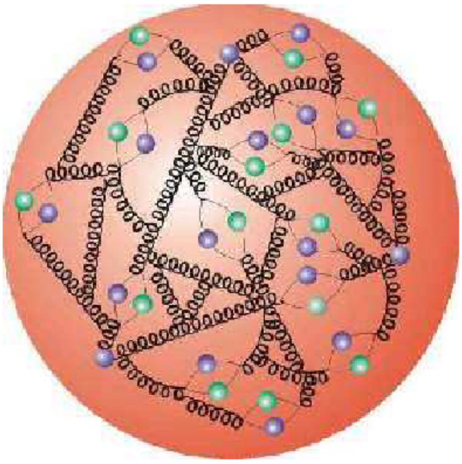

Fig. 1.1: Artistic view of the nucleon. Taken from [1].

models. These effective models break down the complex structure of the nucleon and paint the picture of a few quarks, subsumming the known properties of the baryons. Most of the successful predictions come from calculations based on 'constituent quark models'. This quite simple idea, the complicated inner structure is replaced by three heavy (constituent) quarks, represents a surprisingly good approximation.

Progress in the identification of the relevant degrees-of-freedom, in which the internal symmetries of the underlying fundamental interaction must be reflected, is the most important input for the understanding of the nucleon structure. By measuring as many observables as possible with high accuracy on the experimental side, these model predictions can be tested in detail and the fundamental properties of the strong interaction can by this means be revealed step by step.

In nucleon resonance spectroscopy the following notation is used to classify the excited states

$$\mathbf{L_{2I2J}(M)},$$

where

L is the angular momentum of a decay into πN with $S = 0$, $P = 1$, $D = 2...$

I is the isospin of the resonance

J is the spin of the resonance and

M is the mass of the resonance

In this notation the famous Δ resonance for example writes as $P_{33}(1232)$.

Most data for nucleon resonances was gathered in meson induced excitation experiments via pions and kaons and revealed several complications. First of all, the number of resonances predicted by model calculations is much higher than the number of experimentally detected ones. Since the number of states follows from the number of effective degrees-of-freedom (DOF) in the model, the number of DOF could be too high. The experiments showed that the resonance widths are large and strongly overlapping, which is due to the hadronic decay with very short lifetimes τ of about 10^{-24} s. This allows the conclusion that some states are maybe just too suppressed to be seen, or only have a weak coupling to πN and KN and thus can not be detected experimentally.

Photoexcitation offers another experimental approach and has a different production vertex and thus different coupling to the resonances can be explored. Furthermore, photoproduction of mesons allows to investigate electromagnetic transition amplitudes, introduced later in this chapter. Figure 1.2 shows the total photoabsorption spectra for proton and neutron as a function of the invariant mass of the photon-nucleon system. Some well established resonances are plotted as dotted blue lines. The first three large peaks, best seen in the spectrum for the proton, are called first, second, and third resonance region, and contain several different resonances. The strong overlap of theses excited nucleon states is a huge challenge for the exploration of nucleons.

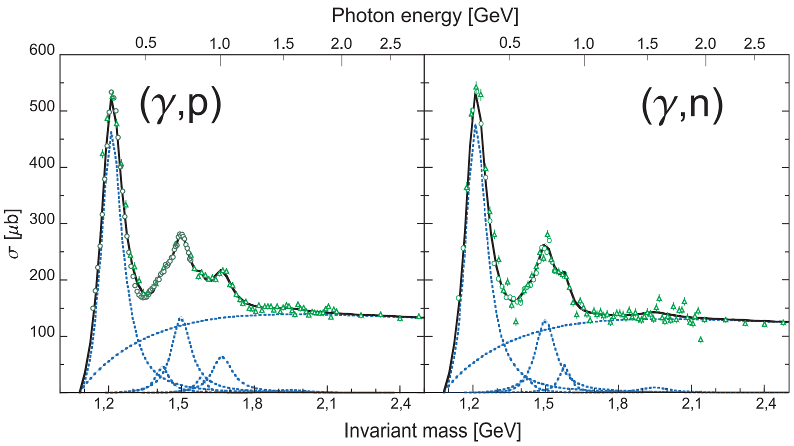

Fig. 1.2: The measured total photoabsorption spectra for the proton on the left hand side, and for the neutron on the right hand side. Most reliably explored resonance contributions are plotted as blue dotted curves. Taken from [7].

Consequently, one of the most important experimental tasks is the disentanglement of these overlaps and extracting single resonances in order to explore their properties as detailed as possible.

1.2 Photoexcitation of Pseudoscalar Mesons

Higher lying resonances with masses larger than 1.6 GeV decay predominantly via intermediate states, in many cases via $\Delta(1232)$ back into the ground state. Since excited nucleon states decay almost exclusively via meson emission, multiple meson final states are the most probable ones for these heavier resonances. It is assumed that the double pion final states are overall the most dominant decay modes, and thus form our prevalent source of information on the photocoupling mechanism for resonances from the third region. To have a closer look into the complications faced in this field, the formalism of photoproduction of pseudoscalar mesons will be discussed now.

To describe the following process in which one pseudoscalar meson is produced

$$\gamma + N \rightarrow m + N', \tag{1.1}$$

we need the scattering matrix S, which gives the probability of a transition of the initial state $|i\rangle$ into the final state $|f\rangle$ as $P(|i\rangle \rightarrow |f\rangle)$, and is defined as

$$S_{if} = \frac{\delta^4(p_{N'} + p_m - p_N - p_\gamma)}{(2\pi)^2} \cdot \sqrt{\frac{M_N^2}{4E_{N'}E_m E_N E_\gamma}} \cdot T_{if}, \tag{1.2}$$

using the kinematics $p_\gamma + p_N = p_M + p_{N'}$, the nucleon mass M_N and the energies and four-momenta E_i, p_i [8, 9]. The Lorentz invariant matrix elements T_{if} describe the transition and can be expressed with Pauli spinors as

$$T_{fi} = \frac{4\pi W}{M_N} \langle \chi(N') | \mathcal{F} | \chi(N) \rangle . \tag{1.3}$$

W is the center-of-mass energy $W = \sqrt{s} = \sqrt{(p_\gamma + p_N)^2}$ and $\mathcal{F}$ is given as

$$\begin{aligned} \mathcal{F} = i\vec{\sigma} \cdot \vec{\epsilon}\mathcal{F}_1 + (\vec{\sigma} \cdot \hat{p}_m)(\vec{\sigma} \cdot (\hat{p}_\gamma \times \vec{\epsilon}))\mathcal{F}_2 + \\ i(\vec{\sigma} \cdot \hat{p}_\gamma)(\hat{p}_m \cdot \vec{\epsilon})\mathcal{F}_3 + i(\vec{\sigma} \cdot \hat{p}_m)(\hat{p}_m \cdot \vec{\epsilon})\mathcal{F}_4, \end{aligned} \tag{1.4}$$

where $\vec{\epsilon}$ is the polarization vector of the photon, $\vec{\sigma}$ a vector with the Pauli matrices, and $\hat{p}_m$, $\hat{p}_\gamma$ are the unit vectors of meson and photon. $\mathcal{F}_i$ are called the CGNL amplitudes after Chew, Goldberger, Nambu and Low [10]. Initially we have $2 \times 2 \times 2$ spin configurations out of which 4 remain, the rest are eliminated due to parity conservation. These four complex amplitudes depend on the center-of-mass energy W and the polar angle θ_m^* of the meson in the center-of-mass frame. A fully model independent description of such a reaction requires knowing all four complex amplitudes $\mathcal{F}_i$. This means determining seven independent real quantities, since the overall phase is arbitrary, and this for each incident photon energy and each meson angle. To have a 'complete' experiment one has to measure unpolarized, single-polarized and double-polarized observables with high precision. Which combination of observables to measure to determine the required variables for a complete description of the process, with as few measurements as possible, is far from trivial.

In 1997 Chiang and Tabakin [11] found an answer to the question, which observables have to be measured to have the 'smallest complete' experiment. By measuring eight well chosen observables, the amplitudes can be uniquely determined and the reaction would be understood. However, this is experimentally overambitious, especially due to the limited precision and therefore, we still need to rely on reaction models. One has to do a so called partial-wave analysis of the observables and is being left with the overall phase depending on W. Every measured observable assists thus in constraining the solutions of partial wave analysis and approximating a precise description of the reaction. The unpolarized differential cross section in the center-of-mass system using the CGLN amplitudes writes as

$$\begin{aligned}\frac{p_\gamma^*}{p_m^*}\frac{d\sigma}{d\Omega} = &\left[|\mathcal{F}_1|^2 + |\mathcal{F}_2|^2 + 1/2|\mathcal{F}_3|^2 + 1/2|\mathcal{F}_4^2 + Re(\mathcal{F}_1\mathcal{F}_3^*)\right] \\ &+ \left[Re(\mathcal{F}_3\mathcal{F}_4^*) - 2Re(\mathcal{F}_1\mathcal{F}_2^*)\right] \cdot \cos(\theta_m^*) \\ &- \left[1/2|\mathcal{F}_3|^2 + 1/2|\mathcal{F}_4|^2 + Re(\mathcal{F}_1\mathcal{F}_4^*) + Re(\mathcal{F}_2\mathcal{F}_3^*)\right] \cdot \cos^2(\theta_m^*) \\ &- \left[Re(\mathcal{F}_3\mathcal{F}_4^*)\right] \cdot \cos^3(\theta_m^*),\end{aligned} \tag{1.5}$$

with p_γ^*, p_m^* and θ_m^* in the center-of-mass system and $\mathcal{F}_i^*$ as the complex conjugated of $\mathcal{F}_i$. The photon field can be expanded in electric and magnetic multipoles ($E_{l\pm}$, $M_{l\pm}$), depending on the angular momentum L and the parities $P_\gamma = (-1)^L$ and $P_\gamma = (-1)^{L+1}$ for electric and magnetic case, respectively. Applying this on the CGNL amplitudes, we can write $\mathcal{F}_i$ as

$$\begin{aligned}\mathcal{F}_1(\theta_m^*) &= \sum_{l=0}^{\infty}\left[lM_{l+} + E_{l+}\right]P'_{l+1}(\cos(\theta_m^*)) + \left[(l+1)M_{l-} + E_{l-}\right]P'_{l-1}(\cos(\theta_m^*)) \\ \mathcal{F}_2(\theta_m^*) &= \sum_{l=0}^{\infty}\left[(l+1)M_{l+} + lM_{l-}\right]P'_{l}(\cos(\theta_m^*)) \\ \mathcal{F}_3(\theta_m^*) &= \sum_{l=0}^{\infty}\left[E_{l+} - M_{l+}\right]P''_{l+1}(\cos(\theta_m^*)) + \left[E_{l-} + M_{l-}\right]P''_{l-1}(\cos(\theta_m^*)) \\ \mathcal{F}_4(\theta_m^*) &= \sum_{l=0}^{\infty}\left[M_{l+} - E_{l+} - M_{l-} - E_{l-}\right]P''_{l}(\cos(\theta_m^*)),\end{aligned} \tag{1.6}$$

with the Legendre polynomials P and the relative orbital momentum l of the final meson-nucleon system. To denote, whether the nucleon spin has to be added or subtracted from l to get the total angular momentum of the final state, the index carries + or −. If we have a clearly one-resonance dominated cross section, like $P_{33}(1232)$ dominates in the case of the single pion cross section, the angular distribution reflects the quantum number of the state, as visible in Fig.1.3.

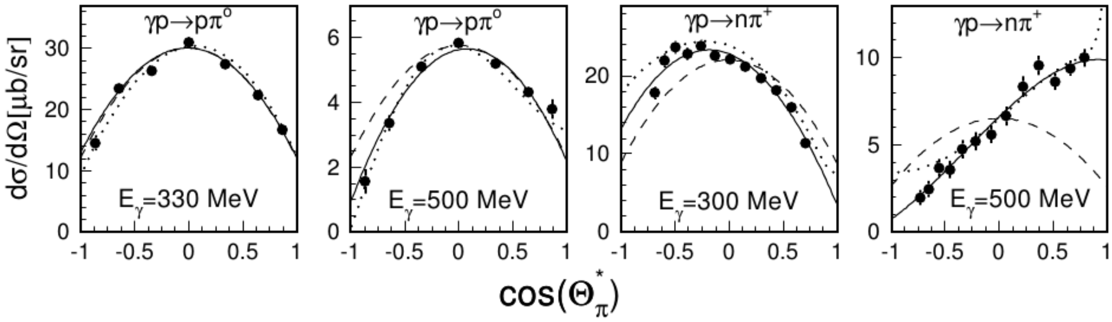

Fig. 1.3: Differential cross section for $\gamma + p \to \pi^0 + p$ (left) and $\gamma p \to \pi^+ + n$ (right). The expected behavior of the M_{1+}-multipole $((5 - 3\cos^3(\theta^*_m)))$ is plotted as dashed curve and very nicely reproduced by the data points from [12, 13] (except for the spectrum on the right, see text). Solid curves: fits to the data, dotted curves MAID2000 model [14] (full calculation with all terms included).

The angular distribution holds a certain ambiguity, since they depend on the spin of the resonance and the order of the photon multipole but leave a freedom in the combination of parities of multipole and resonance. This problem can be overcome by polarization observables, like the beam helicity asymmetry, which is part of this work.

Meson photoproduction is complicated by the treatment of the isospin, since the latter is not conserved at the electromagnetic vertex, in contrast to the hadronic vertex. We can distinguish isoscalar (IS, with $\Delta I = 0$) and isovector (IV, with $\Delta I = 0, \pm 1$) components as part of the electromagnetic current and thus have to reconstruct the amplitudes of the multipoles from different isospin contributions. Splitting up the transition operator in an isoscalar $\mathcal{S}$ and an isovector part $\mathcal{V}$ for the photoproduction of isovector mesons off nucleons we get three independent matrix elements

$$\begin{aligned} A^{IS} &= \left\langle \frac{1}{2}, \pm\frac{1}{2} \right| \mathcal{S} \left| \frac{1}{2}, \pm\frac{1}{2} \right\rangle \\ \pm A^{IV} &= \left\langle \frac{1}{2}, \pm\frac{1}{2} \right| \mathcal{V} \left| \frac{1}{2}, \pm\frac{1}{2} \right\rangle \\ A^{V3} &= \left\langle \frac{3}{2}, \pm\frac{1}{2} \right| \mathcal{V} \left| \frac{1}{2}, \pm\frac{1}{2} \right\rangle, \end{aligned} \tag{1.7}$$

using the notation $\langle I_f, I_{f3} | \, \mathcal{A} \, | I_i, I_{i3} \rangle$.

As an example we will now express the multipole amplitude for single pion photoproduction in isoscalar and isovector parts as follows

$$\begin{aligned}
A(\gamma p \to \pi^+ n) &= -\sqrt{\frac{1}{3}}A^{V3} + \sqrt{\frac{2}{3}}\left(A^{IV} - A^{IS}\right) \\
A(\gamma p \to \pi^0 p) &= +\sqrt{\frac{2}{3}}A^{V3} + \sqrt{\frac{1}{3}}\left(A^{IV} - A^{IS}\right) \\
A(\gamma n \to \pi^- p) &= +\sqrt{\frac{1}{3}}A^{V3} - \sqrt{\frac{2}{3}}\left(A^{IV} + A^{IS}\right) \\
A(\gamma n \to \pi^0 n) &= +\sqrt{\frac{2}{3}}A^{V3} + \sqrt{\frac{1}{3}}\left(A^{IV} + A^{IS}\right). \qquad (1.8)
\end{aligned}$$

A complete description of the photoproduction amplitudes is strongly complicated by the isospin. From the equations 1.8, we deduce that the measurement of at least three of the four channels is necessary in order to designate A^{V3}, A^{IS} and A^{IV}. Consequently, measurements on the proton only are insufficient for determining the isospin amplitudes of the electromagnetic transition, and thus measurements on the neutron are inevitable. Due to the relatively small binding energies and the rather well understood nuclear structure, the deuteron makes the preferable target for measurements on the neutron.

For photoproduction of pseudoscalar meson pairs the situation is even more complicated, since it involves eight complex amplitudes, each one depending on five kinematic variables [15]. Only extracting the magnitude of all amplitudes nonambiguously demands the measurement of eight independent observables. To additionally fix all phases it is necessary to measure 15 observables, and of course ambiguities from the finite statistical precision of the data are not even considered in this calculation. Altogether, it is thus clear that a complete measurement is unrealistic, but nevertheless the measurement of different observables is mandatory for progress in this field.

In the next sections we will have a closer look into the theoretical background and the experimental history of the investigated decay modes.

1.3 The Neutral Channel

Double pion final states are especially interesting for two reasons. First of all, as mentioned in the beginning, these channels are our dominant source of information on higher lying resonances, from 1.6 GeV to the limit of the MAMI energy (about 1.95 GeV in center-of-mass energy), because these states tend to decay sequentially. These sequential decays offer secondly the possibility of exciting (intermediate) resonances which have a low chance of being excited from the ground state. Previous measurements for $\gamma N \to \pi^0\pi^0 N$ have been studied thoroughly up to photon energies of about 0.9 GeV, exploring states from the second resonance region, like $P_{11}(1440)$, $S_{11}(1535)$ and $D_{13}(1520)$. Total cross sections, invariant mass and angular distributions have been measured at the MAMI accelerator in Mainz with the DAPHNE, TAPS and Crystal Ball detectors [16, 17, 18, 19, 20, 21, 22, 23, 24, 25, 26], further at GRAAL in Grenoble [27, 28], at ELSA in Bonn [24, 29] and at JLab with the CLAS detector using electron beams [30].

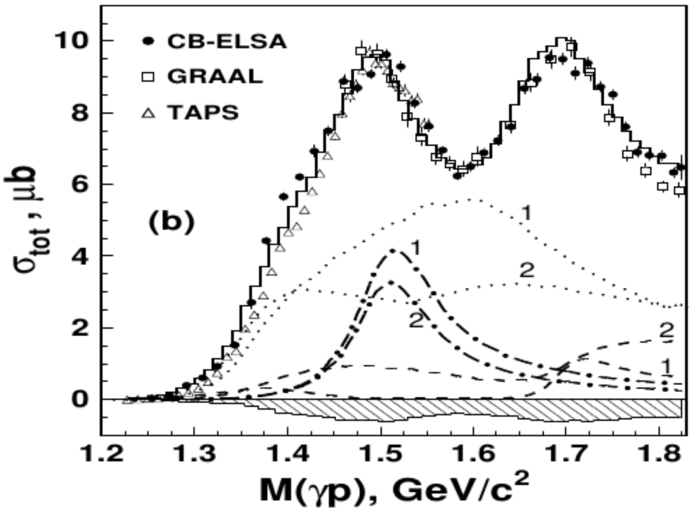

Fig. 1.4: Total cross section for $\gamma p \to \pi^0\pi^0 p$. Full dots: CB-ELSA [29], open triangles: A2-TAPS [24], open squares: GRAAL [27], solid line: Partial wave analysis (PWA) fit. Two different PWA solutions (1 and 2) are plotted (see [24]). Dotted line: D_{33} partial wave, dashed-dotted line: D_{13} partial wave, dashed line: P_{11} partial wave. Taken from [24].

Figure 1.4 shows the total cross section for $\gamma p \to \pi^0\pi^0 p$ as function of the final state center-of-mass energy W. Two different PWA solutions (with similar likelihood [24]) are shown. The D_{33} partial wave contribution gives overall the strongest contribution for both solutions. The contributions from the D_{13} partial wave are large in the second resonance region but only minor in the third one. The contributions from the P_{11} partial wave are small, but increase towards higher energies. In this two PWA solutions the dip between the two resonance regions is produced by the interference of the D_{33} and the D_{13} partial waves.

In figure 1.5 the invariant mass distribution of $\pi^0\pi^0$ and $p\pi^0$ are plotted together with a phase space distribution as thin line and the contributions from $\Delta^+\pi^0 \to \pi^0\pi^0 p$ (dashed) and $p(\pi^0\pi^0)$ (dotted). The total cross section as well as the invariant mass distributions show a clear deviation from a phase space decay of the primary resonance, favoring a sequential decay.

In the absence of a 'complete' experiment, the relevant information about resonances from measurements are extracted using reaction models. To further constrain the fitting parametrization for resonance and background contributions, even

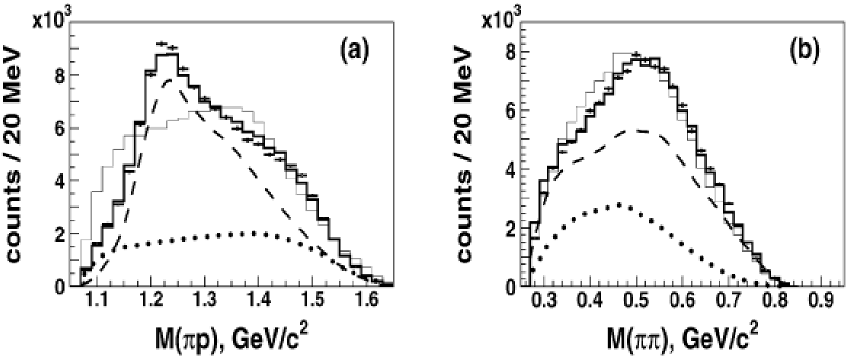

Fig. 1.5: Invariant mass distributions for the double π^0 channel for $W = 1550 - 1800$ MeV. (a): $m(p\pi^0)$, (b): $m(\pi^0\pi^0)$. Crosses: data from [29], solid line: fit to data, thin line: phase space distribution, dashed: $\Delta^+\pi^0 \rightarrow \pi^0\pi^0 p$, dotted line: $p(\pi^0\pi^0)$ distribution (taken from [29]).

coupled channel analyses, which allow to combine results from different meson production channels, are being used. But even at low excitation energies, with only some possible resonance contributions the model, results are still controversial. We will now give a short overview of the most important models and their contributions for this channel.

The basis for (practically) all this models is an effective Lagrangian density which is built from a number of Feynman diagrams. Basic diagrams are resonant ones, Born terms and further background processes, shown in figure 1.6. The difference between these models lays within the set of chosen diagrams and the parametrization for the strength of the different contributions. The composition of diagrams is often very sensitive to small details, since interference effects can lead to dramatic changes in the outcome.

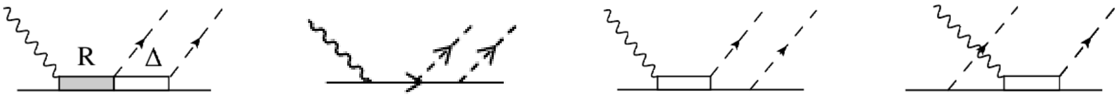

(a) (b) (c) (d)

Fig. 1.6: Basic diagrams of resonant terms (a), N- and Δ-Born terms (b), (c) and further background processes (d).

1.3.1 The Valencia Model

The second version of this model, published in 1996 [31] aimed at the description of all six isospin channels for the $\gamma N \rightarrow \pi\pi N$ reactions for photon energies up to 800 MeV. Including a large (especially for that time) set of diagrams, $P_{11}(1440)$, $D_{13}(1520)$, N- and Δ-Born terms among others, reasonable descriptions for cross section variables of $\gamma p \rightarrow \pi^0\pi^0 p$ and $\gamma p \rightarrow \pi^+\pi^- p$ could be achieved, but a rather poor reproduction for $\gamma p \rightarrow \pi^+\pi^0 n$ lessened its success. The dominant contribution out of the resonant terms was coming from $D_{13}(1520) \rightarrow \Delta\pi \rightarrow N\pi\pi$ sequential decay, and the well reproduction of the double π^0 cross section results ruled out a strong $P_{11}(1440)$ (Roper resonance) contribution predicted by the Saclay model [32]. In section 5.2.3 the role of the Roper resonance will be discussed with regard of the results of this work.

Another upgrade for the Valencia model was given in 2001 [33], aiming at a better description of the $\gamma p \rightarrow \pi^+\pi^0 n$ channel. Including higher lying states from the third resonance region, such as the $D_{33}(1770)$, lead to strong interferences with the basic dominant channels, and thus added a sizeable contribution to the cross section. Additionally, the ρ meson decay channel $D_{13}(1520) \rightarrow \rho n \rightarrow \pi^+\pi^0 n$, shown by [34] to account crucially for the cross section, was included. The set of diagrams for this model is shown in figure1.7.

A newer version from 2005 targeted at reproducing supplementary polarization observables, and beam helicity asymmetry measurements have been compared to this calculations. Figure 1.8 shows the beam helicity asymmetry measurement for double π^0 photoproduction on the proton compared to calculations from three models, two of them are presented in this chapter. This is a perfect example for the sensitivity of polarization observables, because although cross section results could be reasonably reproduced, this model had a rather poor agreement with the data from [35].

1.3.2 The MAID Model

Based on the Mainz MAID model, A. Fix and H. Arenhövel [36] used also the effective Lagrangian approach to predict double pion photoproduction data. Nowadays this model covers a huge range of channels and offers the possibilty to calculate a wide range of observables directly on the website [40], where the energy ranges and binnings can be chosen by the user.

It is very similar to the Valencia model, but includes more higher lying states, such as $F_{15}(1680)$, $D_{15}(1570)$, $S_{11}(1535)$. Figure 1.9 shows the Feynman diagrams included in the MAID model calculations for the double pion channel. Since coupling to neutral pions is not possible for a photon, many background diagrams fall away and only the terms (3), (12)-(18) and (20) can contribute to double neutral pion photoproduction.

According to the MAID model predictions, $F_{15}(1680)$ and $D_{15}(1570)$ play an important role in the double π^0 channel at higher energies. The model claims a predominant coupling of $\gamma p(n) \rightarrow \pi^0\pi^0 p(n)$ to the $F_{15}(1680)$ resonance, whereas $\gamma n(p) \rightarrow \pi^0\pi^0 n(p)$ should couple predominantly to the $D_{15}(1570)$ state. This predicted different coupling for proton and neutron will be the basis of a discussion

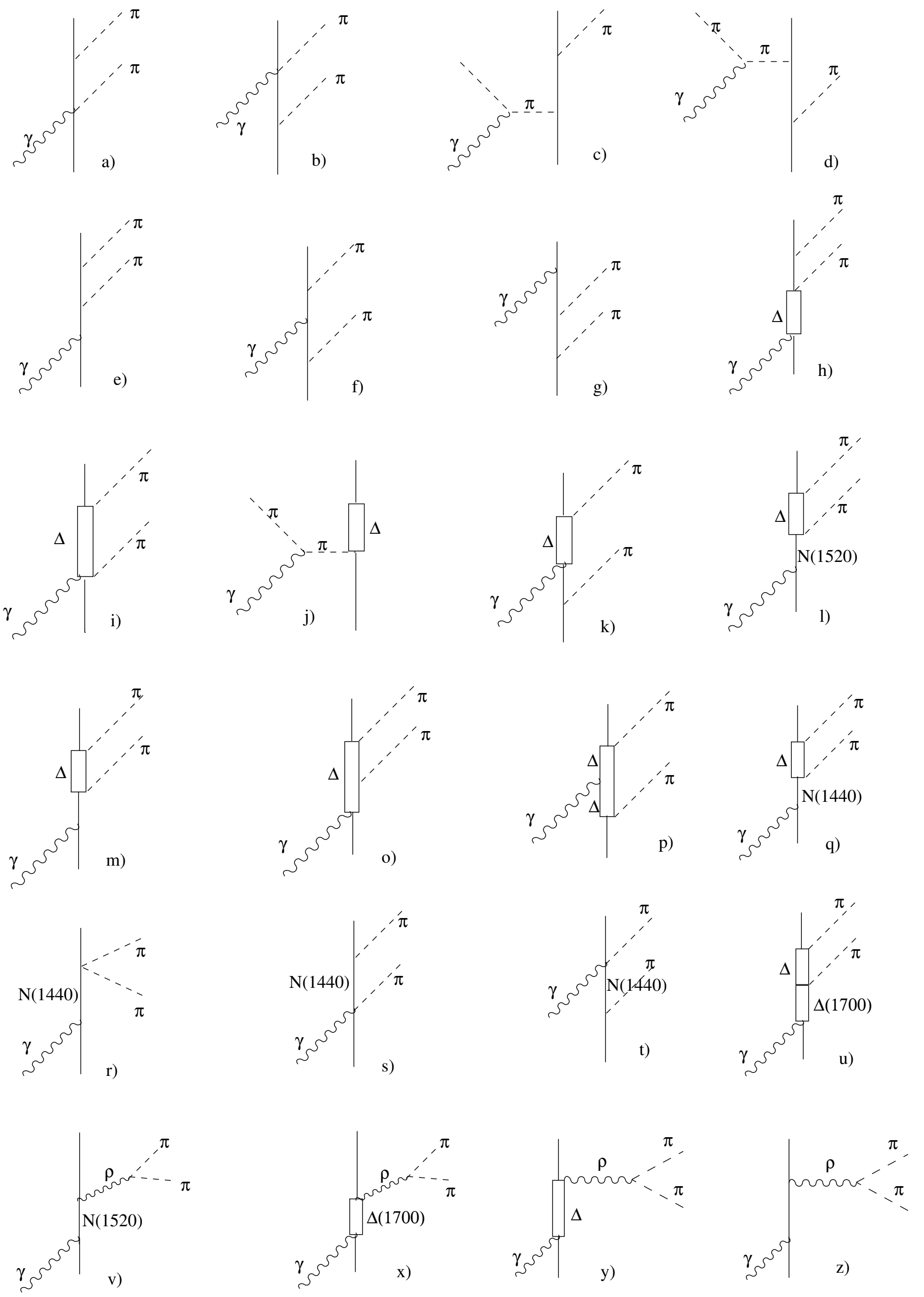

Fig. 1.7: All contributions to the Valencia model from 2001. For the double π^0 photoproduction process only terms *e-h*, *k-m*, *o-r*, and *u* contribute.

of the results from this work in section 5.5.1.

Even though quite close to the Valencia model, the results for the observables can vary rather strongly, actually also for the simpler ones, like total cross sections. This shows again the huge complexity of double pion photoproduction mechanisms, or even photoproduction in general, since very small details can lead to dramatic changes and constructive and destructive interference terms can become huge.

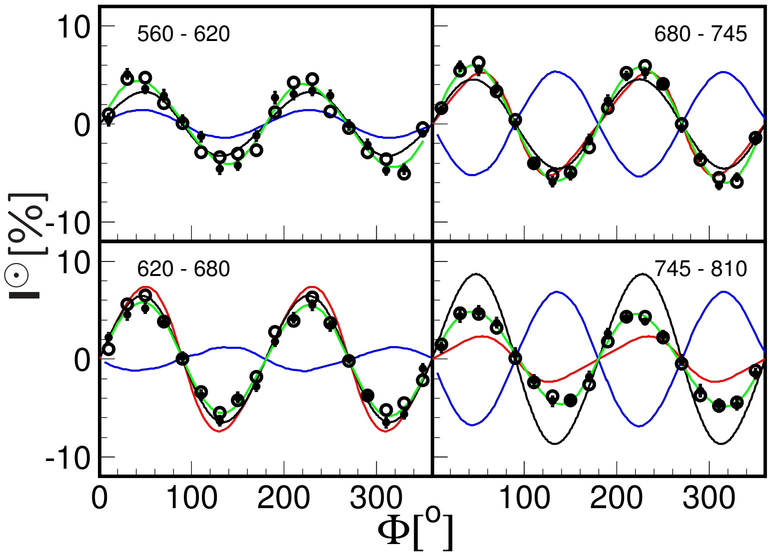

Fig. 1.8: Beam helicity asymmetry data for $\gamma p \to \pi^0\pi^0 p$ for different bins of incident photon energies. Full dots: data points from [35], open dots: $-I^{\odot}(2\pi - \Phi)$ (symmetry condition for $I^{\odot}$, see chapter 4), green curves: fit to data, red curves: model by Fix and Arenhövel [36], blue curves: Roca [37], black curves: Bonn Gatchina model [38], [39].

The red line in figure 1.8 represents the calculations from this model and it can apparently reproduce the experimental data quite well for the lower energies, whereas for the highest energy bins it underestimates the experimental results clearly. In chapter 5 we will retest this model for energies up to about 1.4 GeV in incoming photon energy as we compare the predictions to the results of this work.

1.3.3 The Bonn-Gatchina Model

By fitting experimental results for different meson channels using partial wave analysis (PWA), this model tries to designate resonant and non-resonant contributions. With the rapidly growing data base in the field of photoproduction of mesons the Bonn-Gatchina model predictions became very accurate for many channels and observables.

Amongst many other channels, experimental results for $\gamma p \to \pi^0\pi^0 p$ were thoroughly investigated with the help of the Bonn-Gatchina (BnGa) analysis in [29] and a surprisingly strong contribution from the Roper resonance $P_{11}(1440)$ was extracted from the fits. The most important novelty was the role of the $D_{33}(1700)$ resonance, which the analysis claimed to be essential for the double π^0 cross section in the second resonance region. Through constructive interference with the $D_{13}(1520)$ around 1500 MeV, it accounts for a large part of the first bump of the cross section. The Valencia and the MAID model always favored the $D_{13}(1520)$ to be nearly solely responsible for the first bump in the double π^0 cross section.

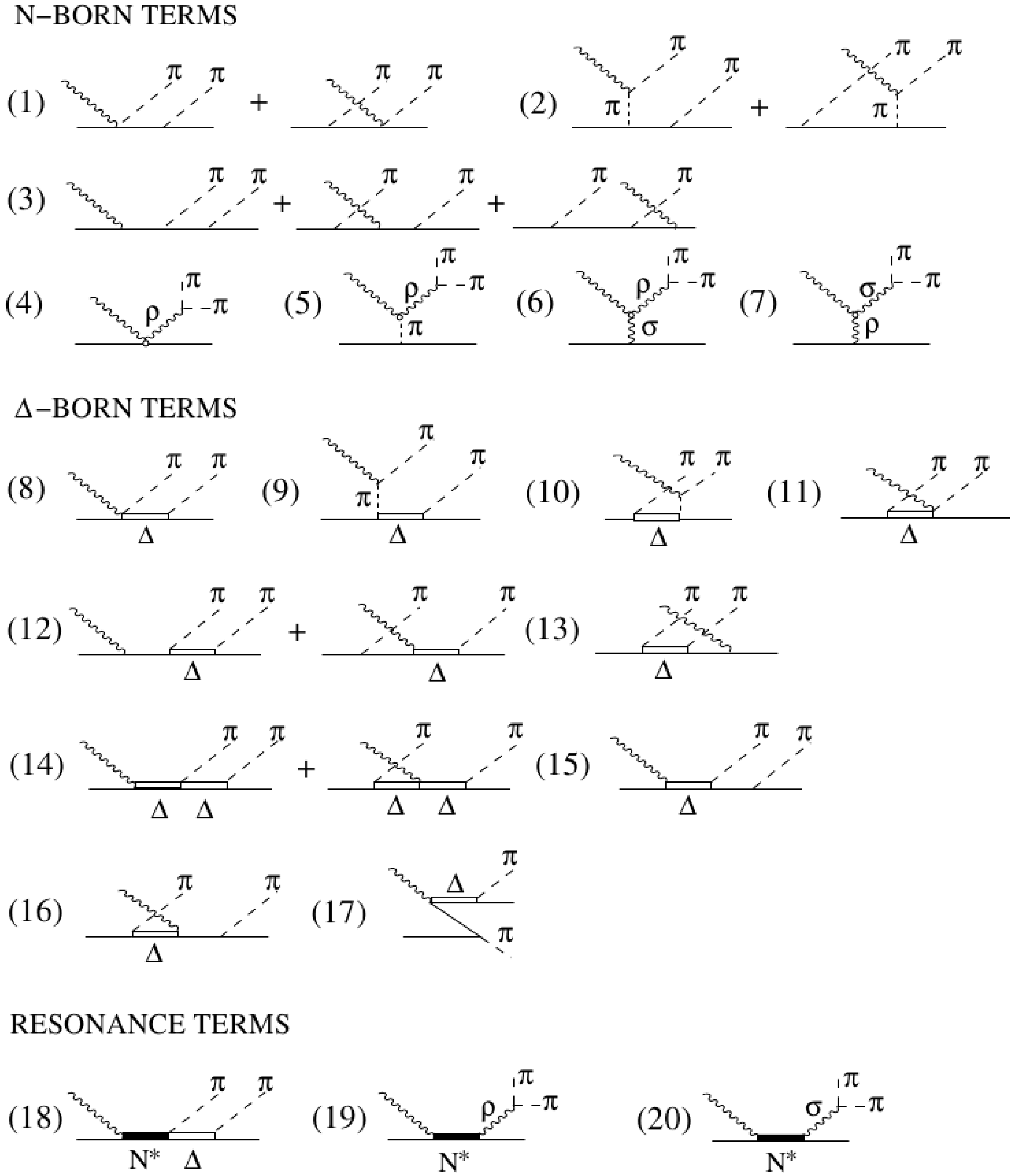

Fig. 1.9: Most important Feynman diagrams enclosed in the MAID model for double pion photoproduction.

Very recently $\gamma p(n) \rightarrow \pi^0\pi^0 p(n)$ was very explicitly analyzed by [26] with a focus on angular distributions. The main statement is the claim of a strong contribution of a $J = 3/2$ wave in the first bump, required to describe the data. As claimed in the Bonn-Gatchina model, a strong $D_{33}(1700)$ coupling to the $\pi^0\pi^0$ final state could do the job, but also rescattering processes of $\pi^+\pi^- \rightarrow \pi^0\pi^0$ are possible and in most models neglected up to now.

As mentionedbefore, the model results are still controversial, even at low energies with a small number of possible resonance contributions. Further experimental input is essential for the progress of these effective models and the large data sample of this work will certainly help containing future model analysis.

1.4 The Mixed-charge Channel

As indicated earlier, the photon cannot couple to neutral pions, and therefore only a few background diagrams contribute to the neutral channel. For the mixed-charge channels, $\gamma p(n) \rightarrow \pi^0\pi^+n(n)$, $\gamma n(p) \rightarrow \pi^0\pi^-p(p)$ and $\gamma p \rightarrow \pi^0\pi^+n$, a photocoupling to the charged pion makes many non-resonant background terms possible and the technical difficulties are duplicated. But in order to uncover the isospin composition of double pion photoproduction, measurements off protons and neutrons plus of different charge combinations of the pions are inevitable.

To investigate the decay of the $D_{13}(1520)$ resonance via emission of a ρ meson the final state $\pi^0\pi^\pm$ has to be measured, since the ρ^0 decays into $\pi^+\pi^-$ but not into $\pi^0\pi^0$. The coupling of the $D_{13}(1520)$ to the ρ meson has been measured at MAMI in 2001 for photon energies up to 820 MeV [41] and ρ meson contribution in the $\pi^0\pi^+$ invariant mass spectra could be experimentally confirmed, by comparing the $m(\pi^0\pi^0)$ and $m(\pi^0\pi^+)$ distributions.

The MAID model offers also calculations for the mixed-charge channels and the most interesting diagrams can be found in figure 1.10.

The diagrams 3(a), representing a sequential decay via the $\Delta(1232)$ resonance, and 3(b), showing the just now discussed ρ-meson decay, are of course the most valuable ones for nucleon resonance investigations. Non-resonant background for 3(a) originates from pion-pole terms (1(c), 1(d), 1(i), 2(c)), from nucleon-nucleon Born-terms (1(a)-1(g)) and corresponding nucleon-Δ Born-terms (2(a)-2(l)) and from ρ-Kroll Rudermann terms (1(h)). By looking at the magnitude of cross section ratios of the three isospin channels for double pion production

$$\begin{aligned}\sigma_{\pi^0\pi^0} &\approx 10\ \mu b\\ \sigma_{\pi^0\pi^\pm} &\approx 55\ \mu b\\ \sigma_{\pi^+\pi^-} &\approx 75\ \mu b,\end{aligned}$$

one can already assume a huge importance of background contributions for the charged and mixed-charge channels. The technical difficulties in handling this huge amount of contributions on the theoretical side reflects itself in the accuracy of the predictions. In figure 1.11, e.g., the beam helicity asymmetry results from [35] for $\gamma p \rightarrow \pi^0\pi^+n$ are compared to different model predictions, which show a rather poor agreement with the data.

As already mentioned above, polarization observables are known to be very sensitive to internal reaction mechanisms and thus are a very strong tool for con-

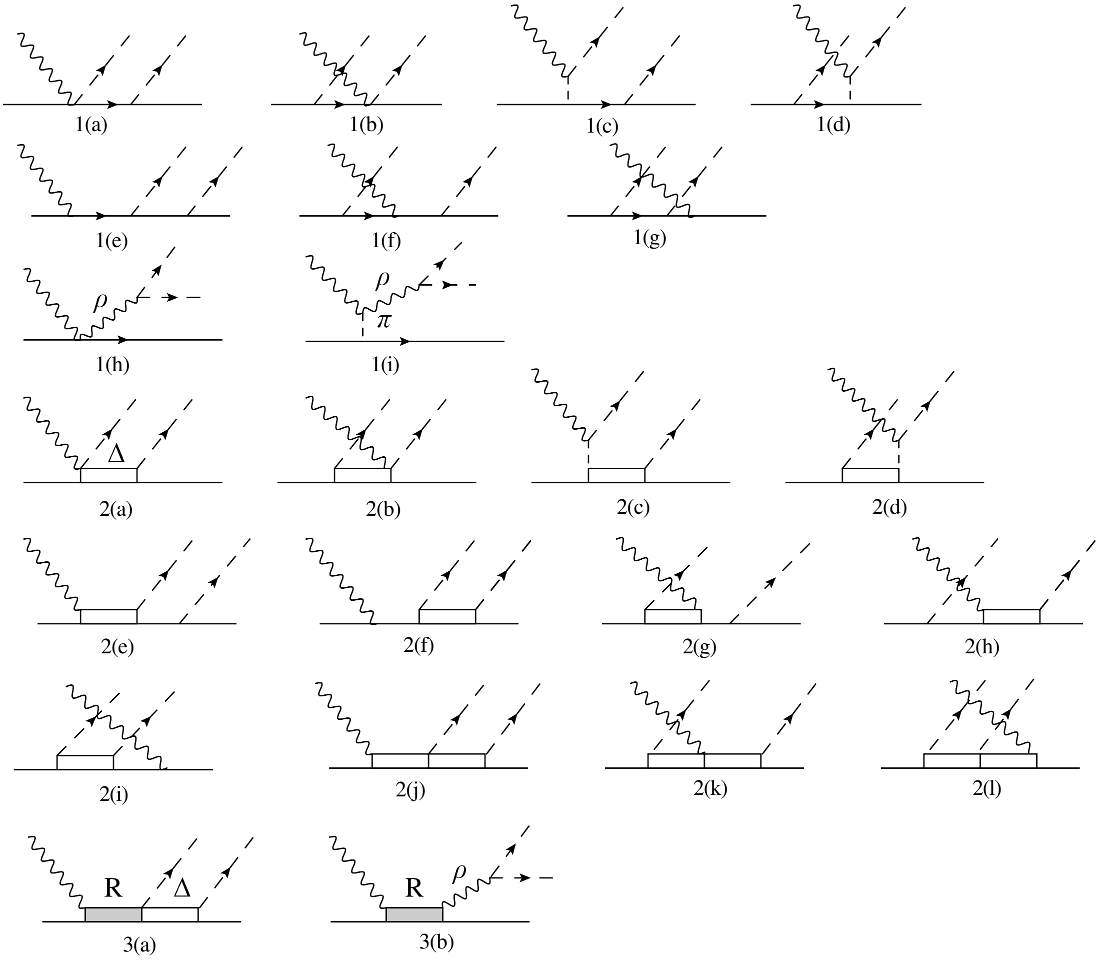

Fig. 1.10: Most interesting Feynman diagrams for the calculations of [36].

straining model assumptions. In figure 1.12 the total cross section for $\gamma p \rightarrow \pi^0\pi^+n$ is shown as function of the incoming photon energy E_γ and experimental results from [25] are compared to model calculations from [33] and [36]. Although the model results agree quite well, there is still a visible difference and this fact shows clearly the huge challenge of the mixed-charge channels for the model calculations. Apart from the total magnitude, where also the data differ partially, both models cannot reproduce the slope with high accuracy.

First precise studies for $\gamma p \rightarrow \pi^0\pi^+n$ were conducted using the DAPHNE and TAPS detectors at MAMI [16, 41] extracting invariant mass distributions and total cross section. In 2003 $\vec{\gamma}\vec{p} \rightarrow \pi^0\pi^+n$ was measured [42] with a longitudinally polarized hydrogen target and a circularly polarized photon beam, aiming at disassembling the total cross section σ into $\sigma_{3/2}$ (spins parallel) and $\sigma_{1/2}$ (spins antiparallel). A clearly dominating $\sigma_{3/2}$ part in the second resonance region confirmed again strong contributions from the $D_{13}(1520)$ state, which could either come from the sequential $D_{13} \rightarrow \Delta(1232)\pi \rightarrow N\pi\pi$ or (not excluding 'or') direct $D_{13} \rightarrow N\rho$

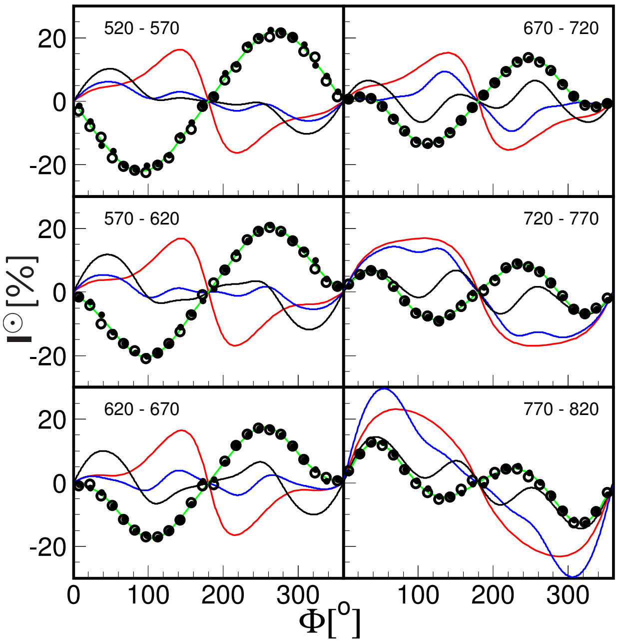

Fig. 1.11: Beam helicity asymmetry data for $\gamma p \rightarrow \pi^0\pi^+n$ for different bins of incident photon energies. Full dots: data points from [35], open dots: $-I^{\odot}(2\pi-\Phi)$, green curves: fit to data, red curves: model by Fix and Arenhövel [36], blue curves: Roca [37], black curves: Roca with 4π acceptance. Taken from [35].

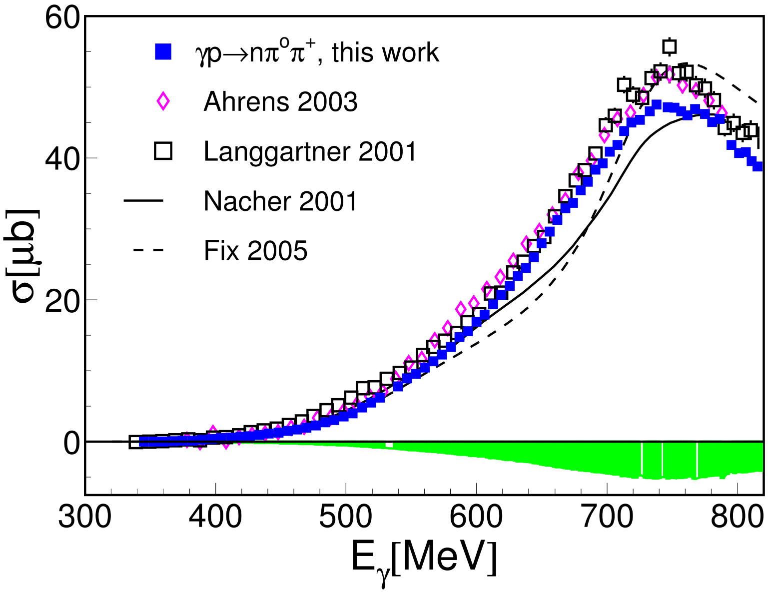

Fig. 1.12: Total cross section data for $\gamma p \rightarrow \pi^0\pi^+n$ as function of incoming photon energy. Blue squares: [25] with systematic errors in green, open black squares: [41], magenta diamonds: [42], model results from Valencia [33] and Two-Pion-MAID [36]. Taken from [25].

decay. Including the very important ρ decay contribution and supplemental inputs from the $D_{33}(1700)$ resonance, the Valencia model achieved a very accurate description of the $\sigma_{3/2}$ constituent but underestimated the $\sigma_{1/2}$ part, as shown in figure 1.13.

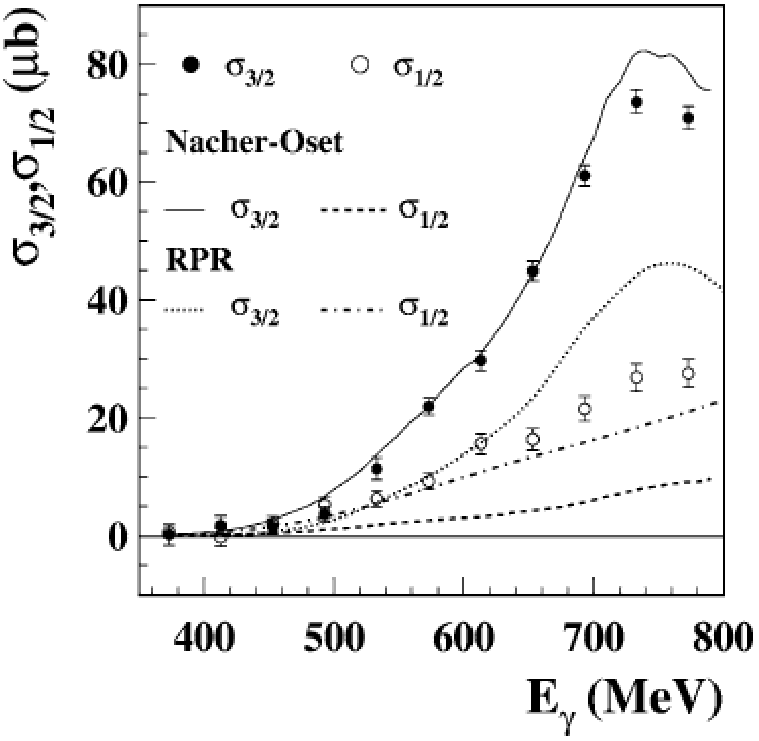

Fig. 1.13: Helicity dependent cross sections as function of the incoming photon energy. Open circles: $\sigma_{1/2}$ cross section, full circles: $\sigma_{3/2}$ cross section, full and dashed lines: model calculations from [33, 43], dotted and dash-dotted lines: model calculations from [44, 45] .

1.5 Motivation

During this chapter we encountered the numerous challenges that arose during decades of nucleon resonance spectroscopy. Some puzzles could be completely or partially solved, but still the lack of understanding of the very complicated processes is evident.

The large amount of background processes and thus technical difficulties coming from strong interferences in the mixed-charge channels, confronts model calculations with huge problems. Measuring again helicity asymmetries for $\gamma p \to \pi^0\pi^+n$ up to higher energies or even for $\gamma n(p) \to \pi^0\pi^-p(p)$ is therefore clearly justified, already in the face of the failure of all models to describe the data from figure 1.11.

Even though less complicated, the processes in the photoproduction of π^0 pairs are far from understood and first neutron results for beam helicity asymmetry and angular and invariant mass distributions will further constrain model calculations and stimulate the progress of their understanding.

Chapter 2

Experimental setup

In the previous chapter we gave an introduction into nucleon resonance photoproduction, the main difficulties in this field, and the most important models for the double pion channels. A detailed guidance through all the processes that lead to the results of this work shall now be given in the next three chapters. At first we concentrate on the production of the data in this chapter, then the whole offline calibration procedure will be explained in chapter 3, followed by detailed conduction through the data analysis processes in chapter 4.

2.1 The MAMI Electron Accelerator

The MAinzer MIcrotron (MAMI) is a high quality electron accelerator, producing unpolarized and polarized continuous wave (cw) electron beams up to energies of 1.5 GeV [46, 47]. Though the electrons are accelerated in bunches, the progression is rapid enough to be seen as continuous by the detectors. This is a very important fact, since it allows to suppress accidental coincident background (see section 4.9).

The acceleration process starts at the electron source [48], where polarized laser light is used to extract polarized electrons of a semi-conductor crystal (*GaAsP*), with a polarization rate up to 85 %. After a first accelerator process in a linear accelerator, the electrons are fed into the first race track microtron (RTM1). A race track microtron consists of a linear accelerator, with a radiofrequency of 2.5 GHz at MAMI and two dipole magnets producing uniform fields at each side to bend the electron beam by 180 degrees, see figure 2.1.

RTM1 accelerates the electron beam up to 18 MeV, then two more stages of RTM accelerator processes follow in RTM2 and RTM3 producing a final beam with energies of 855 MeV. Bending the electrons on the race track trajectories was not possible for a standard RTM, fitting into MAMI, for energies up to 1.5 GeV, especially due to weight restrictions of the magnets. To reach the MAMI-C energies of 1.5 GeV, a harmonic double-sided microtron (HDSM), shown schematically in

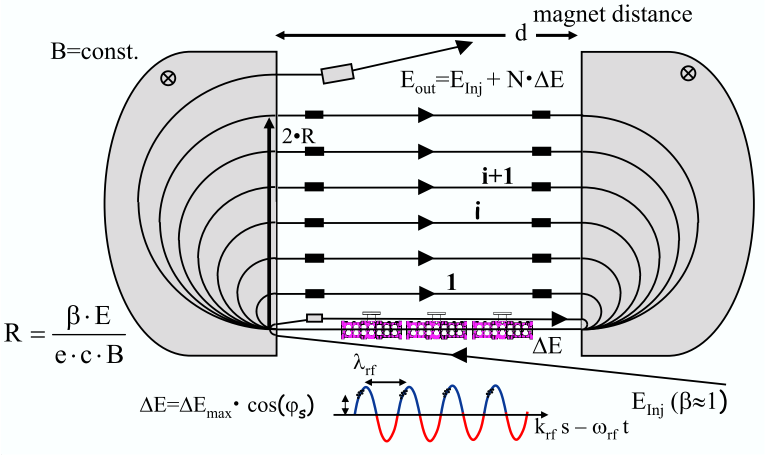

Fig. 2.1: The electrons are accelerated by the field oscillation in the cavity and their trajectory radius increases. Taken from [49].

figure 2.2, was built. The two dipole magnets of an RTM were replaced by four dipole magnets, one at each corner of the HDSM. Using two linear accelerator, one at each long side, the HDSM produces the final, high quality electron beam with energies up to 1.5 GeV.

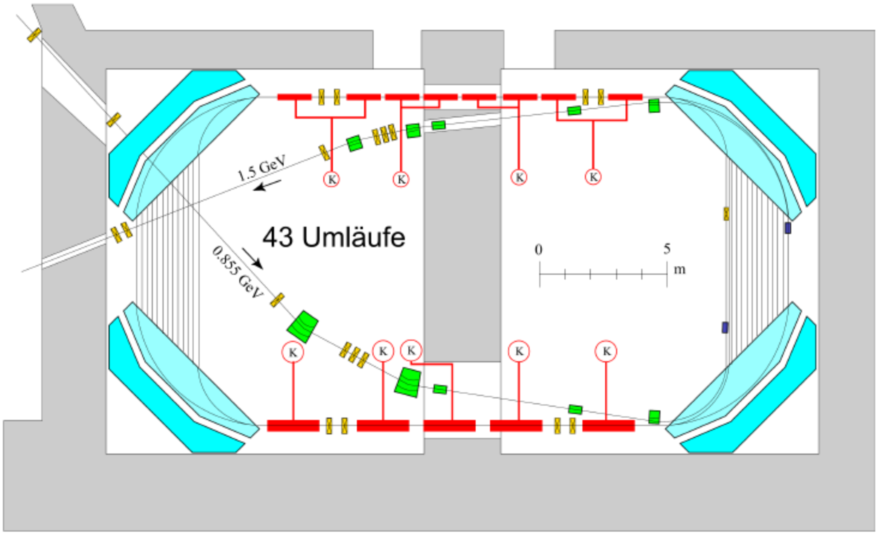

Fig. 2.2: The harmonic double-sided microtron in a schematic overview. Taken from [49].

The MAMI beam shows low emittance, a small energy spread of about 60 keV, can reach a maximum current of 100 μA and was recently even updated to produce energies up to 1.6 GeV. Figure 2.3 shows the compendium of the whole MAMI accelerator apparatus. The electron beam is finally injected in one of the connected experiments A1, A2 (this work), A4 or X1.

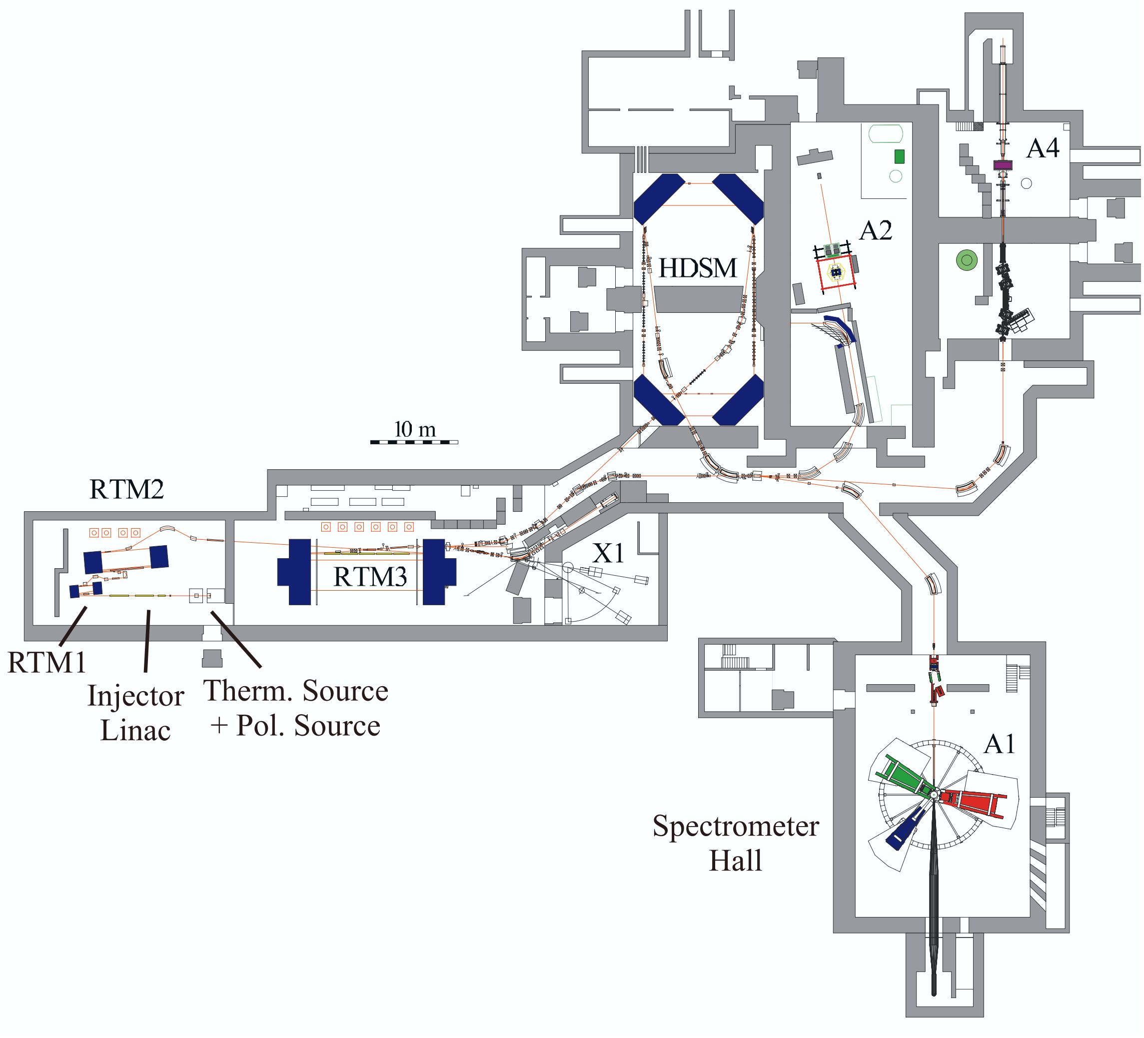

Fig. 2.3: The floor plan of MAMI-C with the four connected experiments A1, A2, A4 and X1.

2.2 Circularly Polarized Photons

The real high energetic bremsstrahlung photons are produced using a thin radiator foil. In this process the electrons might be accelerated by the electrical field of the nucleus leading to bremsstrahlung emission of photons. For the four measurements that provided the data for this work, a thin copper foil with 10 μm thickness, or a Vacoflux 50 foil in the case of the Møller radiator, which is an alloy of cobalt and iron were used. Due to the huge mass difference between the electron and the nucleus, the energy transfer from the electron to the nuclei can be neglected and the energy of the bremsstrahlungs photons can simply be calculated from initial (E_{e^-}) and final (E'_{e^-}) electron energies, as

$$E_\gamma = E_{e^-} - E'_{e^-}. \tag{2.1}$$

The angle of the photons with respect to the trajectory of the incoming electron is very small, since the electron mass is small compared to their energies. For the characteristic angle θ_c, in which 50 % of the bremsstrahlungs photons are emitted we have

$$\theta_c = \sqrt{\langle \theta_\gamma^2 \rangle} \propto \frac{m_{e^-}}{E_i},$$

and further we have for the photon angle θ_γ

$$\frac{d\sigma}{d\theta_\gamma} \propto \frac{\theta_\gamma}{(\theta_\gamma + \theta_c)^2},$$

and thus the photons will mainly fly in the same direction as the incoming electrons. The overall proportionality of the bremsstrahlungs process cross section is

$$\frac{d\sigma}{dE_\gamma} \propto \frac{1}{E_\gamma}. \tag{2.2}$$

To get a circularly polarized photon beam, the electrons have to be spin polarized using a circularly polarized laser light at the electron source. The spin transfer of the two spin states during the bremsstrahlungs process produces then the left and right handed photons. The orientation of the electron produced in the source underlays a selection of a so called Pockel cell [50] and flips randomly with a frequency of 1 Hz. The determination of the absolute helicity orientation of the electrons is far from simple and two methods have been applied. The first measurement is done within the MAMI accelerator machine, where Mott polarimetry is used. A second survey can be done in the experimental hall of A2, where Møller polarimetry was applied (for more information see [50] and [51]).

The production of linearly polarized photons is way more complicated and requires profounder knowledge of solid state physics. Since only circularly polarized photons were used in this experiment, this part will be omitted and I ask the interested reader to inform himself in [52].

The final photon polarization depends on the maximum electron energy E_{e^-} and the relative photon energy $x = E_\gamma / E_{e^-}$ and is given by the relation from Olson-Maximon [53]

$$P_\gamma = P_{e^-} \frac{4x - x^2}{4 - 4x + 3x^2}, \tag{2.3}$$

with the electron polarization P_{e^-}.

Using a 4 mm collimator, which is a lead cylinder with a hole of 4 mm diameter in between radiator foil and target, the photon beam spread could be improved, and a nice beam spot on the target was reached. Although the photon emission angle is already very small, as shown in eq. 2.2, this collimation improves the quality of the beam. The loss of photons can be corrected by performing a so called tagging efficiency correction, explained in detail in section 4.12.2.

2.3 The Photon Tagger

The Glasgow photon tagger consists of a large dipole magnet with a weight of 70 t, which can produce a maximum magnetic field strength of 1.9 T. After the bremsstrahlung process in the radiator, the electrons enter the magnetic field and see their trajectory deflected by the Lorentz force. Along the focal plane, the so called focal plane detectors determine the electron position, as shown in figure 2.4.

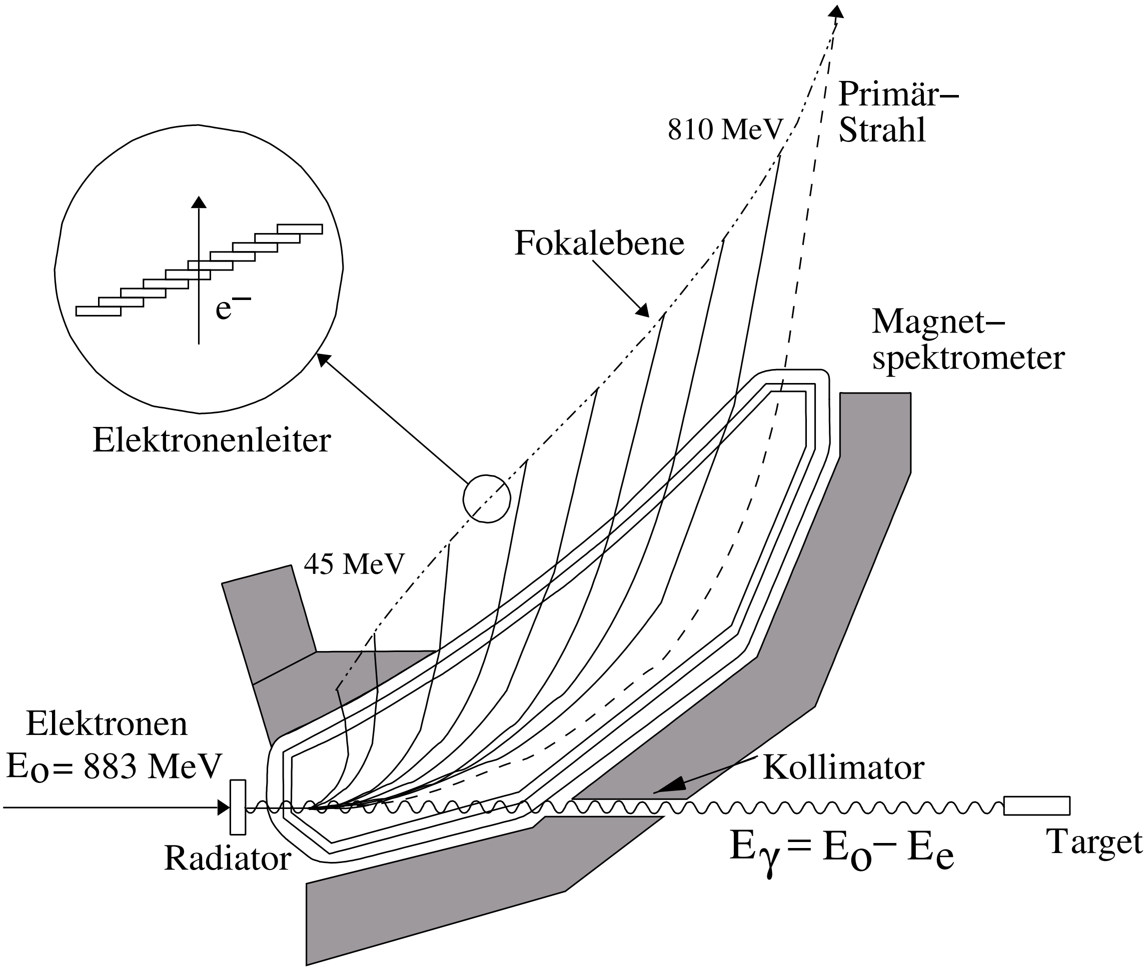

Fig. 2.4: Schematic view of the Glasgow photon tagger. The electrons are bend after the bremsstahlung process and their position is then detected by the overlapping plastic scintillators.

353 overlapping EJ-200 plastic scintillators are installed, covering electron energies from 5 % $< E_{e^-}/E_0$ up to $E_{e^-}/E_0 <$ 93 %. The scintillators are 80 mm long, 2 mm thick and have different widths, from 9 – 32 mm, in order to minimize the spreading of the energy coverage of neighboring tagger elements. The overlap of the elements allows applying a coincidence condition on detected electrons and one finally has 352 logical detectors and an energy resolution of 2 – 5 MeV, given by the overlap. Hamamatsu R1635 photomultipliers perform an individual read

out of the elements and their shielding from the magnetic field is accomplished by steel plates.

The main part of the electron beam (most electrons do not interact with the radiator) is led to the beam dump, where also a Faraday cup is installed to have the beam current monitored. A high beam intensity can lead to a saturation of the tagger elements covering the lowest photon energies (highest electron energies). This is due to the $1/E_\gamma$ distribution of the bremsstrahlungs process. Additionally, also the photomultipliers can get destroyed by too high currents. Therefore, the detection of the lowest photon energies was suspended during our measurements. Detected were the lowest electron energies in element number 1 up to high electron energies in element number 272, covering a photon energy range of $\approx 400 - 1400$ MeV.

Apart from measuring photon energies, the Glasgow photon tagger measures the total flux of electrons, which can be used to determine the number of photons impinging on the target from detection efficiency measurements (see chapter 4.11). For all absolute observalbles, such as total or differential cross sections, knowing the number of total photons is needed for the normalization process.

2.4 Targets

As aforementioned, the measurements were conducted with free protons, using a liquid hydrogen target and with quasi-free protons and neutrons from a liquid deuterium target.

2.4.1 The Liquid Hydrogen Target

A free proton target with high density can be realized using liquid hydrogen [54]. A Kapton cylinder with a length of 10 cm and a diameter of 4 cm, as shown in the photo in figure 2.5 was filled with liquid hydrogen and kept at a temperature of about 20 K, constantly monitored during the measurements, and 1080 mbar of pressure. The thermic isolation was guaranteed by eight layers of foil, a mix of 8 μm of Mylar and 2 μm of aluminium foil. The Kapton cylinder walls are 120 μm thick and the cell is finally installed in a plastic tube, reinforced with carbon fiber to bear up with the pressure from outside, which is due to the $3 \cdot 10^{-7}$ mbar vacuum in the target.

2.4.2 The Liquid Deuterium Target

For the liquid deuterium target the same target cell as for the hydrogen target were used [54]. The length of the target cell can be changed using differing so called entrance window adapters [54]. The three measurements on the deuterium target

Fig. 2.5: Photo of the liquid hydrogen, liquid deuterium target cell, respectively. From [55].

were perfomed with a 3.02 cm target cell length in the May 2009 beam time and with a 4.72 cm target cell length in the December 2007 and February 2009 beam times.

2.5 The Crystal Ball Detector

Since 2002 the Crystal Ball (CB) is installed in the A2 spectrometer hall at MAMI in Mainz. Together with the TAPS detector (see section 2.7) and the high quality electron beam from the MAMI accelerator, precise photoproduction measurements can be performed. The Crystal Ball detector has a long history, dating back into the 1970s, when it was build for the SLAC experiment at SPEAR (Stanford University, California, USA). Later on it was used at DESY (Hamburg, Germany) from 1978 to 1986, then it was out of use until being upgraded in 1995 at Brookhaven National Laboratory and moved to MAMI in 2002. The large list of measurements the Crystal Ball detector made possible is impressive and the highlights can be found in [56].

672 thallium doped sodium iodide (NaI(Tl)) crystals form a ball-like icosahedron, defined by 20 major sides in the shape of equilateral triangles. Each major triangle is subdivided into 4 minor triangles, from where each one is built by nine triangle-shaped crystals, as shown in figure 2.6. Due to its former function as detector of a collider experiment, the Crystal Ball has two holes, where 48 crystals have been left out in total. To have access to inner detectors and the target, CB

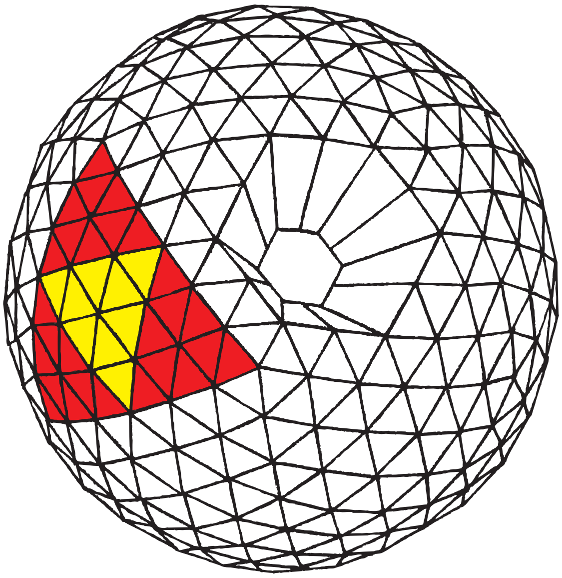

Fig. 2.6: Schematic picture showing the complicated geometrical structure of the Crystal Ball. One of the 20 major triangles is highligthed in red and the subdividing 4 minor triangles, built by nine NaI crystals can be seen.

is divided into two evacuated hemispheres, separated with steel plates of 1.5 mm thickness and an additional air gap of 5 mm, shown in the photo in figure 2.7.

Length	40.6 cm
density	3.67 g/cm^3
critical e^- energy	13.37 MeV
radiation length	2.59 cm
primary decay time	245 ns
Minimum ionizing particle energy deposition	197 MeV
Maximum proton energy	≈ 425 MeV
Maximum charged pion energy	≈ 240 MeV
Polar angular coverage	$\approx 20^o - 160^o$

Tab. 2.1: Some properties of the NaI(Tl) used for the Crystal Ball detector.

Crystal Ball covers 94 % of the whole solide angle region and is thus very well suited for experiments with several photons in the final state. The crystals have several different shapes to make the special geometry of CB possible. The length of 40.6 cm makes about 15 radiation lengths and the side of the truncated triangular pyramid-like shaped crystals is about 5.1 cm in the center and about 12.7 cm at the outer end. A Mylar foil wrapping for each crystal guarantees a good optical isolation and the light output is amplified by photomultipliers of the type *SRC L50B01*, mounted at the outer end of each crystal. A glass window couples the optical signal to the photomultipliers, leading to two air gaps (crystal-glass and glass-photocathode) and thus a small signal loss.

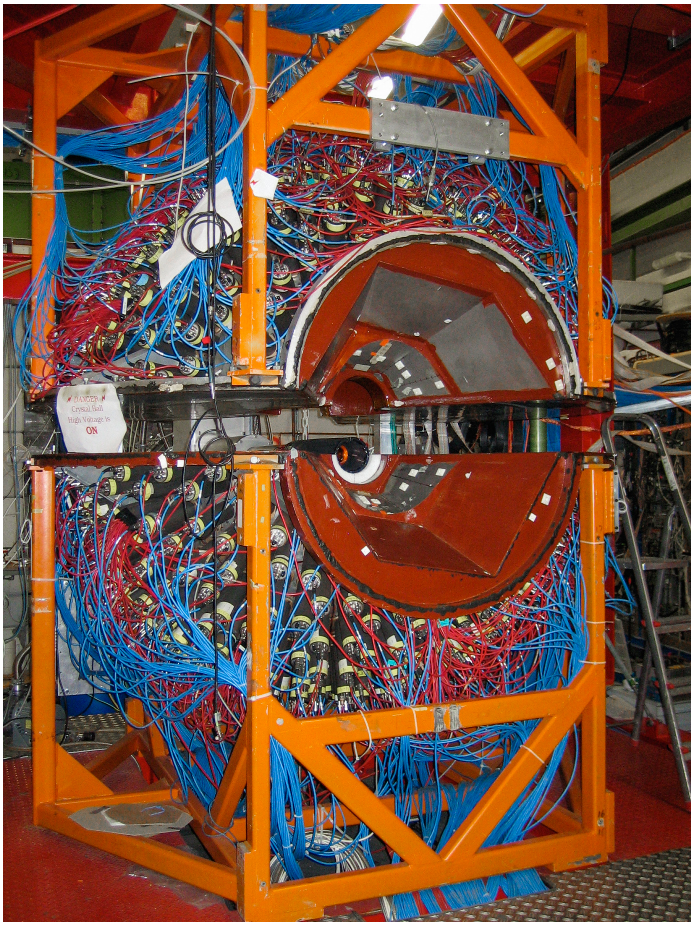

Fig. 2.7: The photo shows the Crystal Ball detector, with the two hemispheres, where the upper part is lifted for maintainance works. Taken from [57]

Typically 98 % of the energy of a photon is deposited in a 13 crystal large cluster and together with the high granularity a very good angular resolution is reached. The energy resolution can be approximated [58] by

$$\frac{\sigma}{E} = \frac{2.7\ \%}{E^{\frac{1}{4}}}, \tag{2.4}$$

with resolution σ the energy E in GeV and is especially good for photons. For protons and charged pions the angular resolution is much lower, due to the very small extension of the hadronic shower, which only spreads over one or two crystals.

Table 2.1 gives some additional properties of the sodium iodide crystals. The energy deposition maximum for protons and charged pions are 425 MeV and 240 MeV, respectively.

2.6 The Particle Identification Detector

To identify the particles nature it is essential to know wheather it is neutral or charged. The Particle Identification Detector (PID) was especially built for this experiment as a so called veto detector at the University of Glasgow [59] and allows good particle identification together with CB. The second inner detector was a multi-wire proportional chamber (MWPC) and although mounted, it was unfortunatelly unfunctional during all our measurements.

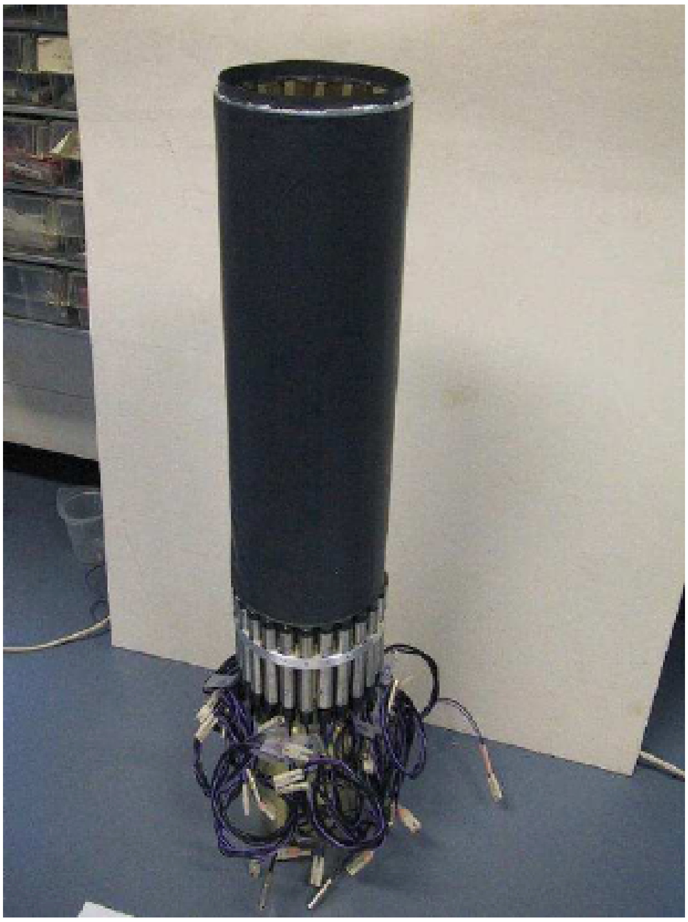

Fig. 2.8: The **P**article **I**dentification **D**etector. Taken from [55]

Apart from a simple discrimination of charged and neutral particles, charged particles can be distinguished using the different energy deposition properties of charged pions, protons and electrons. A two dimensional plot of the deposited energy of a particle versus its total energy deposition in the Crystal Ball allows the discrimination of these particles (see chapter 4). This is especially important for the analysis of the mixed-charge channels, where the identification of charged pions is crucial.

24 $EJ-204$ plastic scintillators with a length of 50 cm and 4 mm thickness form a zylindrical tube, as shown in the photo in figure 2.8. It can be mounted around

the target inside the Crystal Ball detector. The scintillators shape is trapezoid-like, allowing for a tight adjustment, and therefore leaving very few open space. Each element is individually coupled to a Hamamatsu $H3164-10$ photomultiplier via an optical connection by a lucid light guide. For the optical isolation, aluminium foil and an additional layer of black Tedlar PVF Film are wrapped around each szintillator.

Scintillator material	$EJ-204$ plastic scintillators
PID length	50 mm
Proton energy deposition	$1-3$ MeV
Individual szintillator angle coverage	15^o
Minimum ionizing particle energy deposition	$\approx 400\ MeV$
Polar angular coverage (like CB)	$\approx 20^o\ -\ 160^o$

Tab. 2.2: Some technical details about the PID.

To avoid more amounts of material in forward direction, the PID is mounted such that the whole readout aparatus is facing up stream direction. As mentioned, the PID was built for this experiment and positioning it correctly leads to a complete coverage of the Crystal Ball solide angle and an individual azimuthal angular coverage of 15^o.

2.7 The TAPS Forward Wall

The so called **T**wo **A**rmed **P**hoton **S**pectrometer TAPS [60], [61] was built in the eighties with the main purpose of detecting photons with high precision. Due to its miscellaneousness it has a history in many research facilities, most of them specialized in meson production, like the GSI (**G**esellschaft für **S**chwer**I**onenforschung, Darmstadt, Germany), CERN or GANIL (**G**rand **A**ccélérateur **N**ational d'**I**ons **Lourds**, Caen, France), or later at MAMI and ELSA (Elektronen-Stretcher Anlage ELSA, Bonn, Germany), but also at KVI (Kernfysisch Versneller Instituut, Groningen, The Netherlands) for bremsstrahlung experiments.

About 600 hexagonally shaped barium fluoride (BaF_2) crystals allow many different configurations, and this fact makes TAPS a very flexible detector (see photo in figure 2.9). The TAPS crystals consist of two parts, namely the 22.5 cm long and 5.9 cm in diameter wide hexagonal cylinder and the small hexagonal endcap of 2.5 cm length and 5.4 cm in diameter.

In our experiment it was placed as a forward wall detector covering the beam hole in CB for polar angles from about 5^o to 20^o and the whole azimuthal anglular range. Only for the December 2007 beam time TAPS was composed of 384 BaF_2 crystals, arranged as hexagonal wall with eleven rings. For the three beam times

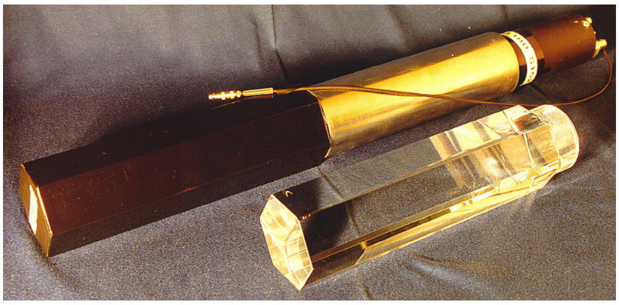

Fig. 2.9: Photo of the hexagonally shaped BaF_2 crystals from the TAPS detector, wrapped in foil for optical isolation.

from 2009, the most inner 18 BaF_2 elements have been replaced by 72 lead tungstate ($PbWO_4$) crystals [62] and the configuration from figure 2.10 with 366 BaF_2 and 72 $PbWO_4$ was the TAPS state for our measurements .

The overall 25 cm BaF_2 material length correspond to 12 radiation lengths and allows stopping protons up to 380 MeV and charged pions up to 185 MeV. BaF_2 has two parts of scintillation light, the decay time of the fast one is in the order of one nanosecond, whereas the decay time of the slow one is in the order of half a microsecond. This special material property allows for a particle distinction using so called pulse-shape analysis (PSA), where the different energy deposition mechanisms of photons and hadrons lead to different ratios of the integrated slow and fast component signals. A detailed discussion of PSA is given in chapter 3.2.4.

Another nice feature is the very good time resolution of BaF_2 due to the fast component, leading to a resolution of about 500 ps and thus allowing particle identification via time-of-flight analysis (see chapter 4.6.2) and a simultaniously accurate energy resolution due to the slow components with its high signal output.

Hamamatsu $R2059-01$ photomultipliers, connected to the smaller endcaps of the crystals provided the individual readout and the optical isolation was guaranteed by several layers of reflecting Teflon foil and an additional layer of aluminum foil.

The $PbWO_4$ crystals have only one light component, which is relatively short ($\tau \approx 10$ ns) and thus leads to a better high rate resistance. Therefore, the two most inner rings of TAPS BaF_2 elements have been replaced by $PbWO_4$ crystals, in order to stand the forward going high flux of particles. Due to the higher density of the $PbWO_4$ material each BaF_2 element could be replaced by four lead tungstate crystals, leading to a higher granularity and thereby a better position resolution. The crystals have a length of 20 cm, corresponding to 22.5 radiaton lengths and are of trapezoidal shape, allowing a perfect replacement of one BaF_2 crystal by four lead tungstate elements. Unfortunatelly the $PbWO_4$ crystals were not yet well prepared due to the short maintainance time before our beam times, and thus the $PbWO_4$ crystals could not be used and TAPS had an acceptance hole in the

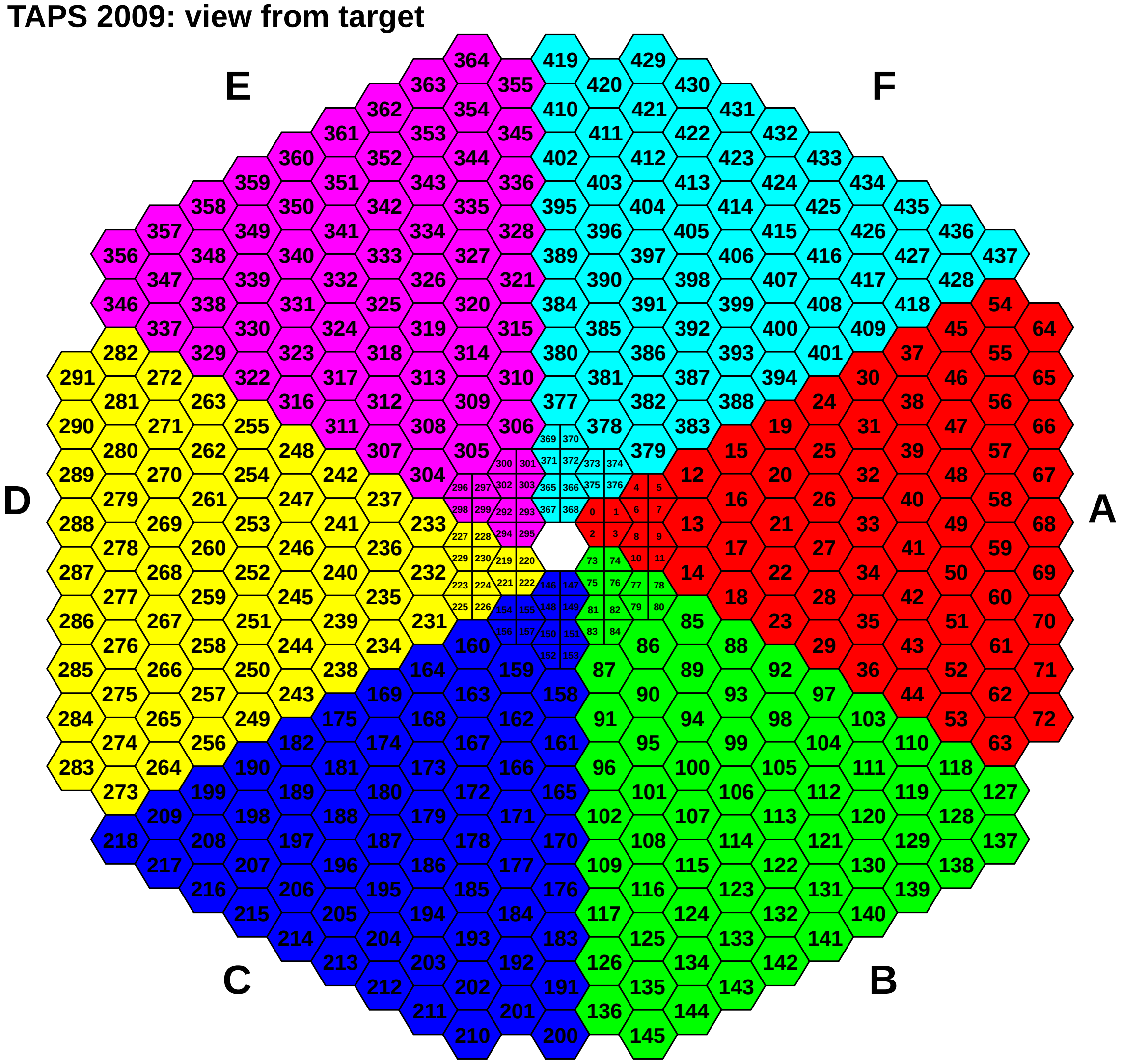

Fig. 2.10: Head-on view of the TAPS geometry of the setup used for the beam times in 2009.

polar region of $\theta < 5^o$.

The readout was provided by Photonis $XP1911$ photomultipliers and for optical isolation each crystal was wrapped in reflecting $VME2000$ and aluminium foil. A overview of the most important properties of the two crystal types can be found in table 2.3.

property	BaF_2	$PbWO_4$
critical e^- energy	13.78 MeV	9.64 MeV
fast decay time	0.9 ns	10 ns
slow decay time	650 ns	30 ns
density	4.89 g/cm^3	8.3 g/cm^3
maximal wavelength of emission	300 nm	425 nm
minimal wavelength of emission	220 nm	420 nm

Tab. 2.3: Comparison of barium fluoride and lead tungstate crystal properties.

2.8 The TAPS Veto Detectors

382 $EJ - 204$ plastic scintillators of hexagonal shape with 5.9 cm diameter are mounted in front of every TAPS element (one BaF_2 or four $PbWO_4$ crystals) to distinguish charged and neutral particles. The Veto elements are individually readout using Hamamatsu $H6568$ photomultipliers, which were connected via wavelength shifting fiber of the type $BCF - 92$. The optical isolation was accomplished by wrapping the whole Veto frame with black foil. Comparable to the particle discrimination with the Crystal Ball and PID detectors, TAPS offers the possibility to distinguish charged particles with a so called $\Delta E - E$ analysis, where the energy loss ΔE in the Veto detectors is plotted against the energy deposition E in the BaF_2 crystals.

The whole detector setup is shown in figure 2.11.

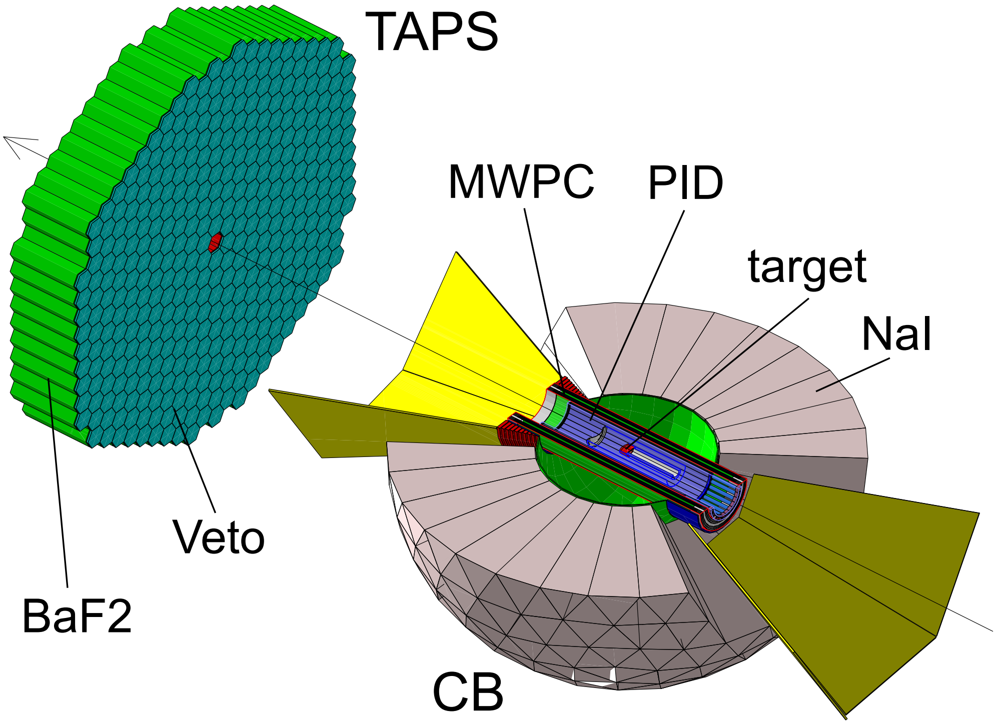

Fig. 2.11: Schematic overview of the detector setup consisting of Crystal Ball, TAPS forward wall as used in 2007 and the PID scintillator barrel. Taken from [63].

2.9 Digitalization

Up to now we explained the whole detector system in detail and end up with signals coming from the photomultipliers of the different detector parts. A further step in the data aquisition procedure is the digitalization of the output signals to enable a convenient treatment of the gathered information. The whole digitalization procedure has to transform the timing and amplitudes of the various signals into a digital form and at the same time be as fast as possible to ensure a maximum amount of statistics during the limited beam time periods. Additionally the digitalization hardware has to be radiation resistant, since these components are mounted close to the detectors in order to avoid time loss due to signal transport. Furthermore a well suited trigger system is required to reduce the recording of unwanted events to a minimum.

This whole readout procedure basis upon a very large and complicated logical structure of (partly) state of the art electronical apparatuses and only an overview of the signal flow will be given here. For a reader with higher ambitions in electronics and technical details, introductions to all detector system electronics can be found in [64], [65] and in [55].

2.9.1 Tagger Readout

So called CATCH multi-hit TDCs, already used for the COMPASS experiment at CERN, provide the time digitalization for the tagger elements. After a discrimination process, where the signal is checked for a certain minimal strength, the **C**OMPASS **A**ccumulate, **T**ransfer and **C**ontrol **H**ardware (**CATCH**) **T**ime to **D**igital **C**onverters (**TDC**) record the timing of all the hits from one event. Part of the split signal coming from the tagger photomultipliers is also sent to a FASTBUS scaler unit, which then counts the number of hits for the corresponding elements.

2.9.2 Crystal Ball Readout

16 adjacent crystals form a logical group and their signals are treated group wise. In a first step the signals from the photomultipliers are led to a splitter, which produces two parts of the signals.

A sampling **A**nalog to **D**igital **C**onverter (sampling **ADC**) samples the delayed signals from the first part. Here the time intervals corresponding to the pedestal[1], the signal and the tail are integrated. Since the pedestal is already subtracted online event-by-event, a calibration of the pedestal position is not necessary in the afterward offline calibration procedure (see chapter 3.2.2).

The second part of the split signals is sent to a **L**eading-**E**dge **D**iscriminator (**LED**) and the signals are checked against two thresholds. If the signal passes the lower threshold, the corresponding time information is converted by a CATCH TDC. The high threshold discriminator information is used to check the particle multiplicity in a later step.

The signals from the 24 PID elements are also split and one part is delayed and then integrated by ADCs, whereas the second part is sent to a discriminator and then to CATCH TDCs for the time digitalization.

2.9.3 TAPS Readout

The TAPS electronics are implemented in so called **V**ersa **M**odule **E**urocard (**VME**) boards, customized by [65]. The analog signal from the BaF_2 crystals is split and sent to two discriminatores, a lower **C**onstant **F**raction **D**iscriminator (**CFD**) and a higher LED. If the signal passes the CFD threshold (about 3 MeV) integration of long and short gate signal in charge to amplitude converters (QCD), and in **T**ime to **A**mplitude **C**onverters (**TAC**) for the time information starts. A very low time walk behavior (see chapter 3.3.2) due to the constant fraction technique allows a very precise time measurements and therefore enables time-of-flight analysis for TAPS. If the signal also overcomes the LED threshold, it is sent to the main

---

[1] The pedestal corresponds to the baseline and corresponds to zero energy.

trigger system and can contribute to the multiplicity trigger. The trigger signal from the main trigger system is then sent to the TAPS TACs and stops the time measurement. Very similar VME boards carry out the readout of the Veto detector signals.

2.10 Trigger

The **D**ata **A**c**Q**uisition (**DAQ**) system is always occupied for a short time when writing an event, and during this time it is unable to record another event (dead time). In order to reduce the encumbrance of the DAQ with unwanted events produced at very low thresholds and simultaniously control the dead time, a trigger acts as an online filter in the data taking procedure. The trigger consists of two parts, namely the CB energy sum trigger (first level[1]) and an overall multiplicity trigger (second level).

For the CB sum trigger the analog energy information of all NaI elements is summed up and compared to a discriminator, which was set to 300 MeV in our experiments. This suppresses many single π events, having thresholds of $\approx$ 150 MeV for $\gamma N \to \pi^{\pm} N$ and of $\approx$ 145 MeV for $\gamma N \to \pi^0 N$ and therefore improves the statistics of double pion events per time. The multiplicity trigger works with a discriminator for signals from groups of 16 elements, forming together a logical group. In our experiment these discriminator thresholds were set to about 30 MeV, and therefore only signals from groups where at least one signal overcomes this threshold can contribute to the overall multiplicity. Events from TAPS can also account for the multiplicity if one of the signals from the six logical sectors, seen in figure 2.10, overcomes the LED1 threshold. Since the multiplicity trigger bases on fix logical sectors only an approximate particle number counting is provided. If two particles hit the same logical group they will be counted as one or if one particles shower is propagated into two or more neighboring groups, multiple contributions are possible.

In our beam times different trigger conditions have been applied, since not all the measurements were aiming at the same meson channels. The December 2007 and the May 2009 beam times were taken with an $M2+$ trigger, only allowing events with at least two hits. An $M3+$ trigger was used for February 2009 and April 2009 beam times, which doesn't influence double π^0 events with their four photon final state, but makes a difference for the mixed-charge final states. Here we have two photons from the π^0 decay and we additionally need the charged pion to contribute to the trigger. It was found that this did not lead to significant systematic effects, as we will see in section 5.

---

[1] Another possible first level trigger is the TAPS $M2$ trigger, where two hits in TAPS can make the trigger independently of a signal from the CB sum trigger.

In all beam times a single first level trigger coming from the CB sum was used, except for the May 2009 beam time additionally the TAPS $M2$ trigger was activated as second first level trigger. In order to avoid any systematic effects no events with a TAPS $M2$ trigger and no CB sum trigger were accepted.

2.11 Beam Time Overview

As already mentioned, four differents measurements yielded the data for this work, namely December 2007, February 2009, April 2009, and May 2009, and all had slightly different experimental conditions. This of course demanded for separate treatments and only at the very end, the results could be added up. Table 2.4 shows the most important characteristics for the measurements.

Parameter	Dec. 2007	Feb. 2009	Apr. 2009	May 2009
'pre anal. amount'	20 GB	9.2 GB	71 GB	23 GB
electron current	10 nA	5 nA	10 nA	4.5 nA
electron energy	1508.4 MeV	1508.4 MeV	1557.5 MeV	1557.5 MeV
tagger magn. field	1.8321770 T	1.8281117 T	1.889231 T	11.89601 T
collimator	4 mm	4 mm	4 mm	4 mm
radiator	10 μm Cu	10 μm Cu	10 μm Cu	Møller foil
target filling	LD_2	LD_2	LH_2	LD_2
target density [mb^{-1}]	231 ± 5	231 ± 5	422 ± 8	147 ± 3
target length	4.72 cm	4.72 cm	10.0 cm	3.02 cm
trigger multipl.	$M2+$	$M3+$	$M3+$	$M2+$
CB E-sum trigger	> 300 MeV	> 300 MeV	> 300 MeV	> 300 MeV

Tab. 2.4: The most important beam time parameters of the four measurements. 'Pre anal. amount' represents the pre analyzed amount of data, i.e. with an identification of the final states explored in this work. 'The tagger magnetic field represents the mean value over the beam time period.

2.12 Software

Having now all detector signals digitized, the analysis procedure can get started. The main goal is to cleanly identify the wanted decay channels and reduce background events to a minimum. The well suited software environment used to analyze the data consists of several software parts. First the main offline analysis software AcquRoot will be discussed in section 2.12.1, followed by an introduction to the simulation software PLUTO^{++} in section 2.12.2 and Geant4 in section 2.12.3. Furthermore, the calibration software CaLib and the advanced analysis software OS-

CAR, both developed in cooperation by our work group, are presented in section 2.12.5 and 2.12.4.

2.12.1 The Main Analysis Software AcquRoot

All data aquisition, data analysis and Monte Carlo event analysis inside the A2 collaboration are in a first step processed using the main analysis software AcquRoot [66]. As stated in the name, it is developed upon the CERN ROOT [67] software and also written in C++. The object-oriented software is built to analyse the binary data files taken in the experiments and additionally the simulation output files produced by Geant4. The offline ASCII calibration files are applied to experimental and simulation data and fed into the detector classes, where now particles are reconstructed from clusters of detector elements that fired.

A very nice feature of the developed software OSCAR (see section 2.12.4) is the massive time reduction for the offline analysis procedure of about an order of magnitude. With the AcquRoot frame work a so called pre-analysis is performed, where the software calibration is applied and first, very loose cuts are set to reduce the amount of data. The pre-analyzed data stored in trees, undergoes now the final analysis procedure implemented in OSCAR, which is fully independent of AcquRoot. The developed calibration software CaLib is also coupled to AcquRoot and OSCAR and offers a simple handling of all calibration steps (see chapter 3).

2.12.2 The Pluto Event Generator

The event generator PLUTO^{++} was especially designed for the HADES experiment at GSI and is written in C++. The *PReaction* class from PLUTO^{++} is like a general reaction process and carries a sequence of particle decays. The application is very straight forward, and thus helps to simulate also more complicated reaction processes. The only setback is the missing of an implemented Fermi momentum model for the applicability to our experiments. Therefore a Fermi momentum distributions has been implemented in PLUTO^{++} by our work group (for more details see [**?**]).

2.12.3 The Geant4 Simulation

The Geant4 [68], [69] simulation software is written in C++ and represents a powerful framework for the simulation of particle interaction with matter. It allows a detailed modeling of the detector setup, all materials and geometries [70]. In this work it was mainly used for the detection efficiency correction, discussed in section 4.11. But additionally it allows saving time and money, since novelties in detector developments can be tested before having them installed.

All A2 detector components, crystals and scintillators, holding material, like the iron plates between the CB spheres and so on, have been implemented with high accuracy. In figure 2.11 the modeling of the A2 detector setup with Geant4 is visualized. Small inaccuracies in the exact reproduction lead to problems with the simulated nucleon detection efficiency and could be solved using corrections deduced from the April 2009 hydrogen beam time (see section 4.11.2).

The generated events from PLUTO^{++} can now be tracked with the A2 Geant4 simulation, where all particles are now simulated and their passages through material are accurately modeled. Finally all detector informations, like timing and energy deposition are stored and can be analysed with AcquRoot and OSCAR very similar to normal data runs.

2.12.4 The Advanced Analysis Software OSCAR

The **O**SCAR **S**implifies **C**oding and **A**nalyzing with **R**OOT (**OSCAR**) is a ROOT-based analysis framework. It consists of six different modules, mainly written by D. Werthmüller and was expanded through the years in order to simplify all sorts of tasks within the analysis process.

The *A2* module is the basic meson reconstruction tool and includes already many different channels. The *analysis* module provides cross section calculations, Fermi momentum distributions, photon fluxes, kinematical calculations and inclusion of theoretical model calculations. The *graph* module takes over data plotting procedure and the *MC* module offers an additional event generator. The *utils* module has file reading, graphical utility functions and cross section data manipulation and storage implemented. Finally the *math* module offers easy access to special mathematical functions.

Due to its independence from AcquRoot, OSCAR can be applied very flexible and has also proven its strenght in the analysis of experimental data from the CBELSA/TAPS experiments [71].

2.12.5 The Calibration Software CaLib

The detector properties and accuracies are changing, sometimes already during short time periods, for example due to a temperature variation. Especially at the beginning of a beam time, many changes are made aiming at improving the data taking procedure. Overall the experimental conditions are never fully stable during beam times, and an offline data calibration is essential to extract accurate final results.

Investigating instabilities of the most important quantities, like the π^0 peak position in the invariant mass of two photons allows the determination of stable periods. In many cases these periods differ for different detector parts, leading to overlapping calibration sets and thus overburden the simple calibration application based on ASCII files.

The main idea is the use of calibration databases, which are filled during the calibration and read in during the analysis process. Using the SQL database software, a table was produced for every calibration parameter containing all detector elements in columns. The problem of overlapping time periods for different detectors was solved by adding additional rows in the table for the different time periods. In the analysis procedure the calibration can now be read in individually for every run file.

At first the histograms for the corresponding calibration step are prepared using the dedicated calibration analysis. In the calibration procedure all histograms of the 'calibrations sets'[1] are merged and the (new[2]) key values, like gains, thresholds, etc., are calculated and written to the database.

The calibration software was initiated by I. Keshelashvili and advanced during this work. Most implementation was done by D. Werthmüller, but all group members helped testing the new software by calibrating various data sets. This software offers a convinient and fast way to reach a very high accuracy of calibration for all detectors and, therefore, a perfect starting ground for precise data analysis.

---

[1] Stable time periods, chosen before the calibration procedure.

[2] Many calibrations have to be done iteratively and one apporximates the correct values with every repetition.

Chapter 3

Calibrations

We already saw how the data taking procedure is performed, how the detectors work and in what steps the readout is done. We now have digitized detector signals and the necessary software ready to start analyzing. But still one important step is missing before the analysis procedure can yield precise results. The very important offline calibration of all detector elements will be discussed in detail in this chapter in sections 3.2 and 3.3, but first we will see how particles can be reconstructed in the different detectors in section 3.1.

3.1 Particle Reconstruction

The most simple reconstruction procedure can be applied for the tagger hits, since their only parameters are the electron beam energy and the magnetic field strength. The reconstruction of particles in Crystal Ball is typical for calorimeters and is based on a comprehensible cluster algorithm. The particle reconstruction in TAPS is the most complicated case, since the crystals do not point towards the target center and hence the position reconstruction is complicated.

3.1.1 Electron Hit Reconstruction In The Tagger

As aforementioned, the electron energy can be calculated from the hit position in the ladder, the initial electron energy and the magnetic field strength. In a first step this dependence has to be calibrated in the tagger energy calibration, see section 3.2.5.

The tagger electronics store an event if a coincident hit in two overlapping detector elements of the ladder occurred. The corresponding time information is saved by the multi-hit TDCs.

The energy of the detected electron now yields the photon energy through

$$E_\gamma = E_{e^-} - E'_{e^-}, \tag{3.1}$$

with the energy of the incoming electron E_{e^-} and the energy of the detected one E'_{e^-}.

In the time window of one event we have usually several tagger hits. Consequently, for every event a list of tagger hits, hence of photon energies and time information is associated. Every tagger channel can store up to three hits in the multi-hit TDCs per event. Although not very probable and of course depending on the beam current, multiple background hits per tagger channel are possible and their recording is essential for a clean subtraction of accidental coincident background (see section 4.9).

3.1.2 Crystal Ball Particle Reconstruction

In a first step all hits in the Crystal Ball that passed the energy threshold of 2 MeV are sorted according to their energies and stored in a list. Now the iterative algorithm starts with the most energetic hit, marks it as logical center of the cluster and takes its TDC information as corresponding particle time. Next, up to 13 neighboring elements are being checked for hits and added to the cluster, while simultaneously being deleted from the initial list in order to avoid the participation of one crystal in more than one clusters. As mentioned before, photons deposit around 98 % of their energy in 13 crystals and therefore all elements further away are ignored. The cluster energy is now given by the sum of all individual energies and the threshold discrimination of 20 MeV can be applied, rejecting too low energetic cluster. All clusters passing the threshold are positioned using a weighted square root energy calculation according to

$$\vec{r}_c = \frac{\sum\limits_{i=1}^{n} \sqrt{E_i} \cdot \vec{r}_i}{\sum\limits_{i=1}^{n} \sqrt{E_i}}, \tag{3.2}$$

where E_i are the individual crystal energies and $\vec{r}_i$ are the crystal centers of gravity. All hits from the list undergo this procedure until all the crystals that fired in an event are classified.

The assignment of the established clusters to charged and neutral particles is done by searching for coincident hits in the PID. Taking into account the initial reaction vertex distribution, which is due to the expanded beam spot on the target and the PID elements angular coverage, an azimuthal coincidence region of ±7° has been established. If a coincident hit in the list of PID hits for this event is found, the cluster is marked as charged, otherwise it is interpreted as neutral. Due to the non-existing granularity of the PID in forward and backward direction, a second hit in the same azimuthal angular region in CB can be marked as charged even though caused by a neutral particle. No problematic effects due to this imperfection could be made out, apparently the number of final state particles is not high enough.

3.1.3 The TAPS Particle Reconstruction

Similar to the CB cluster reconstruction, in a first step all hits passing the CFD cluster threshold of about $3-5$ MeV are sorted according to their deposited energy and stored in a list. The most energetic hit is set as logical cluster center and its time information is set as cluster time. Afterwards all neighboring crystals are checked for a minimum energy deposition and added to the cluster. No limit on the number of neighboring elements is applied as in CB but the clustering algorithm breaks if no further connected element with a valid hit is found. The total cluster energy is just the sum of all energies of the cluster elements, and for the positioning of the cluster logarithmic weights [72], [73] W_i are calculated according to

$$W_i = max\left[0.5 + \log\left(\frac{E_i}{\sum\limits_{i=1}^{n}\sqrt{E_i}}\right)\right], \tag{3.3}$$

where E_i are the individual deposited energies of the cluster elements. The position of the cluster is now given by

$$\vec{r}_c = \frac{\sum\limits_{i=1}^{n} W_i \cdot \vec{r}_i}{\sum\limits_{i=1}^{n} W_i}. \tag{3.4}$$

The more intuitive position determination in CB, where the position is just weighted with the corresponding energy is slightly less precise, since this way low energetic crystals are short weighted. Due to the limited cluster sizes in CB this error is negligible, for cluster position calculations in TAPS one therefore uses logarithmic weighting.

As already mentioned, the position as calculated with equations 3.3 and 3.4 is insufficiently precise since the TAPS elements do not point towards the target, but are arranged as wall, and thus the depth of the shower has to be included into the calculation. The situation is shown in figure 3.1 and the problem is evident.

The depth d of an electromagnetic shower occurring in a crystal is depending on its energy and given by [74] as

$$d_{max} = 2.05 \cdot \left[ln\left(\frac{E}{12.7\ \text{MeV}} + 1.2\right)\right]. \tag{3.5}$$

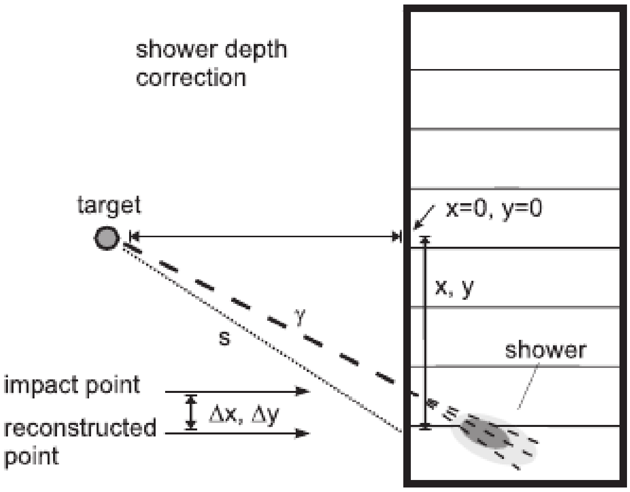

Fig. 3.1: A schematic illustration of a shower in TAPS and its influence on the position determination. Taken from [1].

The position correction Δx and Δy are now given by

$$\Delta x = \frac{x}{L_{corr}} \tag{3.6}$$

$$\Delta y = \frac{y}{L_{corr}}, \tag{3.7}$$

$$\text{where} \qquad L_{corr} = \frac{s}{d_{max}} + 1 \tag{3.8}$$

according to [75].

Subsequently, all established clusters in TAPS are checked for coincident hits from the Veto detectors. Since a charged particle can hit the veto detector of a neighboring element of the cluster center, which is due to the to the smaller arrival angle much more likely for clusters with the center in the outer TAPS rings, not only the cluster centers Veto element, but also its neighboring elements Vetos have to be checked. Additionally, the Vetos of all cluster elements are investigated for coincident hits and the cluster is marked as charged if at least one coincident hit was detected.

3.2 Energy Calibration

In this section the energy calibration of all detector parts will be explained in detail. In most cases one conducts a low energy calibration of all detector elements before the beam time, and a high energy calibration (offline calibration) after the beam time.

The goal of the low energy calibration is to equalize the response of the electronics of all detector elements in order to have an alignment of the thresholds. Equalized thresholds are essential to have a homogeneous discrimination of incoming signals in all crystals, and thus accurate trigger decisions.

The high energy calibration or offline calibration, that every data set undergoes after being measured, is elementary for equalizing the responses of the electronics, but this time for much higher energies of the detected products.

For some detector parts a so called quadratic energy correction, which provides higher order corrections, is applied.

3.2.1 General Energy Calibration

The charge to digital converters (QDC) measure an amount of charge by integrating the electronic signals from the photomultipliers and return a digital channel number c. Since the amount of charge is almost directly proportional to the deposited energy E_{dep} of the measured particle, we can write the relation as

$$E_{dep} = g \cdot (c - p), \tag{3.9}$$

with the gain g and the pedestal position p. The gain gives the proportionality between channel number c and the energy and is of unit [MeV/channel]. Random noise in the detectors leads to a peak in the spectra, which is called pedestal p and represents the position of zero energy.

The energy calibration procedure aims at determining g (and p[1]) so that the energy responses of all detector elements are equalized.

3.2.2 Crystal Ball Energy Calibration

Low Energy Calibration

For the low energy calibration of the Crystal Ball detector a monochromatic source of photons, with a fixed energy of 4.438 MeV was used. Since the pedestal position is already subtracted in the signal treatment, only the gains have to be adjusted. The high voltages were thus leveled in such a way, that all elements have the peak position of the monochromatic photons at the same channel position.

High Energy Calibration

The low energy calibration helps to align the thresholds for the measurement. But the events of interest measured in the experiment have typically much higher energies and thus another correction mechanism has to be applied.

---

[1] Depending on the signal treatment in the electronics.

For a free proton target this mechanism is rather simple, whereas for nuclear targets it is complicated by the unknown contribution from the Fermi momentum. Having the reaction $\gamma p \rightarrow \pi^0 p$ on a free proton, the energies of π^0 mesons and hence the two decay photons can not only be measured but also calculated. Consequently, the gains can be determined straight forward by comparing the two energy values.

For reactions on quasifree nucleons one commonly uses the peak position of the π^0 mesons in the $\gamma\gamma$ invariant mass spectrum. First one selects all neutral clusters of an event, and fills the invariant mass of all cluster pairs into histograms, which are numbered with the crystal number of the central cluster element. Denoting the mean photon energies of element i with $\langle E^i_{\pi^0}\rangle$, and the one of the other element with $\langle E^o_{\pi^0}\rangle$, we can approximate the mean π^0 position in the$\gamma\gamma$ invariant mass spectrum as

$$\left\langle m^i_{\pi^0}\right\rangle = \sqrt{2\left\langle E^i_{\pi^0}\right\rangle\left\langle E^o_{\pi^0}\right\rangle \cdot \left[1-\cos\left(\left\langle \phi^{io}_{\pi^0}\right\rangle\right)\right]}, \tag{3.10}$$

where $\langle \phi^{io}_{\pi^0}\rangle$ is the mean opening angle of the two decay photons.

The integrated electronic signal $S^i_{\pi^0}$ in the ADCs is connected via the gain g to the mean energy $\langle E^i_{\pi^0}\rangle$, since the pedestal position subtraction is done online in the Crystal Ball electronics. Hence we can write

$$\left\langle E^i_{\pi^0}\right\rangle = g_i \cdot S^i_{\pi^0}, \tag{3.11}$$

and the calibration procedure now aims at determining the correct conversion gain $\hat{g}_i$ to have the mean invariant π^0 mass equal to the nominal one as

$$\left\langle \hat{m}^i_{\pi^0}\right\rangle \stackrel{!}{=} m_{\pi^0}. \tag{3.12}$$

From equation 3.11 we can derive a relation between g_i and $\hat{g}_i$ to

$$\hat{g}_i = g_i \cdot \frac{\left\langle \hat{E}^i_{\pi^0}\right\rangle}{\left\langle E^i_{\pi^0}\right\rangle} \tag{3.13}$$

and applying equations 3.12 and 3.10 then yields

$$\hat{g}_i = g_i \cdot \frac{m^2_{\pi^0}}{\left\langle m^i_{\pi^0}.\right\rangle^2} \tag{3.14}$$

The invariant mass value $\langle m^i_{\pi^0}\rangle$ was derived from the center of a Gaussian that was fitted to the invariant mass spectra, taking into account the behavior of the background contribution, as shown in figure 3.2. Since the correction from the last equation depends on the gains of all other elements, the energy calibration requires several iteration steps. For beam times with strongly scattering mean π^0 mass positions, more than a dozen iteration steps were necessary to have an accurate calibration of the data set. Due to large number of crystals in CB, this was the most time consuming calibration step.

Quadratic Energy Correction

For every detected photon some part of the shower is lost, because of the detectors CFD thresholds (see section 3.1.2). Applying the high energy calibration, this losses are being corrected for typical photons from a π^0 meson decay. Since the percentage of the total signal loss is inverse proportional to the deposited energy, the high energy calibration causes an overcorrection for very high energetic photons. Since photons from an $\eta \rightarrow 2\gamma$ decay are often more energetic than the ones from π^0 decays, the mean invariant mass peak position from η mesons are shifted towards higher invariant masses (see Fig: 3.2) and we have

$$\left\langle m_\eta^i \right\rangle \ > \ m_\eta, \tag{3.15}$$

with $\left\langle m_\eta^i \right\rangle$ as the mean invariant mass of photons from an $\eta \rightarrow 2\gamma$ decay.

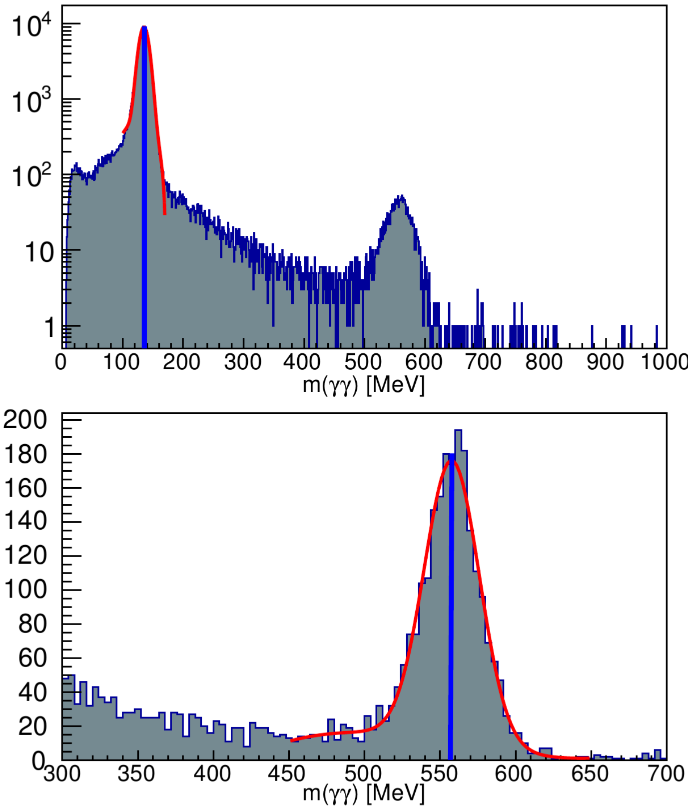

Fig. 3.2: Spectra for the $\gamma\gamma$ invariant mass of all neutral hit combinations in CB for one single crystal. In the upper part (logarithmic scale) the π^0 peak is fitted with a Gaussian and a polynomial background function (not shown) and the peak position is indicated with the blue vertical line. In the bottom plot it is visible, that the peak position of the η mesons is too high and has to be corrected.

To correct for this deficiency of the high energy calibration, one uses a quadratic ansatz according to [76]

$$\hat{E} = a \cdot E + b \cdot E^2. \tag{3.16}$$

The two parameters a and b are to be determined in such a way that finally both mean invariant mass values $\langle \hat{m}^i_{\pi^0} \rangle$ and $\left\langle \hat{m}^i_{\eta} \right\rangle$ are at their nominal positions. Hence we can derive the two conditions

$$\langle \hat{m}_{\pi^0} \rangle = \sqrt{2 \left\langle \hat{E}_{\pi^0} \right\rangle^2 \cdot [1 - \cos(\langle \phi_{\pi^0} \rangle)]} \overset{!}{=} m_{\pi^0} \tag{3.17}$$

$$\langle \hat{m}_{\eta} \rangle = \sqrt{2 \left\langle \hat{E}_{\eta} \right\rangle^2 \cdot [1 - \cos(\langle \phi_{\eta} \rangle)]} \overset{!}{=} m_{\eta}, \tag{3.18}$$

where the mean photon energies $\left\langle \hat{E}_{\pi^0} \right\rangle$ and $\left\langle \hat{E}_{\pi^0} \right\rangle$ can be established by data analysis. Assuming, that applying the energy correction does not alter the mean opening angles $\langle \phi_{\pi^0} \rangle$ and $\langle \phi_{\eta} \rangle$, one can now determine the two parameters individually for each detector element.

3.2.3 TAPS Energy Calibration

Very similar to the Crystal Ball energy calibration, this procedure splits up in three different steps. But here, a calibration using cosmic radiation replaces the low energy calibration from CB. The high energy calibration and the quadratic energy correction are applied in the same way as explained before.

Cosmic Calibration

The precise energy calibration of all TAPS elements, and hence the equal discrimination by the applied CFD thresholds, is very essential for efficient and accurate data taking. This is because most of the electromagnetic background and a large share of the recoil nucleons are detected in TAPS, and wrong discrimination leads either to the recording of many unwanted events or to the rejection of a considerable amount of events of interest.

A calibration procedure with cosmic radiation is very convenient, since no dangerous radiation sources have to be used and the procedure can be done at any time. As it requires the parallel orientation of all detector elements, in order to have equal flight paths for all crystals, it cannot be applied for CB, but only for TAPS.

The principle is the same as for the monochromatic photon source used for the CB low energy calibration. Minimum ionizing particles[1] deposit in average an

---

[1] High energetic charged particles are called minimum ionizing, if their energy deposition does not depend on their energy. Cosmic radiation (mainly muons) is minimum ionizing, because of its very high energy.

energy in the BaF_2 crystals of 37.7 MeV (see [77] for details). The cosmic spectrum of one single $\mathrm{BaF_2}$ crystal is shown in figure 3.3. By fitting the cosmic peak with a Gaussian and the background with an exponential function, one can determine the channel number corresponding to 37.7 MeV. The pedestal position gives the channel number of zero energy and the conversion gain g can be calculated. Having now g and p for a crystal, equation 3.9 is fully determined and the element is well calibrated.

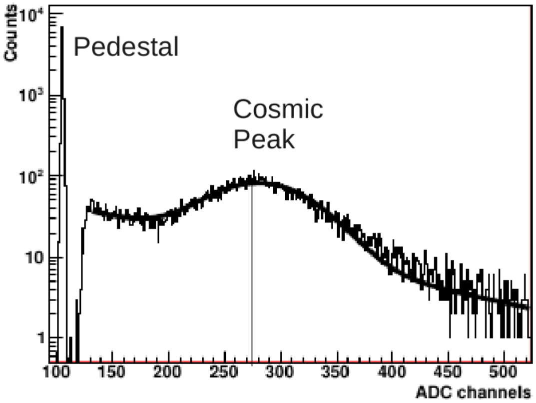

Fig. 3.3: Spectrum of the cosmic radiation for one single $\mathrm{BaF_2}$ crystal. The pedestal position representing zero energy and the cosmic peak representing $\sim$ 37.7 MeV are denoted. Taken from [1] and edited.

Before and after every beam time this calibration procedure is performed, firstly to have a well calibrated detector and secondly to gain a feeling on the stability of the detector during the measurement period.

High Energy Calibration

The offline calibration for the TAPS detector is equal to the one from CB with only one exception. Since the possibility of having both photons from a π^0 decay in TAPS is rather small due to the minor solid angular coverage, the statistics are insufficient for a calibration with two neutral clusters from TAPS. Using always one neutral cluster from CB and one from TAPS, an energy calibration relative to CB is possible, but of course demands to have an already well energy calibrated Crystal Ball detector. Therefore, in the whole calibration procedure the CB energy calibration has to be completed before the high energy calibration of TAPS can be started.

Quadratic Energy Correction

Here again the statistics for π^0 and η decay photon detection in TAPS are insufficient and one has to chose one neutral cluster from CB and one from TAPS. The rest of the procedure is identical to the quadratic energy correction for the Crystal Ball detector (section 3.2.2).

3.2.4 Pulse-shape Analysis Calibration

As aforementioned, a typical feature of the BaF_2 crystals are the two scintillation light components. The high energy calibration of TAPS from section 3.2.3 aimed at the calibration of the long gate signal processing. The so called short gate energy – the signals of the BaF_2 crystals are being integrated over a long and a short period in order to account for the two scintillation lights – is calibrated separately. Since nucleons and photons deposit their energies through different mechanisms, also their portion of the two scintillation light components vary. This principle allows for a discrimination of nucleons and photons in the TAPS detector, conducting a so called pulse-shape analysis [75]. As an important method of particle discrimination in our detector system, pulse-shape analysis has to be fully exploited and therefore a very precise calibration is essential.

As starting point the conversion gains and pedestals from the cosmic calibration (from section 3.2.3) are applied and the long and short gate energies E_l and E_s are used to define

$$\begin{aligned} \phi_{PSA} &= \arctan\left(\frac{E_s}{E_l}\right) \\ r_{PSA} &= \sqrt{E_s^2 + E_l^2}, \end{aligned} \tag{3.19}$$

where $_{PSA}$ stands for pulse-shape analysis. Plotting now the radius r_{PSA} against the PSA-angle ϕ_{PSA} leads to typical structures for photons and nucleons and allows for their discrimination. In general, one now calibrates the short gate gains and pedestals in such a way, that for photons short and long gate energies are equal, hence the photons will form a band along $\phi_{PSA} \approx 45$ degrees. The nucleons PSA-angle varies with the PSA-radius and their bands are bent. Figure 3.4 shows a typical plot for the use of the pulse-shape analysis.

Consequently, histograms are filled for all TAPS clusters central elements with ϕ_{PSA} against r_{PSA}, calculated from the long and short gate energies. Next two PSA-radius intervals have been chosen, one at high and one at low radii. For both intervals the projections onto the ϕ_{PSA}-axis were fitted with a Gaussian and based on the two mean PSA-radii and the two PSA-angles (from the two projections) new pedestals and gains could be calculated by enforcing $E_l = E_s$. The two equations 3.19 should actually be resolvable under this conditions, but since the fitting accuracy is limited, several iterations were necessary for a precise final calibration of the short gates.

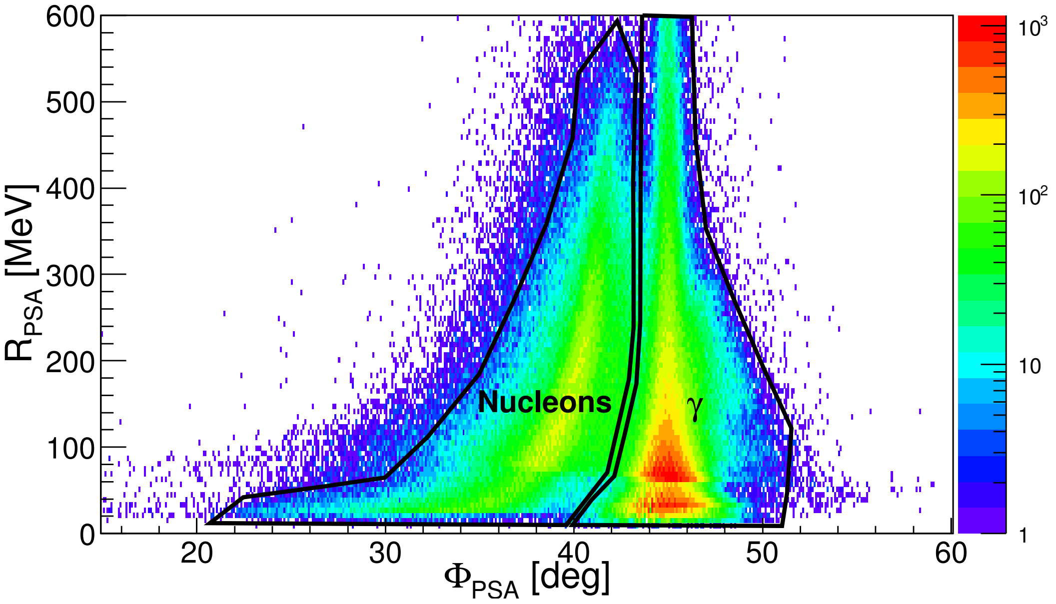

Fig. 3.4: The spectrum of the PSA-angle ϕ_{PSA} plotted against the PSA radius r_{PSA} reveals clearly visible structures for nucleons and photons.

3.2.5 Tagger Energy Calibration

The program *ugcalv2ua* ([78], [79]) is used to calibrate the energy of the tagger elements. Since the conversion from tagger channel to energy depends only on the energy of the incoming electron beam and the magnetic field strength of the dipole magnet, and these variables are both very stable during the typical time period of a beam time, average values can be used. The calculation includes many different measurements that have been done to establish all uncertainties and guarantees a very precise calibration. The program finally yields the mean energy values for each tagger channel and the corresponding energy range coverage.

3.2.6 The PID Energy Calibration

The energy calibration of the PID detector requires the determination of the pedestal position and the conversion gain for all 24 elements. The procedure is to simulate the energy deposition of a proton and now altering the gains and pedestals in the data analysis in order to have an agreement between simulation and data. First proton events were simulated and their deposited energy in the PID was plotted against their deposited energy in the CB for every PID element. For the experimental data events with a $\pi^0 p$ final state were selected, where already loose cuts on the $\gamma\gamma$ invariant mass were applied[2] in order to have a cleaner proton

---

[2] Consequently, the CB and TAPS energy calibration have to be finished before.

signal. For the experimental data, the ADC channel in PID was filled against the deposited energy in CB and in the projections for different CB energy ranges the proton peak position was fitted. The proton peak positions in the experimental data were plotted against the ones from simulation and a linear fit through this points then yielded the pedestal and conversion gain values (for more information on the procedure see [80]).

3.2.7 Veto Energy Calibration

Since the whole Veto wall can be removed from TAPS, a cosmic calibration is possible, when lying it flat on the ground, and thus allowing for equal flight paths of the cosmic radiation through all detectors. But still the dismounting procedure is rather time consuming and for most measurements, also for the ones of this work, the Vetos were not calibrated in this way.

The offline calibration was done in the exact same way as for the PID detector, but of course is even more time consuming, because of the huge number of 384 Veto elements.

3.3 Time Calibration

Not only precise energy information are essential for a precise analysis of the channels, but also a well calibrated time information for all detectors. We will see this for example in section 4.9, where the coincident bremsstrahlung events are chosen based on a statistical selection method, requiring well calibrated time information. In this section we will discuss all calibration procedures applied, that finally lead to very well time calibrated beam times.

3.3.1 General Time Calibration

The time information of a hit is measured by a time to digital converter (TDC), where a time spread is being converted into a channel number. With the channel number c, the physical time t, the conversion gain g ([ns/channel]) and an offset o we have the following relation between channel and time

$$t = g \cdot (c - o). \tag{3.20}$$

Determining the conversion gain g and the offset o is thus the purpose of the time calibration procedure. Unlike the pedestal p from the energy calibration the offset o can be set freely. In general one chooses the offset in a way, that the peak of coincident photon hits are positioned at zero.

The detectors used in this experiment have different time measuring procedures. For the TAPS detector the starting time is given by the hit in the crystal and the stopping time is coming from the trigger, hence the time t is given by

$$t = t_{trigger} - t_{detector}. \tag{3.21}$$

For the Crystal Ball detector on the other hand, the time measuring procedure is exactly reverse and t is thus given by

$$t = t_{detector} - t_{trigger}. \tag{3.22}$$

The trigger time is subject to so called jitter, coming from the electronics and, therefore, it is essential to calculate time differences between detectors in such a way, that the trigger time always cancels.

3.3.2 CB Time Calibration

The Crystal Ball time calibration procedure splits up in three steps. In a first step the offset o from equation 3.20 is determined, followed by the time walk correction and the final rise time correction.

Offset Determination

Since the gains g of the CATCH TDC are fixed at 117 ps, the task is to determine the offsets o from equation 3.20. Therefore, the time differences of all cluster combinations for every cluster center were filled into a histogram, similar to the high energy calibration. Slower particles were rejected using a fixed time window, and thus mostly photon events ended up in the histogram. Now the peak positions for all the elements were determined by a Gaussian fit to the time peaks and the new offset $\hat{o}_i$ is then given by the positions p_i and the old offset o_i as

$$\hat{o}_i = o_i + \frac{p_i}{g_i}, \tag{3.23}$$

where g_i are the individual conversion gains, which are fixed and equal for the CB elements.

Time Walk Correction

A typical feature of the NaI crystals are the relatively slow rise times of the signals, and thus a strong energy dependence of the time measurement, when using LEDs for the thresholds. Hits with higher energies have a steeper rise in the electronic signal and consequently a smaller time difference Δt between the rise of the signal to the crossing of the threshold. This effect is called time walk and has to be corrected for a decent final detector timing.

We fill individual histograms for every CB element, where the time difference to the tagger time and the energy are plotted, as shown in figure 3.5(a). In order to have a cleaner signal, only π^0 events were used and additional cuts on the invariant mass and missing mass of the π^0 were applied (for invariant and missing mass cuts see sections 4.5.2 and 4.5.4).

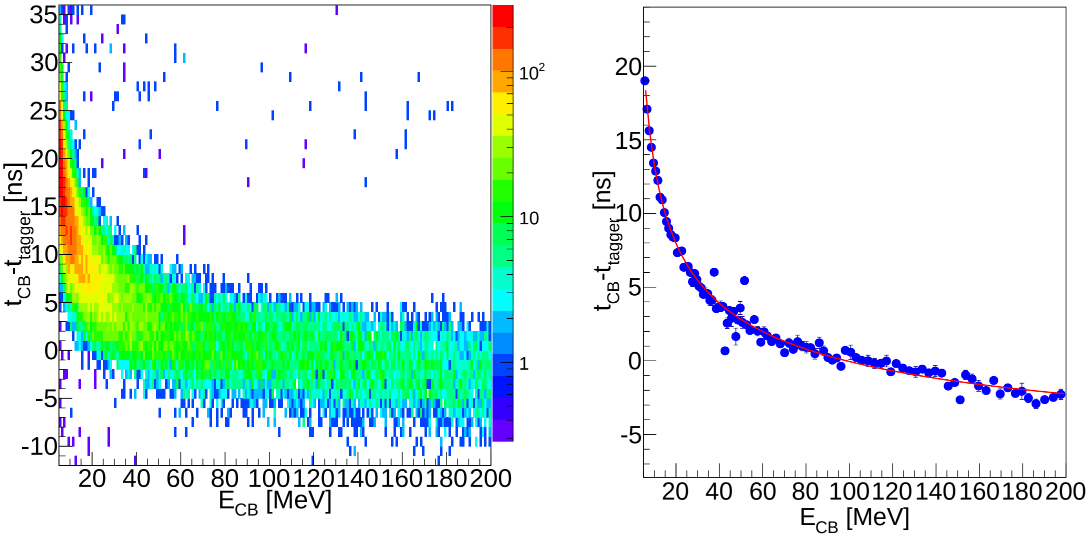

(a)

(b)

Fig. 3.5: Left: the energy dependence of the timing for one CB element is visible, where the color code denotes the number of counts in arbitrary units. Right: The peak positions for different energy slices are plotted as blue dots and the behavior is fitted with the function from equation 3.24.

Projecting this for several energy ranges allows the determination of the peak position using a Gaussian fit, and the peak positions can be plotted (3.5(b)). The fitting was performed using the function:

$$t(E_{CB}) = a + \frac{b}{(E_{CB} + c)^d} \tag{3.24}$$

The four free parameters a, b, c and d were determined for every single element and the time (relative time to the trigger $t = t_{CB} - t_{tagger}$) could be corrected by applying

$$\hat{t} = t - \left[a + \frac{b}{(E_{CB} + c)^d} \right] . \tag{3.25}$$

This procedure garantees an alignment of the individual times of the CB elements.

Rise Time Correction

For some elements the statistics are insufficient for a highly accurate fitting procedure, and therefore the time walk correction can lead to small offsets from zero in the relative timing of the CB elements. To correct this effect, we can shift the time peaks using parameter a from equation 3.24 and we end up with a precisely time calibrated Crystal Ball detector.

3.3.3 TAPS Time Calibration

Since the BaF_2 crystals have a rather fast rise time of the signals and CFDs are used for the timing information, the effects from time walk can be neglected. Therefore, the TAPS time calibration procedure consists of only two steps. Before every beam time, a TDC gain calibration is carried out to have a good timing information during the measurement. Having well adjusted TDC conversion gains g_i, only the offset o_i from equation 3.20 have to be calibrated afterwards.

TDC Gain Calibration

By delaying the stop signal from the TAPS detector elements using different cables of known length and hence known delay, determining the pedestal pulser position and finally plotting the positions against the delays, the gains g_i can be extracted from the slope of a linear fit. The cable lengths were determined using a signal generator and an oscilloscope and a fixed delay time of 10 ns for every cable was established. For more detailed information see [57].

Offset Calibration

To determine the individual offset o_i the time differences of all neutral clusters for every central cluster element were plotted (see figure 3.6(a)). The positions of the coincident peaks p_i were extracted with a Gaussian fit, and the offsets were corrected as for the Crystal Ball using

$$\hat{o}_i = o_i + \frac{p_i}{g_i}, \tag{3.26}$$

with the already adjusted TDC conversion gains g_i from above.

Since altering one offset o_i influences all the other offsets, this procedure has to be done iteratively and depending on the initial calibration quality, up to ten iterations were necessary.

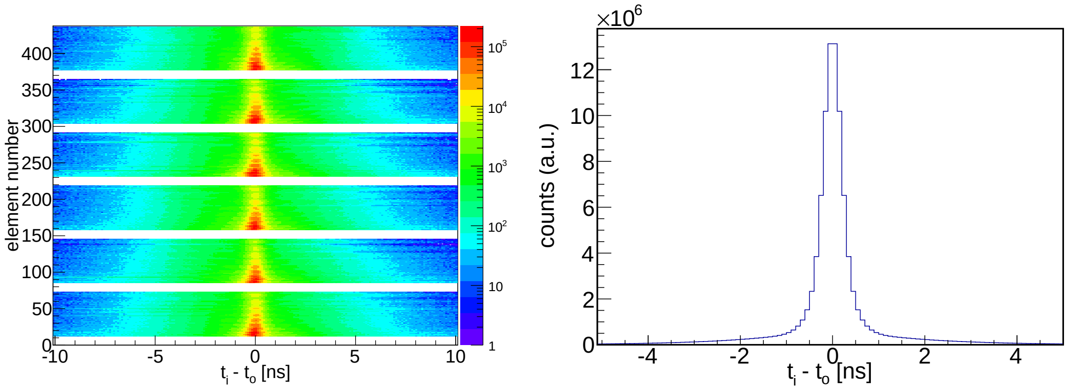

(a) (b)

Fig. 3.6: On the left hand side, the time difference of the center cluster element to all other clusters is plotted. The color code denotes the number of counts in arbitrary units. The offsets o_i are already calibrated and all peaks are nicely aligned at zero. On the right hand side, a projection of all elements reveals the final time resolution. The May 2009 data is shown here and the calibration set with the worst resolution has a FWHM of 848.61 ps and the mean value at -4.41 ps.

3.3.4 Tagger Time Calibration

As for the time measurement in Crystal Ball, were the gains are fixed by the CATCH TDCs, also the tagger times are given with fixed gains by the electronics. Again only the offsets o_i have to be determined and the TAPS detector, with its high time resolution could be used as reference time, which of course implies having an already fully time calibrated TAPS detector.

For all neutral clusters in TAPS, the time difference between the tagger and the TAPS elements were plotted for all activated tagger elements. To enhance the accuracy of the peak position determination, only π^0 events were accepted in TAPS by applying a cut on the invariant mass of the two clusters. The coincidence peak was fitted with a Gaussian in order to determine the peak positions and the new offsets $\hat{o}_i$ were calculated with equation 3.23.

Since the tagger element times do not depend on each other, one single calibration step fixes all offsets properly if the position determination is sufficiently accurate.

Also the PID and Veto time has been calibrated for all beam times, but at no time in the analysis procedure these timings were used and thus only a rough calibration was performed. The procedure was of course also iterative, as for the TAPS or Crystal Ball detectors and performed in the same way.

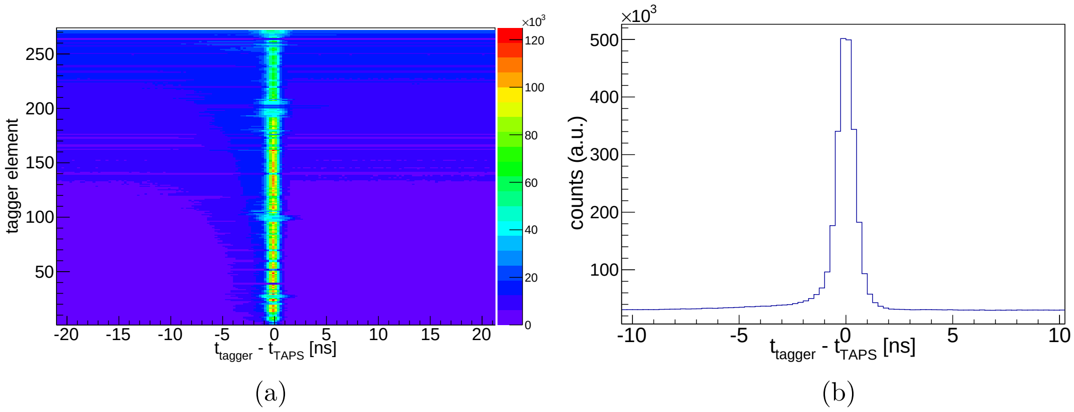

(a) (b)

Fig. 3.7: In (a), the time difference of the tagger element time to all neutral cluster times in TAPS coming from a π^0 decay is plotted. The color code denotes the number of counts in arbitrary units. The offsets o_i are already calibrated and therefore all peaks are aligned at zero. In (b), a projection of all elements reveals the final time resolution. The May 2009 data is shown here and the broadest peak has an FWHM of 888.51 ps and a mean value at 3.52 ps.

Calibration Flow

As mentioned before, the time calibration procedure of some detector parts depends on other detector calibrations, and therefore the procedure demands a correct sequence. In a first step, the TAPS detector time had to be calibrated in order to have a consistent timing of all elements. Next, the tagger time was calibrated relative to the TAPS detector, aligning all tagger element time peaks at zero. The Crystal Ball was then calibrated relative to the tagger time, resulting in consistent timing of all crystals, but also relative to the tagger and thus to the TAPS detector. Finally all time differences (TAPS-tagger, tagger-CB and CB-TAPS) are centered at zero and well aligned for all elements.

3.3.5 Threshold Calibration

As discussed before, several different thresholds are applied during the data taking process. Individual thresholds for all TAPS and CB elements suppressed very low energetic hits, and additionally the multiplicity trigger rejects low energetic clusters. The influence of these thresholds on the detection efficiency is huge, especially for low energetic events and, therefore, a threshold calibration is essential for the simulation process. The threshold values have to be determined as precise as possible and applied accurately in the analysis of experimental and simulated data.

CB Threshold Determination

As explained in section 2.9.2, the signals of 16 adjacent crystals are treated as logical group, hence 45 ($45 \cdot 16 = 720$) discriminators enforce the cluster thresholds and provide the multiplicity trigger in CB.

Since the conversion gains differ for the logical groups, also the thresholds differ in terms of energy. Because the indices of the elements, which exceeded the thresholds are not recorded in the data taking process for the Crystal Ball elements, one has to find the exact energy value of all the thresholds. Assuming that the element with the most energetic hit also had the highest probability of exceeding the threshold, this element was set as 'center' for the threshold determination. The 'centers' of all block were then stored in a list according to their energies. Since also TAPS can contribute to the total multiplicity trigger, a similar list was produced from the six discriminator sectors in TAPS (see section 2.10) and merged with the CB list. Next the energies were filled into a histogram for the corresponding cluster element (see figure 3.8(a)). Depending on the multiplicity trigger (M2+ or M3+) either the two or the three most energetic triggers were filled. The trigger influence on the number of counts in these spectra is clearly visible (see figure 3.8(b) top) as steep rises in the number of counts. To determine the correct energy position, the derivative of each spectrum was calculated, leading to a maximum in the corresponding spectra of the derivatives. A Gaussian fit finally yielded the positions and hence the energy values of the experimentally applied LED thresholds (see figure 3.8(b) bottom). A more detailed discussion of this procedure is given in [81] and [82].

Since the TAPS LED threshold pattern, unlike the one from CB, was recorded in the data, a direct determination of the individual threshold from the pattern is possible. The higher accuracy of this determination method is obvious, when comparing the figures 3.8(b) and 3.9(b). A detailed explanation is given in the next section.

TAPS and Veto Thresholds Determination

In many experiments one tries to suppress the contamination of the data sample through electromagnetic background, which is mostly going in forward direction into the inner TAPS rings. For this purpose the LED thresholds from the TAPS crystals can be set individually and often one sets the inner thresholds higher then the outer ones. However, for the beam times of this work all thresholds have been set to ~ 30 MeV, for which cosmic radiation was used to calculate the correct values. Of course this pre-calibration is influenced by the high energy calibration explained in sections 3.2.3 and 3.2.3 and thus another threshold determination has to be performed.

The calibration uses the recorded LED pattern and a first histogram is being

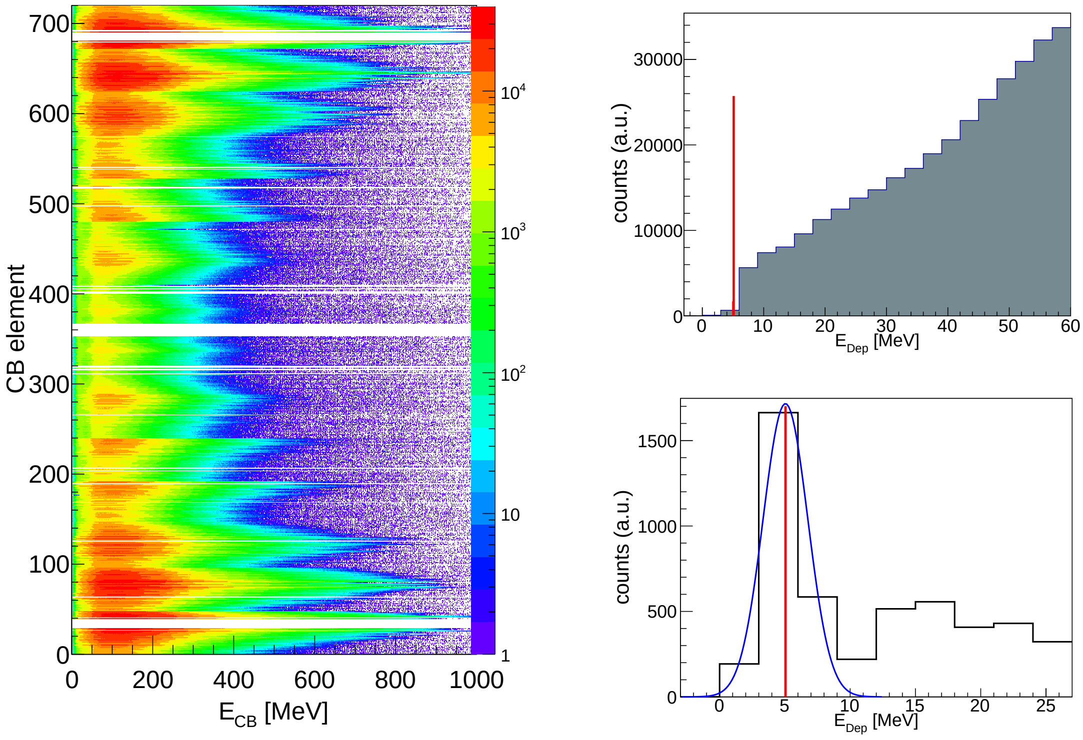

(a) (b)

Fig. 3.8: In (a) all energies are plotted against the corresponding CB elements (see text) and the color code denotes the count number in arbitrary units. In (b) on top, the projection for one element shown, the red line indicates the threshold position determined in (b) bottom, where the derivative is plotted together with a Gaussian fit and again the determined threshold energy drawn as red line.

filled, where all TAPS hits are plotted against the TAPS elements and a second one, where only the hits with a coincident LED threshold bit are filled against the TAPS elements. Dividing now the second histogram by the first one, leads to a very sharp edge and the threshold values are clearly visible when looking into the projections for a single element (see figure 3.9(a)). As for the threshold determination in the Crystal Ball, the derivative of this histogram is then fitted with a Gaussian and the positions were determined (see figure 3.9(b)).

Since detection efficiencies are very sensitive to the individual low energy thresholds, also a precise determination of the BaF_2 CFD and the Veto LED thresholds had to be introduced. First the raw ADC spectra for Veto and BaF_2 were created from the data and their derivatives were again fitted with a Gaussian to extract the channel number of the threshold positions. The individual gains from the Veto and TAPS calibrations (sections 3.2.3 and 3.2.7) were then used to get the corresponding energy values.

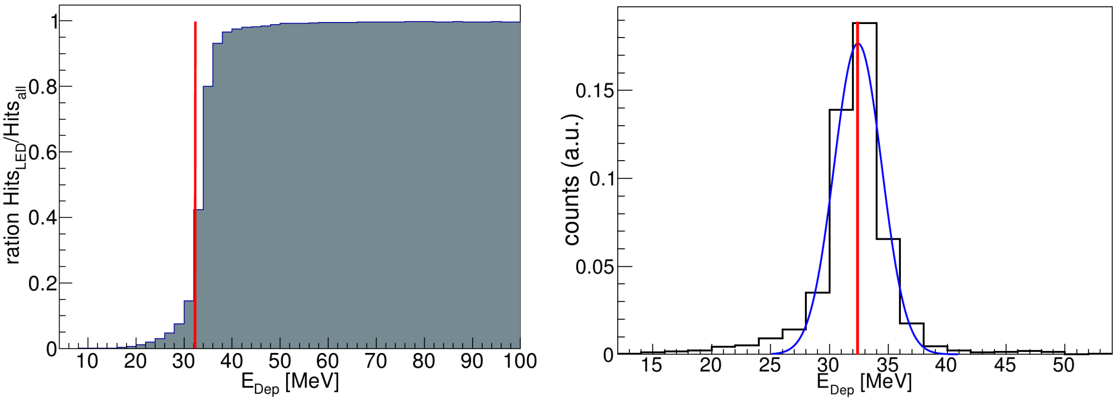

(a) (b)

Fig. 3.9: Figure (a) shows the ratio between the hits with a coincident LED threshold bit and all the TAPS hits for one single element. The very steep rise nicely shows the effect of the applied threshold and the red vertical line indicates the determined threshold position. In (b) the derivative of (a) is shown. The threshold position was designated by a Gaussian fit and is again indicated by the red line.

3.3.6 PID Angle Calibration

In order to maintain the MWPC or the target, the PID detector has to be dismounted and thus its orientation can change in between beam times. In order to know the correlation between the PID elements and corresponding CB segments an azimuthal angle calibration of the PID has to be performed.

We select events that have exactly one hit in CB and one in the PID and create a histogram, where the PID elements are plotted against the azimuthal angle, known from the CB crystals (see figure 3.10(a)). A clearly dominant coincidence peak will now yield the corresponding azimuthal angle of every PID element, as shown in figure 3.10(b). The additional peak, which is always shifted by ≈ 180 degrees stems from events with a neutral and a charged particle produced back-to-back and the charged particle is not detected in the PID.

3.3.7 Calibration Of The Simulated Data

In order to have a data set from simulation that is as realistic as possible, some small calibration steps had also to be applied on the simulation. In the further analysis process the simulation data is used many times and analyzed in the same way as the experimental data.

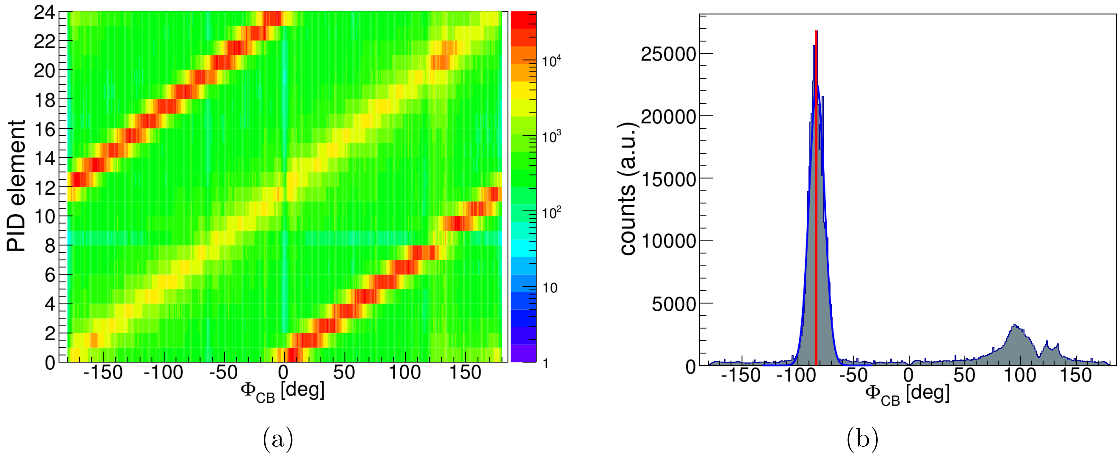

(a) (b)

Fig. 3.10: In (a) the spectrum for one hit in CB and one in PID is shown for all PID elements against the azimuthal angle of the CB cluster. The coincident peaks are clearly visible. In (b) the projection for one element is shown. The exact positions are determined from a Gaussian fit to the coincident peaks.

Energy

First the same calibration procedure was applied as for the data and the two main detector (TAPS and CB) responses have been energy calibrated performing the high energy calibration and the quadratic energy correction.

To reproduce the energy resolution of the two crystal materials from CB and TAPS an artificial smearing of the deposited energy spreading in the crystals had to be performed. As already mentioned, the given energy resolution of the detector materials can be approximated [58] with

$$\begin{aligned} \frac{\Delta E}{E} &= \frac{2\ \%}{(E\ [GeV])^{0.36}} && \text{for CB} \\ \frac{\Delta E}{E} &= 1.8\ \% + \frac{0.8\ \%}{(E\ [GeV])^{0.5}} && \text{for TAPS.} \end{aligned} \tag{3.27}$$

To determine the energy dependent resolution, isotropically distributed photons have been simulated up to energies of 1 GeV. The produced line shapes were fitted with Gaussians, yielding the deposited energies and their resolutions. The established resolutions from equation 3.27 were well reproduced by the simulation data. This fact is visible in figure 3.11, were the simulated resolutions are shown as open squares for CB and TAPS and the parametrized resolutions from equation 3.27 are plotted as full lines. Small deviations only occur for very high photon energies (≈ 800 MeV) in TAPS and are negligible, since only a fraction of photons from π^0 decays have such high energies. This is visible in figure 3.12, where the deposited π^0 decay photon energies are plotted as function of the center-of-mass

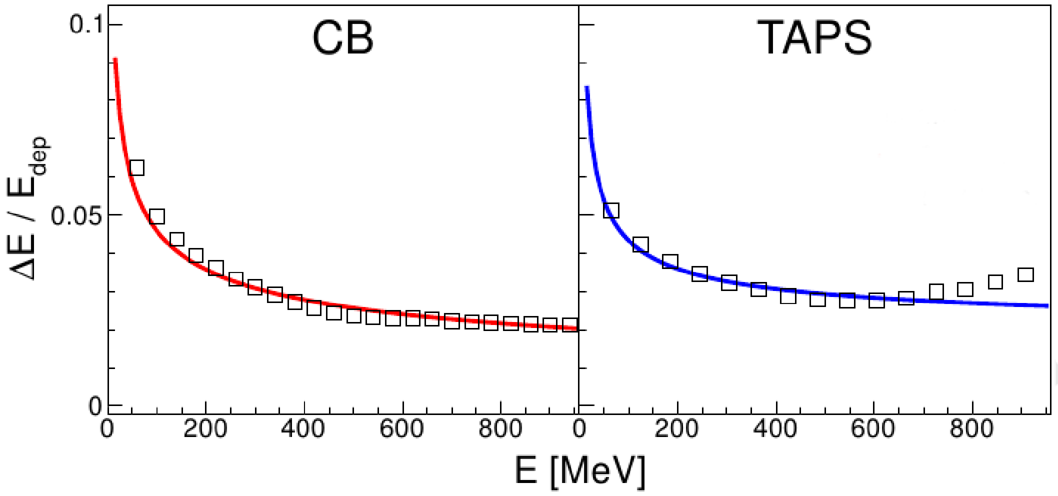

Fig. 3.11: Photon energy resolution from the simulation data as open squares compared to the parametrized resolutions from equations 3.27 as blue and red curves. Taken from [57] and edited.

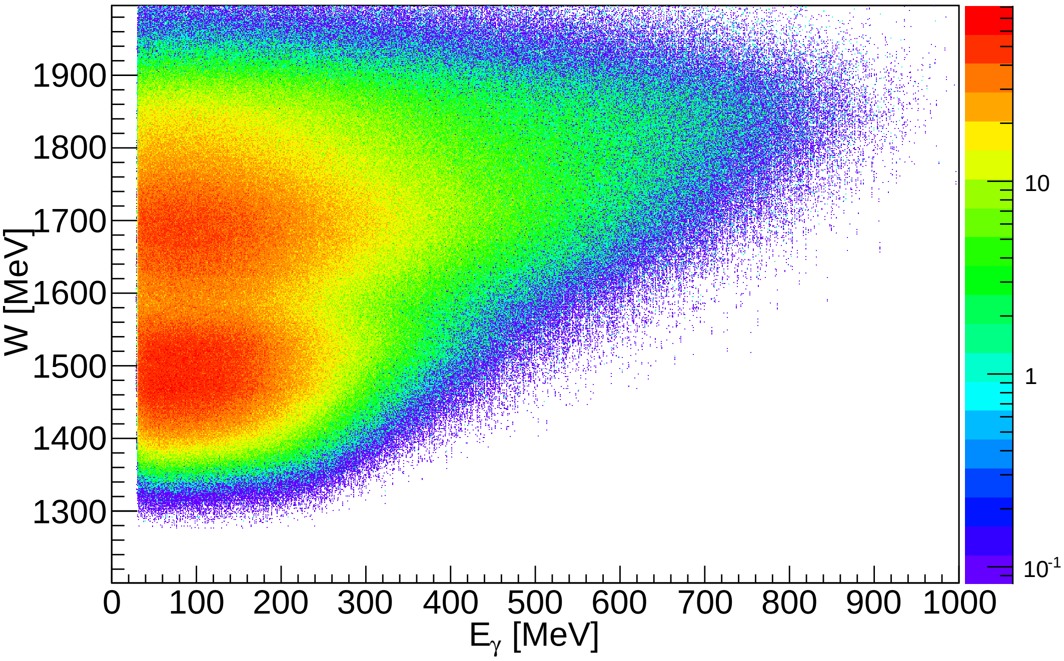

Fig. 3.12: Spectrum of the final state center-of-mass energy W against the deposited energy of the π^0 decay photons for the reaction $\gamma p(n) \rightarrow \pi^0\pi^0 p(n)$.

energy W.

In order to make the simulation as realistic as possible, not only the TAPS and CB energies have been smeared, but additionally also the ones for the Veto and PID detectors.

Furthermore the parametrized energy resolution given in equations 3.27 were applied for the χ^2-minimization procedure, which was used to determine the best combination of two photons to a π^0, and where the absolute energy error has to be included (see section 4.2).

Angles

Also necessary for the χ^2-minimization are the angular resolutions in TAPS and CB. Therefore the isotropically distributed photon simulation data from above was analyzed and spectra with the difference of the measured against the known polar and azimuthal angles of the photons as function of the polar angle[3] θ were created. Only for extreme forward and backward angles and in the gap region between TAPS and CB the errors reached the 5 % level, in average they are around 3 %.

This exactly calculated angular and energetic resolutions improved the χ^2 minimization process but had no significant influence on the total systematic error. A detailed discussion of the systematic errors will be given in section 4.14.

---

[3] The dependence on the photon energy was not included.

Chapter 4

Data analysis

So far the preparation of the experimental data was in the focus. Having now four precisely measured and well calibrated data sets, finally the extraction of the reactions of interest can begin. The analysis procedure can be split up in several steps. First, the correct final states have to be selected (section 4.1) and the π^0 mesons have to be reconstructed (section 4.2). The energy correction from section 4.4 improves the energy resolution of quantities that are used to cut away background events, explained in section 4.5. Thereafter the quality of the selection routine is checked in section 4.6 and the kinematic reconstruction of the final state, used to suppress effects from the Fermi motion is discussed in section 4.7. Next, the application of the software triggers and the tagger random background subtraction are explained in sections 4.8 and 4.9. In section 4.10 we will guide through the extraction of the beam helicity asymmetry, followed by a detailed explanation of the determination of the different detection efficiencies in section 4.11. Finally the photon flux normalization in section 4.12, the procedure of the cross section extraction in section 4.13 and the systematic errors in section 4.14 are discussed.

4.1 Event Selection

In the particle reconstruction procedure shown in section 3.1, charged and neutral clusters were distinguished based on the sensitivity of the PID and the Veto detector with some constraints on coincidence. The first step of the analysis is to choose the final states from the number of combined neutral and charged clusters. In order to structure the detailed discussion and avoid misunderstandings, most sections are split up into four parts according to the different reaction channels. The investigated reactions of this work are

(I) $\gamma p(n) \rightarrow \pi^0\pi^0 p(n) \rightarrow 4\gamma p(n)$

(II) $\gamma n(p) \rightarrow \pi^0\pi^0 n(p) \rightarrow 4\gamma n(p)$

(III) $\gamma p(n) \rightarrow \pi^0\pi^+ n(n) \rightarrow 2\gamma\pi^+ n(n)$

(IV) $\gamma n(p) \rightarrow \pi^0\pi^- p(p) \rightarrow 2\gamma\pi^- p(p)$.

and we have to select the following combinations of charged and neutral clusters:

(I) 4 neutral & 1 charged

(II) 5 neutral & 0 charged

(III) 3 neutral & 1 charged

(IV) 2 neutral & 2 charged

As mentioned, additionally to the quasi-free reactions on the proton, also free proton data was analyzed. Of course in this case the two reactions are

(V) $\gamma p \rightarrow \pi^0\pi^0 p \rightarrow 4\gamma p$

(VI) $\gamma p \rightarrow \pi^0\pi^+ n \rightarrow 2\gamma\ \pi^+ n$.

For all cases, where the treatment of free and quasifree proton was handled equally, no discrimination is made and we always refer to all proton data.

4.1.1 Analysis of $\gamma p(n) \rightarrow \pi^0\pi^0 p(n)$

We select all events, where four neutral and one charged cluster were detected. The neutral hits have to be combined to two neutral pions, using the χ^2-minimization, and the charged hit is the proton candidate. Now pulse-shape analysis is used for events in TAPS and all events are rejected, where the particles can not be assigned properly, that is the proton candidate has to be in the nucleon band and all four photon candidates must lie in the photon band[1]. The pulse-shape analysis will be explained in section 4.5.1. Now a series of kinematic cuts are applied to supress background contributions. Cuts on the invariant and missing mass of the two pions are followed by a cut on the coplanarity of the meson-nucleon[2] system, and furthermore the polar angle of the recoil nucleon can be restricted.

Next, the coincident background of the tagger is subtracted by a statistical method and for cross section calculations, detection efficiency and photon flux normalization have to be performed. For the extraction of the beam helicity asymmetries, the flux normalization cancels in the standard ratio for asymmetry calculation, and only detection efficiencies have to be applied.

---

[1] The pulse-shape analysis procedure is much more effective for $\gamma n(p) \rightarrow \pi^0\pi^0 n(p)$, since there it is more likely to confuse a nucleon with a photon.

[2] The combined pion-pion system is here referred to as meson.

Most measurements at the Crystal Ball @ MAMI experiment are conducted on free proton targets, and in the analysis the recoil nucleon detection is not required. For exclusive reactions on quasifree nucleons the detection of the recoil nucleon is mandatory to have a fully determined final state, which allows to calculate its center-of-mass energy W and thus remove effects from the Fermi momentum. The determination of the detection efficiencies though is complicated by the recoil nucleon. A discussion on that is given in section 4.11.

4.1.2 Analysis of $\gamma n(p) \rightarrow \pi^0\pi^0 n(p)$

We select all events where five neutral clusters were detected and use the χ^2-minimization to find the best combination of four clusters to two π^0 mesons and treat the left-over hit as neutron candidate. Again the hits in TAPS are examined for miss identifications of nucleons and photons, applying pulse-shape analysis. The same kinematic cuts as for the $\gamma p(n) \rightarrow \pi^0\pi^0 p(n)$ reactions are applied, the tagger coincident background is subtracted, and detection efficiencies and photon flux are calculated.

For the two analyses discussed so far, only one of the identification techniques (for the nature of the particle) of the detector system was applied, namely the pulse-shape analysis. The procedure relies more on finding the most probable assignment, using kinematic restrictions. Hence almost non of the particle identification possibilities like, $\Delta E/E$ analysis with Veto and PID or time of flight was exploited, except for the pulse-shape analysis (PSA), which was used to distinguish nucleons and photons after the χ^2 minimization procedure. These unused methods were then applied after all kinematic cuts to test the event selection quality.

The avoidance of systematic effects in the analysis of the simulation data is the reason for the waste of detector system skills. To adequately reproduce the effects from these exploration methods, a superior simulation of the detector system would be required and systematic effects would at the end play a bigger role for the results.

4.1.3 Discrimination Of Charged Particles

For the identification of the mixed-charge final states, a discrimination of protons and charged pions is mandatory, since much background contributions can arise for misidentified charged hits. An example for this is the $\gamma p(n) \rightarrow \pi^0\pi^0 p(n)$ final state, which would end up in the same analysis channel as the $\gamma p(n) \rightarrow \pi^0\pi^+ n(n)$ if one loses one photon[3] and accepts the recoil proton as a charged pion.

The most accurate charged particle discrimination in our detector system is provided by a so called $\Delta E - E$ analysis. Plotting the energy loss of charged

---

[3] The efficiency of the detector system is of course below 100 % and strongly depends on the nature of the particle.

particles in the PID or the Veto detector against the deposited energy in the CB or TAPS crystals allows to distinguish charged pions from protons[4]. Since the resolution of the Veto elements is inferior to the one from the PID, a discrimination of charged particles in TAPS via $\Delta E - E$ analysis would enhance systematic effects and has thus been omitted.

Another distinction alternative is offered by a time-of-flight analysis, where the deposited energy of a particle is plotted against its flight time from the target to the detector. The flight path to the Crystal Ball elements is too short (≈ 0.25 m) and the time resolution of the NaI crystals no accurate anough for precise time-of-flight analysis, in contrast to TAPS, which is placed ≈ 1.5 m from the target and thus enables this method.

For this analysis the only method used to discriminate protons from charged pions was the $\Delta E - E$ analysis with CB and PID. The main reason for this is to keep systematic effects as low as possible. The identification of charged particles with the time-of-flight analysis in TAPS gets ambiguous for high energetic protons, which are no longer stopped in the BaF_2 crystals, but punch through, which results in a false energy information. The time-of-flight analysis was used later in the analysis to monitor the quality of the event selection and the cuts (see section 4.6).

At first a spectrum with the energy loss in the PID against the deposited energy in CB was created. As for the PID energy calibration, proton events have been simulated and the projections (on the y-axis) of the proton band were fitted with a Gaussian. The cut positions for the different slices of CB energy were then fitted and the spectrum could be split up in a charged pion and a proton region. As a consequence of the calibration method, all the proton bands in the data lie approximately at the positions of the proton bands from the simulation. This is shown in figure 4.1, where on the left hand side the experimental data is plotted and on the right hand side the simulation data. The red line represents the cut and splits up protons and charged pions for the experimental data as well as for the simulation data.

4.1.4 Analysis of $\gamma p(n) \rightarrow \pi^0 \pi^+ n(n)$

To identify the final state, we first select events with three neutral and one charged clusters, apply the χ^2 minimization to find the best combination for two π^0 mesons and treat the left over neutral hit as neutron candidate. Hits in TAPS are now tested with the pulse-shape analysis technique.

The charged hit has to be positively identified as a charged pion and thus to be detected in the Crystal Ball detector. This reduces of course the reaction phase space, as events with the charged pion in the polar region 0–20 degrees are excluded,

---

[4] The charged pions in our experiment are approximately minimum ionizing particles, whereas the proton energy deposition still depends strongly on their energy.

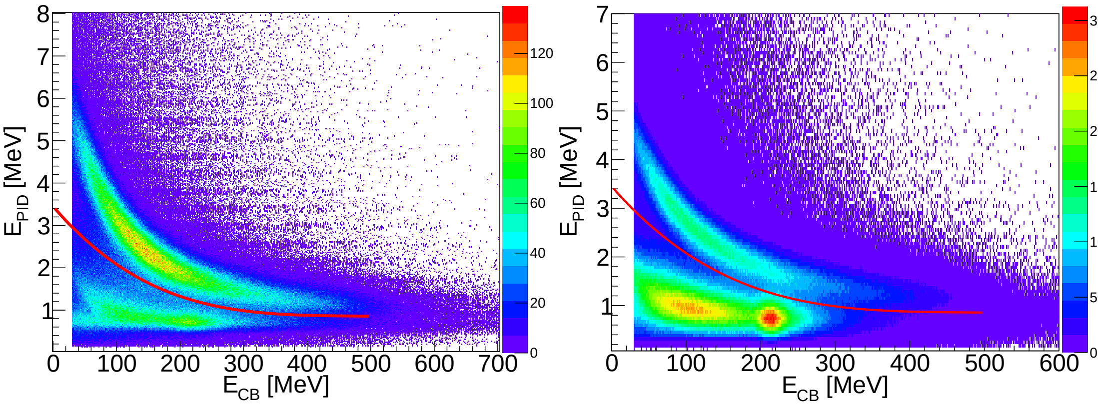

(a) (b)

Fig. 4.1: The spectra show the deposited energy in PID against the deposited energy in CB for the reaction $\gamma n(p) \to \pi^0\pi^- p(p)$, on the left for experimental data and on the right for simulation data. The typical band structures of the proton and the charged pions can be observed. The red line represent the applied cut. All particles above this curve are considered as protons and all particles below as charged pions.

but has only a small effect due to the large coverage of the solid angle of CB of ≈ 94 %. Nevertheless this fact should be kept in mind when the results of this work are interpreted or compared to model results.

Now again the kinematic cuts, as used for $\gamma p(n) \to \pi^0\pi^0 p(n)$ and $\gamma n(p) \to \pi^0\pi^0 n(p)$ were applied, the tagger coincident background events were subtracted and detection efficiencies and the photon flux were calculated.

4.1.5 Analysis of $\gamma n(p) \to \pi^0\pi^- p(p)$

Two charged and two neutral clusters have to be detected in an event, to be selected as possible final state of $\gamma n(p) \to \pi^0\pi^- p(p)$. The two neutral hits are checked for photons, if detected in TAPS and then combined to a neutral pion without any further restriction. The charged hits are then investigated with a $\Delta E - E$ analysis in CB. At least a positively identified charged pion is required, that is to say not two charged pion candidates nor zero are allowed. If the second charged hit is also detected in Crystal Ball, it has to pass the identification as a proton. If it was detected in TAPS, no further restrictions on the event were applied.

From here on, the procedure is the same as for all the above discussed channels.

4.2 π^0 Meson Reconstruction

Out of the number of neutral clusters, their energies and directions the best combination(s) to the π^0 meson(s) is (are) found by a χ^2 test and subsequently the energy resolution of the neutral pions is improved by an energy correction of the photons. We have to distinguish between three cases. Since the reconstruction of the π^0 for $\gamma n(p) \to \pi^0\pi^- p(p)$ is obviously simple, we have to discuss the cases of $\gamma p(n) \to \pi^0\pi^+ n(n)$ with three neutral hits, of $\gamma p(n) \to \pi^0\pi^0 p(n)$ with four neutral hits and of $\gamma n(p) \to \pi^0\pi^0 n(p)$ with five neutral hits.

4.2.1 Reconstruction From Three Neutral Hits

First, all neutral clusters are assumed to be photons, and for all three combinations of photon pairs we calculate

$$\chi^2_{ij} = \left(\frac{m_{\gamma_i\gamma_j} - m_{\pi^0}}{\Delta m_{\gamma_i\gamma_j}}\right)^2, \qquad \text{with} \qquad i,j = 1,2,3, \qquad i \neq j, \tag{4.1}$$

m_{π^0} as the nominal mass of the π^0 meson, $m_{\gamma_i\gamma_j}$ as the invariant mass of the photon pair $\gamma_i\gamma_j$ and $\Delta m_{\gamma_i\gamma_j}$ as the corresponding error in its invariant mass. As it will be shown in section 4.3, $\Delta m_{\gamma_i\gamma_j}$ depends only on the error in the measured angles $\Delta\theta$ and $\Delta\phi$ and the error of the deposited energies ΔE and can therefore be calculated for every combination. As explained in section 3.3.7, these errors have been established with simulation data for CB and TAPS separately.

The best photon combination will yield the smallest value of χ^2 and thus should really originate from the π^0 decay. For this reason the photon combination that minimizes χ^2 is assumed to stem from the π^0 and the left over neutral hit is treated as neutron candidate.

4.2.2 Reconstruction From Four Neutral Hits

Here now the four neutral hits from the decay of the two π^0 mesons produced in the reaction $\gamma p(n) \to \pi^0\pi^0 p(n)$ have to undergo the χ-minimization process. We have again three different combinations and χ^2 now reads as

$$\chi^2 = \left(\frac{m_{\gamma_i\gamma_j} - m_{\pi^0}}{\Delta m_{\gamma_i\gamma_j}}\right)^2 + \left(\frac{m_{\gamma_k\gamma_l} - m_{\pi^0}}{\Delta m_{\gamma_k\gamma_l}}\right)^2 \tag{4.2}$$
$$\text{with} \quad i,j,k,l = 1,2,3,4 \quad \text{and} \quad i \neq j \neq k \neq l.$$

As above, the photon combination that minimizes the χ^2 value is assumed to stem from the corresponding π^0 decays.

4.2.3 Reconstruction From Five Neutral Hits

The final state of the reaction $\gamma n(p) \rightarrow \pi^0\pi^0 n(p)$ is composed of five neutral clusters, from which four stem from the decay of the two intermediate π^0 mesons and one is the recoil neutron. Having four places for five hits grouped in two, leads to 15 possible combinations, and we can again use equation 4.2, but this time the restriction for the indices reads

$$i, j, k, l = 1, 2, 3, 4, 5 \quad \text{and} \quad i \neq j \neq k \neq l.$$

As for the case with three neutral hits, we treat the left over particle as neutron candidate.

4.3 Calculation Of $\Delta m_{\gamma_i\gamma_j}$

The invariant mass of the π^0 meson, built by the photon pair $\gamma_1\gamma_2$, is given by

$$m_{\gamma_1\gamma_2} = \sqrt{2E_{\gamma_1}E_{\gamma_2} \cdot (1 - \cos(\phi_{\gamma_1\gamma_2}))}, \tag{4.3}$$

with the opening angle of the two photons $\phi_{\gamma_1\gamma_2}$ and their energies $E_{\gamma_1}E_{\gamma_2}$ [57]. The error $\Delta m_{\gamma_1\gamma_2}$ from equation 4.1 can be calculated with the standard Gaussian error propagation and reads

$$\Delta m_{\gamma_1\gamma_2} = \sqrt{\left[\frac{\partial m_{\gamma_1\gamma_2}}{\partial \cos(\phi_{\gamma_1\gamma_2})} \cdot \Delta \cos(\phi_{\gamma_1\gamma_2})\right]^2 + \sum_{i=1}^{2}\left[\frac{\partial m_{\gamma_1\gamma_2}}{\partial E_{\gamma_i}} \cdot \Delta E_{\gamma_i}\right]^2}. \tag{4.4}$$

With this we get for $\Delta m_{\gamma_1\gamma_2}$

$$\Delta m_{\gamma_1\gamma_2} = \frac{1}{2} m_{\gamma_1\gamma_2} \cdot \sqrt{\left[\frac{\Delta E_{\gamma_1}}{E_{\gamma_1}}\right]^2 + \left[\frac{\Delta E_{\gamma_2}}{E_{\gamma_2}}\right]^2 + \left[\frac{\Delta \cos(\phi_{\gamma_1\gamma_2})}{1 - \cos(\phi_{\gamma_1\gamma_2})}\right]^2}, \tag{4.5}$$

where $\Delta \cos(\phi_{\gamma_1\gamma_2})$ is given by

$$\Delta \cos(\phi_{\gamma_1\gamma_2}) = \sqrt{\sum_{i=1}^{2}\left[\frac{\partial \cos(\phi_{\gamma_1\gamma_2})}{\partial \phi_{\gamma_i}} \Delta\phi_{\gamma_i}\right]^2 + \sum_{i=1}^{2}\left[\frac{\partial \cos(\phi_{\gamma_1\gamma_2})}{\partial \theta_{\gamma_i}} \Delta\theta_{\gamma_i}\right]^2}. \tag{4.6}$$

With $\cos(\phi_{\gamma_1\gamma_2})$ as

$$\begin{aligned}\cos(\phi_{\gamma_1\gamma_2}) =& \frac{\vec{p}_{\gamma_1} \cdot \vec{p}_{\gamma_2}}{|\vec{p}_{\gamma_1}| \cdot |\vec{p}_{\gamma_2}|} \\ =& \sin(\theta_{\gamma_1}) \sin(\theta_{\gamma_2}) \cos(\phi_{\gamma_1}) \cos(\phi_{\gamma_2}) \ + \\ & \cos(\theta_{\gamma_1}) \cos(\theta_{\gamma_2}) \sin(\phi_{\gamma_1}) \sin(\phi_{\gamma_2}) \ + \\ & \cos(\theta_{\gamma_1}) \cos(\theta_{\gamma_2}) \end{aligned} \tag{4.7}$$

we get for the error $\Delta \cos(\phi_{\gamma_1\gamma_2})$

$$\begin{aligned}\Delta \cos(\phi_{\gamma_1\gamma_2}) \ =& \{ \, [-\sin(\theta_{\gamma_1}) \sin(\theta_{\gamma_2}) \sin(\phi_{\gamma_1} - \phi_{\gamma_2}) \Delta\phi_{\gamma_1}]^2 \ + \\ & [-\sin(\theta_{\gamma_1}) \sin(\theta_{\gamma_2}) \sin(\phi_{\gamma_2} - \phi_{\gamma_1}) \Delta\phi_{\gamma_2}]^2 \ + \\ & [(\cos(\theta_{\gamma_1}) \sin(\theta_{\gamma_2}) \cos(\phi_{\gamma_1} - \phi_{\gamma_2}) - \sin(\theta_{\gamma_1}) \cos(\theta_{\gamma_2}))\, \Delta\phi_{\gamma_1}]^1 \ + \\ & [(\sin(\theta_{\gamma_1}) \cos(\theta_{\gamma_2}) \cos(\phi_{\gamma_2} - \phi_{\gamma_1}) - \cos(\theta_{\gamma_1}) \sin(\theta_{\gamma_2}))\, \Delta\phi_{\gamma_1}]^2\}^{1/2}. \end{aligned} \tag{4.8}$$

As a consequence, the error in the invariant mass of the photon pair $\gamma_1\gamma_2$ depends on the errors of the energies $\Delta E_{\gamma_{1,2}}$ and the errors of the angles $\Delta\theta_{\gamma_{1,2}}$ and $\Delta\phi_{\gamma_{1,2}}$ of the photon pair.

4.4 π^0 Energy Correction

The invariant masses of the reconstructed π^0 mesons are not exactly at their nominal position. The reason for this is the finiteness of the π^0 and η meson peaks in the invariant mass spectra, which have been used to calibrate the energy response of the detectors. They are in fact almost normal distributed in total, but for a single event the invariant mass value of the reconstructed meson is not always at the nominal position.

According to [76] one can correct the energies $E_{\gamma_{1,2}}$ of the photons for every event in such away, that eventually

$$m_{\gamma_1\gamma_2} = m_{\pi^0} \tag{4.9}$$

holds. Denoting the corrected energies of the photons as $E'_{\gamma 1,2}$ and neglecting the angular resolution we can calculate the energy correction as

$$E'_{\gamma 1,2} = \frac{m_{\pi^0}}{m_{\gamma_1\gamma_2}} E_{\gamma_1\gamma_2} = a \cdot E_{\gamma_1\gamma_2}. \tag{4.10}$$

Now the four-vectors of the reconstructed π^0 mesons are simply scaled by a. This correction has proven to be important for the quality of the analysis procedure, for example, it directly influences the resolution of the missing mass distribution.

4.5 Applied Cuts

So far we selected the correct numbers of charged and neutral particles and classified them partially with pulse-shape and $\Delta E - E$ analysis. This event selection procedure is not sufficiently accurate, since many possible background contributions can still end up in our selections. The reason for this are deficiencies in the particle detection sensibility of our system, which can lead to undetected particles or wrongly marked charged or neutral particles. Moreover secondary particles can be produced during the passage of the final state particles through the detector material. Also accidental coincident particles in the PID and Veto detectors (see sections 3.1.2 and 3.1.3) can mimic charged particles, when in fact neutral ones were detected. To minimize this background contributions and ending up with a clean signal, cuts on the kinematics of the reaction can be applied. Of course this procedures will also reject events of interest and hence the task is not to reject as much background as possible but rather to maximize the signal to background ratio. As we will see in the following sections, this can be challenging, since signal and background are not always easy separable. But at first we will discuss the pulse-shape analysis procedure, which was already mentioned in several of the previous sections.

4.5.1 Pulse-shape Analysis

As mentioned before, the pulse-shape analysis is enabled by the special feature of the BaF_2 crystals, which have two sorts of scintillation light components and allow for a discrimination of nucleons and photons. Right after selecting the true number of charged and neutral clusters and the reconstruction of the π^0 mesons, all particles in TAPS are checked for miss identification by differentiating between photons and nucleons. Since this special feature of the TAPS crystals is not included in the detector simulation, wrong rejections have to be kept at the lowest possible level, as they are not reproducible. Therefore the cut regions have been chosen rather wide, leading to a minor influence of the cut.

As explained in section 3.2.4 the calibration procedure positioned the photons at PSA-angles of 45 degrees. In general all events outside a three σ band alongside the ridge of the photons, were rejected as photon candidates. High energetic nucleons though are detected with wrong energy values, because they punch trough the crystals and thus end up at too high PSA-angles for the PSA-radius region from 85 to 380 MeV and therefore no cut could be applied in this region.

The peak and sigma values were determined separately for every TAPS crystal. In figure 4.2 the PSA plots for all TAPS elements are shown for all final state particles of $\gamma p(n) \rightarrow \pi^0\pi^0 p(n)$ and $\gamma n(p) \rightarrow \pi^0\pi^0 n(p)$. The photons show up as the typical band along 45 degrees and the nucleons are visible at smaller PSA-angles.

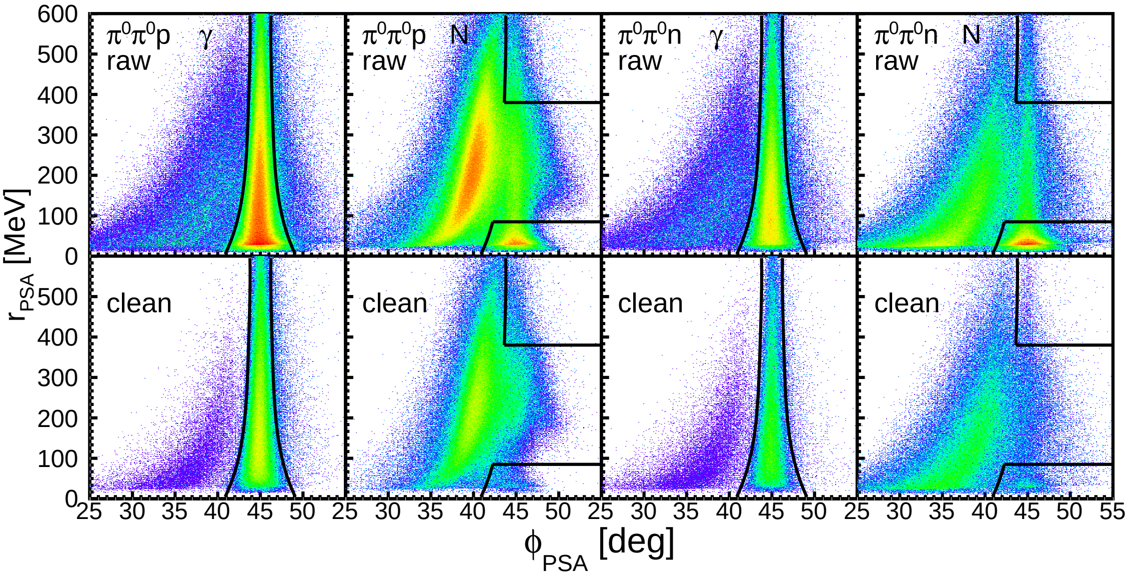

Fig. 4.2: The pulse-shape analysis spectra for the double π^0 channel final state particles. The upper row shows the raw spectra, where no kinematic cuts have been applied. For the spectra in the lower row all kinematic cuts, explained in the course of this section were applied.

The upper row shows the raw spectra, that is to say only the above mentioned analysis steps have been applied and especially in the spectra for the nucleons N the photon background is still visible. The lower row shows the same spectra after all kinematic cuts, which clearly remove most of the background. The black lines represent the average of all PSA cuts on nucleons and photons, and in overall one sees that the effect of the pulse-shape analysis is only small.

4.5.2 The Invariant Mass Cut

The invariant mass of two photons coming from the decay of a former particle depends only on the two photon energies $E_{\gamma_{1,2}}$ and the opening angle $\phi_{\gamma_{1,2}}$ of the two photons and is given by

$$m_{\gamma_1\gamma_2} = \sqrt{2E_{\gamma_1}E_{\gamma_2} \cdot (1 - \cos(\phi_{\gamma_{1,2}}))} \tag{4.11}$$

To reduce background contributions, one can exclude events with invariant π^0 masses, that lie outside a certain region. Since for the two different isospin channels we have a different number of neutral pions, the discussion has to be split up into two parts. First we will discuss the more simple case with only one neutral pion and subsequently the case with two π^0 mesons.

1D Invariant Mass Cut

In figure 4.3 the invariant mass distributions for the two mixed-charge channels are shown. The points represent the experimental data, the dashed lines are polynomial fits to the background and the applied cuts are indicated with the black vertical lines.

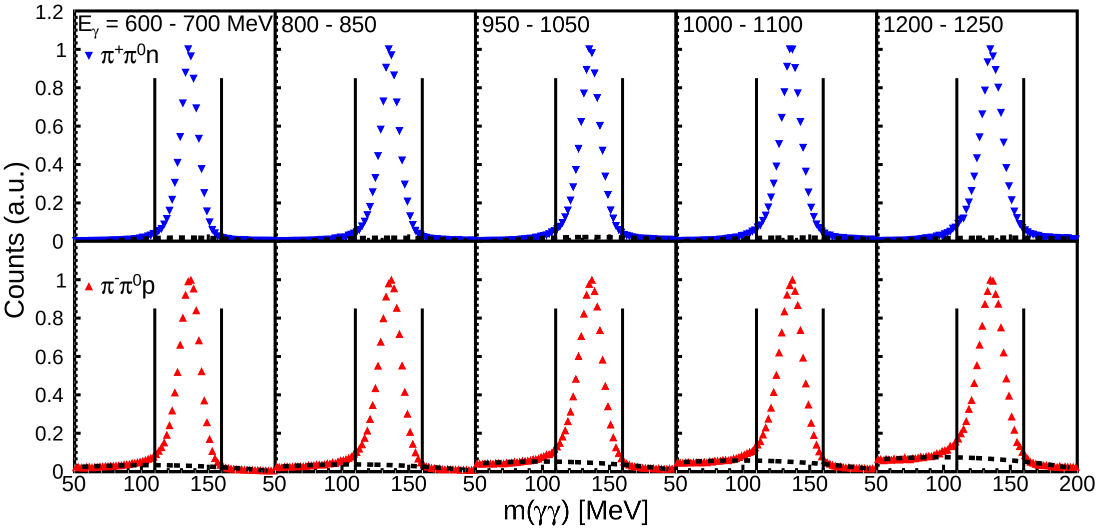

Fig. 4.3: The invariant mass distributions for the two mixed-charge channels for three typical energy regions of E_γ. Top: $\gamma p(n) \to \pi^0\pi^+n(n)$, bottom: $\gamma n(p) \to \pi^0\pi^-p(p)$. Blue/red triangles: experimental data, dashed lines: fit to the background, vertical lines: applied cuts.

The background level increases for higher energies of the incident photon E_γ, but is still rather small. Apart from the aforementioned analysis steps, no further cuts have been applied and only events with $m(\gamma\gamma)$ between 110 and 160 MeV are used for further analysis. The reason for the energy independent application of the invariant mass cut is the minimization of systematic effects.

2D Invariant Mass Cut

For the case of two π^0 mesons, the invariant mass distribution can be plotted two-dimensional, as shown in figure 4.4. Due to the two-dimensionality, the background stacks up below the peak and has to be subtracted carefully. At first one cuts on the invariant mass of the second[5] photon pair from 110 to 160 MeV and looks at the spectra of the other photon pair.

Figure 4.5 shows these spectra for different energy bins of E_γ. The background has been fitted with a polynomial function and the signal to background ratio was

---

[5] This choice is arbitrary and will not have any influence, since the pions are randomized right after their reconstruction.

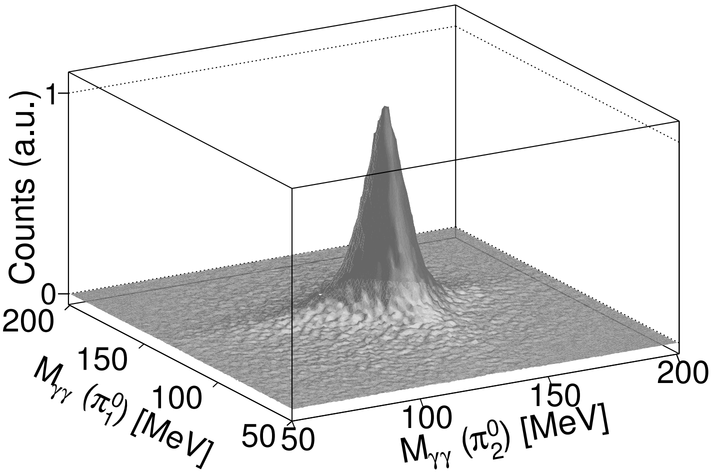

Fig. 4.4: Spectrum for the invariant mass of the two γ-pairs. The peak around 135 MeV clearly shows a large signal for the two π^0 channel and the background portion is small.

calculated. This energy dependent signal to background ratio could then be fitted and applied online in the analysis process. Hence in the analysis, all events with both invariant π^0 masses inside 110 and 160 MeV are used for further analysis and the weight from the signal to background ratio is applied energy dependent.

4.5.3 The coplanarity Cut

So far the reactions of interest have been identified by selecting the correct number of charged and neutral clusters, reconstructing the π^0 meson(s) and cutting on their nominal mass. To further reject background contributions, different cuts on the kinematics of the reactions can be applied. Claiming momentum conservation and assuming the initial state nucleon at rest implies, that the pion-pion system and the recoil nucleon lie within the same azimuthal plane. That is to say, that the angle difference $\Delta\phi$ should lie at 180 ^{o}. Assuming the initial state nucleon at rest and having ϕ independent from the z-direction, hence ϕ is the same in the laboratory frame and the center-of-mass frame, we can calculate $\Delta\phi$ to

$$\begin{aligned} \Delta\phi &= \phi_{\pi\pi} - \phi_N && \text{if} \quad \phi_{\pi\pi} - \phi_N \geq 0 \\ \Delta\phi &= \pi - |\phi_{\pi\pi} - \phi_N| && \text{if} \quad \phi_{\pi\pi} - \phi_N < 0, \end{aligned}$$

with the azimuthal angle of the pion-pion system $\phi_{\pi\pi}$. In the case of a quasifree target, the nucleon in the initial state is of course not at rest and the resolution of $\Delta\phi$ is thus worsened, but still accurate enough to reject background contributions.

Figure 4.6 shows the spectra of the azimuthal angular difference of the pion-pion

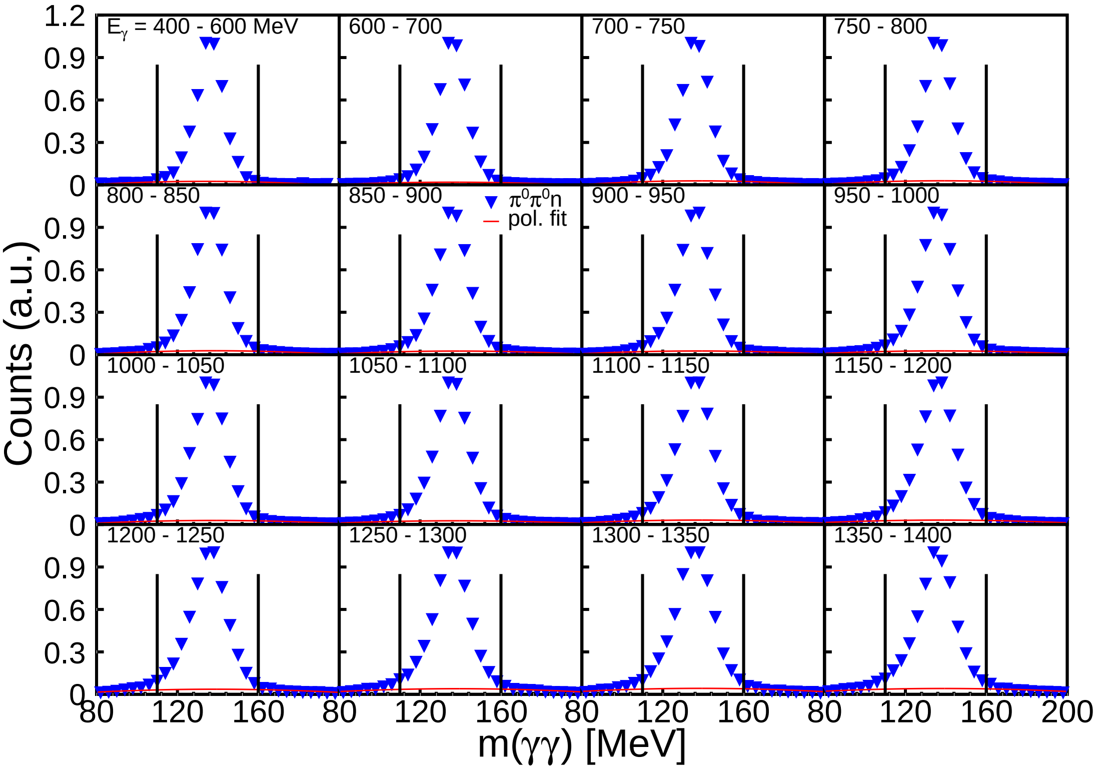

Fig. 4.5: Projections from figure 4.4 onto the axis of π_1^0 for invariant masses of π_2^0 between 110 and 160 MeV for $\gamma n(p) \rightarrow \pi^0\pi^0 n(p)$. The polynomial background function is shown in red and the applied cuts are indicated with the black vertical lines. Even though the background contribution is very small it has been subtracted in the further analysis.

system to the recoil nucleon in the laboratory frame for the neutral channels. The most probable source of background contribution is $\gamma N \rightarrow \eta\pi^0 N$ and the simulation of that channel is shown as green dashed-dotted curves. The dashed black curves show the signal of the reaction and the full curves (blue and red) show the sum of signal and background, which nicely follows the data points. The percentage of background is in the order of 10 % and unfortunately peaks at the same position as the signal. These background events will be rejected by the missing mass cut, explained in the next section.

Figure 4.7 shows the same spectra for the mixed-charge channels, where different sources of background contributions have to be taken into account. For both reactions the most dangerous background is coming from triple pion production, be it via η meson as in $\gamma N \rightarrow \eta N \rightarrow \pi^+\pi^-\pi^0 N$ or directly as in $\gamma N \rightarrow \pi^+\pi^-\pi^0 N$. Additionally, for the reaction on the proton contributions from $\gamma p(n) \rightarrow \pi^0\pi^0 p(n)$ can enter the event selection, if one photon stays undetected, and the proton is miss identified as charged pion.

The background of triple pion production also peaks at the signal position

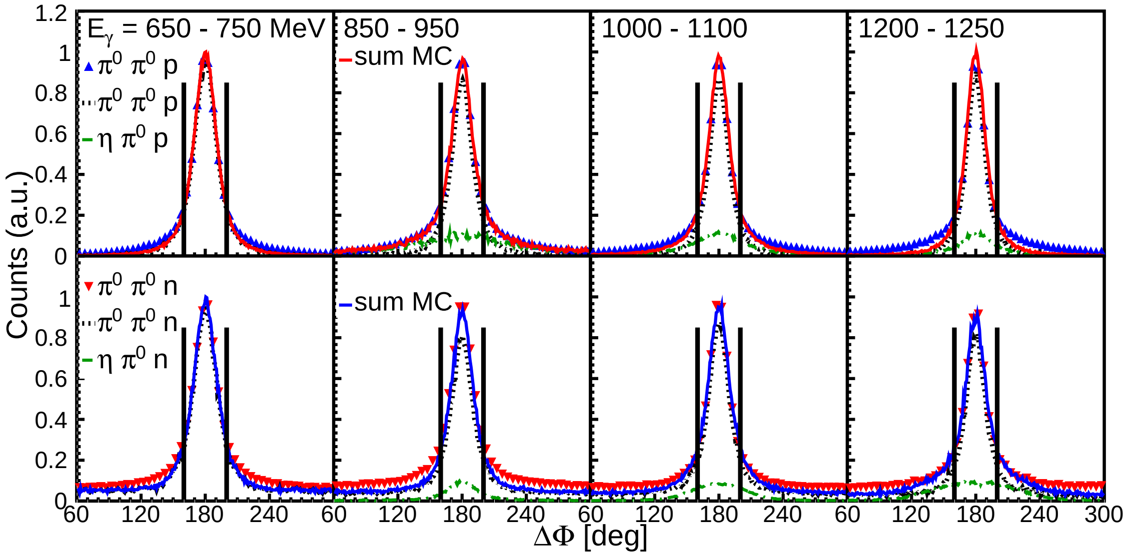

Fig. 4.6: Spectra for the azimuthal angular difference $\Delta\phi$ for the double π^0 channels for different bins of E_γ. The upper row shows the reaction on the proton and the lower row the one on the neutron. Full triangles: experimental data, dashed black curves: simulation data of the signal, green dash-dotted curves: simulation data of $\gamma N \to \eta\pi^0 N$ (background, starting at $\approx$ 800 MeV), solid curves: sum of signal and background. The x-axis range was reduced to 240 degrees, since all contributions decrease smoothly and it makes the line shapes better visible.

and thus cannot be suppressed by this cut. But as for the neutral channel, the background can be rejected by the missing mass cut.

4.5.4 The Missing Mass Cut

Up to now we selected the desired channels based on the correct number of charged and neutral particles, reconstructed the π^0 mesons from the detected photons and subtracted background events by cutting on the nominal mass of the π^0 meson and the coplanarity of the reaction products. The recoil nucleon was demanded in the selection to reduce background events, hence we analyze so called exclusive channels. To further constrain our analysis, we can treat the recoil nucleon as missing particle and study the missing mass of the pion-pion system. It is calculated as follows

$$\Delta m(\pi\pi) = |P_\gamma + P_N - P_{\pi_1} - P_{\pi_2}| - m_N, \tag{4.12}$$

with the energies of the involved particles E_i, their three vectors $\vec{p_i}$ and the nominal nucleon mass m_N. The initial nucleon is assumed to be at rest, and thus the missing mass $\Delta m(\pi\pi)$ should equal to zero, since the nominal rest mass of the proton or the neutron, respectively, are already subtracted in the equation. All background contributions, which can come from, e.g., a wrong assignment of the neutral parti-

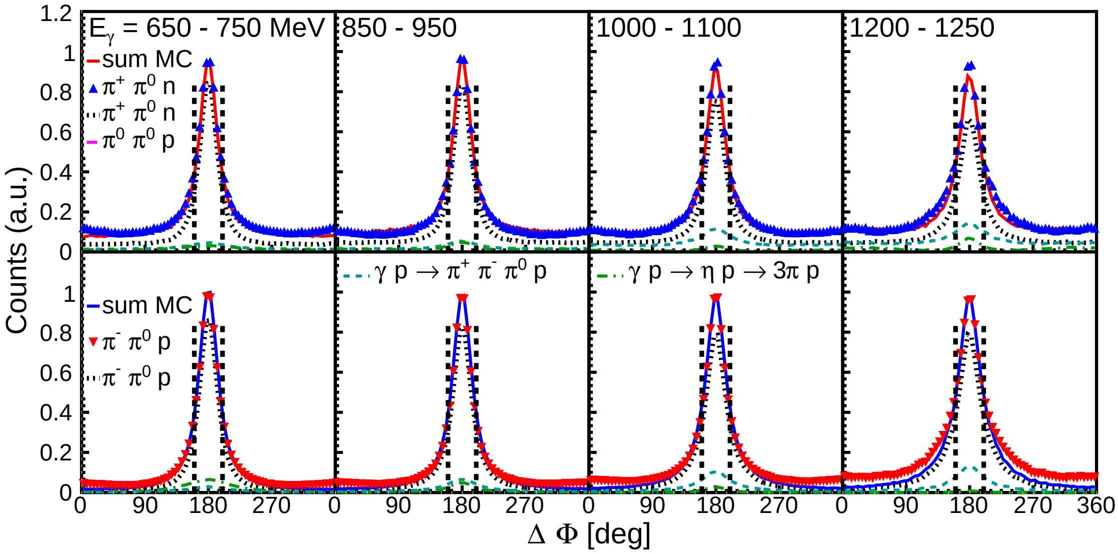

Fig. 4.7: Spectra for the azimuthal angular difference $\Delta\phi$ for the mixed-charge channels. Full triangles: experimental data, black dashed curves: simulation data of the signal, cyan long dashed curves: simulation of $\gamma N \to \pi^+\pi^-\pi^0 N$, green dash-dotted curves: simulation of $\gamma N \to \eta N \to \pi^+\pi^-\pi^0 N$, solid curves: sum of signal and background.

cles to the π^0 or from other channels, where one particle was undetected, will have a missing mass differing from zero.

For the case of the two π^0 channels, the background percentages that showed up in the missing mass spectra are at a very low level. Figure 4.8 shows these spectra for the double π^0 channels, with all above analysis steps already applied. The utilized cuts are indicated as vertical lines and have been chosen symmetrically around zero in order to suppress any systematic effects, that could come from preferring unsymmetrical parts of the Fermi momentum. The notation is the same as for figure 4.6 and again $\gamma N \to \eta\pi^0 N$ has been simulated and is shown as green dash-dotted curves. Due to the larger mass of the η meson ($m_\eta \approx 547$ MeV, $m_{\pi^0} \approx 135$ MeV) the missing mass of these events will be larger then zero (see equation 4.12) and thus will show up on the right side of the signal peak. The cuts were chosen such, that the background percentage is below 5 %.

By fitting the peak of the experimental data with a Gaussian, the positions of the peak and its sigmas could be extracted, and the cuts have been chosen at $\pm 1.5\sigma$. The determined energy dependent missing mass cuts were then applied online in the analysis.

Figure 4.9 shows the same spectra for the mixed-charge channels. The full triangles show the experimental data and the dashed black curves are again the simulation for the signals of the reactions. Since the background contributions for $\gamma N \to \eta N \to \pi^+\pi^-\pi^0 N$ and $\gamma N \to \pi^+\pi^-\pi^0 N$ show a very similar line shape, the

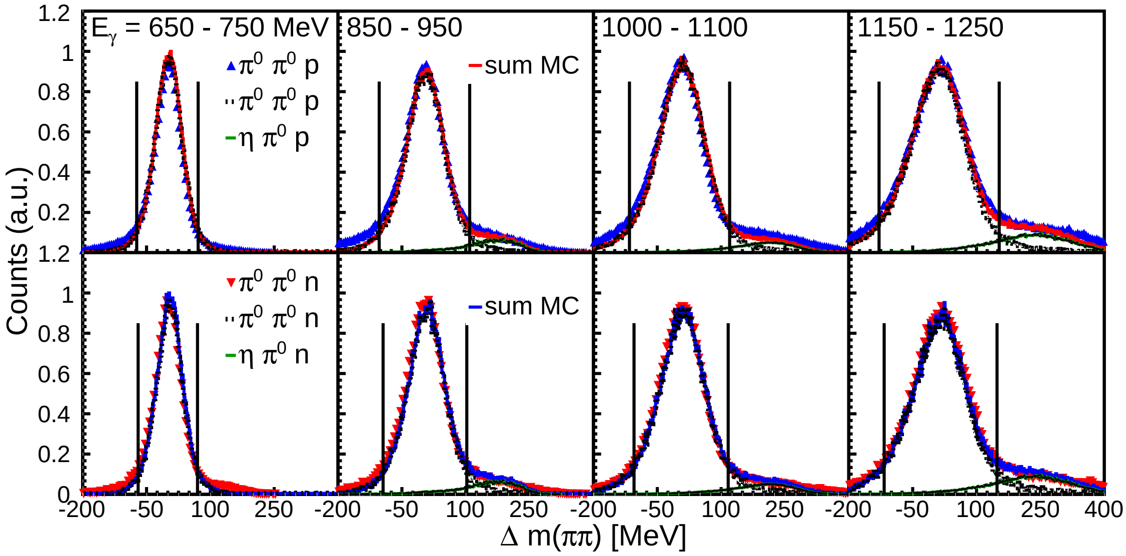

Fig. 4.8: The missing mass spectra for the two neutral channels for typical ranges of the incoming photon energy E_γ. All analysis steps discussed above are already applied and the background contributions are at a very low level. The vertical lines indicate the applied cuts.

fitting results yielded ambiguous portions for these channels and they had to be added up. The solid curves show the sum of all simulation data[6] and reproduce the data very well. The overall background percentage is slightly higher than for the neutral channel but nevertheless can be reduced to a negligible minimum by applying an energy independent missing mass cut of -80 to 80 MeV.

4.5.5 Nucleon Polar Angle

In the analysis of simulation data the polar angle θ_N of the recoil nucleon in laboratory frame was investigated and it was found that it is restricted to ≤ 60 degrees. That is to say, that the percentage of recoil nucleons with higher polar angles is very small and these cases must stem from events with very large Fermi momenta. Consequently, θ_N was restricted to ≤ 60 degrees in the analysis of experimental data and extreme Fermi momenta could be suppressed.

Unfortunately the PID detector position during the December 2007 beam time was incorrect. It was shifted upstream by about 15 *cm* and thus did not cover the whole CB detector. This deficiency led to two different problems in the analysis of this data. Firstly the charged particle identification for events flying into this uncovered region failed and protons and charged pions could not be distinguished anymore from neutrons and photons. Events with misidentified charged clusters can be selected for our analysis and thus lead to contributions from undesired

---

[6] MC stands for Monte Carlo simulation and is often used as short term for simulation.

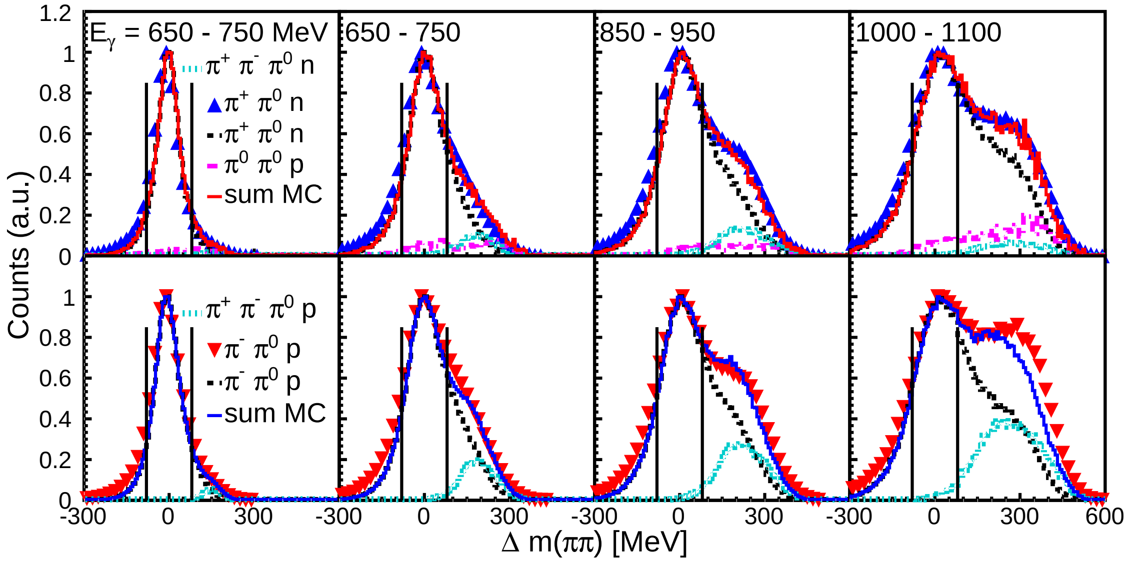

Fig. 4.9: The spectra show the missing mass for the mixed-charge channels for different bins of E_γ. All analysis steps discussed above are already applied and the background contributions can be rejected by conservative, energy independent cuts, indicate by the vertical lines.

channels. The general idea was to reject all events with particles detected in this polar angle region. But by a thorough investigation of this issue, it was discovered that the miss identification of protons as photons does not cause significant effects for $\gamma p(n) \rightarrow \pi^0\pi^0 p(n)$ and $\gamma n(p) \rightarrow \pi^0\pi^0 n(p)$, because most of this events are being rejected by the kinematic cuts. But of course a misidentification of a proton as neutron leads to a leaking of events from $\gamma n(p) \rightarrow \pi^0\pi^0 n(p)$ into $\gamma p(n) \rightarrow \pi^0\pi^0 p(n)$. To suppress this contaminations all events with nucleons detected in the uncovered region have been rejected for this beam time.

For the mixed-charge channel the situation is clearly different and has to be discussed separately. For $\gamma n(p) \rightarrow \pi^0\pi^- p(p)$ with its doubly charged final state no realistic contamination source can be made out, since it would have to come from a triply charged final state[7].

For the reaction on the proton again the main contaminating contribution is coming from its isospin partner, hence from $\gamma n(p) \rightarrow \pi^0\pi^- p(p)$. Misidentifying the proton as a neutron allows passing the event selection for $\gamma p(n) \rightarrow \pi^0\pi^+ n(n)$, and also the further cuts will be passed with large possibility, since the kinematics are equal in average. Therefore also for these channels only events with the nucleon detected in the θ region from 15 to 27 degrees have been rejected.

Secondly the detection efficiency for nucleons is affected by the shift of the PID detector. As we will see in section 4.11 the detection efficiency for the quasifree

---

[7] A possible contamination source is $\gamma p \rightarrow \pi^+\pi^-\pi^0 p$. But this background contamination has already been taken into account in the coplanarity and the missing mass cut

measurements could not be established very accurately, since the detection of the recoil nucleon was mandatory and precisely this is very delicate to simulate. The problem could be solved by extracting a correction factor for the nucleon detection efficiency from the hydrogen data. But since no hydrogen data set with the same conditions, i.e., with a shifted PID was available, the detection efficiency for the December 2007 beam time is not very accurate.

4.6 Event Selection Quality

As already mentioned, some particle identification techniques offered by the detector system have not been used in the analysis procedure and can now be applied to check the event selection for contamination.

4.6.1 The Pulse-shape Analysis

The pulse-shape spectra for the neutral channels have already been shown in figure **??**. The upper row shows the raw spectra, where neither kinematic nor pulse-shape cuts (see figure 4.2) have been applied and clear contaminations can be made out. Especially the pulse-shape spectra of the nucleons have large contributions from photons. The lower row shows the same spectra after all kinematic cuts, but still without the cuts from the pulse-shape analysis, which are shown as black lines. The much lower background percentage is clearly visible and together with the pulse-shape analysis cuts, the kinematic cuts lead to a final event selection, which is nearly free of contamination.

For the mixed-charge channels, we have not only two but three different particles in the final state. But as explained in section 4.1.3, no events with the charged pion in TAPS were accepted, and thus only the spectra of the final state photons and nucleons can be shown. Figure 4.10 shows the pulse-shape spectra for $\gamma p(n) \rightarrow \pi^0\pi^+n(n)$ in the left two columns and for $\gamma n(p) \rightarrow \pi^0\pi^-p(p)$ on the right. Again the upper row shows the raw spectra and the lower one the clean version, with all kinematic cuts applied.

4.6.2 The Time-of-flight Analysis

By plotting the time-of-flight (ToF) of a particle against its deposited energy, it is possible to distinguish different particles, e.g., protons from photons. But since the resolution of this identification method depends on the exact time measurement, a certain minimal distance is required for sufficient accuracy. The Crystal Ball elements are to close to the target, and thus no reliable identification procedure can be conducted. The TAPS detector is placed about 1.5 m downstream from the target and has a very precise time resolution and therefore offers the perfect

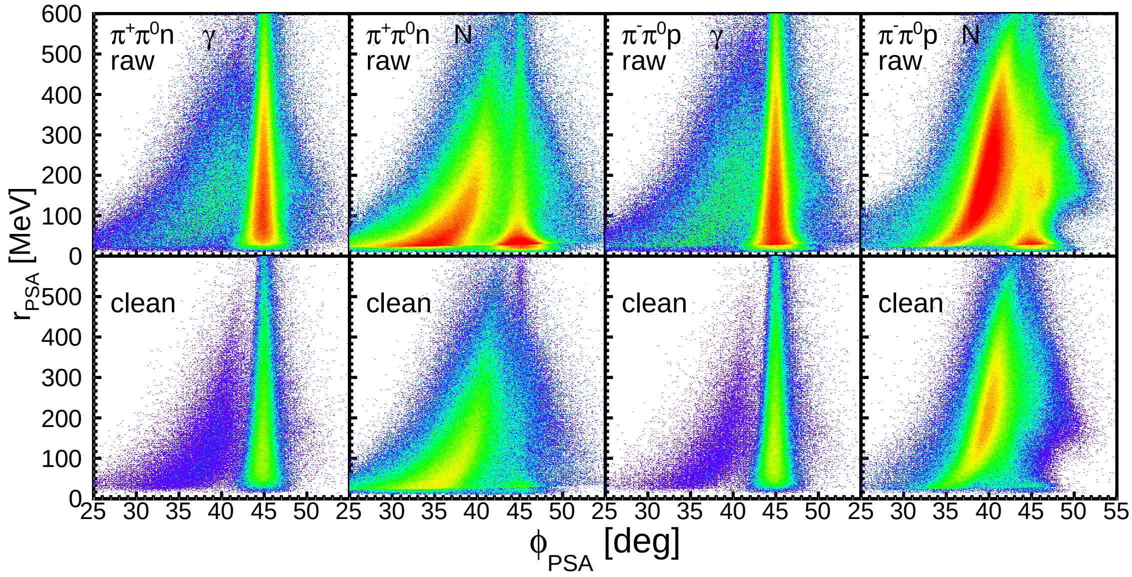

Fig. 4.10: The pulse-shape analysis spectra for the final state particles of the mixed-charge channels. Notation as in figure **??**

conditions for time-of-flight analysis. The flight time of a particle from the target to the TAPS detector can be calculated as follows

$$t_{ToF} = \frac{\Delta t}{s} + \frac{1}{c}, \tag{4.13}$$

where Δt is the time difference between tagger and TAPS, c is the speed of light. Since the flight paths s differ for different crystals, the time-of-flight has to be normalized to 1 meter and hence its unit is [ns/m]. In the time calibartion all time differencies were 'set' to zero for all crystals and therefore the normalized photon flight time $1/c$ must be added to the time-of-flight.

Figure 4.11 shows the time-of-flight against the deposited energy for all final state particles of the two neutral channels. The upper row shows the raw spectra, where no kinematic cuts have been applied and in the lower row the clean spectra are plotted.

The photons are present as vertical band, located at about 3 ns. The protons show again the clear energy dependence as afore seen in the $\Delta E - E$ analysis. For large energies they are not stopped anymore in the crystals but punch through and thus their energy information is false, which is visible as band at about 5 ns. The neutrons deposit their energy indirectly, i.e., in nuclear reactions and elastic or inelastic scattering, secondary particles are produce, which are then detected. Therefore there is no correlation between the neutron energy and the measured deposited energy and hence no clean structure is visible in the time-of-flight spectra. But it is important to mention that no traces of miss identified protons show up in the neutron spectra, which would lead to serious background in all channels.

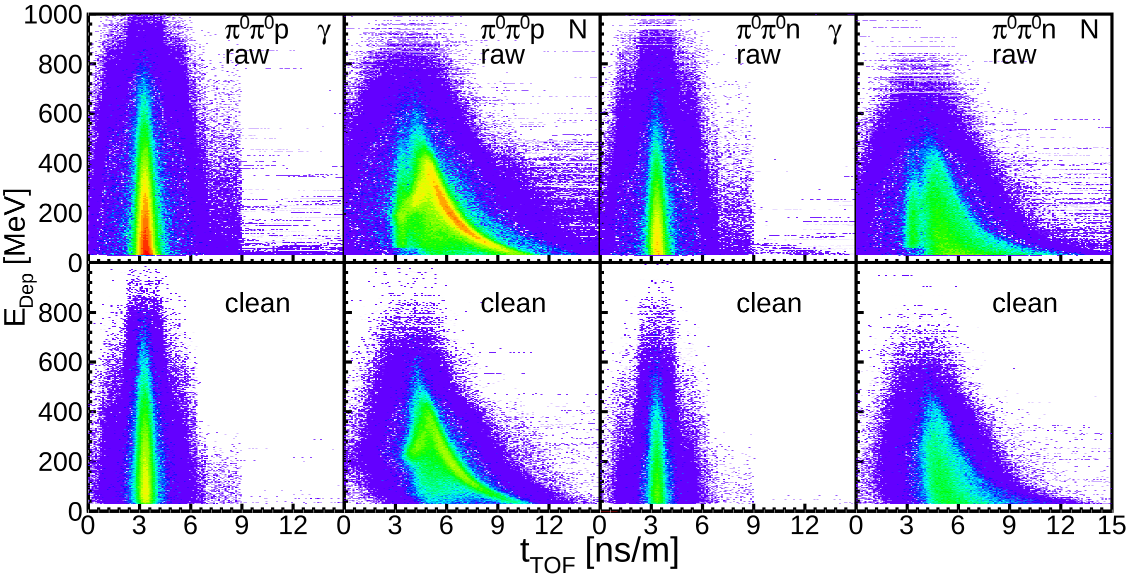

Fig. 4.11: The time-of-flight spectra for all final state particles of the two neutral channels. The upper row shows the raw spectra, without any kinematic cuts, whereas in the bottom row all kinematic cuts are applied.

The contamination in the raw proton spectrum is coming from charged pions and electrons, but these contaminations are realiably rejected by the kinematic cuts, as visible in the bottom row.

Especially in the spectra for the neutron and the proton, clear contamination from the photons can be made out if the kinematic cuts are omitted. Applying all kinematic cuts reduces the contamination visibly and leads to very clean signals.

In figure 4.12 the same spectra are shown for the other isospin channels and again the kinematic cuts clearly reduce the contamination reliably and finally very clean signals are obtained.

4.6.3 The $\Delta E - E$ analysis

To check the identification of the charged particles we can also check the $\Delta E - E$ spectra, but since we used this identification method for the event selection of the mixed-charge channels and of course for $\gamma n(p) \rightarrow \pi^0\pi^0 n(p)$, where no charged particles exist, there is only the proton identification for $\gamma p(n) \rightarrow \pi^0\pi^0 p(n)$ to be checked. In figure 4.13 this spectrum is shown and no contamination from charged pions or electrons can be made out.

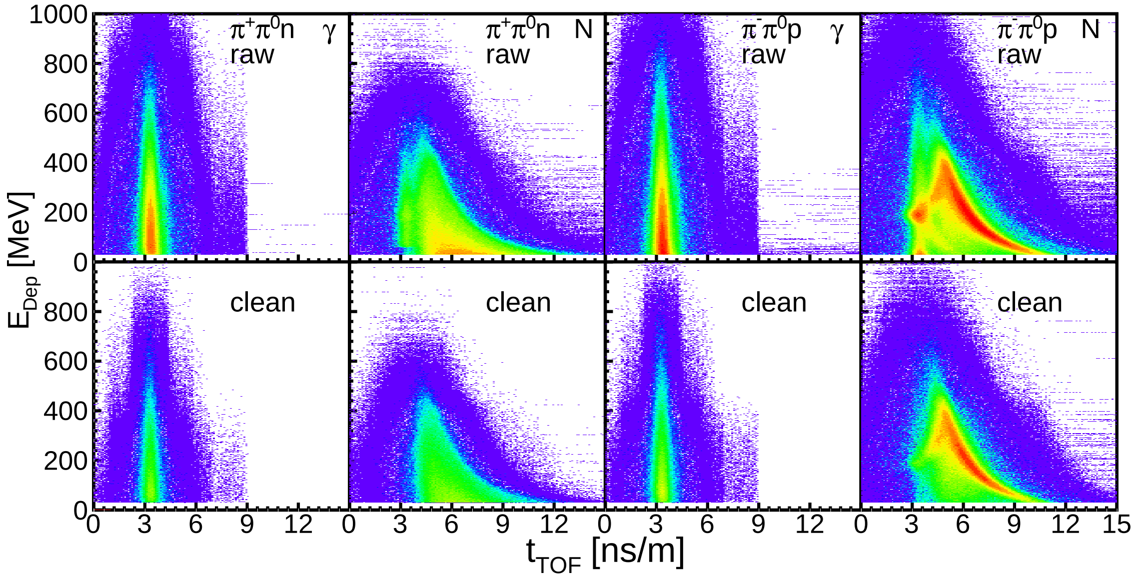

Fig. 4.12: The time-of-flight spectra for the recoil nucleons and the π^0 decay photons of the mixed-charge channels. No kinematic cuts have been applied for the spectra from the upper row. In the lower row all kinematic cuts were applied and the contaminations are strongly reduced.

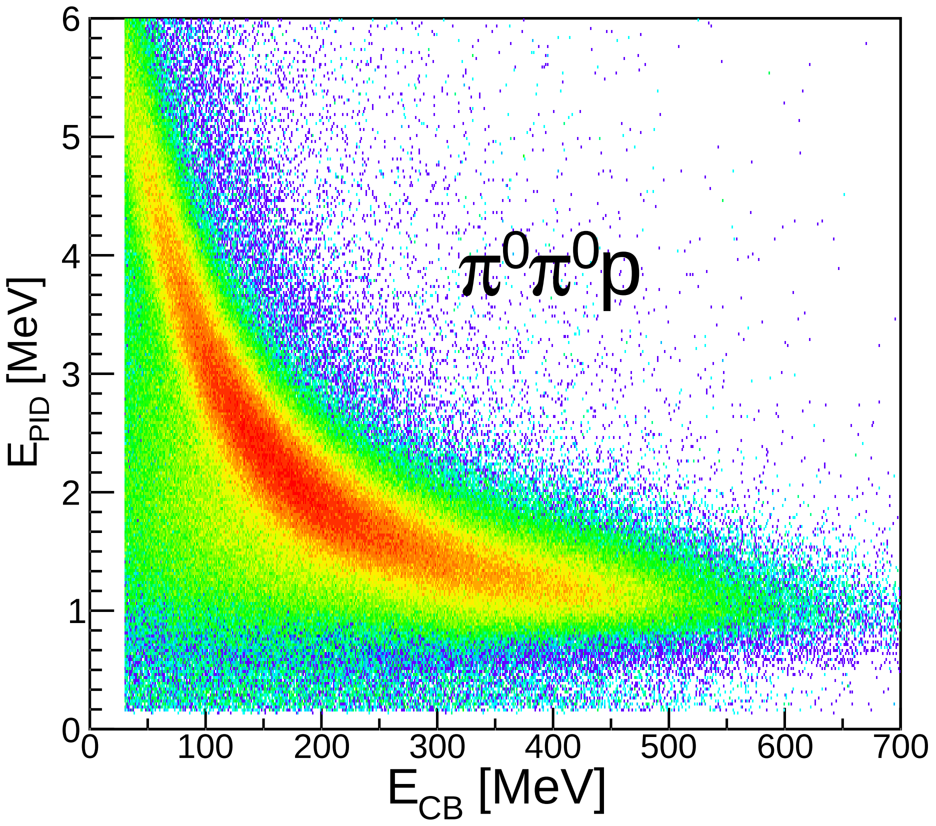

Fig. 4.13: The $\Delta E - E$ spectrum for $\gamma p(n) \to \pi^0\pi^0 p(n)$ after all cuts. No trace of contamination is visible.

4.7 True Center-of-Mass Energy Reconstruction

The center-of-mass energy $W = \sqrt{s}$ cannot be reconstructed from the initial state for quasifree reactions, since the Fermi momentum is unknown. Assuming the initial state nucleon at rest, the center-of-mass energy can be approximated and one ends up with free reactions folded with the Fermi momentum and thus with observables smeared by Fermi motion [83, 57].

Another approach is the reconstruction of W from the final state particles $\pi\pi N$, which presupposes the knowledge of all four-momenta. The measurement of the nucleons is less precise than the one of the photons, since the detector system is optimized for photon detection. Due to the smaller cluster sizes of nucleons[8], the position resolution is worse than for photons and additionally the energy information of the neutron is ambiguous. By correcting the energies of the measured protons one could in principle determine their energy quite precisely, but as the main goal of this work was the measurement on the neutrons, this was omitted. The main reason for this was to have the same systematic effects for the measurements on the neutron as on the proton.

By exploiting the full knowledge of the reaction kinematics one can calculate the energies of the recoil nucleons indirectly from the pion-pion system four-momenta and the position of the nucleons.

First we have to discuss the kinematics of the so called participant-spectator model. The main approximation is the assumption, that the reaction takes solely place on one of the nucleons, while the other one remains in its initial state. We can generalize the case for nucleons, without distinguishing the two cases, where either the neutron is the spectator and the proton the participant or vice versa.

In the initial state we have the participant nucleon with the mass m_P, the energy E_P and the Fermi momentum $\vec{p}_F$. Hence the spectator has the inverse Fermi momentum $-\vec{p}_F$ and the energy E_S and mass m_S. At first we request energy and momentum conservation and neglect the binding energy of the deuteron, which is about 2.2 MeV and get

$$p_D = p_P + p_S = \begin{pmatrix} E_P \\ \vec{p}_F \end{pmatrix} + \begin{pmatrix} E_S \\ -\vec{p}_F \end{pmatrix} = \begin{pmatrix} m_D \\ 0 \end{pmatrix}, \tag{4.14}$$

with the deuteron mass m_D. The energy E_S of the spectator is assumed to be on-shell during the whole reaction process and thus given by

$$E_S = \sqrt{m_S^2 + \vec{p}_F^{\,2}}. \tag{4.15}$$

---

[8] Nucleons deposit their energy in most cases in just one or two crystals.

For the energy E_P of the participant we can write

$$E_P = m_D - E_S = \sqrt{m_S^2 + \vec{p}_F^2}. \tag{4.16}$$

The participant is off-shell (neglect binding energy of the deuteron) and we have

$$\sqrt{m_S^2 + \vec{p}_F^2} \neq \sqrt{m_P^2 + \vec{p}_F^2}. \tag{4.17}$$

We can now calculate the center-of-mass energy $s = W^2$ as

$$s = (k + p_P)^2 = E_\gamma^2 + 2E_\gamma E_P + E_P^2 - (\vec{k} + \vec{p}_F)^2, \tag{4.18}$$

with the four momenta of the photon $k = (E_\gamma, \vec{k})$ and of the participant nucleon $p_P = (E_p, \vec{p}_F)$. Inserting E_P from above leads to

$$s = m_D^2 + m_S^2 + 2E_\gamma(m_D - \sqrt{m_S^2 + \vec{p}_F}^2) - 2m_D\sqrt{m_S^2 + \vec{p}_F^2} - 2E_\gamma p_{F,z}. \tag{4.19}$$

Now the kinetic energy of the recoil nucleon can be calculated from the four-momenta of the pion-pion system (p_M) and the azimuthal and polar angles of the recoil nucleon.

It should be mentioned here, that this calculation is in principle only correct for a decay, where both mesons are produced at the same time. But since the life times of these resonances are very short, the decay vertex are also sufficiently close in the case of a sequqential. As discussed in the introduction, these double pion channels are assumed to decay via sequential decay preferably and hence this calculation is an approximation. But it is a good approximation, since the life time of nucleon resonances are very short and thus the pions are almost produced at the same time. The success of this reconstruction method is visible in the next section, where free and quasifree proton data is shown and agrees very well. We have the following equation

$$\begin{pmatrix} E_\gamma \\ \vec{p}_\gamma \end{pmatrix} + \begin{pmatrix} m_D \\ 0 \end{pmatrix} = \begin{pmatrix} E_M \\ \vec{p}_M \end{pmatrix} + \begin{pmatrix} E_P \\ \vec{p}_P \end{pmatrix} + \begin{pmatrix} E_S \\ \vec{p}_S \end{pmatrix}, \tag{4.20}$$

where P and S can be proton and neutron and m_D is again the mass of the deuteron. From measuring the final state we know: E_γ, E_M, m_D, m_P, m_S, θ_M, ϕ_M, θ_P and ϕ_P and therefore the system is determined and T_P can be extracted. We will just show a short form of the whole calculation, for more details see [83].

To get a well-arranged expression we define

$$\begin{aligned}
A &:= p_{M,x}\sin(\theta_P)\cos(\phi_P) + p_{M,y}\sin(\theta_P)\cos(\phi_P) + (p_{M,z} - E_\gamma)\cos(\theta_P)\\
B &:= E_M - E_\gamma - m_D\\
C &:= (E_M + m_P - E_\gamma - m_D)^2 - (m_S^2 + p_M^2 + E_\gamma^2 - 2E_\gamma p_{M,z})
\end{aligned}$$

and can then calculate the kinetic energy T_P of the participating nucleon as

$$T_P = \frac{-(BC - 2A^2 m_P) + \sqrt{(BC - 2A^2 m_P)^2 - C^2(B^2 - A^2)}}{2(B^2 - A^2)}. \tag{4.21}$$

Another approach to determine the kinetic energy of the recoil nucleon is the use of its time-of-flight. As mentioned before, the distance to the CB crystals is to short for an accurate calculation and hence only events with the recoil nucleon detected in TAPS can be used this way. In this work only the kinematic reconstruction of T_P and hence of W was used.

The reconstruction of the center-of-mass energy of the final state is more reliable for the double π^0 channel, since the energy information for photons is more accurate then the one for charged pions. Nevertheless the reconstruction for the mixed-charge channel works fine and only for high energetic charged pions the energy information is inaccurate.

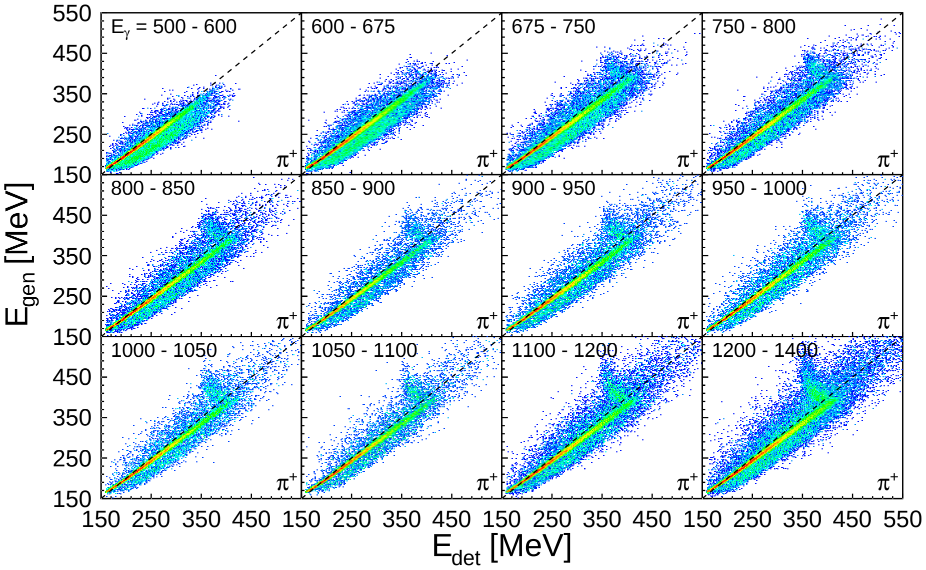

Fig. 4.14: The deposited energy of the detected π^+ against the energy of the generated ones for simulation data. The black dotted line indicates the perfect linear behavior. Up to about 380 MeV the energy resolution is very accurate and only a small portion of the charged pions punch through the crystals and lead to wrong energy information.

Figure 4.14 shows the deposited energy of the detected π^+ against the energy of the generated ones for simulation data. The black dotted line indicates a perfectly accurate energy measurement, i.e., the measured deposited energy agrees with the energy of the particle. The data shows a nearly perfect linear behavior up to about 380 MeV. Only for a very small portion of the charged pions, the energy detection is inaccurate and in the next section it will be shown that this influence is very small.

Figure 4.15 shows the same spectra for the π^-. As for the π^+, the behavior is almost linear up to about 380 MeV and the small perecentage of wrongly measured energies has only a minor influence.

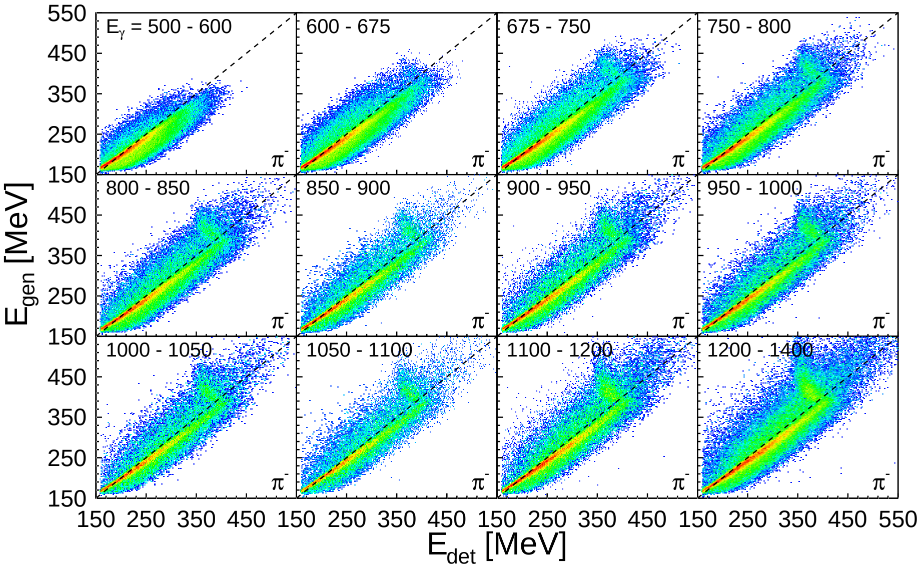

Fig. 4.15: The deposited energy of the detected π^- meson against the energy of the generated ones for simulation data. Up to about 380 MeV the energy resolution is almost linear.

4.8 Software Trigger

For some observables a correct normalization has to be performed and many different factors flow into the final results. Since the detector system is imperfect, particles, and hence events, are lost and have to be corrected for, using so called detection efficiencies. For the detection efficiency determination, it is essential that all experimental circumstances can be reproduced as precisely as possible. In the case of the trigger mechanism, this means that in the analysis process the hardware triggers from the experiment need to be reproduced and finally all the events that are rejected in the data taking process can also be rejected in the analysis of the simulation data.

In the software triggers the energy information of the particles is used and hence the very different responses of the detector system to protons in comparison to neutrons would lead to differing systematic effects. Therefore only photons and charged pions were allowed to make the trigger in the analysis of experimental and simulation data. This is a more stringent condition but allows a final comparison for the reactions on the proton to the ones on the neutron and thus gives a better feeling on the handling of the neutron results.

4.8.1 Energy Sum Trigger

By summing up the contributions from all hits in CB from an event, the total deposited energy can be compared to a threshold and too low energetic events are rejected. In the experiment analog signals from the crystals are used for that and hence the calibrated digitized energies from the analysis can not be used. This becomes clear when looking at the main idea of the energy calibration process, where one aims at equalizing the differing responses of the crystals. By de-calibrating the energies, the analog signal can be approximated [82, 81]. This procedure has been applied for the experimental as well as for the simulated data, using the same values.

4.8.2 Multiplicity Trigger

In the data taking process the multiplicity trigger approximates the number of detected particles by forming logical groups of detector elements and applying a low threshold to the deposited energies. As mentioned above, 16 adjacent crystals from the Crystal Ball detector form such a logical group and a detected hit can contribute to the multiplicity if at least one of the crystal signals exceeds the threshold.

In the TAPS detector each of the six large triangles form a logical sector and as for CB a hit can contribute if one of the crystals that fired has a signal larger then the threshold value.

Most of the electromagnetic background is flying in forward direction in the lab frame and thus detected in the inner TAPS rings. To avoid false trigger decisions from such events, the inner three TAPS rings were excluded from the multiplicity trigger. Shower loss effects at the edges of the detectors can also lead to wrong energy information and therefore distort the multiplicity trigger decisions. For this reason also the most outer TAPS ring was excluded from the multiplicity trigger.

The individual thresholds for the calibrated energies for all TAPS and CB crystals have been established in sections 3.3.5 and 3.3.5 and these values were applied in the analysis of experimental and simulation data.

The $M2+$ multiplicity triggers used in the December 2007 and the May 2009 beam times can for all channels be fired by two photons from the π^0 decay. For the February and April 2009 beam times an $M3+$ multiplicity was demanded to trigger the data recording. This leaves the situation unchanged for the neutral channels, where we have four photons from a π^0 decay in the final state. For the mixed-charge channels also the charged pions have to be included for the multiplicity trigger. But since the detector response for π^+ and π^- are approximately equal, as shown in figures 4.14 and 4.15 no differences in systematic effects will arise from that and the final results from the two channels can be compared without any constraints.

4.9 Tagger Random Background Subtraction

All electrons detected in the tagger during the time window of one event (gate) are written to the data file, and only one of this electrons produced the bremsstrahlung photon, that finally led to the triggering and thus recording of this event. Among this amount of electrons are some with a clear shift in the relative timing to the detector, and in this way could easily be separated by a cut. But some of these tagger hits are very close in the time spectra and lead to so called random coincident background. Consequently, the true energy of the coincident electron and hence the photon has to be extracted statistically by a subtraction of this background for all quantities that depend on the energy of the incoming photon.

One uses the coincident time spectra of tagger and CB, and tagger and TAPS, respectively, where a clear peak marks the coincident hits. In figure 4.16 these spectra are shown for the tagger-CB relative time on the left and the tagger-TAPS relative time on the right hand side. As a consequence of the time calibration procedure, where one calibrates CB and tagger time relative to the TAPS timing, these peaks are nicely aligned at zero for all tagger channels. Over the whole gate time a flat background is visible, which is coming from this amount of uncorrelated electron hits.

Assuming random distributions in energy and time for all uncorrelated hits in the flat background, one can claim also an equal contribution of these hits to all quantities that depend on E_γ and thus perform a statistical subtraction of this background. The method just subtracts from all events in the interval $[t_3, t_4]$ the events from the intervals $[t_1, t_2]$ and $[t_5, t_6]$ normalized to the widths, to get the prompt events marked in green. This is done by weighting all events in the peak interval with $w_p = 1$ and all events in the two background intervals with

$$w_r = -\frac{t_4 - t_3}{t_2 - t_1 + t_6 - t_5}. \tag{4.22}$$

As already mentioned, the time resolution of the TAPS BaF_2 crystals is superior to the one from the NaI crystals of CB. This is also clearly visible in the figure from

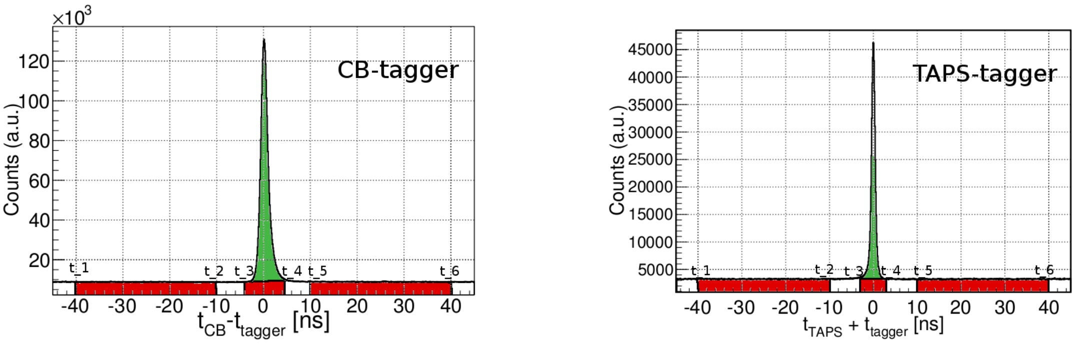

(a) (b)

Fig. 4.16: The coincidence spectra of the tagger-CB time on the left and the tagger-TAPS time on the right hand side for all decay photons from the $\gamma p(n) \rightarrow \pi^0\pi^0 p(n)$ channel. A clear peak at zero contains the coincident events but has a flat background below from random coincident electron hits.

above, and therefore always the weights from TAPS were used if at least one of the decay photons was detected in TAPS. To reach maximum accuracy, the limits of the prompt intervals have been determined for all tagger channels individually. Since the coincidence time peaks of some tagger channels are slightly asymmetric a rather conservative range of $\pm 4\sigma$ has been chosen for the limits of the prompt region.

The statistical error of these method is proportional to the size of w_r and hence inverse proportional to the widths of the background intervals. Therefore the largest possible interval sizes have been chosen and the average weight was around -0.012.

In the simulation data exactly one tagger hit is recorded, because the incoming photon energy is known for every event and hence no background exists and the weight w is always 1.

4.10 Beam Helicity Asymmetry Extraction

As mentioned in the first chapter polarization observables provide very detailed information on internal reaction mechanisms. This huge sensitivity presents model calculations with major challenges and previous results revealed partly strong deficiencies in the models. At least for the beam helicity asymmetry $I^{\odot}(\Phi)$ the experimental extraction is rather straight forward and calculated as classical asymmetry as

$$I^{\odot}(\Phi) = \frac{d\sigma^+ - d\sigma^-}{d\sigma^+ + d\sigma^-}. \tag{4.23}$$

The differential cross sections $d\sigma$ are calculated for the two spin states of the circularly polarized photon, denoted as $^{\pm}$. Many normalization factors, such as photon flux (see section 4.12) and target density cancel out in the ratio. Consequently, the differential cross sections can be replaced by detection efficiency corrected count rates $N(\Phi)/\epsilon$ and equation 4.23 now reads as

$$I^{\odot}(\Phi) = \frac{1}{P_\gamma} \frac{N^+(\Phi)/\epsilon - N^-(\Phi)/\epsilon}{N^+(\Phi)/\epsilon + N^-(\Phi)/\epsilon}, \tag{4.24}$$

with the degree of polarization of the photons P_γ. The difference of the photon states in the total photon flux is at the 0.05 % level and thus negligible.

Φ is defined as the angle between two planes, each one spanned by the center-of-mass three-momenta of two of the four particles $\vec{p}_{\pi_1}$, $\vec{p}_{\pi_2}$, the incoming photon $\vec{p}_\gamma$ and the recoil nucleon $\vec{p}_N$. This situation is illustrated in figure 4.17, where the incoming photon and the recoil nucleon define one plane and the other one is defined by the two outgoing pions.

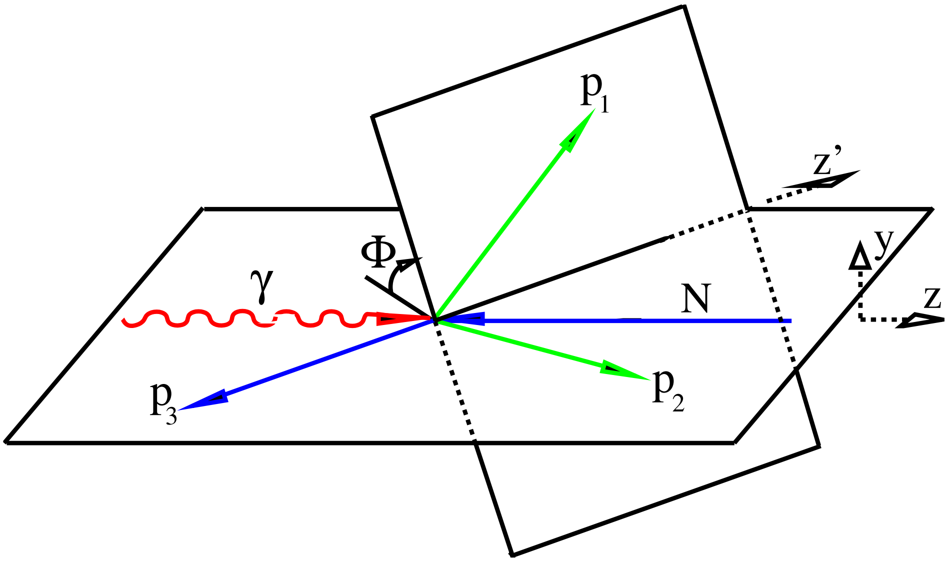

Fig. 4.17: Illustration of the reaction with the two planes spanned by the three-momenta of the pions, the recoil nucleon and the incoming photon. The plane including the incoming photon γ is called reaction plane while the other one is the so called production plane. Distinguishing π_1 and π_2 leads to a range for Φ of 0 to 360 degrees. Taken from [35] and altered.

The arrangement from figure 4.17 has no fixed azimuthal orientation, e.g. it can be rotated around the beam axis and as such effects from the detector geometry are averaged out, and no experimental detection efficiency depending on the azimuthal angle has to be corrected.

Several different combinations of γ, p_1, p_2 and p_3 are possible. At first, the reaction plane shall always be spanned by the incoming photon and the recoil nucleon and the production plane is thus spanned by the two pions. Of course Φ still has a dependence on the ordering of the two pions, where different discriminations are possible.

All asymmetries have to conserve parity and thus $I^{\odot}$ has to fulfill

$$I^{\odot}(\Phi) = -I^{\odot}(2\pi - \Phi). \tag{4.25}$$

The two π^0 from the neutral channels are indistinguishable per se and reaction kinematics have to be included for a discrimination. Leaving the two π^0 randomized basically enforces $I^{\odot}(\Phi)$ to repeat itself after 180° and thus $I^{\odot}(\Phi)$ has to fulfill

$$I^{\odot}(\Phi) = I^{\odot}(\Phi + \pi). \tag{4.26}$$

But the two pions can also be ordered by some kinematic condition and the above equation is no longer valid. For this work a condition on the invariant mass of the pion-nucleon system was applied. We define as particle p_1 the pion with

$$m(\pi^0_1, N) \geq m(\pi^0_2, N) \tag{4.27}$$

and this way the definition of Φ is explicit and we call the pions mass-ordered. We denote the angle by Φ_{1m} and the corresponding asymmetry by $I^{\odot}_{1m}(\Phi_{1m})$, with the m for mass-ordered.

For the mixed-charge final state the most natural definition of p_1 and p_2 comes from the charge of the pions. We define as particle p_1 the charged pion and consequently the π^0 is p_2. The pions arranged in this way are called charge-ordered, and we denote the angle as Φ_{1c} and the corresponding asymmetry as $I^{\odot}_{1c}(\Phi_{1c})$. The 1 in the subscript refers to the definition of reaction plane and production plane.

Additionally we can now exchange also the recoil nucleon with one of the pions and thus get two additional asymmetries. This exchange procedure was not used for the beam helicity asymmetry results of the neutral channel but only for the mixed-charge one. We define the following two additional asymmetries.

$$\begin{aligned} &I^{\odot}_{2c}, \quad \text{with} \quad (p_1, p_2, p_3) = (\pi^0, N', \pi^{\pm}) \\ &I^{\odot}_{3c}, \quad \text{with} \quad (p_1, p_2, p_3) = (\pi^{\pm}, N', \pi^0) \end{aligned}$$

Table 4.1 gives an overview of all the different asymmetries, that have been measured in this work. As mentioned before, the asymmetries $I^{\odot}_{nc}(\Phi_{nc})$ were only measured for the mixed-charge channels.

For the extraction of the beam helicity asymmetries three dimensional histograms have been filled with Φ_{ij}, $\theta^*_{\pi\pi}$ and E_γ or W, for both photon helicity states. The detection efficiencies were calculated with the exact same binning for the three quantities and $I^{\odot}_{ij}(\Phi_{ij})$ was extracted according to equation 4.24.

Asymmetry	reaction plane	production plane	ordering
$I^{\odot}_{1r}(\Phi_{1r})$	γ, N'	π_1, π_2	randomized pions
$I^{\odot}_{1m}(\Phi_{1m})$	γ, N'	π_1, π_2	$m(\pi^0_1, N) \geq m(\pi^0_2, N)$
$I^{\odot}_{1c}(\Phi_{1c})$	γ, N'	π_1, π_2	$\pi_1 = \pi^{\pm}$
$I^{\odot}_{2c}(\Phi_{2c})$	γ, $\pi^{\pm}$	π^0, N'	$\pi_1 = \pi^0$
$I^{\odot}_{3c}(\Phi_{3c})$	γ, π^0	$\pi^{\pm}$, N'	$\pi_1 = \pi^{\pm}$

Tab. 4.1: Overview of the definitions of the four different asymmetries extracted in this work. For the double π^0 channels only the first two asymmetries have been extracted.

The polarization degree of the photons P_γ depends on the degree of polarization of the electrons and on the momentum transfer during the bremsstrahlung process according to [84] (see section 2.2).

4.11 Detection Efficiencies

To measure cross section observables, a normalization procedure is needed and therefore the imperfection of the detector system has to be estimated based on simulation, leading to so called detection efficiencies. For the cross section results these detection efficiencies have been measured as function of the energy, either of the incoming photon E_γ or the final state center-of-mass W and additionally as function of the center-of-mass polar angle of the pion-pion system $\theta^*_{\pi\pi}$.

For the normalization of the differential cross section used to calculate the beam helicity asymmetry, additionally to the energy and the polar angle, also a dependence on the angle Φ_1 (see section 4.10) between production and reaction plane was included. The binning for the calculation of the detection efficiencies was generally chosen equally to the signal histograms, simplifying the normalization process. With 'det' for the detected events and 'gen' for the generated events we can write the detection efficiency ϵ as the fraction of detected and generated events

$$\epsilon(E^{det}, \cos(\theta^{*,det}_{\pi\pi})) = \frac{N^{det}(E^{det}, \cos(\theta^{*,det}_{\pi\pi}))}{N^{gen}(E^{gen}, \cos(\theta^{*,gen}_{\pi\pi}))}. \tag{4.28}$$

In the following two sections the extraction of the detection efficiencies used in this work will be explained in detail. But first some remarks on the detection of recoil nucleons and the complications with their efficiencies.

Demanding the detection of the recoil nucleons is necessary for the measurements on quasifree nucleons, whereas for free proton targets it can be omitted. As things turned out, the A2 simulation software had problems reproducing the real efficiency of the detector system for nucleons. By extracting the detection efficiency for the much simpler case of the free proton target the simulated detection efficiencies could be corrected.

4.11.1 Processing of Simulated Data

For all reaction channels the PLUTO^{++} event generator was used to create the input distributions for the A2 simulation of the detector system. The distribution of the incoming photons was chosen according to the bremsstrahlung spectrum with its $1/E_\gamma$ shape. The lowest energies were set to the reaction thresholds and the highest energies to the energy of the highest tagger channel. From the Fermi momentum distribution of [85] the momentum of the initial state nucleons bound in the deuteron was randomly chosen. According to the participant-spectator model the excited nucleon state was constructed out of the four-momenta of the photon and the participant nucleon.

As discussed in the beginning of this work, the double pion final states are assumed to come predominantly from sequential decays, where in a first decay an intermediate excited nucleon state and one pion are produced, before in the second decay step the nucleon ground state is reached.

For the neutral channel, a decay mode via a Δ resonance[9] was simulated additionally to the classic phase space decay, where the initial state decays directly into two pions and a nucleon.

For the mixed-charge channels on the other hand, decays via Δ and N^* resonances but also a model based initial distribution simulation have been included. For the latter the model of [36] was used to weight the generated events and therefore enforce a 'more' realistic initial distribution. The detection efficiencies based on the model from [36] were not used for the cross section calculations but only for the beam helicity asymmetries.

The four momenta of the generated incoming photon, the recoil nucleon, the charged pions and the π^0 decay photons were then written to a file. The reaction vertex was randomly distributed in a cylindrical volume defined by the beam spot diameter (about 1.3 cm) and the lengths of the targets on a event-by-event basis.

These generated quantities were then set as input for the A2 simulation software, where for every beam time the corresponding detector setup was separately implemented. All final state particles have been tracked in the A2 simulation process and the energy and time information of all the detector elements were recorded. For all channels and all decay modes 40 million events have been simulated. According to the analysis of experimental data the recorded detector responses from the A2 simulation output were then analyzed with the AcquRoot software. For

---

[9] The nature of this Δ resonance is of course energy dependent and is chosen in the generation process by the energy limits of the reactions.

some cases additional smearing had to be used to achieve the most realistic circumstances. The extraction of the tagger channels was straight forward from the known energy of the initial photon and the tagger energy calibration file. As explained above, no random background subtraction had to be performed, since just one correct tagger hit exists.

Identical to the experimental data analysis the established software triggers were applied and bad tagger channels and detector elements have been omitted.

4.11.2 Nucleon Detection Efficiency Correction

To correct for the deficiencies of the A2 simulation with respect to the detection of the recoil nucleons, experimental data from the hydrogen beam time of April 2009 was used. Analyzing the reaction $\gamma p \to \pi^0\pi^0 p$ a correction factor depending on the energy and the lab polar angle of the recoil nucleon was extracted. For final states of the neutron the reaction $\gamma p \to \pi^+\pi^0 n$ was used to correct the detection efficiencies determined with simulation. The approximation one has to make in this method is the similarity of the detector setup, which is fortunately given for the other two beam times from 2009 but is worse for the December 2007 beam time, where the PID detector was shifted up-stream. As described before, the detection of nucleons in the uncovered region is unambiguous, and therefore such events have not been accepted. Only excluding the same region in the analysis of the hydrogen beam time does not do the trick, since the additional material from the PID in this polar angular region in the hydrogen beam time will influence the detection efficiency of photons and charged pions. The usability of the December 2007 beam time results for the different observables will be discussed in the next chapter.

To have the highest possible similarity of the conditions in the analysis of the hydrogen and the deuteron beam times the corrections were calculated individually for every beam time and the thresholds from the deuteron beam times were used for the free proton data analysis.

To estimate the efficiency of the nucleon detection process we can compare the number of events in the inclusive and the exclusive measurement. The detection efficiency for nucleons was calculated as function of their kinetic energy and their polar angle in the lab frame and is just given by the number of events, where the nucleon was detected divided by the total number of events.

$$\begin{aligned} \epsilon_p^d(T_p, \theta_p) &= \frac{N(\pi^0\pi^0 p)}{N(\pi^0\pi^0 p) + N(\pi^0\pi^0)} \\ \epsilon_n^d(T_n, \theta_n) &= \frac{N(\pi^+\pi^0 n)}{N(\pi^+\pi^0 n) + N(\pi^+\pi^0)} \end{aligned} \tag{4.29}$$

T_N and θ_N were extracted from kinematics in any case, weather the nucleon was detected or not.

Extracting the detection efficiency from data instead of simulation offers some advantages. First all material components and geometries are totally accurate and the efficiencies of the PID and Veto detectors are automatically correctly implemented this way. As disadvantage, the additional systematic effects from the analysis of the two reactions have to be named. It was found, that the best way to correct the detection efficiency is in an indirect manner. The detection efficiency correction was not applied directly to the quasifree measurements but indirectly to the simulated efficiencies for the hydrogen beam time. This procedure yields a correction factor f_c, which is again a function of T_N and θ_N and given by

$$f_c(T_N, \theta_N) = \frac{\epsilon_N^{MC}(T_N, \theta_N)}{\epsilon_N^{d}(T_N, \theta_N)}, \tag{4.30}$$

where MC indicates the simulated efficiency and d the one from data. This correction factor was then finally used to correct the simulated efficiencies for the three deuteron beam times. For the application of the correction factor the measured θ_N and the reconstructed T_N, as explained above were taken. For inexistent f_c in the T_N-θ_N plane, the next nearest existing value was taken.

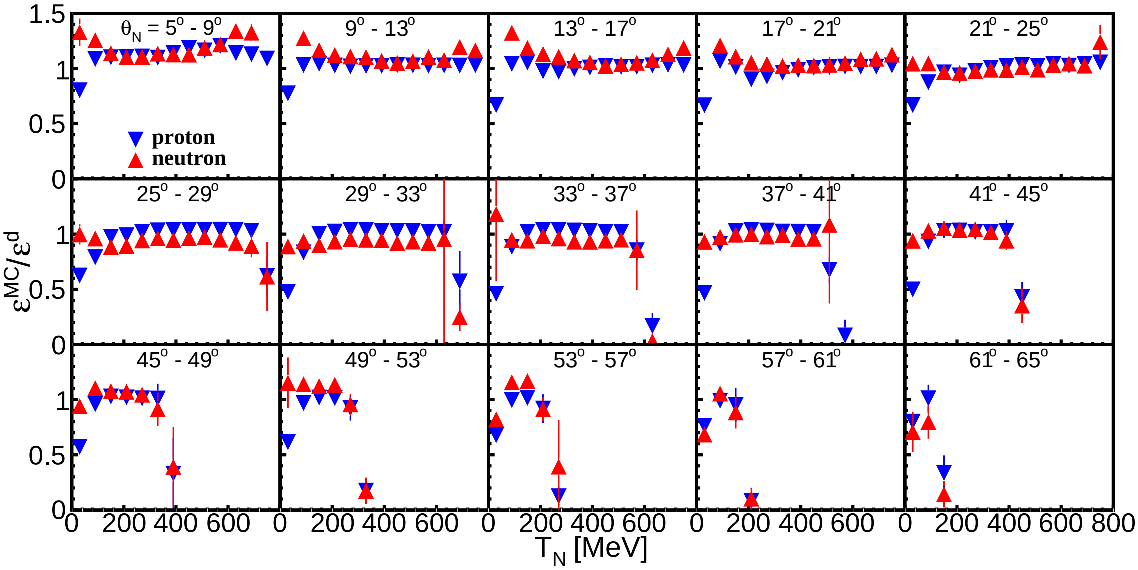

Fig. 4.18: The nucleon detection efficiency correction factor f_c for different bins of θ_N as function of T_N. The proton is shown in blue and the neutron in red.

In figure 4.18 the ratios for the detection efficiencies extracted from data and the ones extracted from simulation are plotted for different bins of the nucleon polar angle as function of the kinetic energy of the nucleon. The proton results in blue as well as the neutron results in red visibly differ from one and show a clear dependence on T_N. For low nucleon energies and polar angles the largest deviations can be observed, showing on the one hand, that the material budget or its influence for the forward direction is underestimated in the simulation (for more details see [57]) and on the other hand also, that the BaF_2 crystals are inferiorly reproduced for nucleons than the NaI crystals. This of course enlarges the influence of the accuracy of the detector thresholds applied in the analysis of TAPS nucleon hits.

As we will see in the next chapter, this correction worked fine for the channels of this work and the previously measured inclusive results could be reproduced very reasonably with our exclusive measurements on the free protons.

4.11.3 Detection Efficiency Results

Using the nucleon detection efficiency corrections and the additional corrections for the A2 simulation, such as the additional material budget in the beam hole of the CB or the correct physics model (see [57] for a detailed discussion) the detection efficiencies for all channels and beam times were calculated as function of the energies E_γ or W and the polar angles in the center-of-mass of the pion-pion system $\theta^*_{\pi\pi}$. For the beam helicity asymmetry the angle Φ_1 was used as additional quantity and the same binning was chosen for all efficiencies as for the signal histograms, simplifying the normalization process.

The Double π^0 Channels

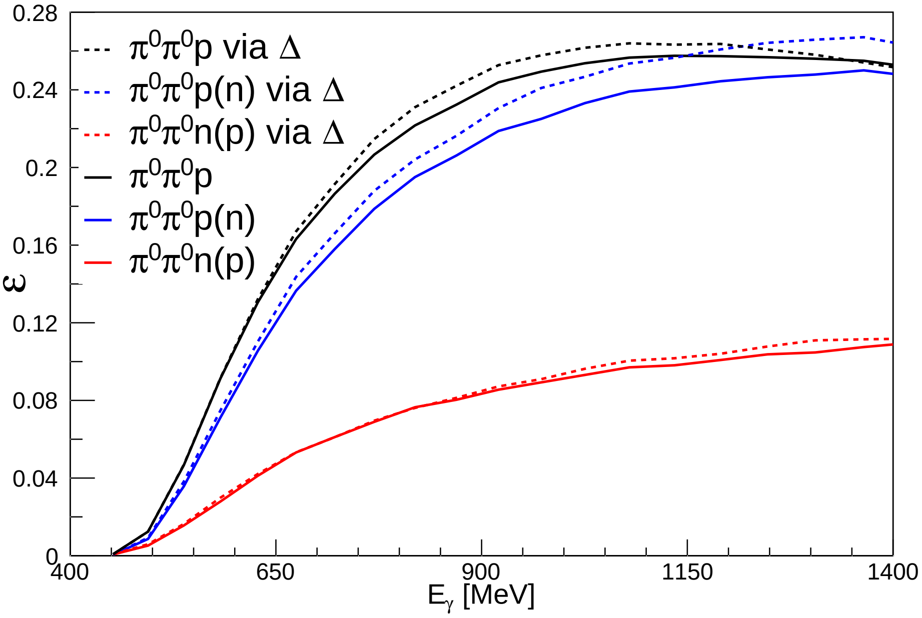

Fig. 4.19: The final integrated detection efficiencies as function of E_γ for all neutral channels. Full lines: phase space simulation, dashed lines: sequential decay simulation via intermediate Δ resonance. Black line: $\gamma p \to \pi^0\pi^0 p$, blue line: $\gamma p(n) \to \pi^0\pi^0 p(n)$, red line: $\gamma n(p) \to \pi^0\pi^0 n(p)$.

Figure 4.19 shows the integrated detection efficiencies as function of the energy of the incoming photon for all double π^0 channels. The simulations via sequential decay with an intermediate Δ resonance shown as dashed lines are compared to phase space simulation, shown as full lines. As expected, the efficiency for the reaction with the neutron in the final state is about two times lower than the ones for the proton final states. The 'late' rise of the efficiencies is not due to the threshold of the reaction, which lies at about 300 MeV but due to the high energy sum trigger, that was set fixed at 450 MeV. As aforementioned, wrongly calibrated software triggers can lead to strong effects and it was found to suppress these effects very efficiently by applying this higher threshold for all cross section calculations.

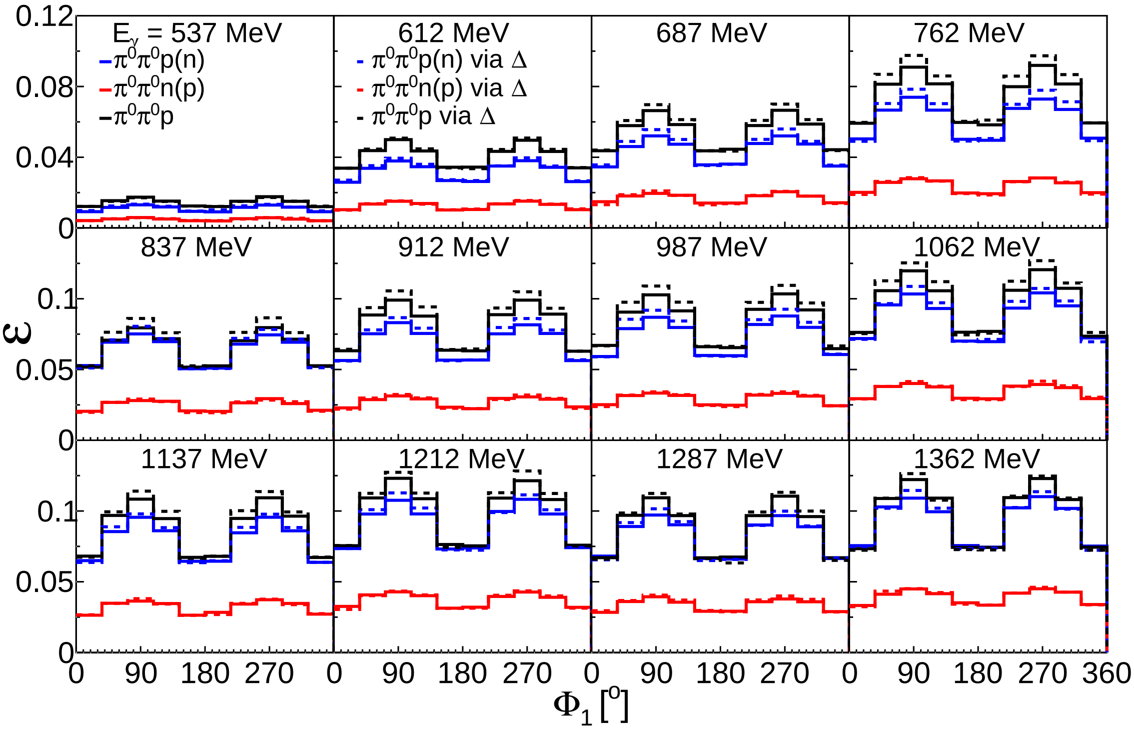

Fig. 4.20: Projections of the three dimensional detection efficiencies used for the normalization of the count rates from the beam helicity asymmetry extraction as function of ϕ_1 for different bins of E_γ. Notation as in figure 4.22.

Figure 4.22 shows the detection efficiencies as function of $\cos(\theta^*_{\pi\pi})$ for 20 energy bins from the energy sum threshold up to the highest energies. In very forward direction most events get lost because of the unused PbWO$_4$ crystals, covering polar angles up to about 5 degrees.

The differences between sequential and phase space simulated detection efficiencies are rather small. For all final results of the double π^0 channels, for cross sections and beam helicity asymmetries pure phase space simulation was thus used.

For the beam helicity asymmetries the detection efficiencies were calculated as function of $\theta^*_{\pi\pi}$, E_γ or W and Φ_1, as defined in section 4.10 and with mass-

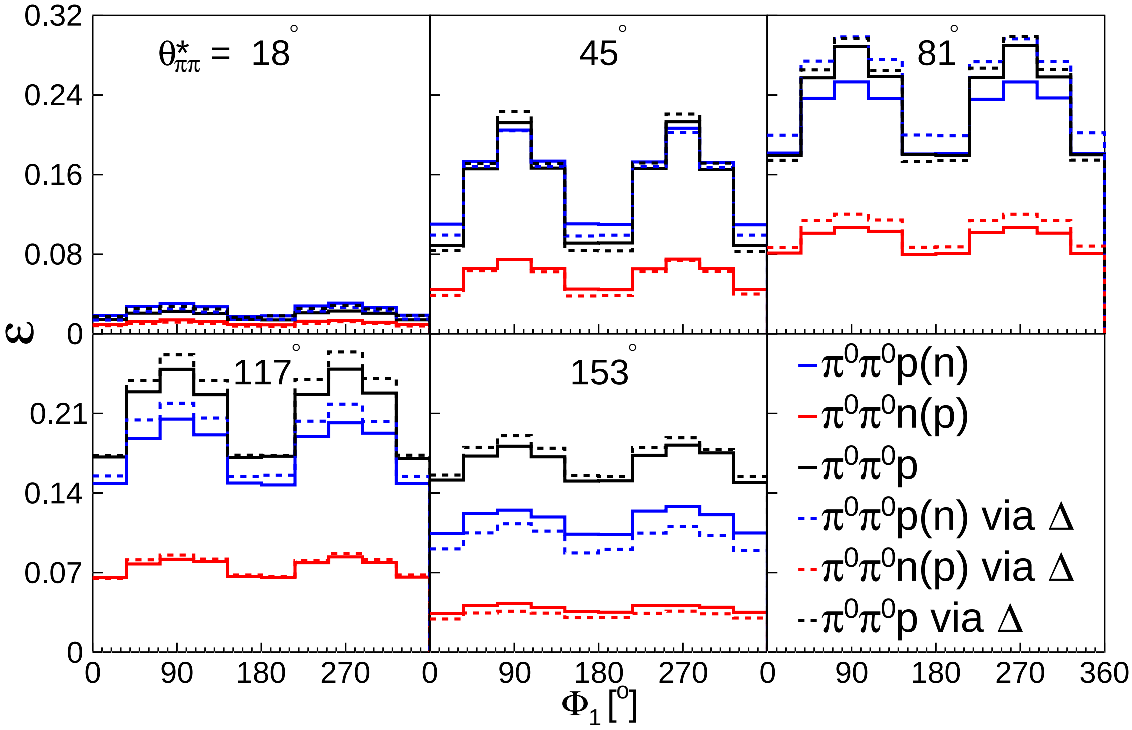

Fig. 4.21: Projections of the three dimensional detection efficiencies as function of ϕ_1 for different bins of $\theta^*_{\pi\pi}$. Notation as in figure 4.22.

ordering of the two pions. Figure 4.20 shows the detection efficiencies as function of the angle Φ_1 for different bins of the incoming photon energy E_γ. A strong dependence on Φ_1 is visible and comes from detector geometry effects. At Φ_1 values of $\approx 0, 180$ and 360 degrees, the efficiencies reach their troughs. This Φ_1 values are reached when the two planes are parallel (or 'anti-parallel') and as such lie parallel to the beam line and hence go through the forward and backward holes in the detector. Therefore a larger percentage of particles stays undetected and the detection efficiency is smaller.

In figure 4.21 the detection efficiencies are again shown as function of Φ_1 but this time E_γ is integrated out and the five bins of $\theta^*_{\pi\pi}$ are plotted.

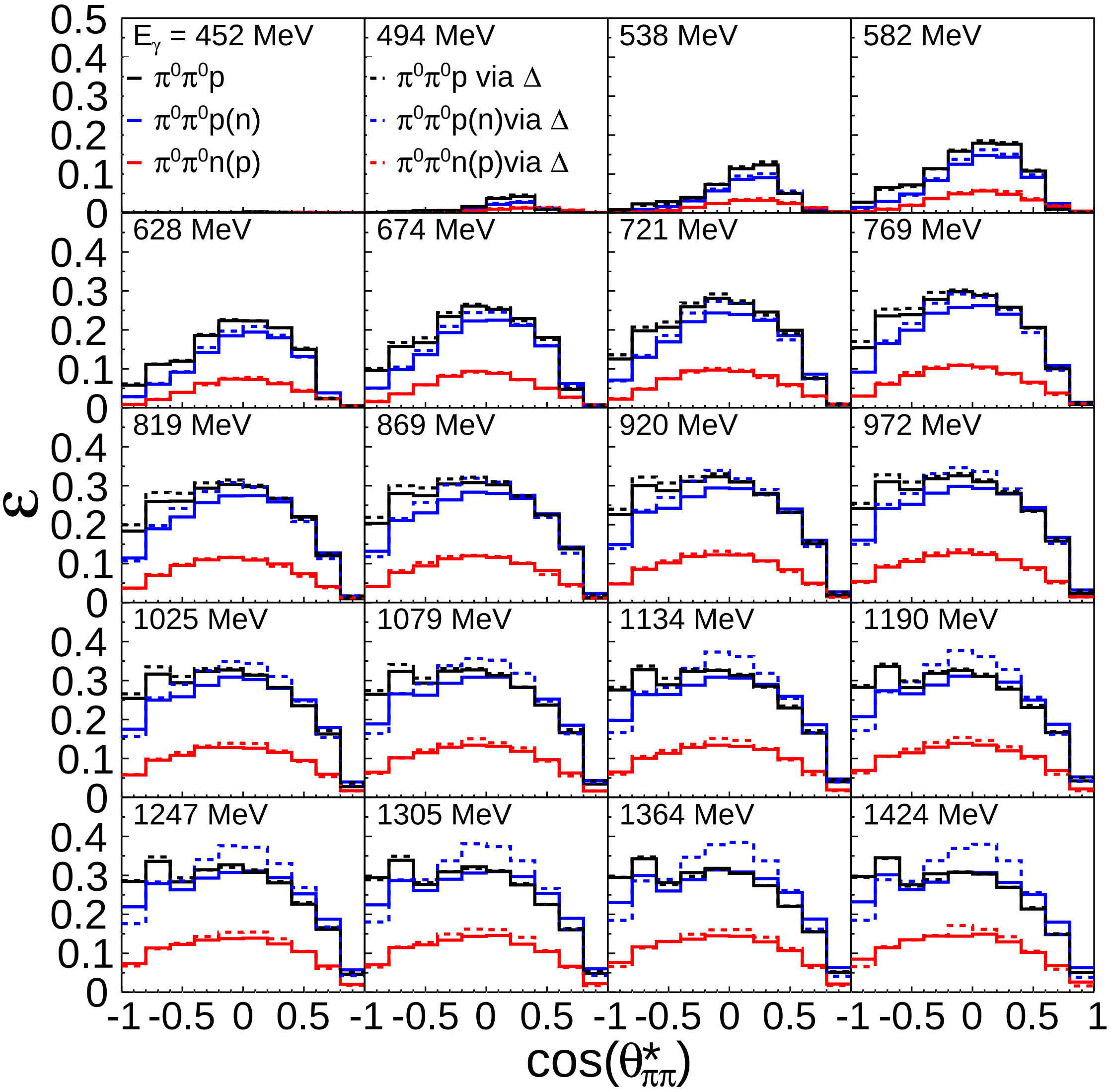

Fig. 4.22: The final detection efficiencies for the phase space simulation for different bins of E_γ as function of the center-of-mass polar angle of the pion-pion system for all measurements of the neutral channels. Full lines: phase space simulation, dashed lines: sequential decay simulation via intermediate Δ resonance. Black lines: $\gamma p \to \pi^0\pi^0 p$, blue lines: $\gamma p(n) \to \pi^0\pi^0 p(n)$, red lines: $\gamma n(p) \to \pi^0\pi^0 n(p)$.

The Mixed-charge Channels

Figure 4.23 shows the integrated detection efficiencies as function of the energy of the incoming photon for all mixed-charge channels. The simulations via sequential decay with an intermediate Δ^+ resonance for the $\pi^+\pi^0$ final state and an intermediate Δ^0 resonance for the $\pi^-\pi^0$ final state, shown as dashed lines are compared to phase space simulation, shown as full lines.

From fitting the invariant mass distributions of the pion-nucleon and pion-pion

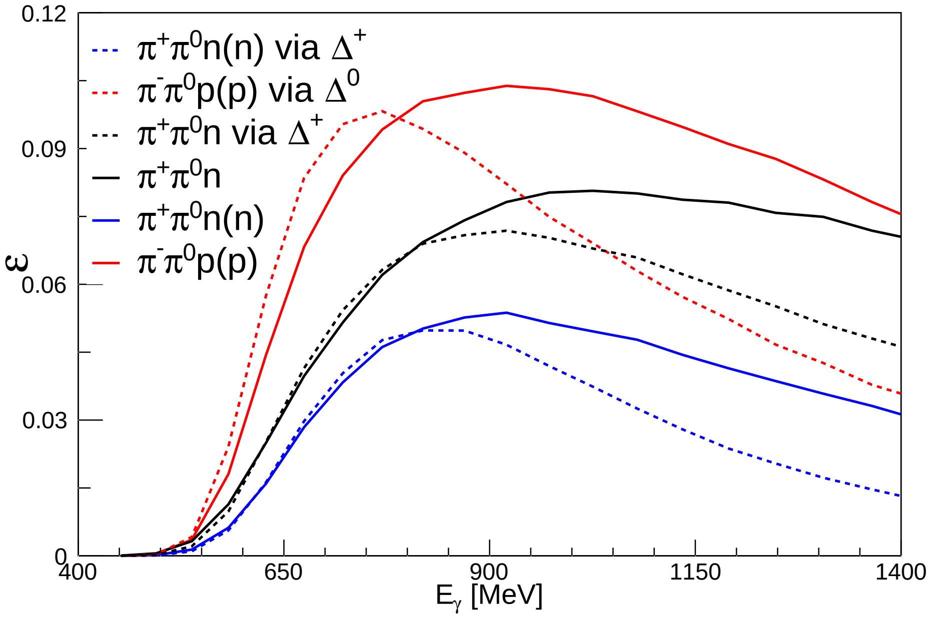

Fig. 4.23: The final integrated detection efficiencies as function of E_γ for all neutral channels. Full lines: phase space simulation, dashed lines: sequential decay simulation via intermediate Δ resonances. Black line: $\gamma p \rightarrow \pi^0\pi^0 p$, blue line: $\gamma p(n) \rightarrow \pi^0\pi^0 p(n)$, red line: $\gamma n(p) \rightarrow \pi^0\pi^0 n(p)$.

systems ($m(\pi N)$, $m(\pi\pi)$) contributions from decays via Δ^0 for the $\pi^+\pi^0$ final state and from decays via Δ^+ for the $\pi^-\pi^0$ were found to be in the order of 15 %. This does not mean that a sequential decay like $\gamma p \rightarrow \Delta^0\pi^+ \rightarrow \pi^+\pi^0 n$ is favored over $\gamma p \rightarrow \Delta^+\pi^0 \rightarrow \pi^0\pi^+ n$, but that more background terms (like pion pole terms) are possible for reactions with the charged pion produced first. But nevertheless, it makes sense to extract the portions of the different decay modes in this way, since detection efficiencies only depend on the kinematics of the reactions.

For the extraction of the cross sections for the mixed-charge channels, a final simulation with contributions from both, the phase space and the sequential decay simulation was used. To suppress different systematic effects for the different mixed-charge channels the portions were estimated from fitting the invariant mass distributions of the pion-nucleon system for the free proton data for the three highest energies of W. This is shown in figures 4.25 and 4.26, where the experimental data from $\gamma p \rightarrow \pi^0\pi^+ n$ are shown as black stars and the different contributions from the simulations as full lines.

The clearly dominant contributions from the decay with the $\pi^\pm$ produced in the first decay step (from now on denoted as 'first sequential decay') are shown in red. The black lines represent the phase space decay simulation and the blue lines the 'second sequential decay'. The sum of all contributions are shown as green lines. The other sequential decay contribution is about as strong as the one from the phase space simulation. It makes sense to look at the highest energies only,

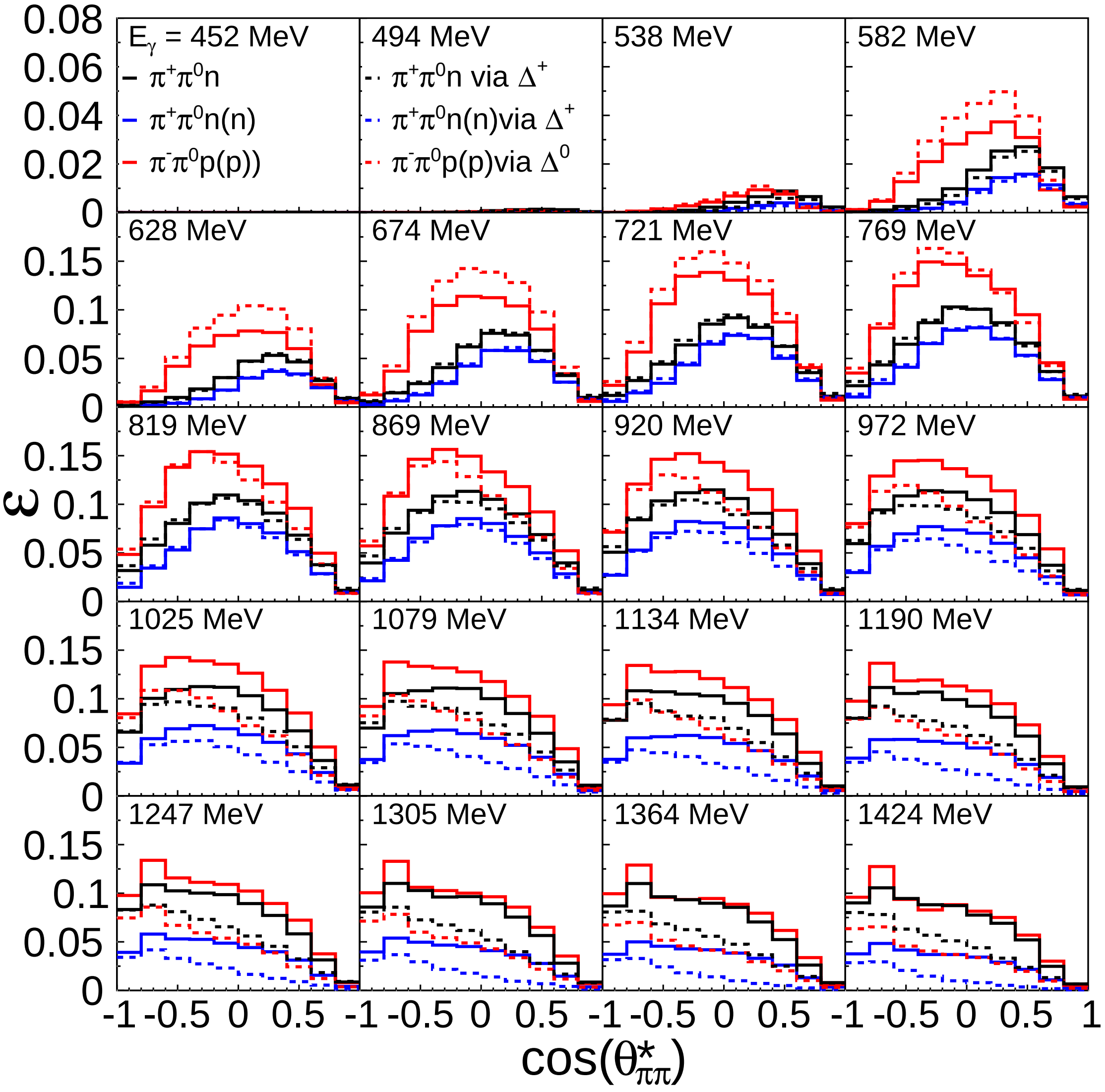

Fig. 4.24: The final detection efficiencies for the mixed-charge channels for different bins of E_γ as function of the center-of-mass polar angle of the pion-pion system. Full lines: phase space simulation, dashed lines: 'first sequential decay' simulation. Black lines: $\gamma p \to \pi^0\pi^0 p$, blue lines: $\gamma p(n) \to \pi^0\pi^0 p(n)$, red lines: $\gamma n(p) \to \pi^0\pi^0 n(p)$.

since here the different contributions show themselves more clearly, and thus the fitting procedure is more reliable. Even though this way of estimating the portions of the different decay modes seems to work, the systematic effects grow for every additional decay mode, that is included. It is safe to rely as little as possible on this portion extraction principle for cross section calculations. Therefore only contributions from phase space and 'first sequential decay' mode simulation was used and the mixing was chosen as 3 : 7 for $PS : \Delta$.

As expected, the efficiency for the reaction with the neutron in the final state is about two times lower than the ones for the proton final states. As for the neutral channels, the energy sum threshold was set fixed at 450 MeV in order to supress systematic effects.

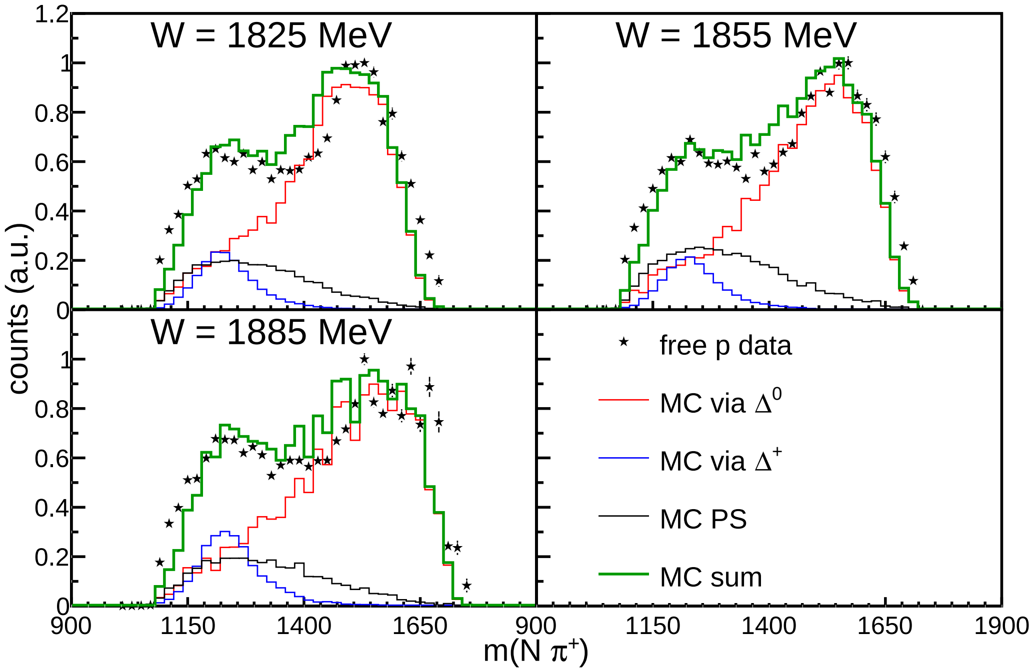

Fig. 4.25: The distributions of $m(\pi^+n)$ for $\gamma p \to \pi^0\pi^+n$ for the three highest bins in W fitted with the three different simulations. Black stars: free proton data, black lines: phase space simulation, blue lines: sequential decay simulation via Δ^0, red lines: sequential decay simulation via Δ^+, green lines: sum of all simulations.

As for the double π^0 channel, the efficiencies for the beam helicity asymmetry were calculated as function of Φ_1 for five bins of θ^* and 100 bins of E. As mentioned above, apart from sequential decay via Δ resonances and classical phase space simulation also a model based initial distribution was chosen. This was implemented in a FORTRAN code written by A. Fix ([36]), where the four vectors of all three final state particles and the initial photon are used as input and a differential cross section value is calculated. In our analysis all quantities based on this simulation have then been weighted with this values and this way a start distribution according to this model could be reached. In figure 4.27 the detection efficiencies for the three different simulations are shown. The notation is chosen as above, where the black color code stands for $\gamma p \to \pi^0\pi^+n$, the blue one for $\gamma p(n) \to \pi^0\pi^+n(n)$ and the red one for $\gamma n(p) \to \pi^0\pi^-p(p)$. The full lines represent the phase space simulation (PS), the dashed lines the sequential decay mode simulation via Δ and the dotted lines the model based simulations. The differences in detection efficiencies between the three simulations types are rather small in comparison to the variation as function of Φ_1, but rise towards higher energies.

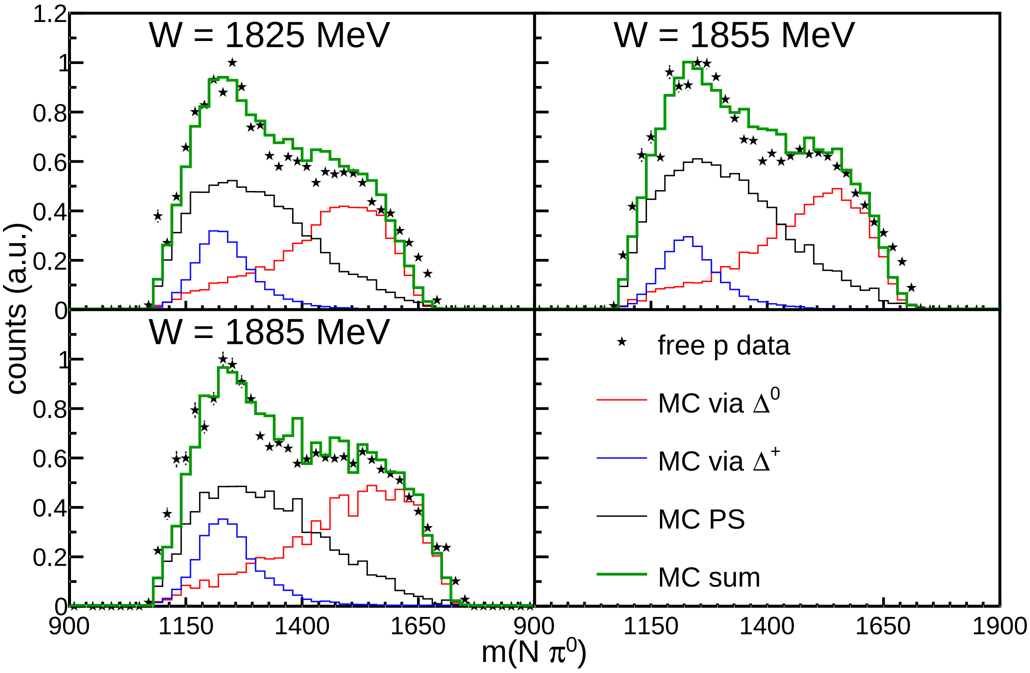

Fig. 4.26: The distributions of $m(\pi^0 n)$ for $\gamma p \to \pi^0\pi^+ n$. Notation as in figure 4.25.

But nevertheless the final beam helicity asymmetry results were calculated using phase space simulation only, since practically no difference could be made out for the beam helicity asymmetry results of $\gamma p \to \pi^0\pi^+ n$ for the different simulations (see section 5.1.5).

In figure 4.28 the detection efficiencies for the three mixed-charge channels are shown for the five bins of θ^*. The notation is as in figure 4.27.

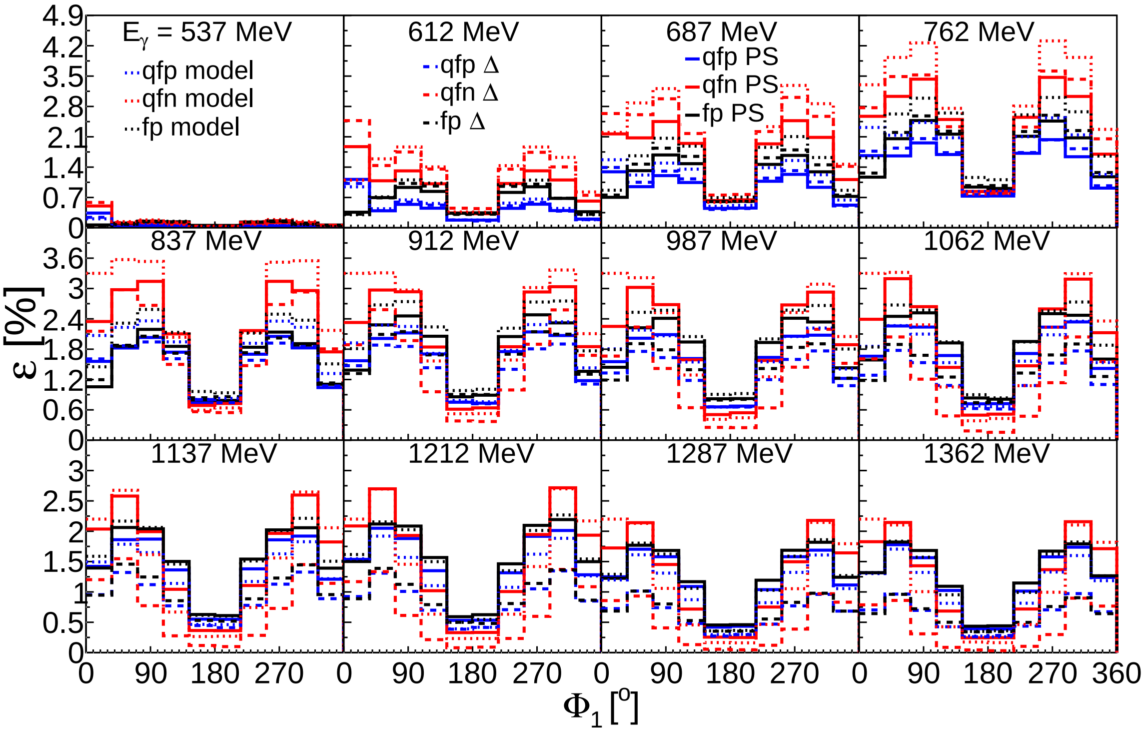

Fig. 4.27: The detection efficiencies as function of the angle Φ_1, integrated over the whole θ^* range and for twelve different bins of E_γ. Black lines: $\gamma p \rightarrow \pi^0\pi^+ n$ (fp), blue lines: $\gamma p(n) \rightarrow \pi^0\pi^+ n(n)$ (qfp), red lines: $\gamma n(p) \rightarrow \pi^0\pi^- p(p)$ (qfn). Full lines: phase space simulation, dashed lines: sequential decay mode simulation, dotted lines: model based simulation.

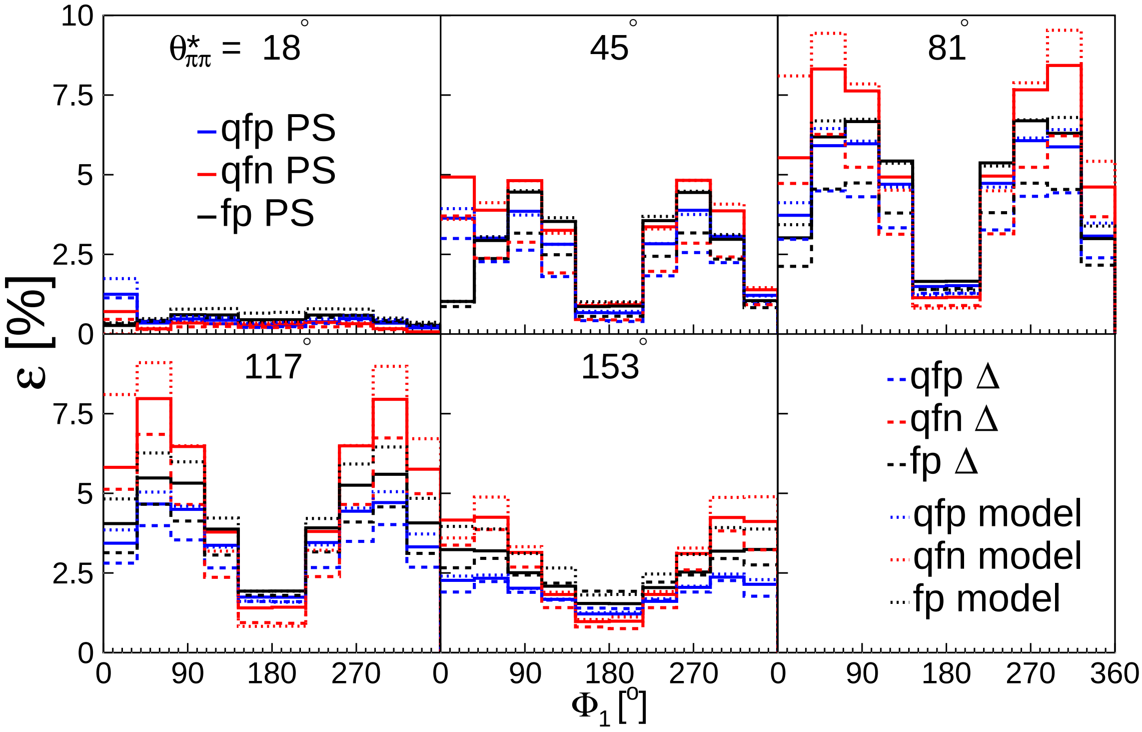

Fig. 4.28: The detection efficiencies as function of the angle Φ_1, integrated over the whole energy range and for five different bins of θ^*. Black lines: $\gamma p \rightarrow \pi^0\pi^+ n$ (fp), blue lines: $\gamma p(n) \rightarrow \pi^0\pi^+ n(n)$ (qfp), red lines: $\gamma n(p) \rightarrow \pi^0\pi^- p(p)$ (qfn). Full lines: phase space simulation, dashed lines: sequential decay mode simulation, dotted lines: model based simulation.

4.12 Photon Flux

For all absolute observables the total number of photons that impinged on the target during the measurement have to be known in order to normalize properly. From the total number of electrons $N_{e^-}(c_n)$ per tagger channel c_n the number of photons $N_\gamma(c_n)$ per channel can be calculated via the efficiency of the photon tagger apparatus $\epsilon_{tagger}(c_n)$ as

$$\epsilon_{tagger}(c_n) = \frac{N_\gamma(c_n)}{N_{e^-}(c_n)}. \tag{4.31}$$

4.12.1 Electron Flux Correction

During the experimental measurements the number of electrons per tagger channel is recorded in the data stream. The tagging efficiency on the other hand depends strongly on the diameter of the collimator and the beam current and has to be measured in a separate measurement. In general, once per day a so called tagging efficiency measurement, which yields the tagger efficiency $\epsilon_t(c_n)$ is performed.

For the data acquisition of the tagger detector a separate DAQ (tagger DAQ), which differes from the one of the rest of the detector system is used. The so called electron scalers, counting the total number of detected electrons base on the tagger DAQ busy signals. These signals only count the electron flux as long as the detector system is not occupied and ready to take data. Due to the independence of the two DAQs also their recording speed is different and a correction has to be applied, using the two live times Γ_{Total} of the total detector system and Γ_{tagger} of the tagger, as established in [86]. The corrected electron flux N'_{e^-} can be calculated as

$$N'_{e^-} = N_{e^-}\frac{\Gamma_{Total}}{\Gamma_{tagger}}, \tag{4.32}$$

where for this measurements the correction factors were in the order of 25 %.

4.12.2 Tagging Efficiency Measurements

To monitor the efficiency of the tagger apparatus during the period of a beam time, normal data taking had to be halted and a very sensitive lead glass detector was used to count the exact number of photons. The measurements had to be performed at extremely low beam intensities, since firstly the efficiency of the lead glass detector decreases strongly for higher rates and secondly random coincident tagger hits have to be avoided. Under the assumption of an equally efficient tagger detector for higher intensities the tagging efficiency during normal data runs can be extracted this way.

The measurements at this very low rates are fudged by cosmic radiation and other background, and therefore background measurements were performed right before and after any tagging efficiency measurement. These background data is then normalized and subtracted from the counts of the tagging efficiency measurements.

4.12.3 Precise Time Dependence Extraction

The quality of the electron beam from MAMI changes during time, mostly just slightly but sometimes considerably, and as such influences the tagging efficiency. Additionally the exact position of the beam has a huge influence on the total photon flux, and therefore taking simply an averaged value of the tagging efficiency will not yield an accurate normalization, but a time dependence has to be extracted. An ionization chamber at the end of the photon beam line monitors the photon flux during normal data taking, but unfortunately only relatively. Nevertheless this relative flux data from the P2 ion chambers in combination with the rates in the tagger detectors can be used to extract an accurate time dependence of the tagging efficiency. This is done by normalizing the relative tagging efficiency values from the P2/tagger ratio with absolute measurements. Figure 4.29 shows the time dependence of the absolute tagging efficiency for the May 2009 beam time, where the nine red crosses represent the results from the tagging efficiency measurements and the black dots show the P2/tagger ratio.

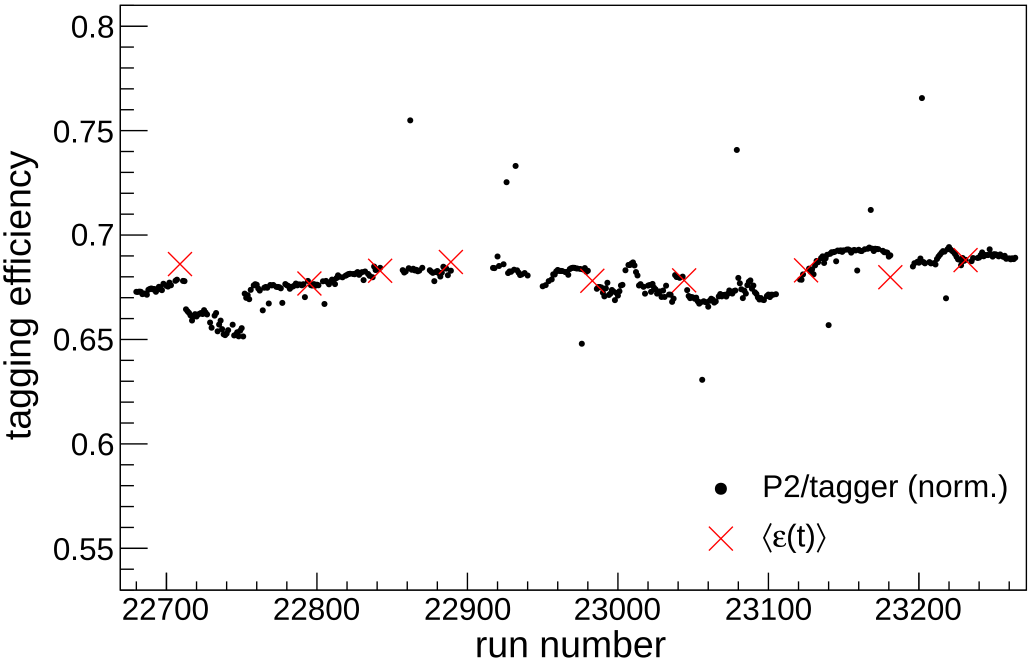

Fig. 4.29: The time dependence of the tagging efficiency. The values, shown as red crosses are averaged over all tagger channels and the P2/tagger ratio is normalized to them. Taken from [57].

The final time dependent tagging efficiencies for every single tagger channel can be extracted using

$$\epsilon(c,t) = \frac{1}{N_m}\sum_{i=1}^{N_m} \epsilon_i(c) \cdot \frac{N_c}{\sum\limits_{i=1}^{N_c} \hat{\epsilon}(c_i)} \cdot \langle \epsilon(t) \rangle \,, \tag{4.33}$$

with the total number of measurements N_m and the number of tagger channels N_c. The energy dependence in the first term was found to be very small. The second term contains the time dependent average of the efficiency of all tagger channels and as such includes the time dependence. The number of tagger counts were extracted separately for every run and the normalization to the absolute measurements was performed using a χ^2-minimization.

4.12.4 Photon Energy Dependent Flux

The run and tagger channel dependent photon flux $N_\gamma^r(c)$ was extracted from the number of electrons per run per tagger channel $N_{e^-}^r(c)$ and the corresponding tagging efficiency $\epsilon_{tagger}^r(c)$ according to equation 4.31. For the application in the normalization process, an energy dependent representation of the photon flux is necessary. Since the tagger channels cover different widths of energy regions the so called bin-overlap method [57] had to be applied to convert the channel dependent flux into an E_γ dependent one.

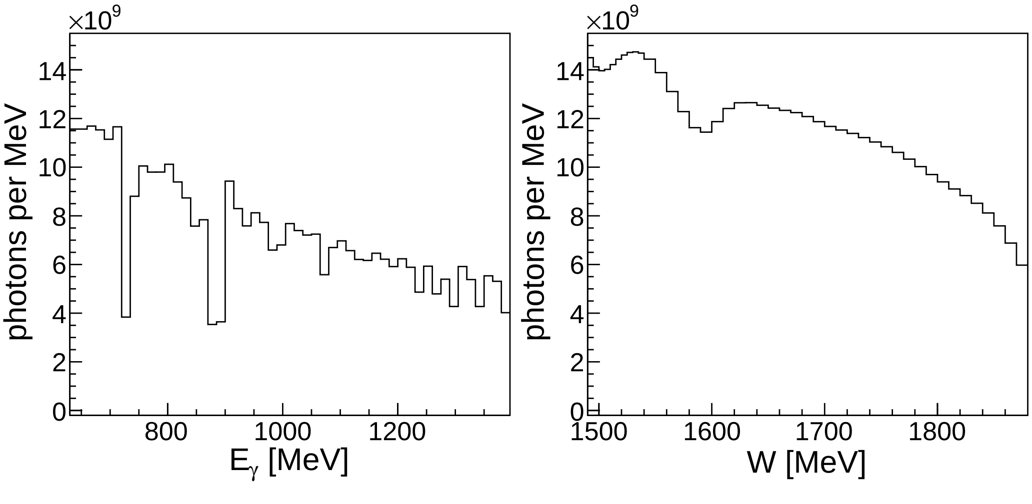

Fig. 4.30: The photon flux as function of the energy of the incoming photon on the left hand side and as function of the center-of-mass energy W on the right hand side. Taken from [57].

The photon flux as function of the energy of the incoming photon is shown in figure 4.30 on the left hand side. The flux is calculated with the same energy binning as the signal histograms for the cross sections and therefore the normalization process was straight forward. As already mentioned, no flux normalization had to be applied for the beam helicity asymmetry calculation, since the difference in the total number of the two photon states are negligible and the flux thus cancels in the ratio.

4.12.5 Center-of-Mass Energy Dependent Flux

The task here is to find the number of photons for a certain value of W having $N_\gamma(c)$ given. In other words all possible W values that can be reached starting from the energy E_c of a tagger channel and the given Fermi momentum distribution of the deuteron [85] have to be calculated and normalized. The procedure is in fact rather simple and requires the energy of the tagger channel E_c and its error ΔE_c, the photon flux of the tagger channel $N_\gamma(c)$, the Fermi momentum distribution, and the mass of the spectator nucleon m_S and the deuteron m_d. Now one million (10^6) times a randomly chosen Fermi momentum is applied to E_c and the corresponding W and ΔW are calculated and filled in a histogram, where again the bin-overlap method is applied. The normalization is done by weighting every value with $N_\gamma(c)$ and the number of iterations [57]. The result is shown in figure 4.30 on the right hand side.

4.13 Cross Section Extraction

In the analysis histograms for E_γ or W, $\cos(\theta^*_{\pi\pi})$ and the invariant mass distribution for the[10] π^0 were filled. In case of the neutral channel a cut on the invariant mass of the first of the randomized pions was applied and the invariant mass of the second one was filled. The yields were then extracted from the integral of the counts in the invariant mass distributions, separately for all energy and polar angle bins. For the E_γ dependent histograms again the bin-overlap method [57] was used in the filling process. Since the background contributions are very low, no further background subtraction method was applied and the signal is just given by the integral of $m(\gamma\gamma)$ from 110 to 160 MeV.

Figure 4.31 shows the signals for $\gamma n(p) \rightarrow \pi^0\pi^0 n(p)$ for 10 $\cos(\theta^*_{\pi\pi})$ bins and a fixed center-of-mass energy $W = 1555$ MeV and an energy bin width of 10 MeV. No signal fitting had to be applied, since the background percentage is not even visible and hence of course negligible.

In figure 4.32 the signal of the invariant mass of the decay photons of the π^0 meson is shown for $\gamma p(n) \rightarrow \pi^0\pi^+ n(n)$. Also here no signal fitting was necessary, because of the very low percentage of background contributions.

---

[10] For the double π^0 channel just one of the two randomized π^0 was chosen.

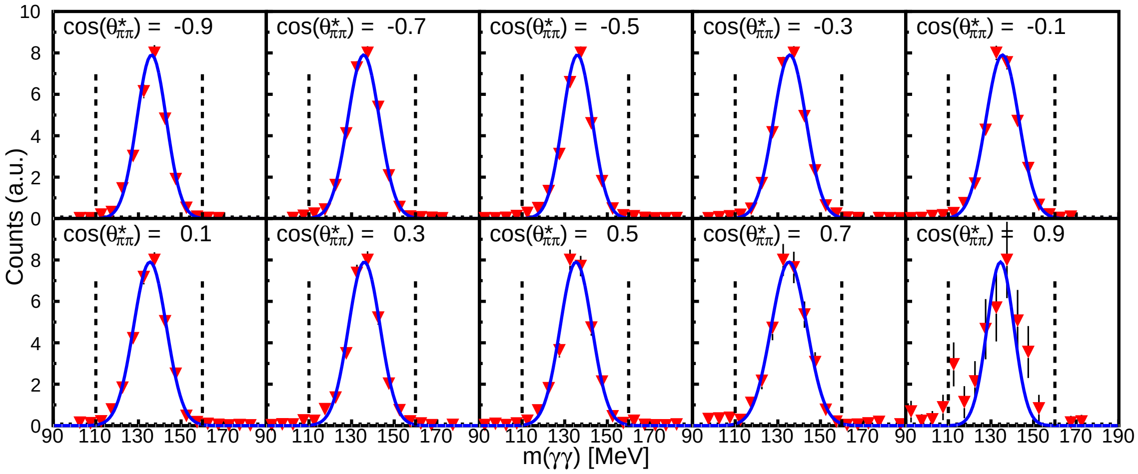

Fig. 4.31: Extraction of the signal for the cross section results. The invariant mass distribution of the decay photons of the 'second' π^0 meson is shown for the reaction $\gamma n(p) \rightarrow \pi^0\pi^0 n(p)$. 10 bins of $\cos(\theta^*_{\pi\pi})$ have been chosen for the final cross section extraction. The energy range shown is $W = 1550 - 1560$ MeV. Red triangles: data points, blue lines: Gaussian fit, black dashed lines: applied cuts.

4.13.1 Cross Section Calculation

Having the energy E and the cosine of the polar angle of the pion-pion system in the center-of-mass $\cos(\theta^*_{\pi\pi})$, the differential cross section is given by

$$\frac{d\sigma}{d\Omega}(E, \cos(\theta^*_{\pi\pi})) = \frac{N(E, \cos(\theta^*_{\pi\pi}))}{N_\gamma(E) \cdot \Delta\Omega \cdot \epsilon_{det}(E, \cos(\theta^*_{\pi\pi})) \cdot \rho_t \cdot \Gamma_r/\Gamma}, \tag{4.34}$$

with the following definitions:

E:	energy E_γ or W
$\Delta\Omega$:	solid angle of $\cos(\theta^*_{\pi\pi})$ bin in [sr]
Γ_r/Γ:	branching ratio of π^0 decay in 2γ
	for neutral channels: Γ_r^2/Γ
	for mixed-charged channels Γ_r/Γ
$\epsilon_{det}(E, \cos(\theta^*_{\pi\pi}))$:	detection efficiency as function of e and $\cos(\theta^*_{\pi\pi})$
$N(E, \cos(\theta^*_{\pi\pi}))$:	number of detected events as function of E and $\cos(\theta^*_{\pi\pi})$
$N_\gamma(E)$:	number of photons as function of E

The target density was calculated as

$$\rho = \frac{N_A \cdot l \cdot \rho_m}{M_N}, \qquad \text{with} \tag{4.35}$$

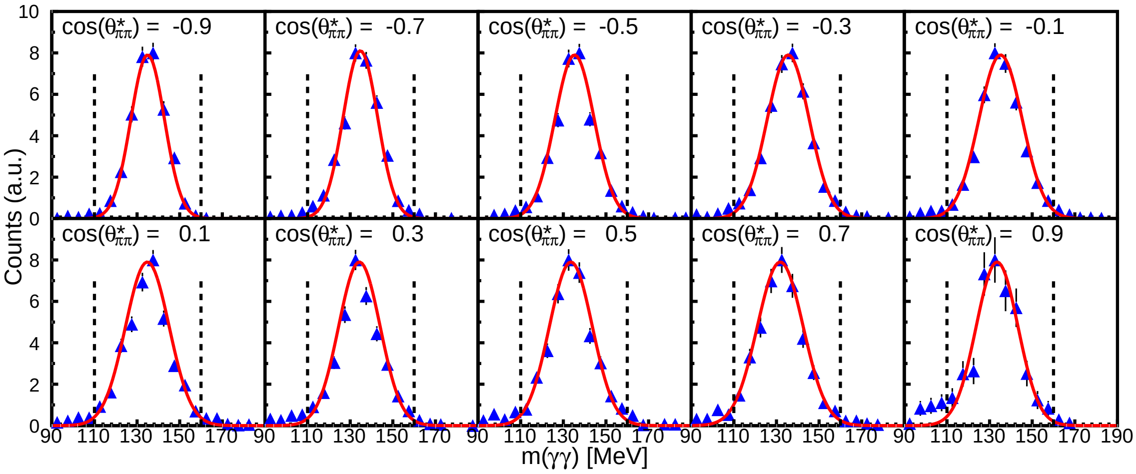

Fig. 4.32: Signal extraction for the cross section of $\gamma p(n) \to \pi^0\pi^+ n(n)$. Energy range as in figure 4.31, blue triangles: data points, red lines: Gaussian fit, black dashed lines: applied cuts.

N_A: Avogadro constant $N_A = 6.02214 \cdot 10^{23}$ mol^{-1}
ρ_m: density of target material
for liquid Deuterium $\rho_{LD_2} = 0.16324$ g/cm^{-3} at 1080 mbar
for liquid Hydrogen $\rho_{LH_2} = 0.071$ g/cm^{-3} at 1080 mbar
l: target length
Dec. 2007 and Feb. 2009 $l = (4.72 \pm 0.05)$ cm
May 2009 $l = (3.02 \pm 0.03)$ cm
Apr. 2009 $l = (10.0 \pm 0.03)$ cm
M_m: molar mass of atomic target material
for Deuterium $M = 2.014$ g/mol^{-1}
for Hydrogen $M = 1.00794$ g/mol^{-1}

For the target densities in $1/b$, with barn $b = 10^{-24}\ cm^2$ we get

$$\begin{aligned} \rho_{D,F} &\approx 0.23039\ b^{-1} && \text{for Dec. 2007 and Feb. 2009} \\ \rho_M &\approx 0.14741\ b^{-1} && \text{for May 2009} \\ \rho_A &\approx 0.422\ b^{-1} && \text{for Apr. 2009} \end{aligned}$$

To have a constant $\Delta\Omega$ for all bins and thus simplify the integration process to get the total cross section from the differential one, the transformation $\theta \to \cos(\theta)$ with $d\cos(\theta) = -\sin(\theta)d\theta$ can be used. The total cross section can this way be extracted from the differential one as

$$\sigma(E) = \int \frac{d\sigma}{d\Omega}(E, \cos(\theta^*_{\pi\pi}))d\Omega \approx \frac{4\pi}{N_{ct}} \sum_{i=1}^{N_{ct}} \frac{d\sigma}{d\Omega}(E, \cos(\theta^*_{\pi\pi}))d\Omega, \tag{4.36}$$

with the number of $\cos(\theta^*_{\pi\pi})$ bins N_{ct}.

4.14 Systematic Uncertainties

Due to the huge complexity of nucleon resonance spectroscopy, be it at the level of the experiment or at the level of data processing, systematic errors play a non-negligible role and are usually in the range of about 10 % for quasifree meson production. In this section we will guide through the extraction of these systematic errors, that can be expected to have the largest influence on the final results.

4.14.1 Target Length

Since the lengths of the targets go directly into the target density (see equation 4.35) and thus into the final result, their uncertainties have to be included. We have different values for the different targets, but the relative error remains about the same. This is because the uncertainty of the deformation of the target window causes an uncertainty in the target density, which is correlated to the length of the target.

For the December 2007 and the February 2009 beam times the target length is given as (4.76 ± 0.05) cm. For May 2009 it is (3.02 ± 0.03)cm and for April 2009 it is given as (10.0 ± 0.08) cm. This leads to an average systematic error of about 1.1 %.

4.14.2 Photon Flux

The systematic error here is coming from the tagging efficiency measurement. It was estimated in [57] to be about 2.8 %.

4.14.3 Empty Target Contributions

Apart from the reactions happening inside of the target cell, there are also reactions with the target cell material, which act as background and have to be subtracted. Actually, for this purpose dedicated empty target measurements ought to be conducted during every beam time. Unfortunately for the measurements of this work, only for the May 2009 beam time very few runs with empty target have been measured and the final statistics are insufficient. Nevertheless the cross section was extracted for only one $\cos(\theta^*_{\pi\pi})$ bin and the error could be roughly estimated to be at the 3 % level.

4.14.4 Analysis Cuts

The choice of the analysis cuts influences the final results, since different cuts can lead to different signal to background ratios due to restricted phase spaces or different particle handling for real and simulated particles. The kinematic cuts from section 4.5, like invariant mass, missing mass and coplanarity cut are found to have the strongest influence and thus also the largest systematic effects. To extract the systematic error the standard cut positions were changed by ±3 % and the cross section was calculated to extract the relative difference.

4.14.5 Nucleon Detection Efficiency Correction

In section 4.11.2 it was explained, that the detection efficiencies had to be corrected by extracting correction factors from the analysis of the free proton data. The influence of the analysis cuts plays also a role here and thus has an influence on the final results. To estimate this effect the same procedure as in section 4.14.4 was applied and the relative change in the nucleon detection efficiency correction factors was extracted.

4.14.6 $\Delta E - E$ Analysis

For the mixed-charge final state an additional uncertainty is coming from the discrimination of charged pions and protons with the $\Delta E - E$ analysis. The determined cut from section 4.1.3 is therefore shifted by ±3 % and the cross section results are compared to extract energy dependent (relativ) systematic errors.

4.14.7 Summation of Errors

The four sources of systematic errors were treated as independent and summed up according to

$$\Delta_{sys}(E) = \sqrt{\sum_{i=1}^{n} \left(\Delta^{i}_{sys}(E)\right)^2}, \tag{4.37}$$

were E can again be E_γ or W. In figure 4.33 we show the W dependent relative systematic errors for all neutral channels. As expected the neutron data suffers the most from systematic effects and has an average of about 5.5 %, if one overlooks the lowest energies. quasifree and free proton data are a little below the 5 % level. Apart from the lowest energies only very small energy dependence can be made out.

Figure 4.34 shows the relative systematic errors for the mixed-charge channels. The whole analysis is in general more delicate, because of the necessity to not only detect charged pions but also distinguish them properly from protons. Additionally more background has to be removed, as can be seen in the missing mass and coplanarity spectra in figures 4.9 and 4.7. The larger background percentage increases the influence of the cut positions on the signal to background ratio and thus leads to larger systematic effects.

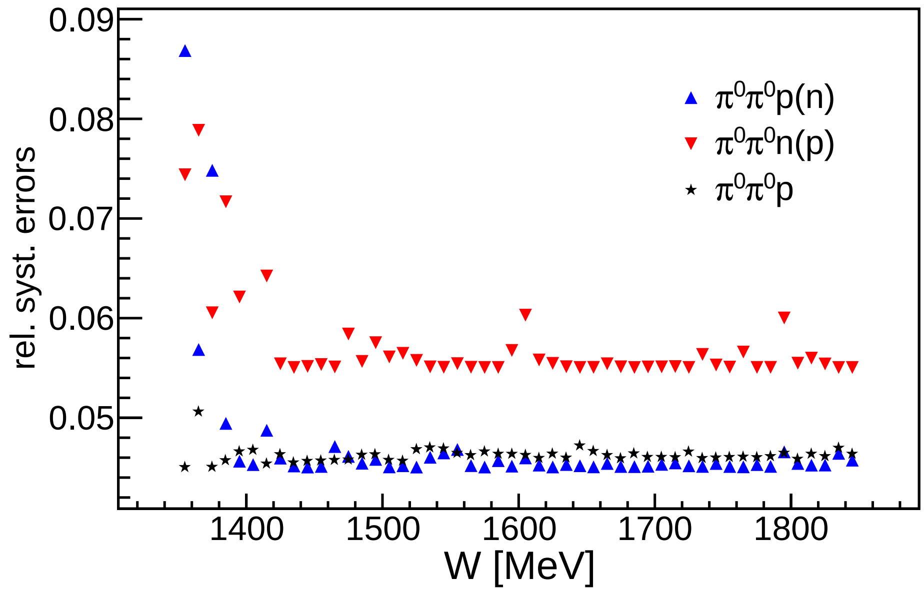

Fig. 4.33: The relative systematic errors for the three neutral channels as function of W. Black stars: $\gamma p \to \pi^0\pi^0 p$, blue triangles: $\gamma p(n) \to \pi^0\pi^0 p(n)$, red triangles: $\gamma n(p) \to \pi^0\pi^0 n(p)$.

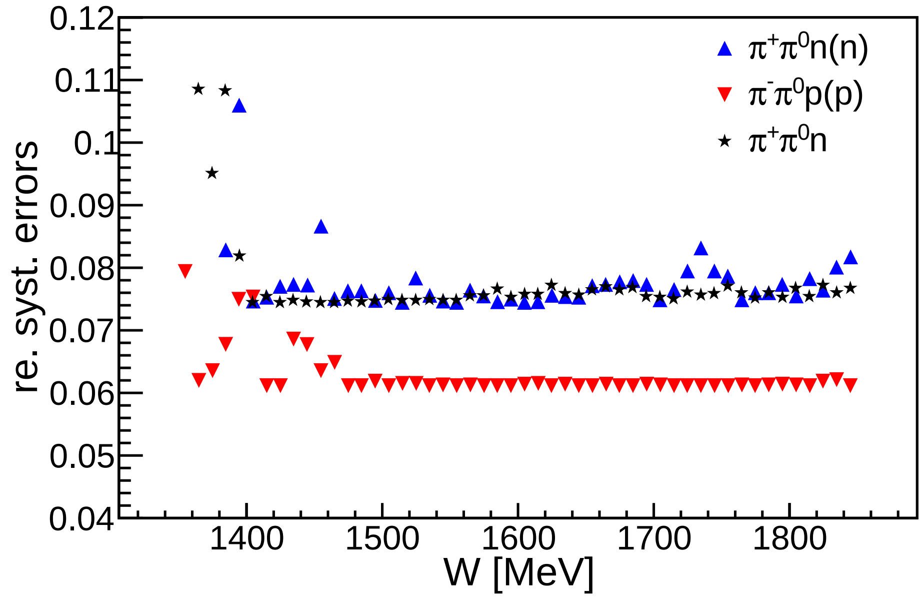

Fig. 4.34: The relative systematic errors for the mixed-charge channels as function of W. Black stars: $\gamma p \to \pi^0\pi^+ n$, blue triangles: $\gamma p(n) \to \pi^0\pi^+ n(n)$, red triangles: $\gamma n(p) \to \pi^0\pi^- p(p)$.

‘

Chapter 5

Results

In the previous chapters the long and complicated way from the production of bremsstrahlung photons until the extraction of the final observables has been explained, and encountered difficulties and their solutions have been discussed in detail. In this chapter now the final results shall be presented. First, the beam helicity asymmetry results will be shown in section 5.1, followed by total and differential cross section results in section 5.2. For both sections a split-up in neutral channel and mixed-charge channel results was chosen. The beam helicity asymmetry results for the double π^0 channels can be found in section 5.1.4 and the ones for the $\pi^{\pm}\pi^0$ channels in section 5.1.5. The cross section results were split up in total cross section results for the neutral and the mixed-charge channel in section 5.2.1, angular differential cross section results in section 5.2.2 and mass differential cross section results in section 5.2.3. In the following always the full statistics is presented if not mentioned otherwise. This means all deuterium beam times were added up. Of course it was always first checked that no significant discrepancies between the different data sets existed.

Finally in section 5.3 the results are summarized and two observations will be discussed and possible conclusion are drawn.

5.1 Beam Helicity Asymmetries

As explained in section 4.10, the calculation of Φ as angle between production and reaction plane is not per se clear and different definitions have been used. For the results of the double π^0 channels the reaction plane was always spanned by the incoming photon and the recoil nucleon (indicated by the index 1), and therefore only two different asymmetries were extracted, namely one with randomized pions $I^{\odot}_{1r}(\Phi_{1r})$ and one with mass-ordered pions $I^{\odot}_{1m}(\Phi_{1m})$.

For the channels with the charged pions three additional asymmetries were extracted, but the one with randomized pions was omitted, since it caries the least information.

5.1.1 Extraction of Parameters

Due to its symmetry properties the beam helicity asymmetry $I^{\odot}(\Phi)$ can be fitted with a sine series according to

$$I^{\odot}(\Phi) = \sum_{i=1}^{\infty} A_n \cdot \sin(n \cdot \Phi). \tag{5.1}$$

Terms of order higher than four are already in agreement with zero and thus carry no more information. Fitting the asymmetries with these sine series allows for a more compact way to present the results. All results are presented in the 'classical' way and additionally in the form with the extracted parameters A_n (see for example figure 5.6).

5.1.2 Influence of Detection Efficiency Corrections

As discussed in section 4.11.3 three different simulation were used to extract detection efficiencies for the correction of the beam helicity asymmetry results for the mixed-charge channels. In a first step the influence of these different corrections had to be examined and the results from $\gamma p \rightarrow \pi^0\pi^+ n$ were taken as testing ground. In figure 5.1 four results from the free proton data are shown for the beam helicity asymmetry for different energies of W. The results only differ by the detection efficiency correction that was used.

For the green points no correction was used, for the black points a correction using a mixing of phase space and 'first sequential decay" mode simulation was applied, for the blue points a pure phase space simulation correction was used, and for the red points the correction with the model based simulation was implemented. For the mixed simulations only a sequential decay via Δ^+ was used, and the ratio of contributions from phase space to sequential was 3 : 7. All results agree very nicely, showing that the influence of the detection efficiency for this asymmetry observable is cancelling out in the integration over $\theta^*_{\pi\pi}$. Nevertheless the detection efficiency correction was applied for all further results of $I^{\odot}(\Phi)$ with the exception of the free proton data results for $\gamma p \rightarrow \pi^0\pi^0 p$ from figure 5.2.

5.1.3 Comparison To Previous Results

In a first step the analysis procedure can be checked by comparing the free proton results to previous results for the beam helicity asymmetry from [35]. In figure 5.2 the results from this work are shown as black stars and the previous results as blue triangles. Since the previous results were measured at MAMI-B ($E_{e^-}^{max} = 883$

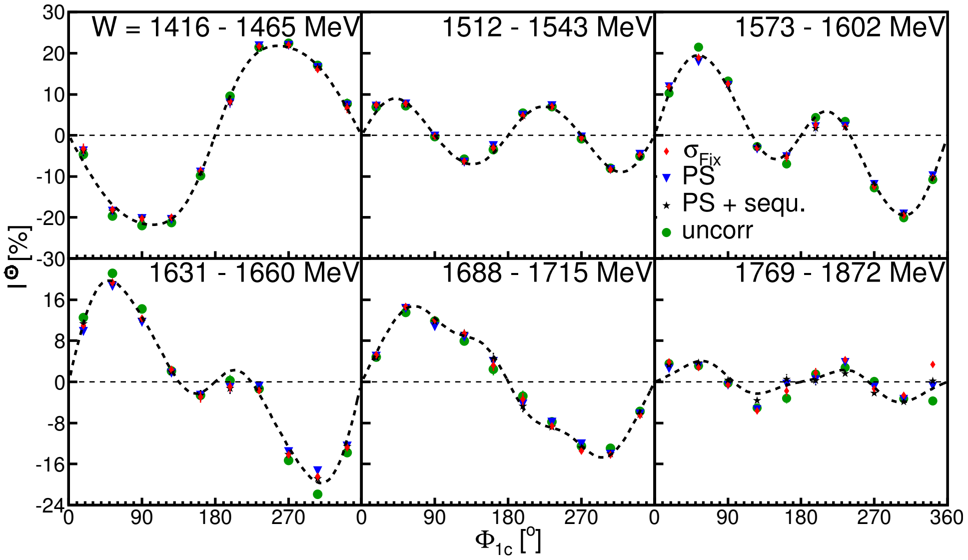

Fig. 5.1: The influence of the detection efficiency correction from different simulations is shown by comparing the results of the beam helicity asymmetry for $\gamma p \rightarrow \pi^0\pi^+n$. Green dots: uncorrected, black stars: corrected with sequential decay and phase space simulations (with 7 : 3, see text), blue triangles: corrected with pure phase space simulation, red diamonds: corrected using model based simulation.

MeV), only lower energies of the incident photons can be compared. The blue and black dashed lines represent fits to the data, using equation 5.1. In contrast to the present analysis the previous results have been measured inclusively, i.e., without requiring the detection of the recoil proton. Actually, this could have been done also with the free proton data in this work, but in view of the analysis of the quasifree data, the exclusive analysis had to be tested.

The agreement between the results is excellent and shows clearly, that the analysis procedure works fine. Moreover it shows that detection efficiency effects should not have a large influence, since both results were obtained without detection efficiency correction, but still no effects from the deficiency of nucleon detection show up.

The results from $\gamma p \rightarrow \pi^0\pi^+n$ are compared to previous results in figure 5.3 and the agreement is fine as well, though less good than the agreement for the neutral channel. The results of this work are represented by blue stars and the results from [35] as black triangles. The blue dashed lines are again fits to the data of this work using equation 5.1. The small discrepancies in the agreement could come from different systematic effects, since again the previous data were obtained by an inclusive analysis of the reaction, whereas in this work an exclusive analysis was applied.

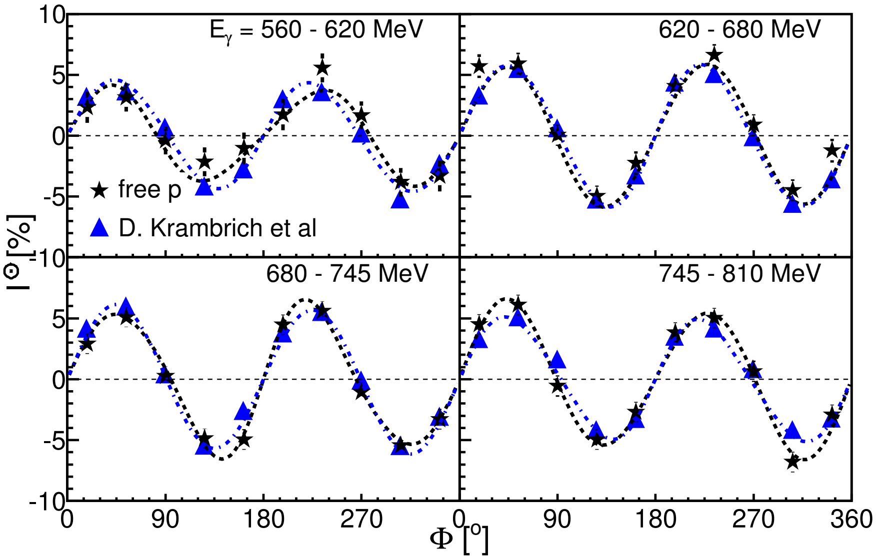

Fig. 5.2: The beam helicity asymmetry results for $\gamma p \rightarrow \pi^0\pi^0 p$ compared to previous results for $\gamma p \rightarrow \pi^0\pi^0(p)$ from [35]. Black stars: this work, blue triangles: [35], black dashed and blue dashed-dotted lines: fits to the data with equation 5.1.

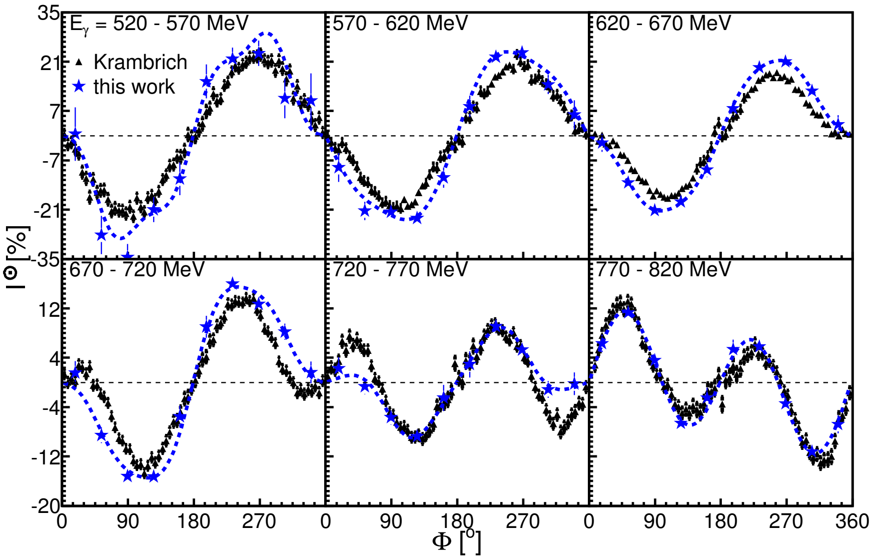

Fig. 5.3: The beam helicity asymmetry results for $\gamma p \rightarrow \pi^0\pi^+ n$ compared to previous results for $\gamma p \rightarrow \pi^0\pi^+(p)$ from [35]. Black triangles: previous results, blue stars: this work. The blue dashed lines show again the fit with the sine series to the data of this work.

5.1.4 The Neutral Channels

Figure 5.4 shows the results for the beam helicity asymmetry with randomized pions for $\gamma p(n) \rightarrow \pi^0\pi^0 p(n)$, and $\gamma p \rightarrow \pi^0\pi^0 p$. Apart from the two first energy bins the results for free proton (black stars) and quasifree proton (blue triangles) agree very well, showing that the influence of the Fermi motion can be reliably

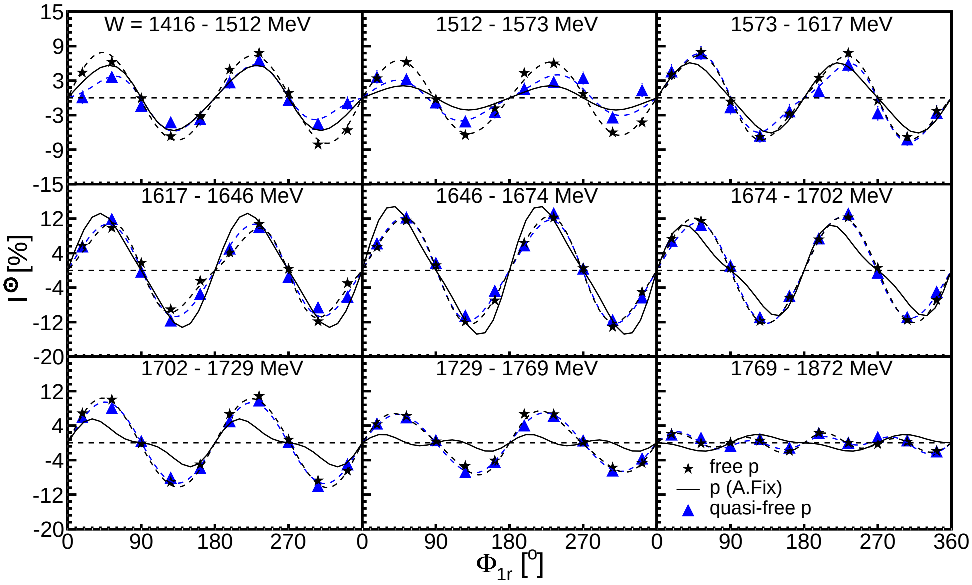

Fig. 5.4: The beam helicity asymmetry results $I_{1r}^{\odot}(\Phi_{1r})$ with randomized pions for free and quasifree proton results, compared to model calculations for the free proton from [36]. Black stars: $\gamma p \rightarrow \pi^0\pi^0 p$, blue triangles: $\gamma p(n) \rightarrow \pi^0\pi^0 p(n)$, full lines: model results, dotted lines (blue and black): fits to data.

removed by a full reconstruction of the kinematics of the final state.

The quasifree neutron results are shown in figure 5.5 as red triangles together with the free proton results, again plotted as black stars. Astonishingly they agree very good with the proton results. This comes as a surprise, especially in the third resonance region, where for example the MAID model predicts different predominant coupling for proton and neutron, as we have seen in section 1.3.2. This is also visible in the model predictions for proton and neutron, which are totally different in the third resonance region.

Apart from some energy bins, the model predictions are not able to reproduce the experimental data exactly. Especially for the neutron data in the second and third resonance region, the model is completely out of phase and under- or overestimates the asymmetry.

The parameters of the fits to the data from figure 5.4 and 5.5 with equation 5.1 are shown in figure 5.6. As mentioned in section 4.10, the beam helicity asymmetry $I^{\odot}(\Phi)$ has to fulfill

$$I^{\odot}(\Phi) = I^{\odot}(\Phi + \pi), \tag{5.2}$$

if the pions are indistinguishable as in the case of randomized pions. This leads to the fact that the uneven parameters A_1 and A_3 have to vanish. This is in fact the case for the results (within statistical errors). Moreover, a clear dominance from parameter A_2 is visible, whereas A_4 only carries a small portion of the information.

To extract more information and therefore test the model in more detail, a

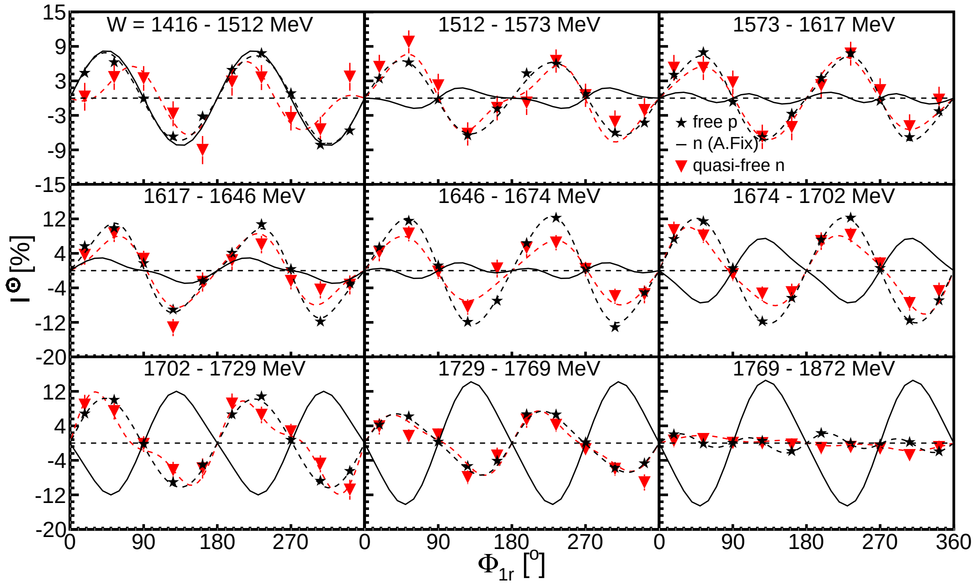

Fig. 5.5: The beam helicity asymmetry results $I^{\odot}_{1r}(\Phi_{1r})$ with randomized pions for free proton and quasifree neutron results, compared to model calculations for the neutron from [36]. Black stars: $\gamma p \rightarrow \pi^0\pi^0 p$, red triangles: $\gamma n(p) \rightarrow \pi^0\pi^0 n(p)$, full lines: model results, dotted lines (red and black) fits to data.

kinematic ordering of the two π^0 has been chosen according to

$$m(\pi^0_1, N) \geq m(\pi^0_2, N). \tag{5.3}$$

A very nice piece of information would be the knowledge of the 'first' and 'second' pion, in the case of sequential decays. Unfortunately this information can not be extracted from the experimental results and only a kinematic restriction could be applied to gain an ordering process. Equation 5.3 does not generally distinguish between first and second pion by their time of production, since several different decay possibilities exist, where once the first produced pion has a higher invariant mass together with the nucleon and once the second pion. This fact makes reasoning very difficult, but at least allows to restrain model predictions more strictly.

In figure 5.7 the beam helicity asymmetry for free and quasifree proton results are presented, but this time with mass-ordered pions. Now equation 5.2 is visibly not fulfilled anymore and thus all parameters A_n carry information. The data are compared to four different theoretical predictions. The full black line represent the model results from [36] and the dashed black lines are predictions from [26]. The agreement of the first one is apart from some energy bins not very good, and the latter fails completely to reproduce the experimental data. The most accurate model results are the two solutions from [87], which in general agree reasonably well with the data. The two solutions differ in a few partial waves, where they have different resonance contributions.

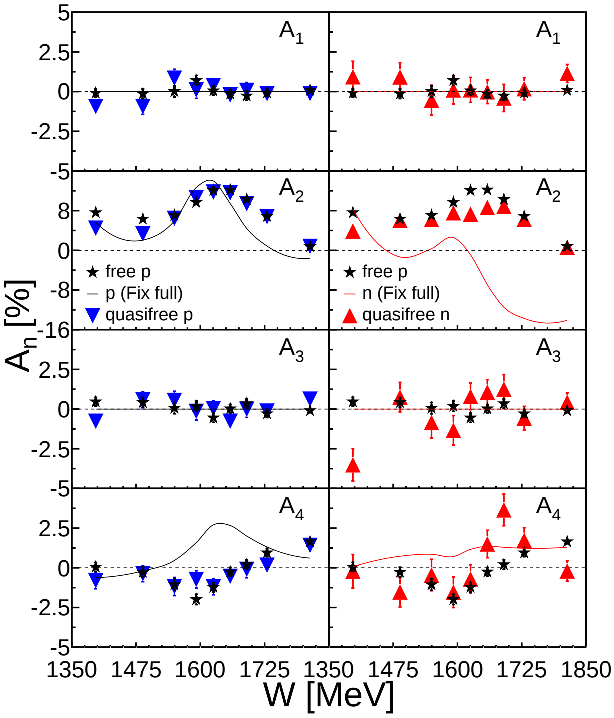

Fig. 5.6: Parameters A_n from the sine series of equation 5.1 as function of the center-of-mass energy W for randomized pions. Black stars: $\gamma p \rightarrow \pi^0\pi^0 p$, blue triangles: $\gamma p(n) \rightarrow \pi^0\pi^0 p(n)$, red triangles: $\gamma n(p) \rightarrow \pi^0\pi^0 n(p)$, full lines: model results from [36].

Again the agreement between free and quasifree proton results is obvious and clearly supports the chosen analysis procedure.

The results of the quasifree neutron data set are compared to the ones from the free proton data and to the model results from [36] in figure 5.8. Even with a restriction on the reaction kinematics according to equation 5.3 the agreement between neutron and proton results remains unchanged. The model results also fail to reproduce the mass-ordered beam helicity asymmetry data.

In figure 5.9 the information from the last two figures is again present in a compact form, where the extracted parameter A_n are shown as function of W. The free proton data, shown as black stars, agree nicely with the quasifree ones, shown as blue triangles. Apart from some energy bins around $W = 1650$ MeV the neutron results, represented by the red triangles agree quite good with the free proton results. For proton and neutron results, all model calculations can quite nicely reproduce the A_1 parameter, but have a rather poor agreement with A_2. Even though A_3 and A_4 are rather small, a clear discrepancy between the models and the data can be observed.

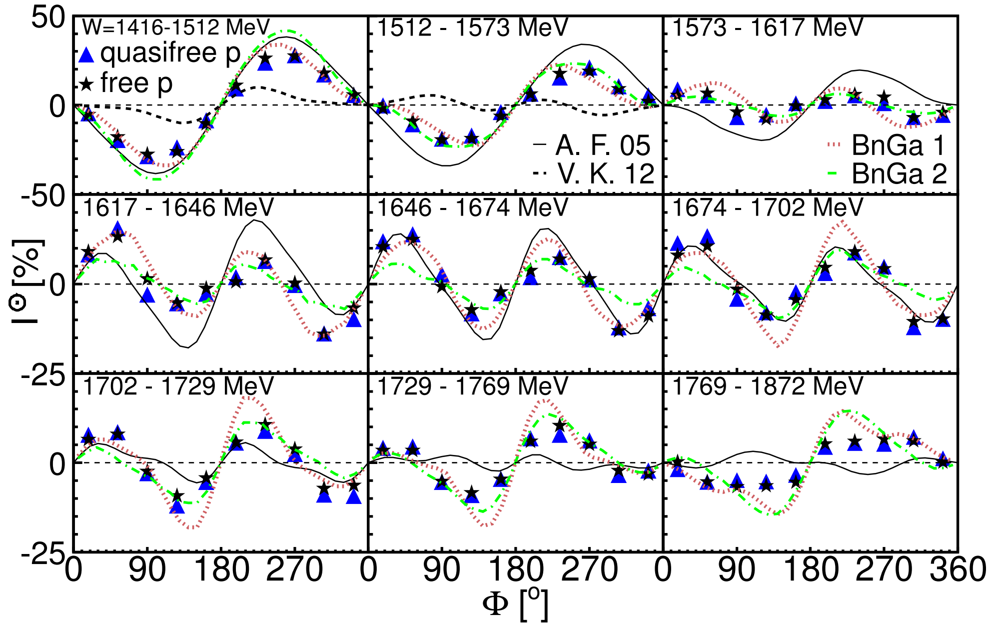

Fig. 5.7: Beam helicity asymmetries with mass-ordered pions for free and quasifree proton data compared to four different model predictions. Black stars: free proton data, blue triangles: quasifree proton data, full black lines: model calculations from [36], dashed black lines (only for two lowest energy bins): model calculations from [26], dotted red lines: solution BnGa2011-1 from [87], green dash-dotted lines: solution BnGa2011-2 from [87].

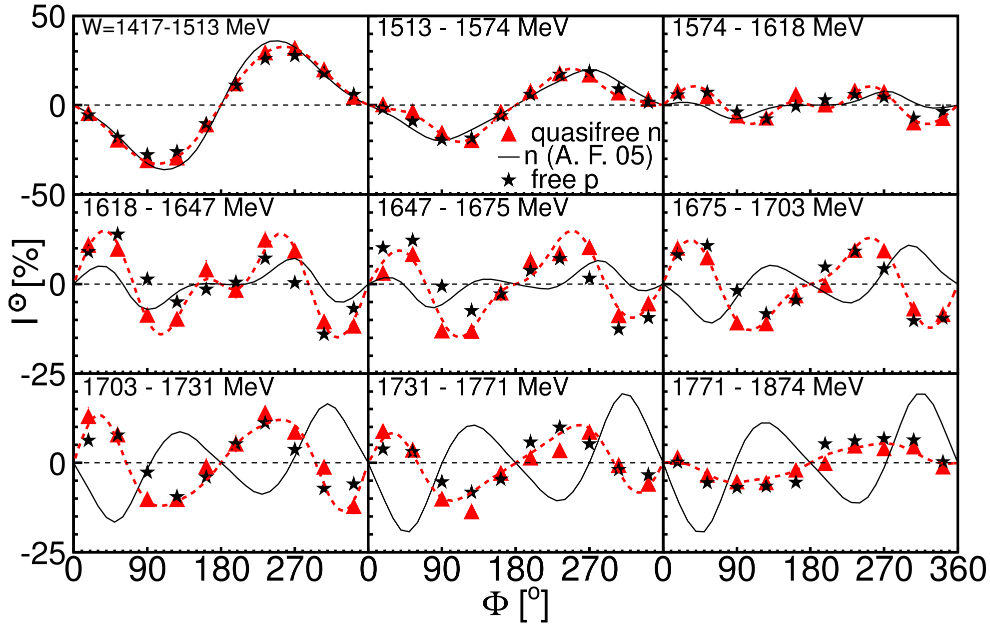

Fig. 5.8: Beam helicity asymmetries with mass-ordered pions for quasifree neutron and free proton results compared to the model calculations from [36]. Black stars: free proton data, red triangles: quasifree neutron data, full black lines: [36].

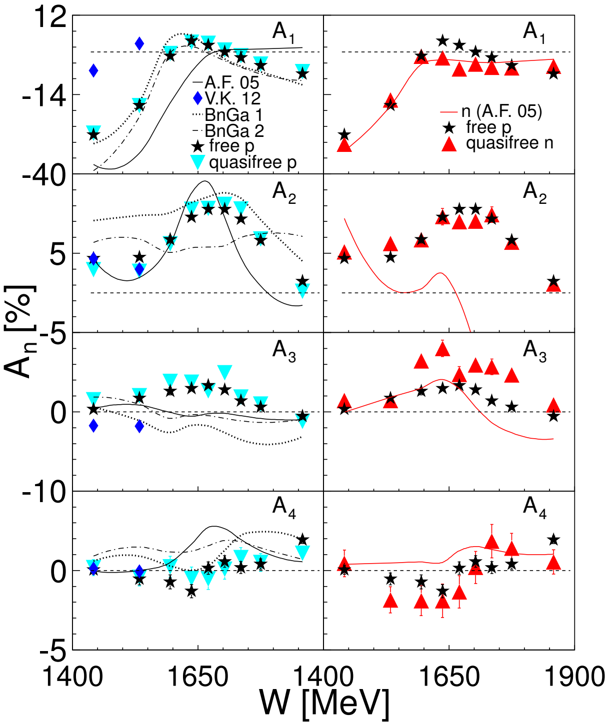

Fig. 5.9: Coefficients of the fits to the mass-ordered asymmetries from the last two pictures as function of W. Black stars: free proton data, blue triangles: quasifree proton data, full black/red lines: model calculations for proton and neutron from [36], blue diamonds (only for two lowest energy bins): model calculations from [26], black dotted lines: solution BnGa2011-1 from [87], black dash-dotted lines: solution BnGa2011-1 from [87].

5.1.5 The Mixed-charge Channels

For the results of the mixed-charge channels, four different beam helicity asymmetries have been extracted, as defined in section 4.10. In figure 5.10 the mass-ordered asymmetry $I^{\odot}_{1m}(\Phi_{1m})$ is shown for the first definition of Φ, where recoil nucleon and incident photon span the reaction plane, and the two pions span the production plane. The free and quasifree proton results are compared to the model calculations from [36] for twelve bins of W.

The center-of-mass energy W in the reaction $\gamma p \to \pi^0\pi^+ n$ was always reconstructed from the initial state photon and proton four-momenta and a nice agreement between the results from the free and quasifree proton was observed.

As explained in the last chapter, an event was only accepted if the charged pion was detected in the Crystal Ball. This procedure restricts the reaction phase space by some part, and this fact had to be considered in the model calculations. Model results with such a restricted reaction phase space are shown as full lines in figure 5.10. The dashed lines represent the model calculations from [36] with full reaction phase space. This restriction has only a very small effect, as can be seen by the very tiny difference between the two model curves.

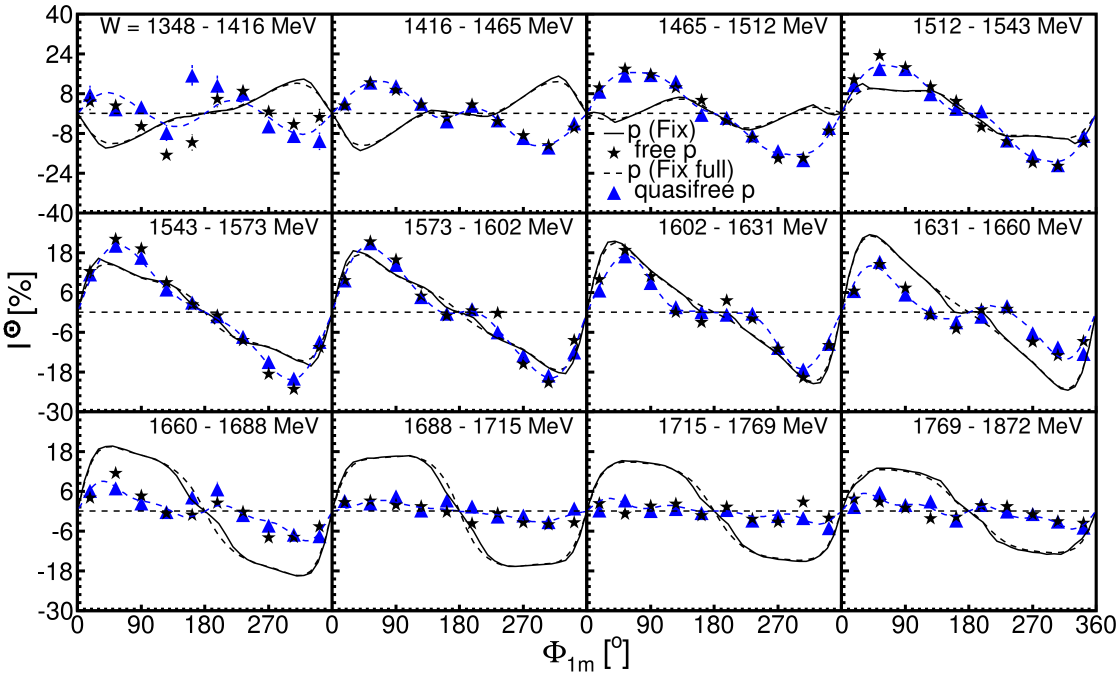

Fig. 5.10: Beam helicity asymmetry $I^{\odot}_{1m}(\Phi_{1m})$ with mass-ordered pions and the first definition of Φ. Black stars: $\gamma p \to \pi^0\pi^+ n$, blue triangles: *ReacPiP*, black solide and black dashed lines: model calculations from [36], blue dashed lines: fit to quasifree data.

Also for the mixed-charge channels the asymmetries are sizable, and free and quasifree proton data agree very well, except for the first energy bin. Apart from the energy bins number four to seven, the model results cannot reproduce the experimental results accurately. Towards higher energies the model completely overestimates the size of the asymmetries.

The quasifree neutron results for the mass-ordered asymmetries are compared to the free proton results and the model calculations for the neutron from [36] in figure 5.11. Only around 1550 MeV in W the model can reproduce the data, whereas for the rest of the energy bins it is completely off.

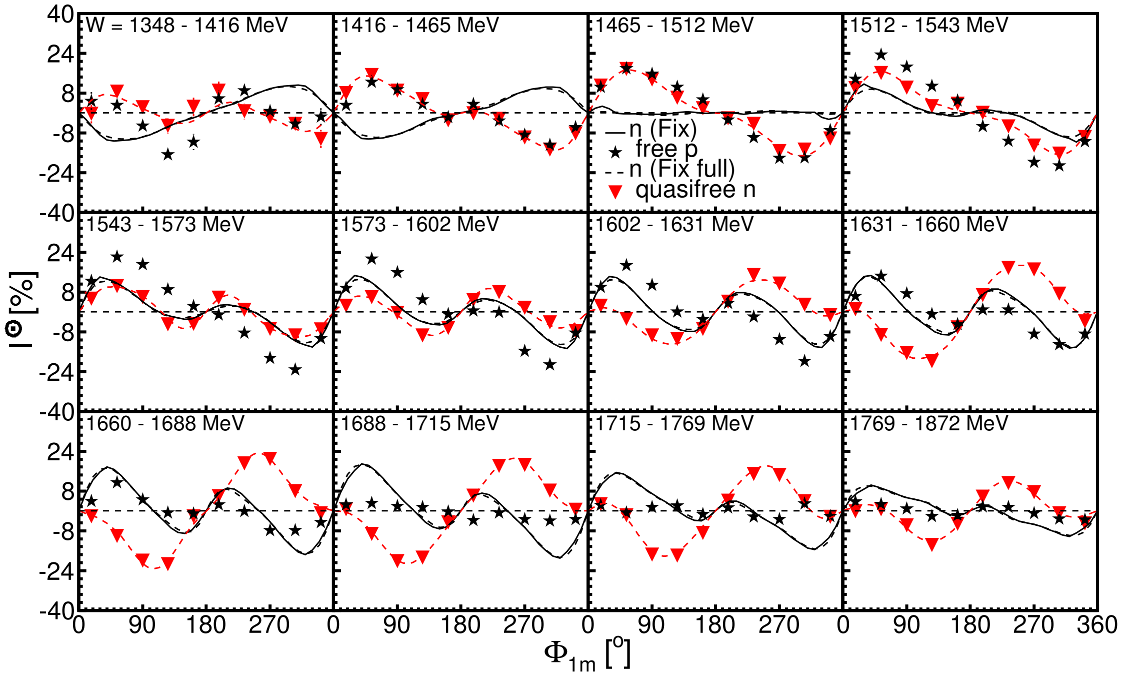

Fig. 5.11: Beam helicity asymmetry $I^{\odot}_{1m}(\Phi_{1m})$ with mass-ordered pions for the quasifree neutron data. Black stars: free proton data, red triangles: quasifree neutron data, full lines: 'restricted' model from [36], dashed lines: full model from [36].

In contrast to the beam helicity results from the neutral channel, where proton and neutron are very similar, here a clear difference can be made out. At higher energies, where the proton asymmetry is rather small, the neutron data still shows large asymmetries. The coefficients of the fit with the sine series are shown in figure 5.14, where they can be nicely compared to the coefficients of the second beam helicity asymmetry $I^{\odot}_{1c}(\Phi_{1c})$, with charge-ordered pions.

First the results for the charge-ordered asymmetries are presented in figures 5.12 and 5.13. The quasifree proton results are again shown as blue triangles and compared to the free proton results represented by black stars. The restricted and full model results from [36] are again shown as full and dashed lines, respectively. The agreement of the two proton results is also here very promising, and allows to interpret the quasifree neutron data as very good approximation of free neutron data. The model results fail again to reproduce the experimental results for all energy bins, but come rather close for the energies shown in the middle row. At higher energies they are again strongly overestimating the asymmetries.

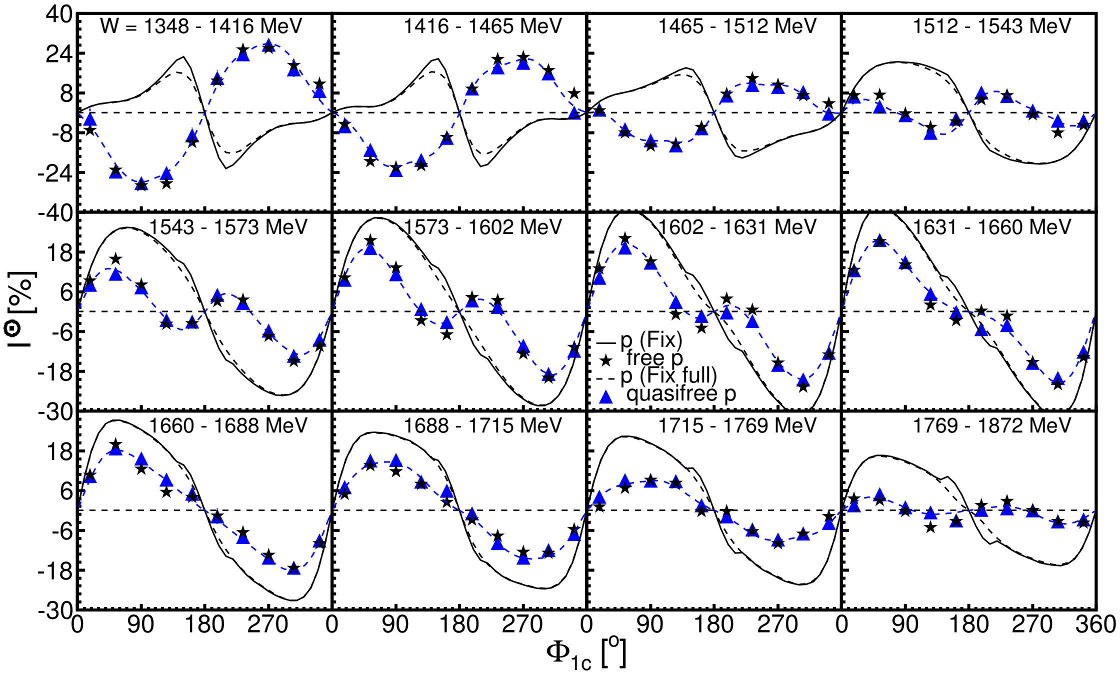

Fig. 5.12: $I^{\odot}_{1c}(\Phi_{1c})$ for free and quasifree proton data. Black stars: free proton data, blue triangles: quasifree proton data, full lines: 'restricted' model from [36], dashed lines: full model from [36].

The neutron results for $I^{\odot}_{1c}(\Phi_{1c})$ from figure 5.13 show large asymmetries. Up to about 1570 MeV, they agree well with the proton data, which may be a hint to a very similar coupling of proton and neutron in this energy region for the mixed-charge final states. The model on the other hand agrees much better towards higher energies and is totally off phase for the lowest energies.

This fact is well visible in figure 5.14, where the coefficients of the fits for the two asymmetries $I^{\odot}_{1m}(\Phi_{1m})$ and $I^{\odot}_{1c}(\Phi_{1c})$ are shown. The model predictions for the A_1 parameter have no zero-crossing, whereas all experimental results show one. The odd coefficients A_1 and A_3 should not depend on the ordering of the two pions, since parity conservation demands

$$I^{\odot}(\Phi) = -I^{\odot}(2\pi - \Phi). \tag{5.4}$$

The even coefficients on the other hand clearly change from the mass-ordered to the charge-ordered asymmetries.

For the two remaining asymmetries $I^{\odot}_{2c}(\Phi_{2c})$, where $\pi^{\pm}$ and the incident photon define the reaction plane and π^0 and recoil nucleon are chosen as p_1 and p_2 and

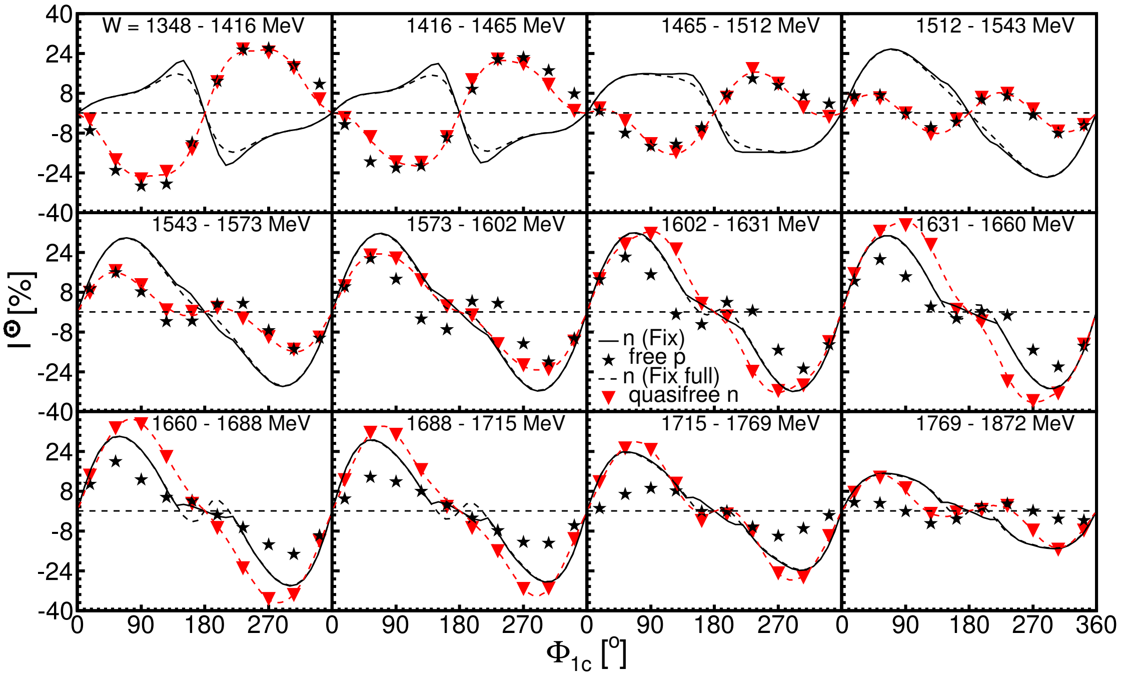

Fig. 5.13: $I^{\odot}_{1c}(\Phi_{1c})$ for free proton and quasifree neutron data. Black stars: free proton data, red triangles: quasifree neutron data, full lines: 'restricted' model from [36], dashed lines: full model from [36].

$I^{\odot}_{3c}(\Phi_{3c})$, where π^0 and the incident photon span the reaction plane and $\pi^{\pm}$ and recoil nucleon are chosen as p_1 and p_2, only the coefficients are shown in figure 5.15.

The two asymmetries are again large and show very different shapes. The model predictions for $I^{\odot}_{2c}(\Phi_{2c})$ have a rather poor agreement for A_1 but are able to reproduce A_2 pretty good, especially for the proton results. A_3 and A_4 are only small as before, and the agreement is hard to evaluate.

The model results for the neutron for $I^{\odot}_{3c}(\Phi_{3c})$ completely disagree with the experimental data, and also for the proton results, only A_2 can be reproduced reasonably, but only for the higher energies. As far as theorists can tell, no connection between $I^{\odot}_{1c}(\Phi_{1c})$, $I^{\odot}_{2c}(\Phi_{2c})$ and $I^{\odot}_{3c}(\Phi_{3c})$ exists, meaning they are in no way complementary or can be deduced one from another. Possible connections have been tested with the experimental data, by probing different summation and subtraction methods, but as expected from theory side, no significant systematic has been found.

In figure 5.16 the three different charge-ordered asymmetries for the quasifree proton data are shown together with their corresponding model predictions.

The experimental data as well as the model show a clear phase shift of $I^{\odot}_{1c}(\Phi_{1c})$ and $I^{\odot}_{2c}(\Phi_{2c})$ with respect to $I^{\odot}_{3c}(\Phi_{3c})$.

The situation is very similar for the quasifree neutron results for these three asymmetries, shown in figure 5.17, although not for the first three energy bins.

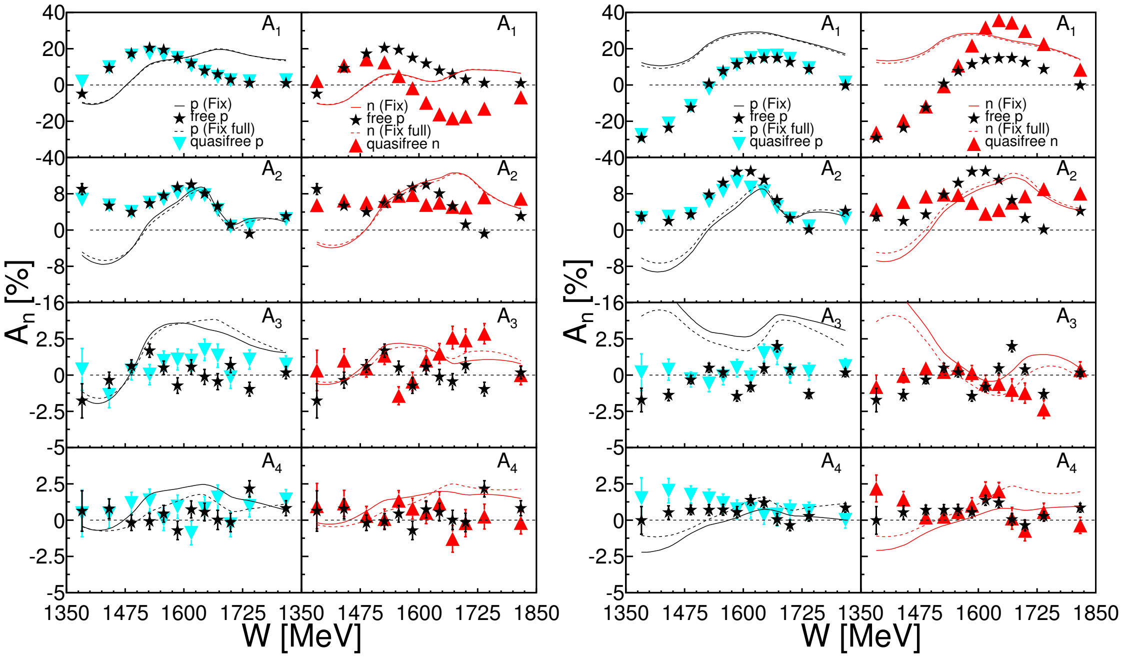

(a) (b)

Fig. 5.14: Coefficients of the fits to the asymmetries shown in figure 5.10, 5.11, 5.13 and 5.13. On the left hand side the results for the mass-ordered asymmetries and on the right hand side the ones for the charge-ordered asymmetries. Notation as in the four previous figures.

Finally in figure 5.18 the A_1 and A_2 coefficients for the three charge-ordered asymmetries for quasifree proton and quasifree neutron data are shown for five bins of $\theta^*_{\pi\pi}$. This representation allows to compare the dominant parts of the different asymmetries in the most compact and clear way. For extreme angles of $\theta^*_{\pi\pi}$ the asymmetries are no longer defined, since recoil nucleon and incident photon are colinear and the definition of two planes is no longer possible. Due to the relatively large bins in $\theta^*_{\pi\pi}$, a behavior distinct from zero is still visible. Of course the final integrated asymmetries are dominated by the asymmetries around 90 degrees. This is also one explanation for the cancellation of the detection efficiency correction in the integrated asymmetries.

One obvious relation between the three asymmetries seems to exist for the dominant A_1 coefficients as follows

$$A_1(I^{\odot}_{1c}) \approx A_1(I^{\odot}_{2c}) \approx -A_1(I^{\odot}_{3c}), \tag{5.5}$$

but nevertheless no general relation can be made out, since equation 5.5 is clearly not fulfilled for the A_2 parameters.

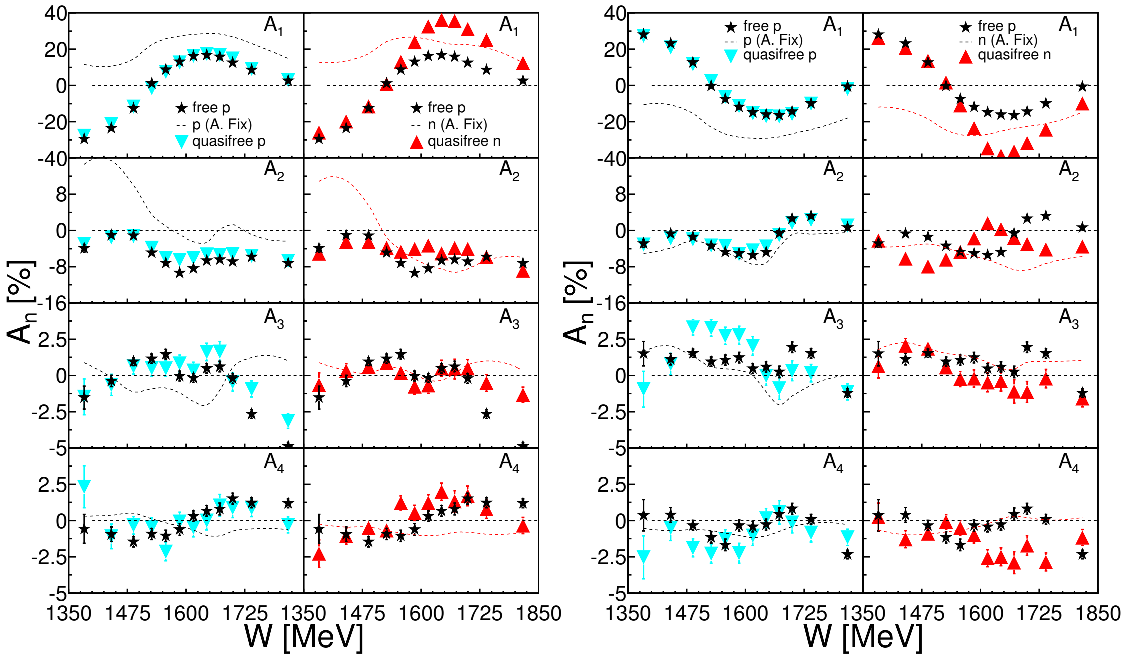

(a) (b)

Fig. 5.15: Coefficients of the fits to the asymmetries $I^{\odot}_{2c}(\Phi_{2c})$ and $I^{\odot}_{3c}(\Phi_{3c})$ compared to the model results from [36]. Left hand side: $I^{\odot}_{2c}(\Phi_{2c})$, right hand side: $I^{\odot}_{3c}(\Phi_{3c})$. Black stars: free proton data, red triangles: quasifree neutron data, full lines: 'restricted' model from [36], dashed lines: full model from [36].

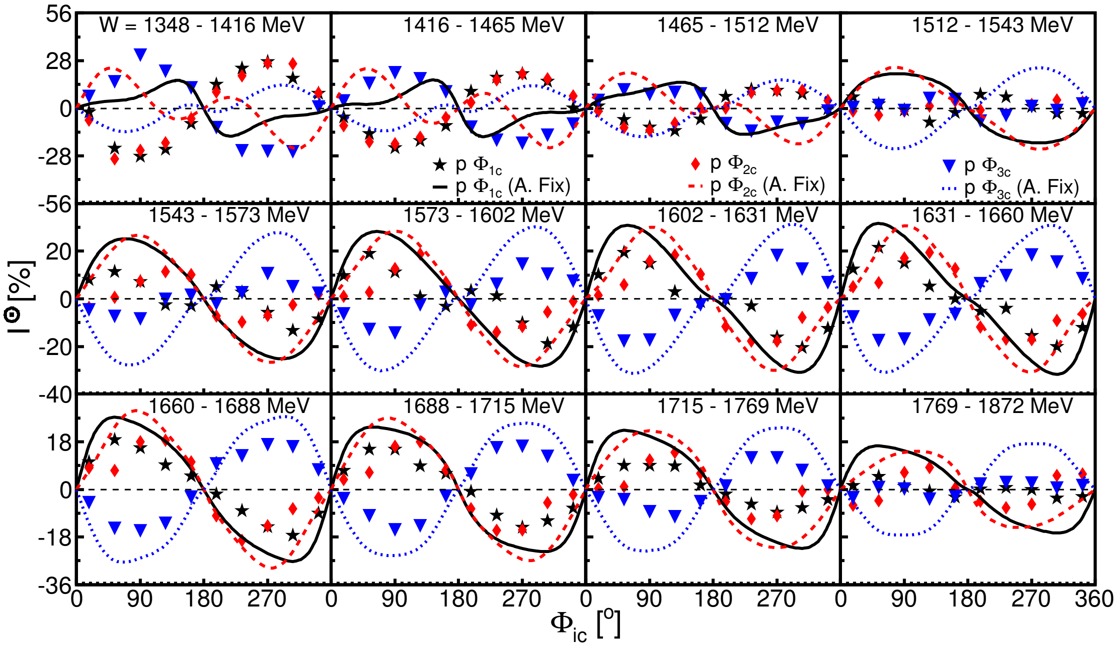

Fig. 5.16: Comparison of the three charge-ordered asymmetries $I^{\odot}_{nc}(\Phi_{nc})$ for the quasifree proton data. Black stars: $I^{\odot}_{1c}(\Phi_{1c})$, red diamonds: $I^{\odot}_{2c}(\Phi_{2c})$, blue triangles: $I^{\odot}_{3c}(\Phi_{3c})$, full black lines: model results for $I^{\odot}_{1c}(\Phi_{1c})$, dashed red lines: model results for $I^{\odot}_{2c}(\Phi_{2c})$, dotted blue lines: model results for $I^{\odot}_{3c}(\Phi_{3c})$. All model results again from [36].

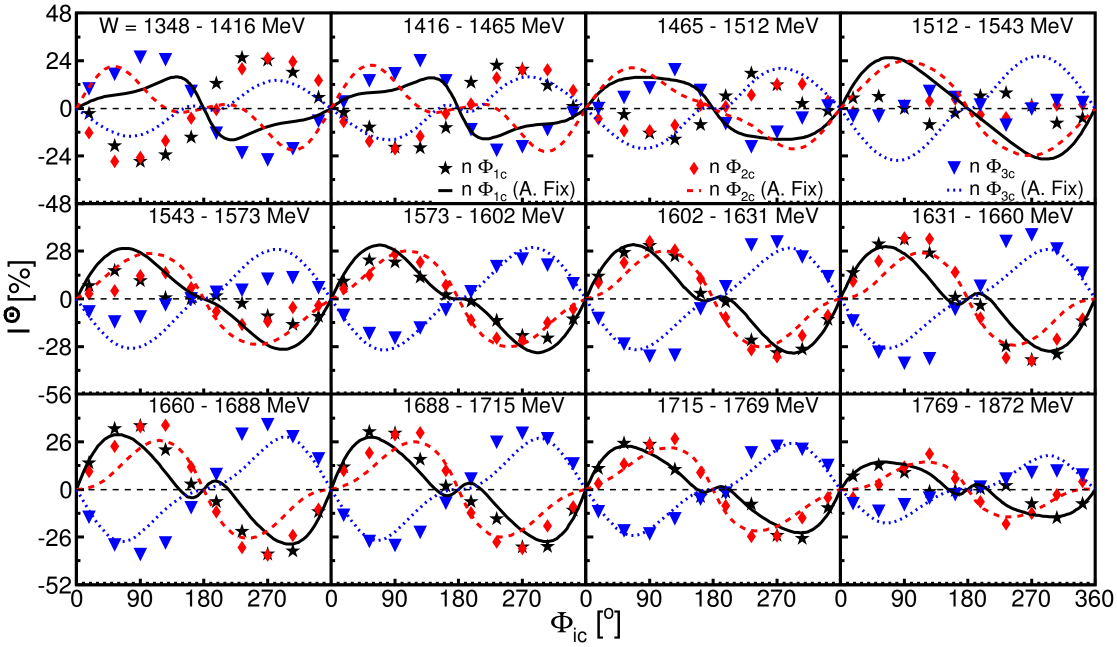

Fig. 5.17: Comparison of the three charge-ordered asymmetries $I^{\odot}_{nc}(\Phi_{nc})$ for the quasifree neutron data. Notation as in figure 5.16.

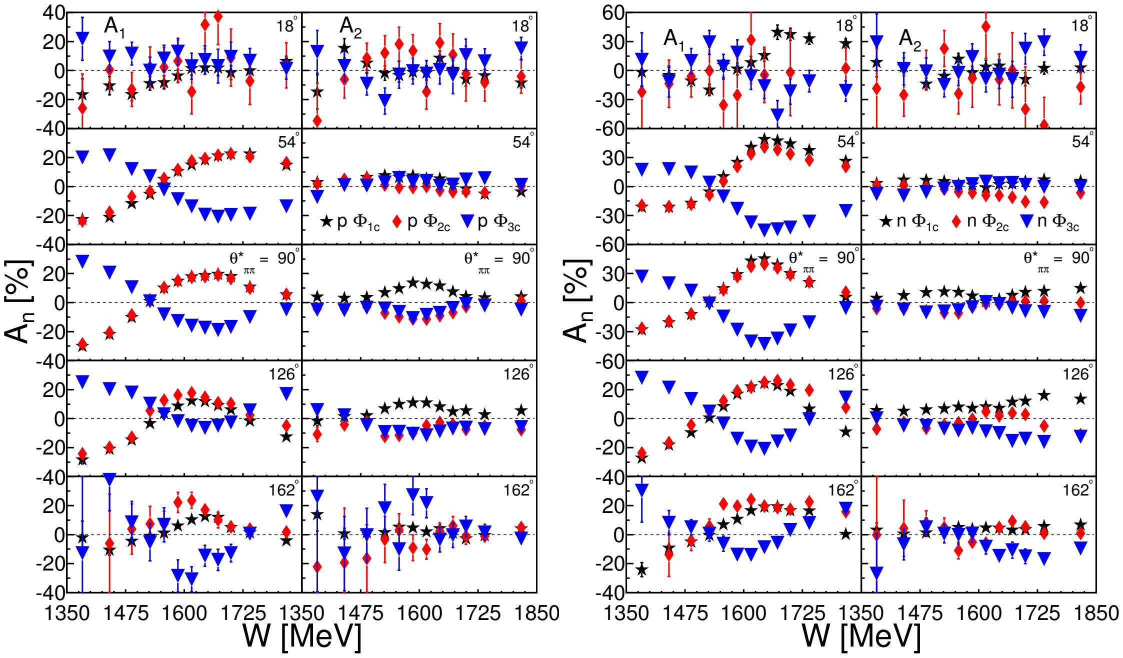

(a) (b)

Fig. 5.18: A_1 and A_2 coefficients for different bins of $\theta^*_{\pi\pi}$ for the three charge-ordered asymmetries $I^{\odot}_{nc}(\Phi_{nc})$ for all mixed-charge channels. Left hand side: quasifree proton data, right hand side: quasifree neutron data. Left columns: A_1 coefficients, rigth columns: A_2 coefficients. Black stars: $I^{\odot}_{1c}(\Phi_{1c})$, red diamonds: $I^{\odot}_{2c}(\Phi_{2c})$, blue triangles: $I^{\odot}_{3c}(\Phi_{3c})$. Curves: model results with same colo code.

In summary the following statements about all beam helicity asymmetry results shown in this section can be made:

- All asymmetries are sizable over the whole energy range and the statistical quality is very good.
- All asymmetries have been checked with equation 5.4 and parity conservation is always fulfilled within statistical errors.
- The agreement of free and quasifree proton results is excellent for all different asymmetries and for both isospin channels.
- The model calculations reproduce the neutral channel results better than the ones from the mixed-charge channels, where much more non-resonant background diagrams have to be included.

5.2 Cross Sections

In comparison to asymmetry results, where many systematic effects cancel in the ratio, and no total normalization is necessary, the extraction of cross section results is more delicate. In this section we will present total cross sections, compared to previous results and model calculations, as well as differential cross sections for both isospin channels. For the double π^0 channel as well as for the mixed-charge channels previous results exist from measurements on the free proton. They shall act as control for the analysis procedure, by comparing them to our free proton results.

For the results of this work the December 2007 beam time could not be included for the cross section observables, presented in this section 5.2. The reason for this are non-negligible descrepancies between the two quasifree beam times from 2009 and the one from 2007. These discrepencies are mostly due to the shifted PID position, which unfortunatelly could not be accurately corrected by the use of simulation and which was especially complicated for the nucleon detection efficiency correction (see section 4.11.2).

5.2.1 Total Cross Sections

The most classical observable for scattering and spectroscopy experiments is the total cross section σ. It is though experimentally rather difficult to extract due to the necessity of a correct total normalization and at the same time it does not hold very much detailed information about reaction processes and involved resonances.

The Neutral Channels

In figure 5.19 the total cross section results for all proton data is shown. It is compared to previous results from MAMI from [26], shown as full green stars and also from [26] shown as open red stars. Also plotted are two model predictions from A. Fix [36], based on the MAID model and plotted as dotted magenta curve and from A.V. Anisovich [87], based on the Bonn-Gatchina model and plotted as full blue curve. To check the analysis with the same conditions as for previous results, also an inclusive analysis was performed, where only the detection of the four decay photons of the two pions was mandatory, and the recoil nucleon detection was optional. The inclusive results are shown as full black dots and agree perfectly with the previous results from MAMI. The red triangles represent the exclusive measurement on the free proton and also agree reasonably well with the previous data. The small discrepancies in the second bump are clearly within the corresponding systematic errors, plotted as red shady area at the bottom. The blue triangles represent the quasifree proton results for the sum of the May 2009 and February 2009 beam time and the corresponding systematic errors are shown as blue shady area. They are slightly lower between 1450 and 1750 MeV, which could be from small effects from final state interaction or other effects, which are still not understood. Such discrepancies between free and quasifree proton data was also observed for many other meson channels, such as η photoproduction off ^{3}He or single π^0 photoproduction off deuterium, see for example [88] or [89].

The model calculations from [36] strongly underestimate the height in general, and especially in the low energy tail of the first bump, where only contributions from a few different resonances are possible, they fail completely to reproduce the experimental results. Only between 1500 and 1550 MeV a nice agreement is obtained, and this is also the region where the beam helicity asymmetry results are in quite good agreement.

A good interpretation of the latter observation is a clear dominance of one resonant contribution (most probably from $D_{13}(1520)$), and thus a less complicated situation with interferences and most probably also less non-resonant background contribution.

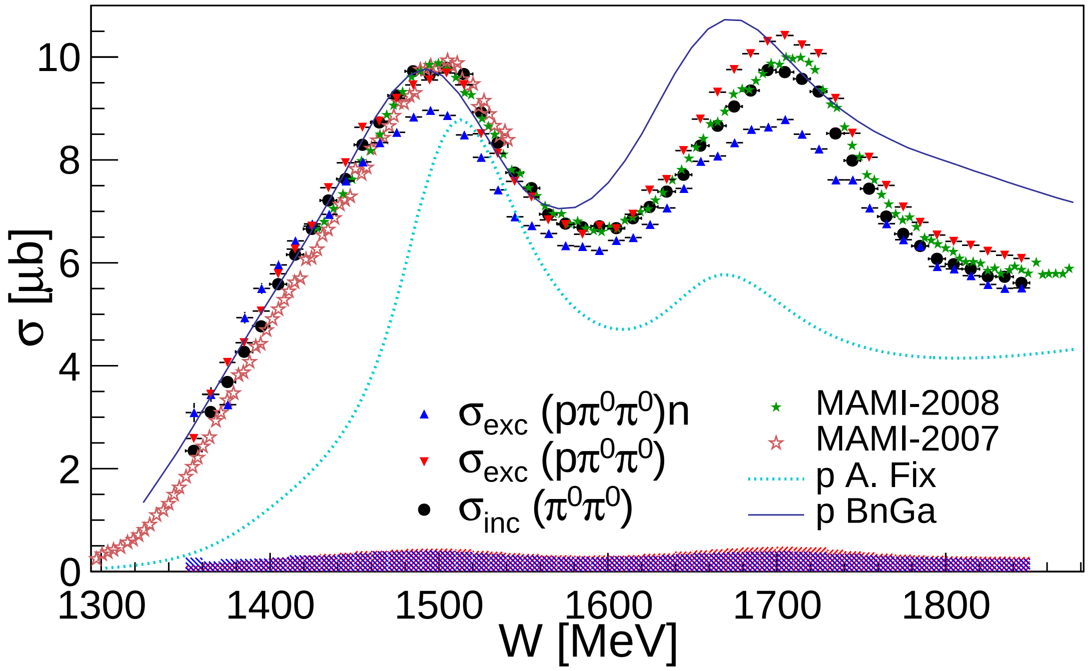

Fig. 5.19: Total cross section as function of the center-of-mass energy W for free and quasifree proton data. Black full dots: inclusive measurement on hydrogen $\gamma p \rightarrow \pi^0\pi^0(N)$, red triangles: $\gamma p \rightarrow \pi^0\pi^0 p$, blue triangles: $\gamma p(n) \rightarrow \pi^0\pi^0 p(n)$, green full stars: $\gamma p \rightarrow \pi^0\pi^0(p)$ data from [26], open red stars: $\gamma p \rightarrow \pi^0\pi^0(p)$ data from [26] (only up to 885 MeV in E_γ), dotted magenta line: model results from [36], full blue line: model results from [87].

The model results from [87] on the other hand are able to reproduce the experimental data very well up to about 1580 MeV and also reproduce the height of the second bump well, which was often a problem in previous models. But nevertheless, the agreement for higher energies is not very good and the position of the second bump is at too low energies in W. This observations can not be easily deduced from the results of the beam helicity asymmetries, where both model solutions achieve a good agreement with A_1 over the whole energy range, but rather poorly reproduce A_2 and A_3 at practically all energies.

In figure 5.20 the quasifree neutron results are compared to the ones from the quasifree proton. The results of the neutron, shown as red triangles show a less pronounced double bump structure than the proton results, shown again as blue triangles. Furthermore, the neutron data are in general slightly higher and seem to have different contributions in the region between the two bumps. This is also visible in the insert, where the ratio of the neutron and the proton cross section is shown. The ratio peaks around 1600 MeV and falls below one for low and high energies. The systematical errors are shown at the bottom, using the same color code as for the data points.

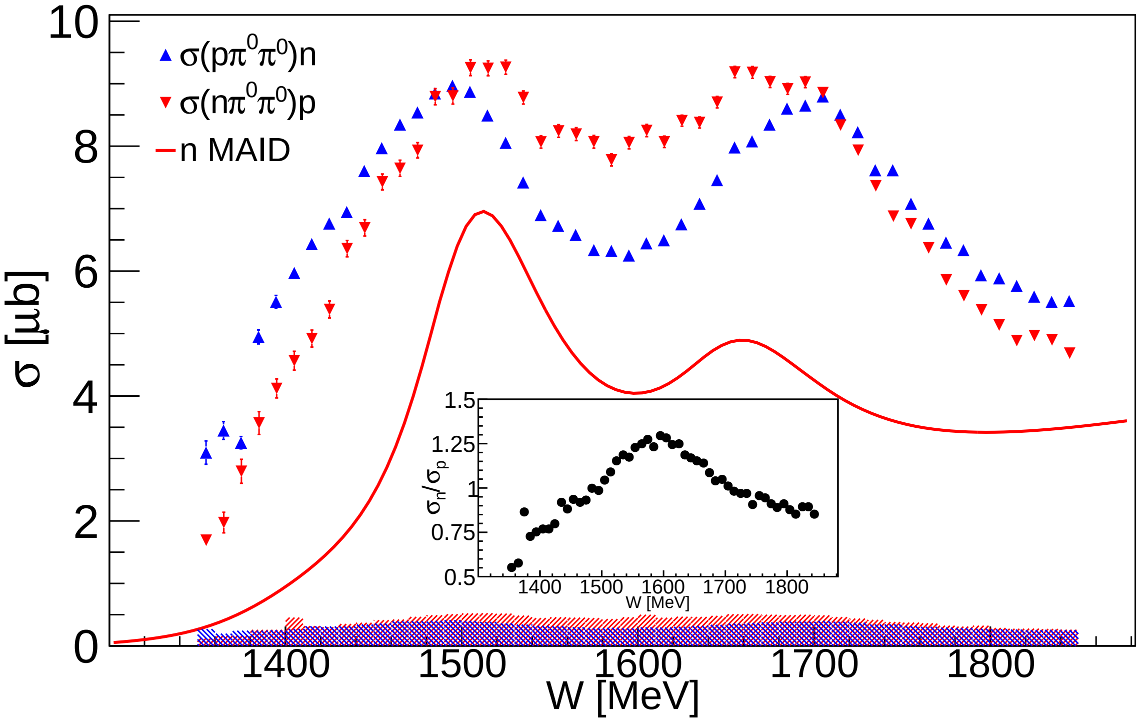

Fig. 5.20: Total cross section for $\gamma n(p) \rightarrow \pi^0\pi^0 n(p)$ compared to $\gamma p(n) \rightarrow \pi^0\pi^0 p(n)$ and model calculations from [36]. Red triangles: quasifree neutron data, blue triangles: quasifree proton data, full red line: model calculations for the neutron from [36], insert: ratio of proton and neutron cross section.

The model calculations for the neutron from A. Fix [36] are shown as full red line and as for the proton data clearly underestimate the experimental results. For the neutron case the agreement is worse than for the proton case, where an agreement around 1525 MeV could be observed. As for the proton, the model totally underestimates the third resonance bump.

The Mixed-charge Channels

For the total cross section of the mixed-charge channels no reasonable inclusive analysis could be performed, since only identifying two photons and one charged pion does not exclude a sufficient percentage of background. Therefore the exclusive measurement on the hydrogen had to serve as control for the analysis. For that matter, the center-of-mass energy was reconstructed in two different ways for the free proton data. Once directly from the energy of the incomming photon and once from the final state four-momenta, using the kinematic reconstruction of the kinetic energy of the nucleon.

In figure 5.21 the total cross section for all mixed-charge channels are shown as function of W. The black dots represent the free proton data with W reconstructed from E_γ and the cyan stars show the free proton data with a kinematic reconstruction of W. Previous results for $\gamma p \to \pi^+\pi^0(n)$ from F. Zehr [25] are shown as green diamonds and agree very good with the free proton data from this work. This shows that the analysis procedure can be trusted and that the kinematic reconstruction of W from the final state is not influenced by the energy resolution of the detector system for charged pions. If not mentioned otherwise, the W for the free proton data is always reconstructed from E_γ.

The quasifree proton results are very similar to the free one, but seem to be broadened around the maximum position. The quasifree neutron agrees well with the quasifree proton at lower energies but differs significantly towards higher energies. A possible explanation for the shape difference of free and quasifree results will be discussed in section 5.3.

The model results from [36] are very similar for proton and neutron and agree very well for the height of the cross sections. However, they somehow underestimate the steepness of the rise, and on the other hand overestimate the cross section at higher energies, where especially for the neutron the third resonance peak is expected to be seen in the model, but totally absent in the experimental data. This could be related to an old problem in nuclear physics and will be discussed in section 5.3. In general the model results are closer to the experimental data for the total cross section of the mixed-charge than for the one of the neutral channel. This comes obviously as a surprise, because as discussed in the first chapter, in calculations for the mixed-charge channels much more non-resonant background contributions have to be considered and thus the task is relevantly complicated.

The systematic errors for $\gamma p \to \pi^0\pi^+n$ were omitted in the figure in order to maintain transparency, but as shown in section 4.14.7, they are at the same level as the ones for the quasifree proton case.

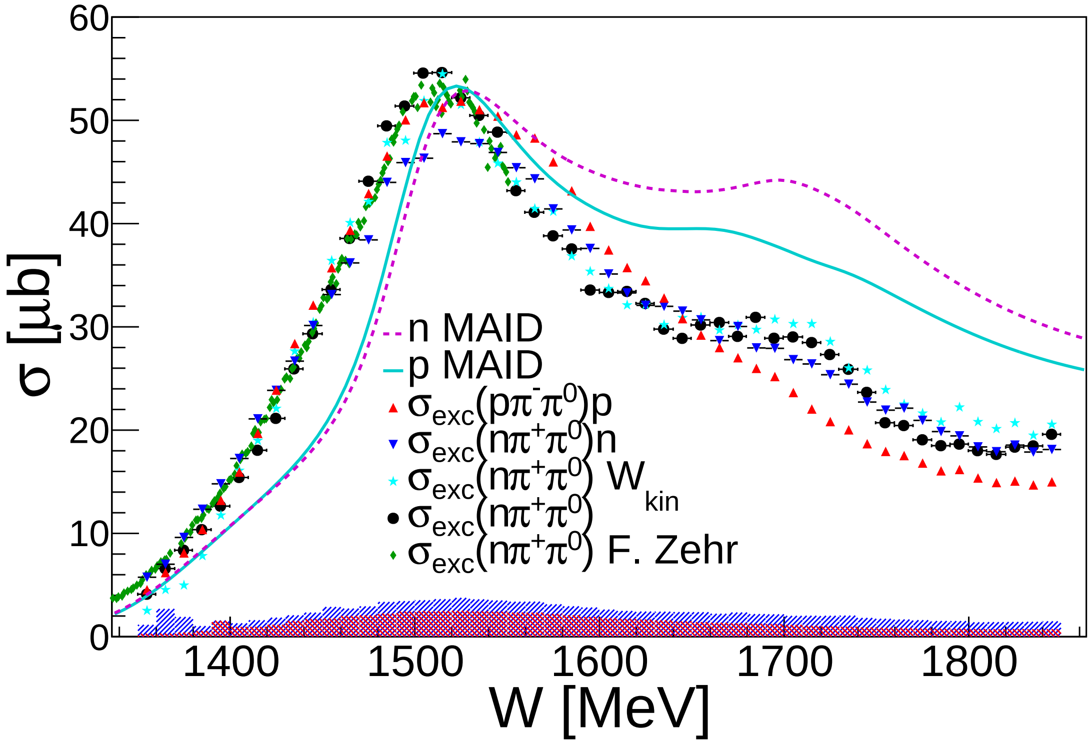

Fig. 5.21: Total cross section for all mixed-charge analysis channels as function of W. Black dots: $\gamma p \rightarrow \pi^0\pi^+ n$ of this work, cyan stars: $\gamma p \rightarrow \pi^0\pi^+ n$ of this work with kinematic reconstruction of W, green diamonds: inclusive measurement of $\gamma p \rightarrow \pi^+\pi^0 n$ from [25], blue triangles: $\gamma p(n) \rightarrow \pi^0\pi^+ n(n)$, red triangles: $\gamma n(p) \rightarrow \pi^0\pi^- p(p)$, full cyan line: proton results from [36], dashed magenta line: neutron results from [36]. The systematic errors for the quasifree proton is shown as blue and for the quasifree neutron as red shady area.

5.2.2 Angular Differential Cross Sections

A more detailed test for model calculations are differential cross sections. In this section the differential cross sections as function of $\cos(\theta^*_{\pi\pi})$ will be presented and compared to model calculations. For both isospin channels ten bins of $\cos(\theta^*_{\pi\pi})$ and 19 bins of W were chosen.

The Neutral Channels

In figure 5.22 the differential cross sections for all neutral channels are shown. The free inclusive and exclusive proton data, shown as black dots and green stars, agree very well, except for very forward angles, where again the nucleon detection efficiency leads to certain inaccuracies. The free and quasifree exclusive proton data are also in good agreement, and only differ in some energy bins at forward angles. The neutron results are very similar to the proton data at lower energies, but differ significantly at forward angles for higher energies.

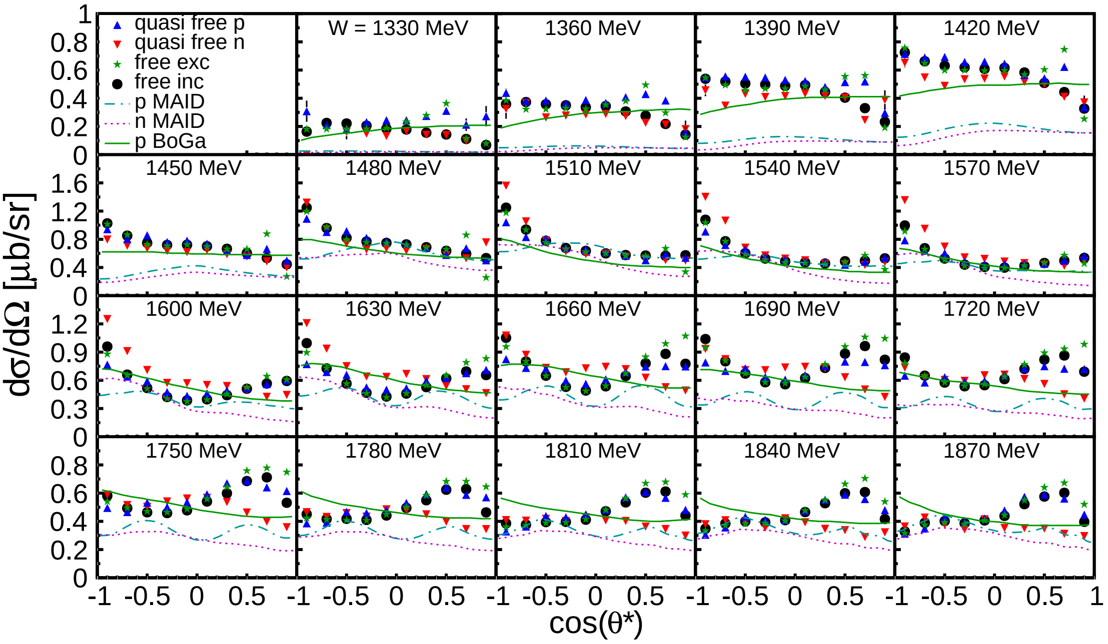

Fig. 5.22: Differential cross sections for 19 bins of the center-of-mass energy W as function of $\cos(\theta^*_{\pi\pi})$ for all neutral channel results. Black dots: free inclusive proton data, green stars: free exclusive proton data, blue triangles: quasifree proton data, red triangles: quasifree neutron data, full green curves: model results for the proton from [87], dash-dotted cyan curves: model results for the proton from [36], dotted magenta curves: model results for the neutron from [36].

The model results from [87] agreed well for the total cross section, where only for the higher energies some discrepancies were observed. For the reproduction of the differential cross section clear differences can be made out, especially for lower and higher energies. This fact shows that differential cross sections are a more detailed test for model calculations than the total cross sections. A very good agreement can be observed for energies from 1450 up to 1570 MeV, hence in the region of the first bump, where most probably one resonance contribution is dominating and implemented very accurately in the model. Especially at forward angles for higher energies, the reproduction of the experimental results is rather poor and the results of this work can give good input for further improvement of the model.

As already seen for the total cross section results of [36], the total height is completely underestimated by the model. The angular dependence is reproduced quite nicely in the first bump region, where the distributions are rather flat. For higher energies the proton results are completely off and can neither reproduce the distribution nor the total height of the experimental data. For the neutron results the angular dependence of the data is much better reproduced by the model. This could be accidental, since the shape of the neutron data is much flatter than the one from the proton, but nevertheless the results look quite promising and the data of this work should help to improve future results from this model.

The Mixed-charge Channels

In figure 5.23 the differential cross sections for all mixed-charge channels are shown and compared to model calculations from [36]. The free and quasifree proton data, shown as black dots and blue triangles, agree very well for low energies, up to 1405 MeV and for higher energies, from about 1550 MeV.

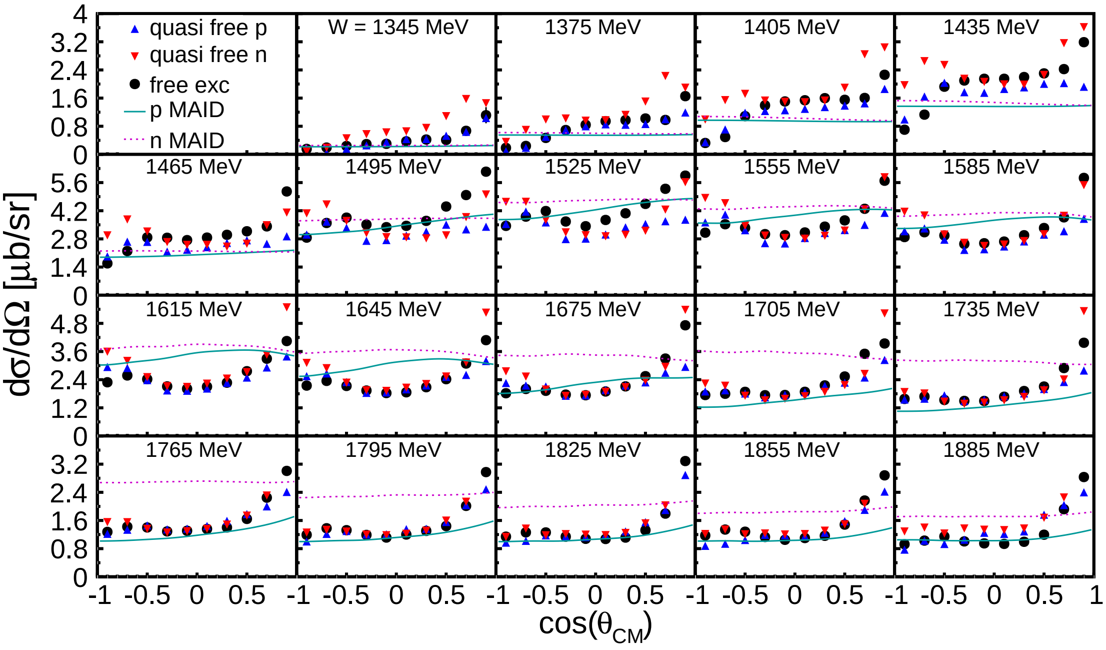

Fig. 5.23: Differential cross sections for 19 bins of the center-of-mass energy W as function of $\cos(\theta^*_{\pi\pi})$ for the mixed-charge channels. Black dots: free exclusive proton data, blue triangles: quasifree proton data, red triangles: quasifree neutron data, full cyan curves: model results for the proton from [36], dotted magenta curves: model results for the neutron from [36].

In between, the agreement is less good, especially at forward angles, and this is also reflected in the total cross section, where a broadened peak for the quasifree data was observed. To check if this broadening effect in the quasifree data could come from the reconstruction procedure of the center-of-mass energy, where the energy resolution of the charged pion is the critical part, also the free proton data was analyzed in this way, and a nice agreement between the two analysis methods for the free proton data was found (see 5.21). This excludes an artificial broadening of the quasifree data and the question of the source of this broadening remains an interesting topic and will be discussed in section 5.3.

For most energy bins the neutron and proton data are very similar, which is actually quite astonishing if one thinks of the results for the beam helicity asymmetry, where the difference between proton and neutron is larger in general.

Except for a few energy bins, the model results can not reproduce the experimental data at all and in most cases the distribution is very flat. The experimental results though show a strong dependence on the center-of-mass polar angle and will be challenging to reproduce for future model calculations. Especially the neutron results of the model are practically just flat and unable to reproduce the experimental data, even though the total cross section results were in reasonable agreement. This results clearly show, that the mixed-charge channels are still not well understood and more input is mandatory for the improvement of the models.

5.2.3 Mass Differential Cross Sections

For reactions with many meson final states mass differential cross sections can yield to some extend resonance contributions. For higher energies the sequential decays become visible in dominating resonance contributions.

The Neutral Channels

In figure 5.24 the invariant mass distributions of the pion-pion system are shown for 19 bins of W for all neutral channels. The free and quasifree proton data, shown as black dots and blue triangles, respectively are in good agreement. The quasifree neutron results are plotted as red triangles and show very similar distributions as the proton, except for three energy bins around 1630 MeV.

The full green curves represent the model results from [87] and have a very good agreement up to center-of-mass energies of about 1600 MeV. From here on up they slightly overestimate the experimental results, as it was also the case for the total cross section.

The model results from [36] are shown as dash-dotted cyan curves for the proton and as dashed magenta curves for the neutron. As a consequence of the underestimation of the total cross section, also the height of the mass distributions cannot be reproduced. The shape of the distributions though looks quite promising, but here it should also be mentioned that due to the impossibility of distinguishing the two pions, the distributions are very close to phase space, i.e., as if no sequential decay would occur, and the two pions would have been produced in a phase space like decay.

The invariant mass distributions of the nucleon-pion systems carry more information. They are shown in figure 5.25 for all neutral channels. The notation is the same as for the previous figure, and again a nice agreement of the free and quasifree proton results can be observed. The distributions have more pronounced structures than the ones from the pion-pion invariant mass distributions. A clear structure

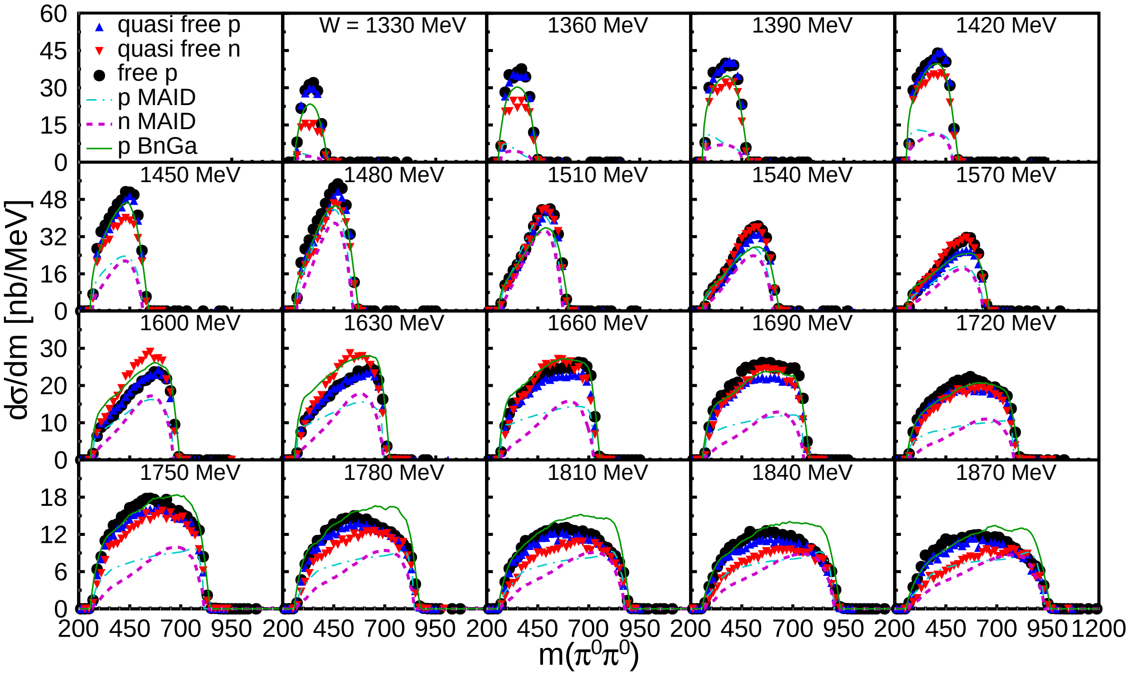

Fig. 5.24: Differential cross sections for 19 bins of the center-of-mass energy W as function of the invariant mass of the pion-pion system for all neutral channels. Black dots: free exclusive proton data, blue triangles: quasifree proton data, red triangles: quasifree neutron data, dash-dotted cyan curves: model results for the proton from [36], full green curves: model results for the proton from [87], dashed magenta curves: model results for the neutron from [36].

around the mass of the $\Delta(1232)$ resonance is visible throughout all energy bins. Towards higher energies a second structure appears at a mass around 1530 MeV, showing contributions from sequential decays via a resonance with a higher mass than the $\Delta(1232)$. As we have seen in the introduction of this work, contributions from the $D_{13}(1520)$ have been discussed intensively during the past years and could also be confirmed in different experiments. Consequently, the second peak in the invariant mass distributions could come from sequential decays via the $D_{13}(1520)$ resonance.

Interestingly, the appearance of the second peak comes already at lower energies for the neutron than for the proton (especially visible at $W = 1660$ MeV). Already at 1600 MeV in W the structure shows a small second peak, and it seems to lie around 1400 MeV. This would indicate possible contributions from the $P_{11}(1440)$ resonance. At the same time the proton shows stronger contributions from the higher lying resonance than the neutron, clearly visible in the four highest energy bins. Even though the differences between proton and neutron are rather small, they are still remarkable and it would be interesting to see if other (than [36]) theoretical models could reproduce this fact. This observation is consistent with the experimental results for the beam helicity asymmetry, where the difference

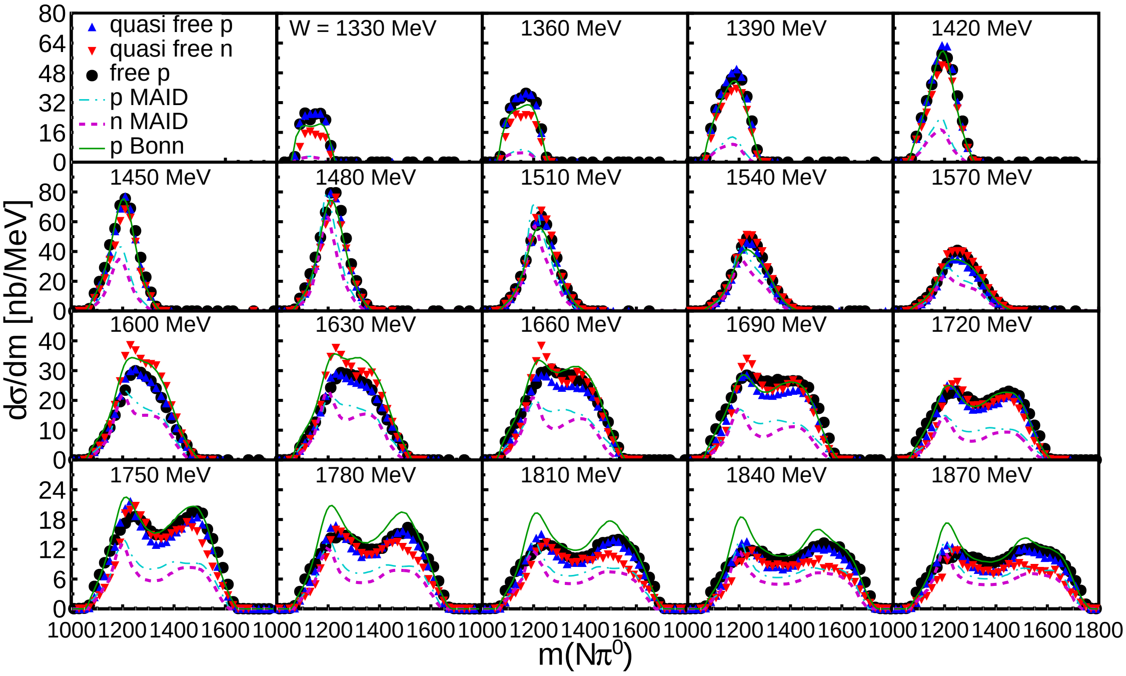

Fig. 5.25: Differential cross sections for 19 bins of the center-of-mass energy W as function of the invariant mass of the pion-nucleon system for all neutral channels. Black dots: free exclusive proton data, blue triangles: quasifree proton data, red triangles: quasifree neutron data, dash-dotted cyan curves: model results for the proton from [36], full green curves: model results for the proton from [87], dashed magenta curves: model results for the neutron from [36].

between proton and neutron results also peaks around 1650 MeV in W (see figure 5.9). Also for the total cross section results the same behavior was observed and different contributions for proton and neutron in this energy region can be assumed. Having not only calculations from one model for the neutron would allow to study this fact and draw conclusions regarding the different contributions that lead to the diverging in the observables. Unfortunatelly, [87] does not provide yet calculations for the neutron and the interpretation of the results has to rely on the model calculations from [36], and thus only few conclusions can be drawn.

For the proton on the other hand [87] provides very good calculations, which also agree perfectly for the mass differential cross sections up to about 1750 MeV. For the highest energy bins it seems as if the model results would slightly overestimate the contributions from the sequential decay via Δ or $D_{13}(1520)$.

The model results from [36] are of course still too low, but reproduce the differences between proton and neutron quite well. As for the experimental data, the neutron shows a stronger contribution of a higher lying resonance already at about 1630 MeV, whereas the proton is still dominated by the $\Delta(1232)$ contribution at this energy. This observations should allow to identify certain resonance contributions on the theory side by carving out the different inputs for the calculations of proton and neutron in these energy regions.

The proton is experimentally and theoretically much better explored than the neutron and consequently, one expects also better model results for the proton. For the model calculations from [36] for the double π^0 channel though the proton and neutron calculations show about equal agreement, and this allows to make two different assumptions. On the one hand, it is possible that the difference in resonance contributions for the calculation of proton and neutron results is only minor and this small difference is well implemented in this model. On the other hand though one could argue that neither the proton nor the neutron data are very accurately reproduced (height) by the model results and as such the practically equal 'agreement' for proton and neutron is rather by chance.

As we have seen for the beam helicity asymmetry results of the double π^0 channel, proton and neutron are similar for the experimental data, but are completely different for the model results towards higher energies. For the cross section observables from this chapter though, the model calculations for proton and neutron are rather similar. It seems as if one of these presumably small differences in the model for the two nucleons lead to large effects for the beam helicity asymmetry. This fact shows again the huge sensitivity of polarization observables to small details in the reaction mechanisms.
The ratio of the helicity amplitudes for a coupling of the $N_{11}(1440)$ to γp or γn, respectively was determined in [90] as

$$\frac{A_{1/2}(N_{11}(1440) \to p\gamma)}{A_{1/2}(N_{11}(1440) \to n\gamma)} \approx \frac{0.06 \pm 0.004}{0.04 \pm 0.010}. \tag{5.6}$$

This clearly does not favor a stronger contribution of the Roper for $\gamma n \to \pi^0\pi^0 n$ than for $\gamma p \to \pi^0\pi^0 p$ and the observation can not be explained this way. This would thus mean that the difference in the mass distributions for proton and neutron stem from another resonance or a different interference of background contributions. In this energy region also a contribution from the unknown narrow structure, observed in the η photoproduction on the neutron at about 1670 MeV is possible. In a sequential decay $\gamma n \to R \to P_{11}(1440)\pi^0 \to \pi^0\pi^0 n$, where R represents this narrow structure, the helicity amplitudes for proton and neutron for a coupling to the Roper resonance become irrelevant and the difference between the nucleons could in fact be explained by a contribution of the $P_{11}(1440)$.

Applying a cut on the invariant mass distribution of the pion-nucleon system from 1310 to 1430 MeV (on the structure that is visible at 1660 MeV) allows to further investigate this hypothesis. The total cross section on the neutron for events with $m(N\pi^0)$ between 1310 and 1430 MeV is shown in figure 5.26, and compared to the cross section from 5.20.

Already the original cross section data, shown as black dots seem to have some

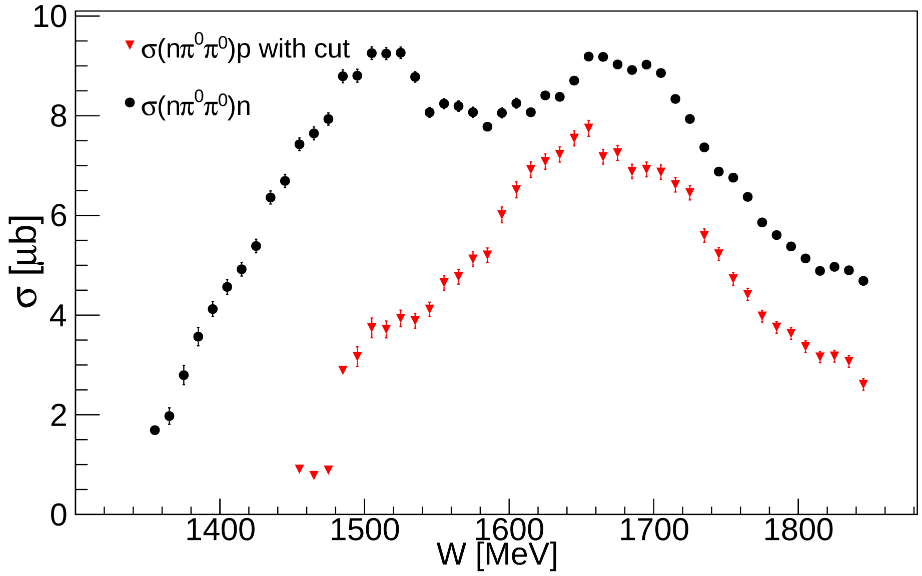

Fig. 5.26: Total cross section for the reaction on the neutron with cut on $m(N\pi^0)$. Black dots: original neutron, red triangles: results with cut on $m(N\pi^0)$.

sort of structure around 1670 MeV. It has to be mentioned though, that this structure is within the flactuations observed over the whole energy range and it is most probably an effect of the analysis. The cross section results with the cut on the nucleon-pion invariant mass are shown as red triangles. The structure around 1660 MeV seems to remain unchanged by the applied cut and a coupling of the unknown structure to the double π^0 channel cannot be confirmed.

The Mixed-charge Channels

Even more information is carried by the invariant mass distributions of the mixed-charge channels, since the two pions are always distinguishable. In figure 5.27 the distributions of $m(\pi^{\pm}\pi^{0})$ for all mixed-charge channels are shown for 19 bins of W.

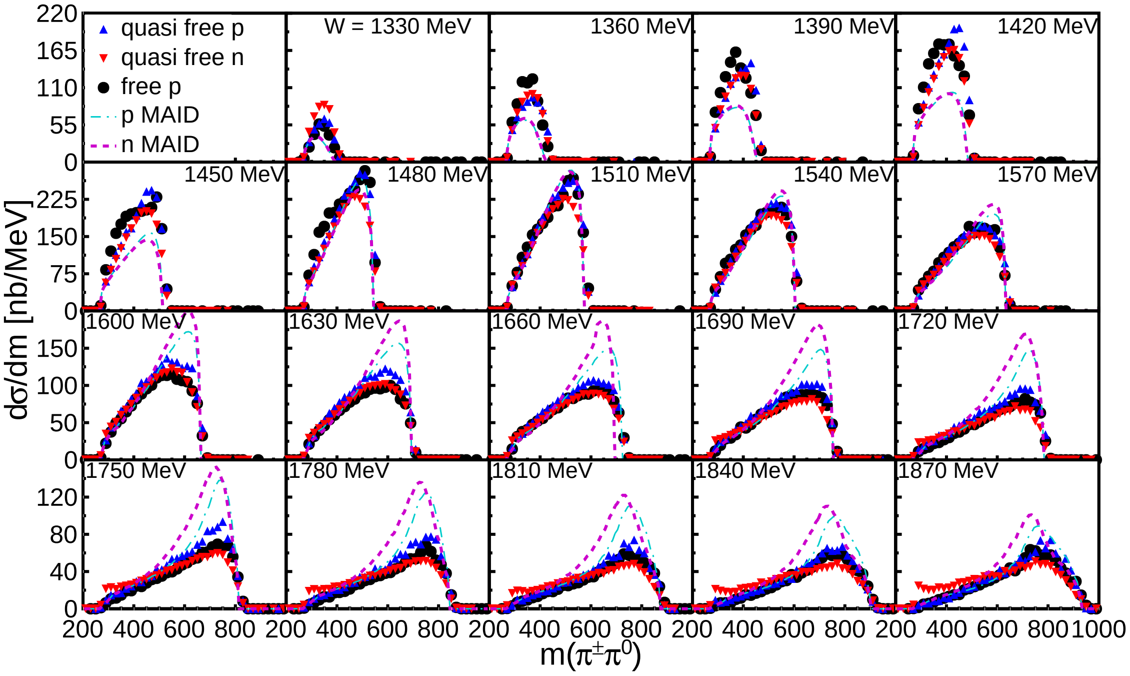

Fig. 5.27: Differential cross sections for 19 bins of the center-of-mass energy W as function of the invariant mass of the pion-pion system for all mixed-charge channels. Black dots: free exclusive proton data, blue triangles: quasifree proton data, red triangles: quasifree neutron data, dash-dotted cyan curves: model results for the proton from [36], dashed magenta curves: model results for the neutron from [36].

As for the total cross section results, the free and quasifree proton results, shown as black dots and blue triangles, do not agree in height for all energy bins, but show a very similar shape. At low energies the distributions show no significant structure and resemble the ones from the neutral channels. Already at about 1450 MeV the distributions get asymmetric and seem to have some contributions from the ρ meson, which has an invariant mass of about 775 MeV[1], but due to its very large width can also spread down to much lower masses. Towards the highest energies this contribution appears even more clearly, and seems to be equal for proton and neutron. The neutron data has a very steep rise at low invariant masses for higher W bins, which does not appear in the proton data. For lower energies all three channel results show steep rises at low invariant masses, but for

---

[1] According to the Partcile Data Group [74] the ρ has a mass of 775.11 ± 0.34 MeV and a width of 147.8 ± 0.9 MeV

both proton data it flattens towards higher energies, whereas for the neutron it gets even more prominent.

The model results from [36] are able to reproduce the data quite well up to about 1570 MeV and even perfect agreement is reached between 1480 and 1540 in W. This could be the imprint of the $D_{13}(1520)$ resonance, which is supposed to dominate in this energy region and has also strong contributions in the model. For higher energies the model overestimates the distributions.

Here the model results show very strong contributions from the sequential decay $D_{13}(1520) \to \rho N \to \pi^{\pm}\pi^0 N$, whereas this ρ meson contribution is much weaker in the experimental data. This results will clearly help to improve the model. It seems as if the only problem in the model for this observable is an overestimation of the ρ meson contribution.

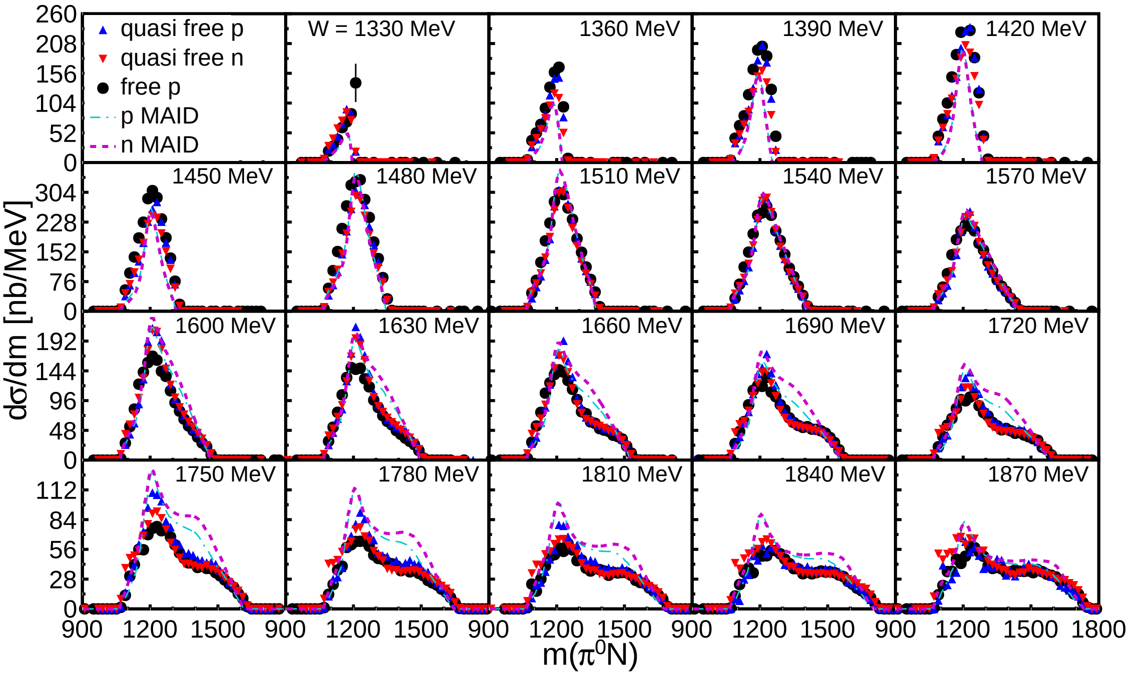

Fig. 5.28: Invariant mass distributions as function of the π^0-nucleon mass for all mixed-charge channels. Black dots: free exclusive proton data, blue triangles: quasifree proton data, red triangles: quasifree neutron data, dash-dotted cyan curves: model results for the proton from [36], dashed magenta curves: model results for the neutron from [36].

The invariant mass distribution of the π^0-nucleon system is shown in figure 5.28 for all mixed-charge channels. At low energies again no specific structure is visible and quasifree proton and neutron and the free proton results agree well. Above 1570 MeV a considerabley dominant contribution from the $\Delta(1232)$ resonance is visible, i.e., the π^0 meson stems predominantly from a decay of a $\Delta(1232)$ resonance.

Towards higher energies the neutron results show again a very sharp rise at the lowest invariant masses. A first assumption was, that this comes from systematic effects from the detector thresholds. But even changing the applied thresholds did not influence this structure visibly and hence a clear difference between proton and neutron data at low invariant mass is really existing.

At last the differential cross sections as function of $m(\pi^{\pm}N)$ are shown for the mixed-charge channels in figure 5.29. The agreement between the free and quasifree proton data, shown again as black dots and blue triangles is good. According to the total cross section results, differences are visible in the peak region, i.e., around 1450 MeV in W, where the free proton is clearly higher. Unlike for the neutral channel, the neutron results are very similar to the one from the proton and again only differ at high energies and low invariant masses, where the neutron data has a sharp rise.

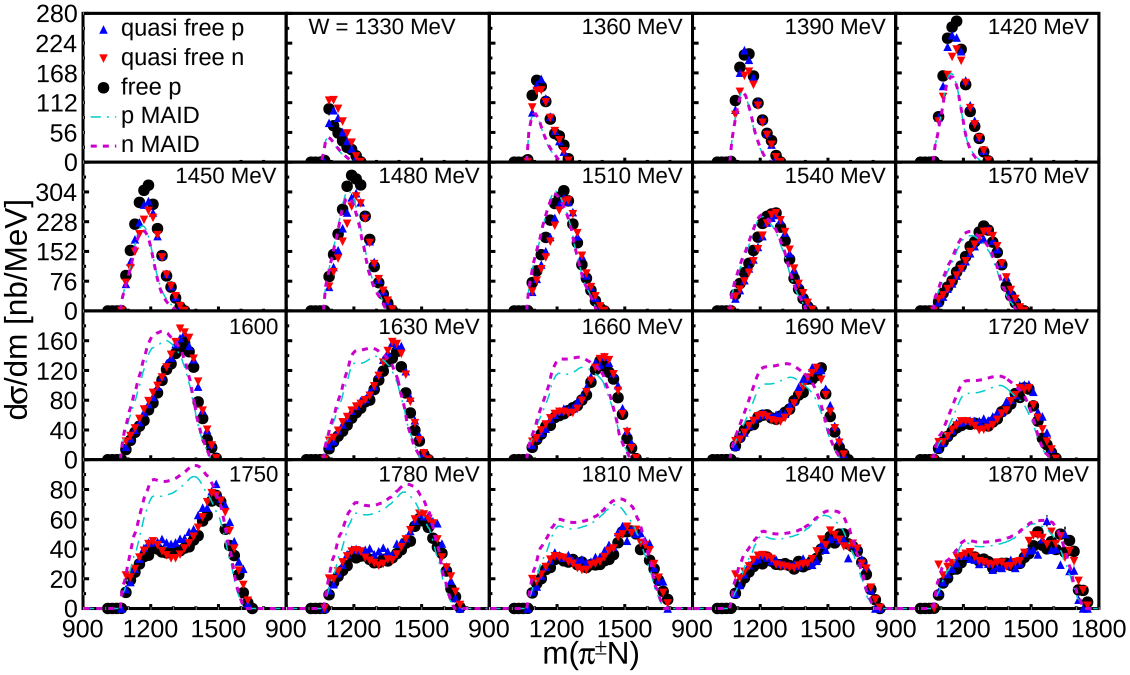

Fig. 5.29: Invariant mass distributions as function of the $\pi^{\pm}$-nucleon mass for the mixed-charge channels. Black dots: free exclusive proton data, blue triangles: quasifree proton data, red triangles: quasifree neutron data, dash-dotted cyan curves: model results for the proton from [36], dashed magenta curves: model results for the neutron from [36].

The model results from [36] have again a perfect agreement with the experimental data in the region of the peak in the total cross section. At lower energies the distributions are too low and towards higher energies they overestimate again the total height. As a logical consequence of the overestimation of the $D_{13}(1520)$ contributions for $m(\pi^0N)$ (figure 5.28) and the ρ meson contribution in $m(\pi^0\pi^{\pm})$ (figure 5.27), an overestimation of the Δ contribution is now observed.

The agreement of experimental data and model calculations for the mixed-charge channel depends strongly on the observable. The total cross section for example is even better reproduced for the mixed-charge channel than for the neutral channel by the calculations of [36]. The angular and mass differential cross sections are about euqally reproduced for the two isospin channels. However, the beam helicity asymmetry data is much better reproduced for the neutral channel than for the mixed-charge channel. This is astonishing since the neutral channel has only a small amount of possible contributions at lower energies, and thus an agreement for the cross section calculations could be expected at low energies. For the calculations of the mixed-charge channel on the other hand lots of non-resonant background terms have to be considered, and the calculations are much more complicated. The model results for the total cross section of the mixed-charge channel though reasonably reproduce the experimental data at lower energies.

As mentioned in the introduction, the height difference of the three double pion cross sections ($\sigma_{\pi^+\pi^-} \approx 75$ μb, $\sigma_{\pi^\pm\pi^0} \approx 55$ μb, $\sigma_{\pi^0\pi^0} \approx 10$ μb) already hints at strong non-resonant background contributions for the charged and mixed-charged double pion channels. It seems as if these large background contributions are quite well implemented in the model, but not so their individual percentages, since for the results of the more sensitive beam helicity asymmetry the model results have a rather poor agreement.

In the following section the most interesting observations will now be summarized and some of them discussed in more detail.

5.3 Discussion

At first an overview of all measured observables from the last section is given in a summary in section 5.4 followed by a discussion of the most interesting observations in section 5.5.

5.4 Summary

$I^{\odot}_{1r}(\Phi_{1r})$ for the neutral channels

For the randomized beam helicity asymmetry of the neutral channel, sizable asymmetries have been measured. Not only do quasifree and free proton data agree well, but astonishingly, also the neutron is in good agreement with the proton. The model from A. Fix [36] can reproduce the proton data quite well up to about 1600 MeV but fails for the higher energies and for the neutron results.

$I^{\odot}_{1m}(\Phi_{1m})$ for the neutral channels

The asymmetries for the mass-ordered pions of the double π^0 channels are even larger than for the randomized pions, but proton and neutron data still agree surprisingly good. The two model solutions for the proton from [87] agree quite well with the experimental data. The overall agreement of the model results from [36] with experimental data is rather poor, but still slightly better for the proton than the neutron.

$I^{\odot}_{1m}(\Phi_{1m})$ for the mixed-charge channels

The agreement for neutron and proton data is not as good as for the neutral channel. The model results from [36] show a rather poor agreement with the experimental data.

$I^{\odot}_{1c}(\Phi_{1c})$ for the mixed-charge channels

The odd parameters are within statistical errors in good agreement with the ones from $I^{\odot}_{1c}(\Phi_{1c})$. The model results from [36] can not reproduce the experimental data.

$I^{\odot}_{2c}(\Phi_{2c})$ and $I^{\odot}_{3c}(\Phi_{3c})$ for the mixed-charge channels

These two asymmetries have never been measured before and have no connection to $I^{\odot}_{1c}(\Phi_{1c})$ according to A. Fix. Though it seems as if for the A_1 coefficients $A_1(I^{\odot}_{1c}) \approx A_1(I^{\odot}_{2c}) \approx -A_1(I^{\odot}_{3c})$ holds true within small fluctuations.

$\sigma(W)$ for the neutral channels

Previous results from the free proton could be nicely reproduced. The quasifree proton data is about 10 % lower between 1450 and 1750 MeV but agrees at the energy limits. The neutron cross section shows a less pronounced double bump structure than the proton and is especially higher between 1500 and 1720 MeV.

$\sigma(W)$ for the mixed-charge channels

The previous results from free proton measurements are in good agreement with the present results. The two reconstruction methods for W, used for the free proton data do not lead to significant differencies. Quasifree proton and quasifree neutron data show a broadened peak with a lower height than the free proton data. This could come from in-medium modification of the involved resonances in larger nuclei, as it was already discussed years ago. A discussion about this follows in the next section.

$d\sigma/d\Omega$ for the neutral channels

The agreement of free and quasifree proton data is quite good, except from some energy bins, where the extreme forward angles still suffer a bit from the nucleon detection efficiencies. At lower energies the proton and neutron results agree well, but do less so for higher energies, where the neutron has a rather flat distribution. The model results from [36] and [87] can reproduce the data well around 1570 MeV but not so for the other energies.

$d\sigma/d\Omega$ for the mixed-charge channels

The free and quasifree proton data disagree at low energies and forward angles but show good agreement for higher energies. The shape of neutron and proton data is quite similar over the whole energy range. The model calculations from [36] is not reproducing the experimental data and in general too flat.

$d\sigma/dm$ for the neutral channels

Free and quasifree proton data agree well over the whole energy range. The neutron data differs visibly at higher energies for the $m(\pi^0)N$ distributions. Clear contributions from a structure with a mass of about 1400 MeV appear for the neutron data, but not as strong for the proton data. A possible coupling of the unknown narrow structure from $\gamma n \rightarrow \eta n$ could not be confirmed. At higher energies non of the models can accurately reproduce the experimental data.

$d\sigma/dm$ for the mixed-charge channels

In all of the three different mass distributions a clear contribution from the sequential decay $D_{13}(1520) \rightarrow \rho N \rightarrow \pi^0\pi^\pm N$ is visible. The dominance of the 'first sequential decay' is confirmed by the data. Interestingly the neutron and proton data always differ at higher energies, where the neutron shows a very sharp rise at low invariant masses, which is not observed for the proton. The model from [36] overestimates the contribution from a decay via the ρ meson.

5.5 Interesting Observations

In this final section the most interesting discoveries shall be emphasized again, and if possible connections to theory or previous results shall be derived. For both cases no final conclusion can be drawn, but the discussions shall motivate future exploration of these hints on the experimental, as well as on the theory side.

5.5.1 Similarity of Proton and Neutron

In the results for the beam helicity asymmetry for the neutral channel a surprising similarity between proton and neutron data was observed and this not only for the simpler case of randomized pions, but also for the mass-ordered asymmetry

$I^{\odot}_{1m}(\Phi_{1m})$ (see figure 5.9). The model results from [36] does have very similar A_1 coefficients for proton and neutron, but the A_2 coefficients differ significantly over the whole energy range. Unfortunately, no model results from A.V. Anisovich ([87]) are available up to now for the reaction on the neutron, and thus the only information for possible explanations has to come from [36]. Using model calculations with switched off background or resonance contributions for proton and neutron would maybe shed some light on this issue and allow to detect dominant contributions, which make the difference between proton and neutron results. This way wrongly weighted contributions for the neutron model could be found and the model could be improved.

In the case of the mixed-charge channel the agreement between proton and neutron for the beam helicity asymmtery is clearly worse. However, all cross section observables of the mixed-charge channel are very similar for the two nucleons. For this channel further effort on the theory side is highly desirable. Not only calculations for $\gamma p \rightarrow \pi^0\pi^+ n$ but also for $\gamma n \rightarrow \pi^0\pi^- p$ are needed and would help to interpret the measured observables and extract resonant contributions.

Very recent calculations from [36] for the beam helicity asymmetry with 'switched off' non-resonant background contributions showed practically no asymmetry for proton and neutron over the whole energy range. Consequently, the asymmetry is produced by the non-resonant background terms. A similar investigation for the neutral channel would be very interesting, since less background terms can contribute and thus the extraction of the contributions leading to the asymmetry should be much simpler.

5.5.2 In-medium Modification of Resonances

The total photoabsorption on the proton and the neutron show clear structures, called the first, second and third resonance region. This is visible in figure 5.30, where especially for the absorption on the proton three clear peaks are visible.

In figure 5.31 the total photoabsorption on the proton is shown again, but this time the so far known contributions from the different meson decay channels are drawn. For example the first resonance peak is clearly dominated by single pion production and the strongest contribution comes from the single π^0 channel, indicated as red open circles. In the second resonance region the reaction $\gamma p \rightarrow \pi^0\pi^+ n$, shown as full blue dots makes a large part of the total signal and only the contributions from $\gamma p \rightarrow \pi^+ n$ and $\gamma p \rightarrow \pi^+\pi^- p$, shown as red full dots and blue full squares are stronger.

Measurements of the photoabsorption on different nuclei, such as ^{7}Li, Be, C, Al, Cu, Sn, Pb, ^{238}U [92, 93, 91] led then to an astonishing discovery. The peaks of the second and third resonance region are strongly suppressed. This is shown in figure 5.32, where the total photoabsorption cross section per nucleon for Be and

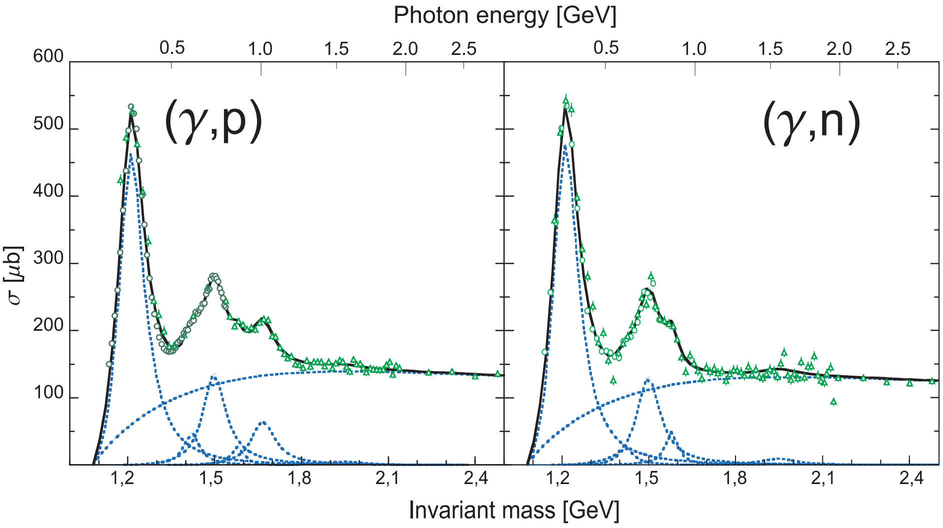

Fig. 5.30: The total photoabsorption spectra for proton and neutron. The first resonance region is dominated by the $\Delta(1232)$ resonance, the second resonance region mainly by the $D_{13}(1520)$ and the third resonance region by the $F_{15}(1580)$, where the last one is supposed to dominate only for the proton. Taken from [7].

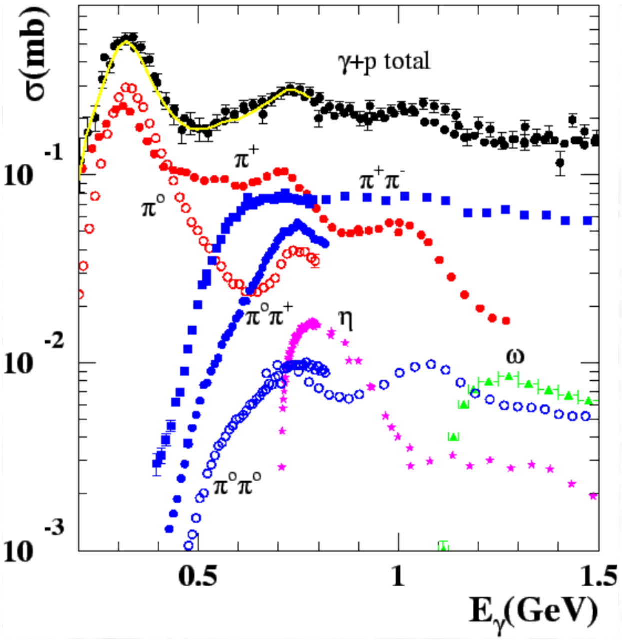

Fig. 5.31: The total photoabsorption spectra for proton with indicated channel contributions. In the third and especially the second resonance region the $\pi^0\pi^0$ channel, shown as open blue circles and the $\pi^{\pm}\pi^0$ channel, shown as full blue circles are contributing significantly to the total signal.

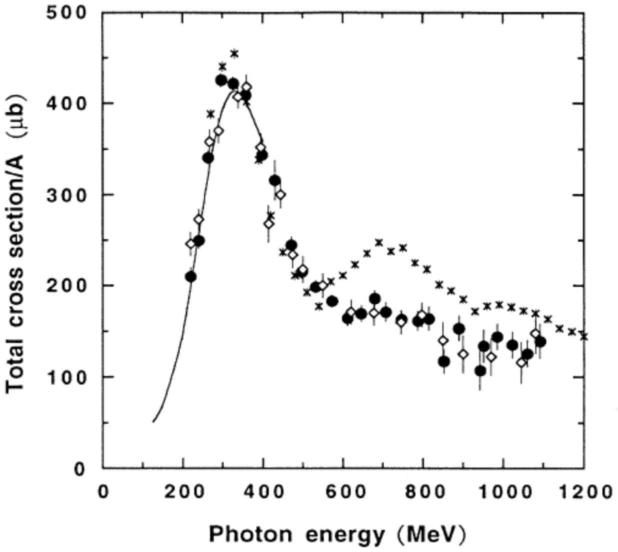

Fig. 5.32: The total photoabsorption cross section per nucleon for Be and C compared to the one on the proton. Full circles: Be, open diamonds: C, crosses: ^{2}H. Taken from [91].

C are compared to the one on the free proton. Interestingly the peak of the first resonance region is practically unchanged, whereas the second and third resonance peak vanish completely. For the second resonance peak the main assumption at this time was an in-medium modification of the $D_{13}(1520)$ resonance, which would presuppose an in-medium modification of the ρ meson. This topic has been intensively discussed and many experiments have been dedicated to investigate mass shifts or broadening of the ρ meson in nuclear matter. But since no significant effects could be detected this issue remained unsolved.

In the results for the total cross section of the mixed-charge channels a clear broadening of the quasifree cross section of the proton compared to the case of the free proton could be observed. Since this broadening effect is not coming from the reconstruction method, but has to come from nuclear effects, the question of the source for this effect still remains interesting. From the results of the mass differential cross sections for the mixed-charge channel significant contributions from the sequential decay of the $D_{13}(1520)$ via the ρ meson can be assumed. The results of this work hint again at in-medium effects. The fact that the measurements were performed with a deuteron target are clearly interesting. If this effect comes from in-medium modification of the ρ meson, it comes as a surprise that it is already seen on the very light deuteron nucleus.

Further inverstigations of the mixed-charge channels with quasifree reactions should help to clarify the role of the $D_{13}(1520) \rightarrow \rho N \rightarrow \pi^0\pi^\pm N$ and additionally maybe reignite the discussion and investigation of in-medium modification of the ρ meson.

References

[1] F. Zehr, *Double pion photoproduction off the proton at threshold and in the second resonance region*, Ph.D. thesis, Universität Basel (2008).

[2] F. X. Lee, D. B. Leinweber, L. Zhou, J. M. Zanotti and S. Choe, *N^* Masses from an Anisotropic Lattice QCD Action*, Nucl. Phys B (Proc. Suppl.) **106**, 248 (2002).

[3] D.G. Richards, *Excited nucleon spectrum using a non-perturbatively improved clover fermion action*, Nucl. Phys B (Proc. Suppl.) **94**, 206 (2001).

[4] Ch. Chen et al., *Spectrum of Hadrons with Strangeness*, Few-Body Systems **53**, 293 (2012).

[5] G. Eichmann, *From quarks and gluons to baryon form factors*, Prog. Part. Nucl. Phys. **67**, 234 (2012).

[6] I.G. Aznauryan et al., *Studies of Nucleon Resonance Structure in Exclusive Meson Electroproduction*, Int. J. Mod. Phys. **22**, 1330 (2013).

[7] B. Krusche and S. Schadmand, *Study of non-strange baryon resonances with meson photoproduction*, Prog. Part. Nucl. Phys. **51**, 399 (2003).

[8] M. Benmerrouche, N. C. Mukhopadhyay and J. F. Zhang, *Effective Lagrangian approach to the theory of η photoproduction in the $N^*(1535)$ region*, Phys. Rev. D **51**, 3237 (1995).

[9] D. Drechsel and L. Tiator, *Threshold pion photoproduction on nucleons*, J. Phys. G **18**, 449 (1992).

[10] G. F. Chew, M. L. Goldberger, F. E. Low and Y. Nambu, *Relativistic Dispersion Relation Approach to Photomeson Production*, Phys. Rev. **106**, 1345 (1957).

[11] W.-T. Chiang and F. Tabakin, *Completeness rules for spin observables in pseudoscalar meson photoproduction*, Phys. Rev. C **55**, 2054 (1997).

[12] F. Härter, Ph.D. thesis, University of Mainz (1996).

[13] K. Büchler et al., *Photoproduction of positive pions from hydrogen with PHOENICS at ELSA*, Nucl. Phys A **580**, 570 (2001).

[14] D. Drechsel, O. Hanstein, S.S. Kamalow, L. Tiator, *Unitary Isobar Model - MAID2000*, Nucl. Phys A **145**, 645 (1999).

[15] W. Roberts and T. Oed, *Polarization observables for two-pion production off the nucleon*, Phys. Rev. C **71**, 055201 (2005).

[16] A. Braghieri et al., Phys. Lett. B **363**, 46 (1995).

[17] F. Härter et al., Phys. Lett. B **229**, 401 (1997).

[18] A. Zabrodin et al., Phys. Rev. C **55**, R1617 (1997).

[19] A. Zabrodin et al., Phys. Rev. C **60**, 055201 (1999).

[20] M. Wolf et al., Eur. Phys. J. A **9**, 5 (2000).

[21] V. Kleber et al., Eur. Phys. J. A **9**, 1 (2000).

[22] W. Langgärtner et al., Phys. Rev. Lett. **87**, 052001 (2001).

[23] M. Kotulla et al., Phys. Lett. B **578**, 63 (2004).

[24] A.V. Sarantsev et al., Phys. Lett. B **659**, 94 (2008).

[25] F. Zehr et al., Eur. Phys. J. A **48**, 98 (2012).

[26] V. Kashevarov et al., Phys. Rev. C **85**, 064610 (2012).

[27] Y. Assafiri et al., Phys. Rev. Lett. **90**, 222001 (2003).

[28] J. Ajaka et al., Phys. Lett. B **651**, 108 (2007).

[29] U. Thoma et al., *N^* and Δ^* decays into $N\pi^0\pi^0$*, Phys. Lett. B **659**, 87 (2008).

[30] M. Ripani et al., Phys. Rev. Lett. **91**, 022002 (2003).

[31] J. A. Gómez Tejedor and E. Oset, *Double pion photoproduction on the nucleon: study of the isospin channels*, Nucl. Phys. A **413**, 600 (1996).

[32] L. Y. Murphy and J-M. Laget, *Reaction mechanisms in two-pion pho- toproduction on the proton: I- Meson exchange picture*, DAPHNIA/SPhN pp. 96–10 (1996).

[33] J. C. Nacher et al., *The role of $\Delta(1700)$ excitation and ρ production in double pion photoproduction*, Nucl. Phys. A **295**, 696 (2001).

[34] K. Ochi, M. Hirata and T. Takaki, *Photoabsorption on a Nucleon in the* D_{13}(1520) *Resonance Energy Region*, Phys. Rev. C **56**, 1472 (1997).

[35] D. Krambrich et al., Phys. Rev. Lett. **103**, 052002 (2009).

[36] A. Fix and H. Ahrenhövel, *Double-pion photoproduction on nucleon and deuteron*, Eur. Phys. J. A **25**, 115 (2005).

[37] L. Roca, Nucl. Phys. A **192**, 748 (2005).

[38] U. Thoma et al., Phys. Lett. B **659**, 87 (2008).

[39] A.V. Sarantsev et al., Phys. Lett. B **94**, 659 (2008).

[40] *MAID*, `http://wwwkph.kph.uni-mainz.de/MAID//`.

[41] W. Langgärtner et al., *Direct observation of a rho-decay of the D13(1520) baryon resoance*, Phys. Rev. Lett. **87**, 052001 (2001).

[42] J. Ahrens et al., *Helicity dependence of the* $\vec{\gamma}p \to n\pi^+\pi^0$ *reaction in the second resonance region*, Phys. Lett. B **551**, 49 (2003).

[43] J.C. Nacher, E. Oset, Nucl. Phys., *Study of polarization observables in double-pion photoproduction on the proton*, Nucl. Phys. A **372**, 697 (2002).

[44] H. Holvoet, *Study of the helicity dependence of double pion photoproduction on the proton*, Ph.D. thesis, Universiteit Gent (2000).

[45] H. Holvoet, M. Vanderhagen, unpublished (????).

[46] H. Herminghaus et al., *The design of a cascaded 800 MeV normal conducting C.W. race track microtron*, Nucl. Instr. Meth. **138**, 1 (1976).

[47] K.-H. Kaiser et al., *The 1.5 GeV harmonic double-sided microtron at Mainz University*, Nucl. Instr. Meth. A **593**, 159 (2008).

[48] K. Aulenbacher, *Polarized beams for electron accelerators*, Eur. Phys. J. Spec. Top. **198**, 361 (2011).

[49] M. Dieterle, *Photoproduction of* π^0*-Mesons off Quasi-Free Proton and Neutrons*, Master thesis, Universität Basel (2010), `http://jazz.physik.unibas.ch/site/theses.html`.

[50] K. Aulenbacher, C. Nachtigall et al., *The MAMI source of polarized electrons*, Nucl. Inst. and Meth. A **391**, 498 (1997).

[51] D. Krambrich, *Aufbau des Crystal Ball-Detektorsystems und Unter- suchung des Helizitätsasymmetrie in* $\gamma p \to n\pi^+\pi^0$, Ph.D. thesis, Universität Mainz (2007).

[52] A. Schmidt, *Photoproduktion neutraler Pionen am Proton mit linear polarisierten Photonen im Bereich der Schwelle*, Ph.D. thesis, Universität Mainz (2001).

[53] H. Olsen and L.C. Maximon, *Photon and Electron Polarization in High- Energy Bremsstrahlung and Pair Production with Screening*, Phys. Rev. **114**, 887 (1959).

[54] A. Thomas, *Crystal Ball Hydrogen (Deuterium) Target manual* (2013).

[55] *A2 Collaboration Website* (2013), `http://wwwa2.kph.uni-mainz.de`.

[56] B. M. K. Nefkens for the Crystal Ball Collaboration, *Highlights of Crystal Ball Physics*, Mod Phys. A **20**, 1575 (2005).

[57] D. Werthmüller, *Experimental study of nucleon resonance contributions to* η*-photoproduction on the neutron*, Ph.D. thesis, Universität Basel (2013).

[58] E. F. McNicoll et al., *Experimental study of the* $\gamma p \to \eta p$ *reaction with the Crystal Ball detector at the Mainz Microtron (MAMI-C)*, Phys. Rev. C **82**, 035208 (2010).

[59] D. Watts, Calorimetry in Particle Physics, Proceedings of the 11th International Conference, Perugia, Italy, 2004, World Scientific, Singapore p. 560 (2005).

[60] R. Novotny, *The* BaF_2 *photon spectrometer TAPS*, IEEE Trans. Nucl. Sci. **38**, 379 (1991).

[61] A. R. Gabler et al., *Response of TAPS to monochromatic photons with energies between 45 and 790 MeV*, Nucl. Instr. Meth. A **346**, 168 (1994).

[62] S. Bender, *Aufbau und Test eines Bleiwolframat-Kalorimeters für das Crystal Ball/TAPS-Experiment an MAMI*, Diploma thesis, Universität Mainz (2009).

[63] M. Oberle et al., *Measurement of the beam-helicity asymmetry* $I^{\odot}$ *in the photoproduction of* π^0*-pairs off the proton and off the neutron*, Phys. Let. B **237**, 721 (2013).

[64] D. Krambrich, *Aufbau des Crystal Ball-Detektorsystems und Untersuchung der Helizitätsasymmetrie in* $\gamma p \to p\pi^0\pi^0$, Ph.D. thesis, Universität Mainz (2007).

[65] P. Drexler, *Entwicklung und Aufbau der neuen TAPS-Elektronik*, Ph.D. thesis, Universität Giessen (2004).

[66] J. R. M. Annand, *Data Analysis within an AcquRoot Framework* (2008), `http://www.nuclear.gla.ac.uk/~acqusys/doc/AcquRoot.11.08.pdf`.

[67] R. Brun and F. Rademakers, *ROOT - An Object Oriented Data Analysis Framework*, Nucl. Instr. and Meth. A **389**, 81 (1997).

[68] S. Agostinelli et al., *Geant4 - a simulation toolkit*, Nucl. Instr. Meth. A **506**, 250 (2003).

[69] J. Allison et al., *Geant4 developments and applications*, IEEE Trans. Nucl. Sci. **53**, 270 (2006).

[70] D. Glazier, *A Geant4 simulation for the CrystalBall@MAMI Setup* (2012), `http://www2.ph.ed.ac.uk/nuclear/G4/G4A2CBSimulation-06-12.pdf`.

[71] L. Witthauer, private communication (2012).

[72] K. Molenaar, *Performance of TAPS in the Tagged Photon Beam of MAMI*, Diploma thesis, Rijksuniversiteit Groningen (1992).

[73] T. C. Awes et al., *A simple method of shower localization and identification in laterally segmented calorimeters*, Nucl. Instr. Meth. A **311**, 130 (1992).

[74] *PDG Atomic and Nuclear Properties*, `http://pdg.lbl.gov/2012/AtomicNuclearProperties/index.html`.

[75] V. Hejny, *Photoproduktion von η-Mesonen an Helium 4*, Ph.D. thesis, Universität Giessen (1998).

[76] M. Pfeiffer, *Photoproduction of η mesons from ^{3}He*, Ph.D. thesis, Universität Giessen (2002).

[77] M. E. Röbig, *Eichung des TAPS-Detektorsystems mit Höhenstrahlung*, Diploma thesis, Universität Giessen (1991).

[78] J. C. McGeorge et al., *Upgrade of the Glasgow photon tagging spectrometer for Mainz MAMI-C*, Eur. Phys. J. A **37**, 129 (2008).

[79] J. C. McGeorge, *ugcalv2ua* (2010).

[80] T. C. Jude, *Strangeness Photoproduction off the Proton at Threshold Energies*, Ph.D. thesis, University of Edinburgh (2010).

[81] M. Unverzagt, *Bestimmung des Dalitz-Plot-Parameters α für den Zerfall $\eta \to 3\pi^0$ mit dem Crystal Ball am MAMI*, Ph.D. thesis, Universität Bonn (2008).

[82] S. Schumann, *Strahlungsbegleitete* π^0*-Photoproduktion am Proton*, Ph.D. thesis, Universität Bonn (2007).

[83] M. Dieterle, *Comparison of the Experimental Resolution in Case of Using a 1.76 or 4.76 cm* LD_2 *Target*, Master project work, Universität Basel (2009), `http://jazz.physik.unibas.ch/site/theses.html`.

[84] H. Olsen and L.C. Maximon, *Highlights of Crystal Ball Physics*, Phys. Rev. **114**, 887 (1959).

[85] M. Lacombe et al., *Parametrization of the deuteron wave function of the Paris N–N potential*, Phys. Lett. B **101**, 139 (1981).

[86] J. R. M. Annand, *The Glasgow/Mainz Bremsstrahlung Tagger Operations Manual* (2008).

[87] A.V. Anisovich et al., *Properties of baryon resonances from a multichannel partial wave analysis*, Eur. Phys. J. A **15**, 48 (2012).

[88] L. Witthauer, D. Werthmüller et al., *Quasi-free photoproduction of* η*-mesons off* ^{3}*He nuclei*, Eur. Phys. J. A **47**, 89 (2013).

[89] M. Dieterle, Ph.D. thesis, Universität Basel (in preparation).

[90] J. Beringer et al. (Particle Data Group), *Review of Particle Physics*, Phys. Rev. D **86**, 010001 (2012).

[91] M. Anghinolfi et al., *Behavior of the Be and C total photonuclear cross section in the nucleon resonance region*, Phys. Rev. C **47**, R922 (1993).

[92] N. Bianchi et al., *Total hadronic photoabsorption cross section on nuclei in the nucleon resonance region*, Phys. Rev. C **54**, 4 (1996).

[93] N.Bianchi et al., *Measurement of the total photonuclear cross section for* ^{238}U *photofission in the nucleon resonance region*, Phys. Lett. B **299**, 219 (1993).

Curriculum Vitae

Personal

Full name: Markus Oberle
Date of birth: January 15, 1982
Place of birth: Aarau, Switzerland

Education

2010–2014	Ph.D. studies at the University of Basel Ph.D. in Experimental Physics
2008–2010	Master studies at the University of Basel Master of Science in Physics
2004–2008	Bachelor studies at the University of Basel Bachelor of Science in Physics
1999–2003	Grammar school, Neue Kantonsschule Aarau Specialization in economics and law

Assistant Position

2010-2014	Teaching assistant: coordinator for excercices to introductory physics lectures

The following professors I would like to thank for their lectures:
PD Dr. A. Aste, Prof. G. Baur, Prof. B. Binggeli, Prof. C. Bruder, PD Dr. K. Hencken, Prof. S. Goedecker, Prof. H.-J. Hug, Prof. H.-C. Im Hof, Prof. N A'Campo, Prof. J. Jourdan, PD Dr. D. Kiselev (geb. Rohe), Prof. B. Krusche, Prof. D. Loss, Prof. E. Meyer, PD Dr. T. Rauscher, Prof. C. Schönenberger, Prof. F.-K. Thielemann, Prof. D. Trautmann

Acknowledgments

During all the time of this work I could benefit from the knowledge and the helfulness of many people. I would now like to thank them all and I hope I don't forget anyone.

At first I would like to thank B. Krusche for the opportunity to do a Ph.D. under his wings. I am very grateful for all the helpful discussions we had and all the good ideas he gave me. Thanks to him I also had the opportunity to go to several international conferences and this meant a lot to me.

For the very friendly and professional atmosphere we always had in our group I would like to thank: I. Jaegle, F. Pheron, Y. Maghrbi, R. Troyer, I. Keshelashvili, T. Rostomyan, D. Werthmüller, M. Dieterle, L. Witthauer, A. Käser, T. Strub and S. Garni. I really enjoyed working with all of you and I am very grateful for that.

As next I want to thank all the members of the A2 collaboration, it was a pleasure working with all of you.

And lastly I want to thank my parents and family, you all mean a lot to me and you always supported and motivated me. And of course to Valeria, te amo.